

Low-Stress UV-Curable Hyperbranched Polymer Nanocomposites for High-Precision Devices

THÈSE N° 4877 (2010)

PRÉSENTÉE LE 26 NOVEMBRE 2010

À LA FACULTÉ SCIENCES ET TECHNIQUES DE L'INGÉNIEUR
LABORATOIRE DE TECHNOLOGIE DES COMPOSITES ET POLYMÈRES
PROGRAMME DOCTORAL EN SCIENCE ET GÉNIE DES MATÉRIAUX

ÉCOLE POLYTECHNIQUE FÉDÉRALE DE LAUSANNE

POUR L'OBTENTION DU GRADE DE DOCTEUR ÈS SCIENCES

PAR

Valérie GEISER

acceptée sur proposition du jury:

Prof. K. Scrivener, présidente du jury
Prof. J.-A. Manson, Dr Y. Leterrier, directeurs de thèse
Prof. L. Berglund, rapporteur
Prof. J. Brugger, rapporteur
Dr E. Nouzille, rapporteur



ÉCOLE POLYTECHNIQUE
FÉDÉRALE DE LAUSANNE

Suisse
2010

ABSTRACT

The aim of this thesis was to investigate the process-structure-property relationships of UV-curable hyperbranched polymer (HBP)/silica nanocomposites. Special attention was paid to the interplay between photo-conversion, rheological behavior, shrinkage, and stress dynamics. This knowledge was used to maximize the shape fidelity and dimensional stability of imprinted nano-patterns made with these nanocomposites. Two different processing routes, resulting in different nanocomposite morphologies, were compared. The first and more conventional approach was ultrasonic, solvent-assisted mixing with solid silica nanoparticles followed by UV curing, which led to a discrete dispersion of silica particles in the matrix. The second and more novel approach was a dual-cure process combining UV and sol-gel processing with liquid tetraethyl orthosilicate. The sol-gel process, using a low-viscosity organometallic precursor, overcame the potential processing issue of the highly viscous particulate nanocomposites and led to a hybrid material with a homogeneous silica network at nanometer scale.

Rheological analysis of silica nanoparticle suspensions up to the concentrated regime in the HBP showed an exponential increase of the viscosity with the particle fraction for well-dispersed discrete particle systems. A liquid-to-solid transition occurred in the 5 to 10 vol% range, which was correlated with an immobilized layer of polymer hydrogen-bonded to the silanol groups on the surface of the particles, as was confirmed by calorimetric analysis.

Polymerization kinetics of HBP nanocomposites and hybrids were analyzed by means of photo differential scanning calorimetry using an autocatalytic model. A time-intensity-superposition principle with power-law dependence was established, which invalidated the classic radiation dose equivalence principle. Gelation and modulus build-up were monitored using photo-rheology. The calorimetric and rheological data were combined in the form of time-intensity-transformation diagrams. It was found that gelation was delayed with respect to conversion up to 36% when lower UV intensities were used, which favored reduce polymerization stresses.

The dynamics of polymerization shrinkage and internal stress build-up were investigated using photo-hyphenated interferometry and beam-bending methods. The linear shrinkage of the HBP was as low as 4.5%, which was further reduced to 3.3% with the addition of 20 vol% nanoparticles. The residual stress of HBP/SiO₂ nanocomposites was below 5.5 MPa. That is well below the level of standard non-reinforced resins, in spite

of an increased stiffness. For the sol-gel hybrids with 20 vol% SiO₂, stress reduction by 50% with simultaneous stiffness increase by 20% with respect to corresponding particulate composites was demonstrated. The coefficient of thermal expansion was also lowered by 30%.

Finally, nanogratings with a period of 360 nm and a step height of 12 nm were fabricated using UV-nanoimprint lithography with a glass or nickel master in a low-pressure (max. 6 bar) and rapid (≈ 1 min) process. Stable gratings were imprinted in the composite material containing up to 25 vol% of silica nanoparticles, despite the high viscosity of such compositions. Thanks to the exudation of a HBP-rich surface layer, the shape fidelity in terms of period of the replicated patterns was within 98% of the master, with shape distortion increasing with internal stress. The obtained nanogratings were used as a substrate for grating high refractive index TiO₂ waveguides and then applied as wavelength-interrogated optical sensors (WIOS). An immunoassay with the polymer WIOS showed the same ultrahigh detection sensitivity as the standard glass-based devices. Therefore, the novel polymer-based sensor should be useful to probe contaminants in liquids with concentrations as low as a few ppb.

Keywords: UV curing, photo-polymerization, hyperbranched polymer, internal stress, residual stress, nanoimprint lithography, wavelength-interrogated optical sensor.

KURZFASSUNG

Die Zielsetzung dieser Studie war die Untersuchung des Zusammenspiels von Herstellungsmethode, Struktur und Eigenschaften von UV-aushärtenden Nanoverbundwerkstoffen aus hochverzweigten Polymeren und Siliciumdioxid. Insbesondere wurden das Polymerisationsverhalten, rheologische Eigenschaften, Polymerisationsschrumpfung und die Entwicklung von Eigenspannungen untersucht, mit dem Ziel, Stabilität und Formtreue von Nanostrukturen zu verbessern, die mittels Nanoprägelithographie hergestellt wurden.

Zwei verschiedene Methoden zur Herstellung von Verbundwerkstoffen wurden untersucht, die zu verschiedenen Morphologien führten. Die erste, eher konventionelle Methode war das Mischen eines Nanopulvers mit dem Polymer im Ultraschall und nachfolgende UV-Polymerisation. Dies führte zu einer diskreten Verteilung der Nanopartikel in der Polymermatrix. Bei der zweiten, zuvor weniger untersuchten Methode handelte es sich um einen Zweistufen-Prozess, welcher zum ersten einen Sol-Gel Prozess mit flüssigem Tetraethylorthosilikat, und zum zweiten einen UV-Polymerisation-Schritt umfasste. Dank der geringen Viskosität des niedermolekularen anorganischen Vorläufers konnten die Probleme, welche bei der Verarbeitung von Verbundwerkstoff üblicherweise auftreten und ihre Ursache in den hohen Viskositäten beim Einmischen der Nanopartikel haben, vermieden werden. Das auf diese Weise erhaltene Material war durch das Vorliegen eines Siliciumdioxid-Netzwerks gekennzeichnet, dessen Morphologie im Nanometer-Bereich sich als homogen erwies.

Rheologische Untersuchungen der Nanopartikel-Suspensionen zeigten eine exponentielle Abhängigkeit der Viskosität vom Partikelgehalt. Dies galt für gut dispergierte Suspensionen bis zu hohen Konzentrationen, bei denen zudem ein Übergang von flüssigem zu festem Verhalten im Bereich von 5-10 vol% beobachtet wurde. Dieser Übergang wurde auf eine Immobilisierung von Polymerketten auf der Oberfläche der anorganischen Partikel zurückgeführt, die durch Wasserstoffbrückenbindungen mit Silanolgruppen auf der Partikeloberfläche vermittelt wurde. Dieser Zusammenhang wurde durch kalorimetrische Untersuchungen bestätigt.

Die Reaktionskinetik der Polymerisation wurde mittels eines Photo-Differential-Scanning-Kalorimeters untersucht und auf der Grundlage eines autokatalytischen Modells analysiert. So wurde ein Zeit-Intensität-Überlagerungsprinzip gefunden, das einem

Potenzgesetz folgte, während sich das üblicherweise erwartete klassische Strahlungsenergie-Gesetz als nicht zutreffend erwies.

Gelbildung und die Zunahme des Schermoduls während der UV-Aushärtung wurden mittels Photorheologie untersucht. Die Resultate konnten zusammen mit kalorimetrischen Daten in Zeit-Intensität-Umsatz-Diagrammen dargestellt werden. Damit konnte gezeigt werden, dass bei kleinen UV-Intensitäten die Gelbildung erst bei erhöhtem Polymerisationsumsatz (bis zu 36%) stattfindet, wodurch kleinere Eigenspannungen zu erwarten sind.

Durch eine interferometerbasierte Methode wurde die Polymerisations-schrumpfung gemessen. Sie konnte durch die Zugabe von 20 vol% Nanopartikel gegenüber dem reinen Polymer um 33% verringert werden. Die Eigenspannungen, die während der Vernetzung entstanden, wurden aus der Krümmung von Verbundwerkstoff-beschichteten Aluminiumlamellen bestimmt. Die Verbundwerkstoffe wiesen Werte unter 5.5 MPa auf, was trotz der höheren Steifigkeit solcher Materialien deutlich unter den Werten von Standard-Polymeren liegt. Für Sol-Gel-Verbundwerkstoffe mit 20 vol% SiO₂-Gehalt wurde gegenüber den konventionell hergestellten Verbundwerkstoffen eine Spannungsreduktion um 50% bei gleichzeitigem Steifigkeitsgewinn um 20% und um 30% reduziertem Wärmeausdehnungskoeffizient gemessen.

Durch UV-Nanoprägelithographie mit einem Nickel- oder Glas-Formstück wurde ein Rasterprofil mit einer Periodizität von 360 nm und einer Stufenhöhe von 12 nm hergestellt. Dazu waren nur ein kleiner Druck (max. 6 bar) und kurze Durchlaufzeiten (≈ 1 min) nötig. Stabile Rasterprofile aus Verbundwerkstoffen mit einem Gehalt von bis zu 25 vol% SiO₂ konnten hergestellt werden, trotz der hohen Viskosität solcher Materialien. Dank der Ausscheidung von einer polymerreichen Phase an der Profiloberfläche wurde eine Formtreue in Bezug auf die Periodizität von 98% erzielt, aber eine Zunahme der Eigenspannungen führten zu Profildeformation.

TiO₂-Wellenleiter auf einem Polymersubstrat mit Rasterprofil wurden in einem wellenlängenabhängig angesteuerten optischen Sensor verwendet. Dieser neuartige Polymersensor zeigte eine ebenso niedrige Nachweisgrenze für Verunreinigungen in flüssigen Reagenzien wie der Standard-Glassensor, die in der Größenordnung von wenigen ppb lag.

Schlüsselwörter: UV Aushärten, Photo-polymerization, hochverzweigte Polymere, Eigenspannungen, Nanoprägelithographie, wellenlängenabhängig angesteuerter Sensor.

ACKNOWLEDGEMENTS

I gratefully acknowledge the provision of funding for the work described in this thesis from the Swiss National Science Foundation. I would like to thank Prof. Jan-Anders E. Månson, the director of my thesis, for giving me the opportunity to work on this interesting project in his laboratory.

My special thanks go to Dr. Yves Leterrier, my thesis co-director, for his excellent scientific guidance, availability for discussions and motivating enthusiasm towards this project in general and any new results in particular.

I am obliged to Prof. Marco Sangermano from Politecnico di Torino and Dr. Guy Voirin from CSEM for fruitful discussions and for allowing me to perform measurements in their laboratories. I would like to thank Dr. Riccardo Ruggerone, Dr. Young-Hyun Jin and Dr. Sara Dalle Vacche from LTC for their significant scientific contributions. Dr. Max Wiki from Dynetix, Dr. Rosendo Sanjines and Dr. Jean-Marc Vesin from EPFL also have agreed to help me without hesitation at essential moments of this project. I would like to thank Yannick Roulin from LTC and the team of the IMX workshop for their availability in various matters.

Further, I would like to thank Henrik Bernquist from Perstorp AB for the continuous supply of materials throughout this project. The companies Momenite, Clariant and Degussa also provided me with samples, which I gratefully acknowledge.

The time at LTC was very pleasant, thanks to the members of this lab. At the beginning of my PhD, my first office mate told me that our office had always had and would always have the best vibes. His prophecy has come true! Thank you Christian, Chrystèle, Robert and Charly for the pleasant atmosphere, your support, and especially all the good laughs we had. I am very happy to have met Chiara and Sandra, who became good friends during numerous coffee breaks and dinners, of which we will hopefully have many more in the future. A very big thank you goes to Sabrina, Sarah, Doro and all my other dear friends from “home” for having crossed fingers whenever it was necessary.

The most important acknowledgement that I will make goes to my parents for always being so incredibly proud of me!

TABLE OF CONTENTS

1	INTRODUCTION	15
1.1	OBJECTIVE AND CHALLENGES	17
1.2	OUTLINE.....	19
2	STATE OF THE ART	23
2.1	POLYMERIZATION SHRINKAGE AND INTERNAL STRESS.....	23
2.1.1	<i>Strategies for Shrinkage and Stress Reduction</i>	<i>24</i>
2.1.2	<i>Surface Instabilities</i>	<i>26</i>
2.2	HYPERBRANCHED POLYMERS	27
2.3	PHOTO-POLYMERIZATION.....	30
2.3.1	<i>Free-Radical and Cationic Polymerization.....</i>	<i>30</i>
2.3.2	<i>Kinetics of Photo-Polymerization.....</i>	<i>31</i>
2.3.3	<i>Shrinkage and Stress in UV-Curable Polymers</i>	<i>33</i>
2.3.4	<i>Gelation, Vitrification and Time-Intensity-Transformation Diagrams.....</i>	<i>34</i>
2.3.5	<i>Influence of Filler on Reaction Kinetics</i>	<i>35</i>
2.4	COMPOSITES	35
2.4.1	<i>Nanocomposites.....</i>	<i>36</i>
2.4.2	<i>Hybrid Sol-Gel Composites</i>	<i>38</i>

2.5	NANOSTRUCTURES.....	41
2.5.1	<i>Nanostructures in Biosensors.....</i>	41
2.5.2	<i>Nanostructuring of Polymers</i>	42
3	MATERIALS AND METHODS	45
3.1	MATERIALS.....	45
3.1.1	<i>Hyperbranched Polymer.....</i>	45
3.1.2	<i>Photoinitiator</i>	47
3.1.3	<i>Silica Nanopowder.....</i>	48
3.1.4	<i>Precursor and Coupling Agent for Sol-Gel Process.....</i>	49
3.1.5	<i>Sample Preparation.....</i>	50
3.2	EXPERIMENTAL METHODS.....	51
3.2.1	<i>UV Lamp.....</i>	51
3.2.2	<i>UV-VIS Absorption.....</i>	51
3.2.3	<i>Thermo-Gravimetric Analysis (TGA)</i>	52
3.2.4	<i>Rheology.....</i>	52
3.2.5	<i>Photo-Rheology</i>	52
3.2.6	<i>Differential Scanning Calorimetry (DSC).....</i>	53
3.2.7	<i>Modulated Differential Scanning Calorimetry (MDSC).....</i>	53
3.2.8	<i>Photo Differential Scanning Calorimetry (PHOTO-DSC)</i>	54
3.2.9	<i>Shrinkage: Photo-Interferometry</i>	54
3.2.10	<i>Internal Stress: Beam Bending.....</i>	57
3.2.11	<i>Dynamic Mechanical Analysis (DMA).....</i>	58
3.2.12	<i>Thermo-Mechanical Analysis (TMA)</i>	58
3.2.13	<i>Transmission Electron Microscopy (TEM)</i>	59
3.2.14	<i>Surface Roughness: Profilometer.....</i>	59
3.2.15	<i>Atomic Force Microscopy (AFM)</i>	59
3.2.16	<i>Nuclear Magnetic Resonance (NMR).....</i>	60
4	RHEOLOGICAL BEHAVIOR AND IMMOBILIZED POLYMER FRACTION OF CONCENTRATED HBP/SILICA SUSPENSIONS.....	63
4.1	MICROSTRUCTURE	64
4.2	INFLUENCE OF NANOFILLER ON RHEOLOGICAL BEHAVIOR.....	64
4.3	INFLUENCE OF NANOFILLER ON GLASS TRANSITION BEHAVIOR	69
4.4	LIQUID-TO-SOLID TRANSITION	71
4.5	IMMOBILIZED POLYMER IN HBP/SILICA SUSPENSIONS.....	74
4.5.1	<i>Viscosity Increase and Effective Particle Fraction</i>	74
4.5.2	<i>Modeling of AS Suspensions.....</i>	75
4.5.3	<i>Modeling of HL Suspensions.....</i>	78
4.5.4	<i>Discussion on the Exponential Scaling of the Viscosity</i>	79
4.5.5	<i>Calorimetric Aspects of Polymer Immobilization</i>	81
4.5.6	<i>Discussion</i>	84
4.6	SUMMARY.....	86

5	PHOTO-CALORIMETRY, PHOTO-RHEOLOGY AND TIME-INTENSITY-TRANSFORMATION DIAGRAMS.....	89
5.1	PHOTO-CALORIMETRIC ANALYSIS.....	90
5.1.1	Conversion and Conversion Rate.....	90
5.1.2	Time-Intensity Superposition	92
5.1.3	Influence of Silica Particles on Conversion.....	93
5.2	CONVERSION MODELING.....	95
5.2.1	Influence of Intensity.....	95
5.2.2	Influence of Composition and Nanostructure	99
5.3	PHOTO-RHEOLOGICAL ANALYSIS.....	101
5.3.1	Modulus and Phase Data	101
5.3.2	Influence of Intensity.....	102
5.4	TIME-INTENSITY-TRANSFORMATION DIAGRAMS.....	104
5.5	SUMMARY.....	106
6	SHRINKAGE AND STRESS DYNAMICS AND THERMO-MECHANICAL ANALYSIS .	109
6.1	SHRINKAGE DYNAMICS	109
6.2	SHEAR MODULUS DYNAMICS.....	113
6.3	INTERNAL STRESS DYNAMICS.....	115
6.4	STRESS RELAXATION BY SURFACE WRINKLING	118
6.5	THERMO-MECHANICAL PROPERTIES.....	124
6.5.1	Thermal Stability.....	124
6.5.2	Glass Transition Temperature.....	124
6.5.3	Dynamic Mechanical Analysis.....	125
6.5.4	Coefficient of Thermal Expansion	127
6.6	SUMMARY.....	129
7	SOL-GEL HYBRID NANOCOMPOSITES	133
7.1	DUAL-CURE PROCESS	133
7.2	PHOTO-CALORIMETRIC ANALYSIS.....	139
7.2.1	Autocatalytic Conversion Modeling	142
7.3	PHOTO-RHEOLOGY AND TIME-INTENSITY-TRANSFORMATION DIAGRAMS	144
7.4	THERMO-MECHANICAL PROPERTIES AND INTERNAL STRESS.....	148
7.5	SUMMARY.....	152
8	NANOSTRUCTURING AND APPLICATION TO OPTICAL SENSORS.....	155
8.1	UV-NANOIMPRINT LITHOGRAPHY PROCEDURE.....	156
8.2	PROCESS INFLUENCES ON SHAPE FIDELITY OF HBP COMPOSITE NANOGRATINGS	157
8.2.1	Photo-Cured Grating Data	157
8.2.2	Discussion on Process-Structure Relations.....	161
8.2.3	Summary of Grating Formation Process.....	163
8.3	HYBRID SOL-GEL NANOGRATINGS.....	164
8.4	APPLICATION TO OPTICAL SENSORS	167

8.4.1	<i>Detection Principle</i>	167
8.4.2	<i>HBP Composite WIOS</i>	168
8.4.3	<i>Laser Coupling Test</i>	169
8.5	IMMUNOASSAY	171
8.6	SUMMARY.....	172
9	CONCLUSIONS	175
9.1	SUMMARY OF THE RESULTS.....	175
9.2	MAIN ACHIEVEMENTS.....	179
9.3	OUTLOOK.....	179
	APPENDIX A – LIST OF SYMBOLS AND ACRONYMS	183
	SYMBOLS	183
	ACRONYMS	187
	APPENDIX B – MDSC PROTOCOL	189
	REFERENCES	193
	PUBLICATIONS RELATED TO THIS WORK	212
	JOURNAL PUBLICATIONS.....	212
	CONFERENCES.....	212
	CURRICULUM VITAE	213
	EDUCATION.....	213
	WORK EXPERIENCE.....	213

1 INTRODUCTION

Three-dimensional patterns with dimensions in the nanometer range, so called nano-patterns (Figure 1-1), are used in various applications, such as optical sensors¹, transistors², lab-on-a-chip devices³, and spectrometers⁴. The efficiency of such devices is strongly dependent on the geometric accuracy of the patterns, the reason for which dimensionally stable materials such as glass and silicon are often selected, in spite of high cost. Polymers are thus increasingly investigated as a low-cost alternative.⁵⁻⁷ High throughput of nano-patterns and devices with a resolution under 10 nm can be achieved with cost-effective methods such as nanoimprint lithography^{8,9}. However, the main drawback of polymers is the lack of dimensional stability^{10,11}, due to excessive levels of internal stress resulting from polymerization shrinkage¹² and cool-down from the process temperature¹³. Combined with low stiffness, high coefficient of thermal expansion¹⁴ and surface tension driven viscous flow¹⁵, these stresses lead to distortion and eventual decay of the nano-pattern.

Approaches towards stress reduction include photo-polymerization^{16,17} with UV light, an extremely rapid crosslinking method that transforms liquid precursors into rigid solids within a few seconds. The process is carried out at room temperature; therefore, thermal stresses only result from possible exothermic effects and are usually negligible. Photo-polymerization in combination with nanoimprint lithography was successfully implemented for the production of nano-patterns.^{18,19} The introduction of an inorganic non-shrinking phase into the polymer matrix is also effective to reduce overall shrinkage, e.g., shrinkage reduction from 7% to 2.5% was achieved with the addition of 57 vol% glass filler.²⁰ The composite approach is attractive, because it also improves the thermo-mechanical stability of small-scale structures, thanks to increased hardness, stiffness, scratch resistance, and reduced coefficient of thermal expansion.²¹⁻²⁵ However, an increase in the stiffness of the material can have a disadvantageous effect on the internal stress, as has been shown for highly filled dental composites.²⁶

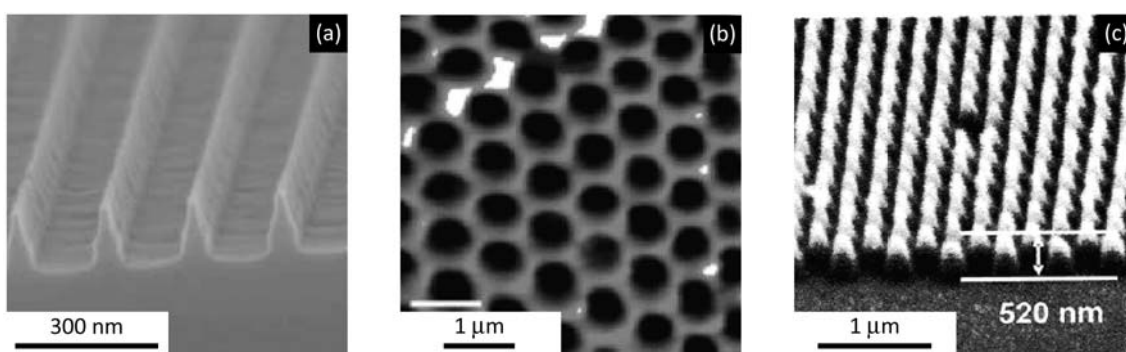


Figure 1-1 Examples of nano-patterns. (a) GaAs pattern produced by electron beam lithography²⁷, (b) polyaniline honeycomb produced by electropolymerization around assembled colloids and subsequent etching of the colloids²⁸, and (c) PMMA pattern produced by nano-casting²⁹.

For UV-curable formulations, the filler has to be in the nanometer range to prevent scattering of the light on the particles and to ensure transparency of the material. In this case, even small amounts of nanofiller drastically alter the viscoelastic properties of the material, transforming the liquid-like polymer into a solid-like composite paste.³⁰⁻³³ This represents a challenge for processing, and the problem is often overcome with the use of solvents. A cheaper and more environmentally friendly solution is *in situ* sol-gel processing, where the inorganic phase is formed through condensation of an organometallic precursor inside the polymer matrix. *In situ* sol-gel chemistry was successfully applied in combination with photo-polymerization.³⁴⁻³⁶ The microstructure of this class of composites has shown to be very different from the particulate composites³⁷

and, therefore, distinct differences in mechanical behavior can be expected between particulate nanocomposites and hybrid sol-gel composites.

A further approach towards shrinkage reduction is the use of hyperbranched polymers (HBP)^{38,39}. HBP are macromolecules that are characterized by a highly branched structure and multiplicity of reactive chain-ends. They belong to the family of dendritic polymers⁴⁰⁻⁴², but are less perfectly branched than the monodisperse dendrimers. HBP have very distinct rheological properties, i.e., they show low Newtonian viscosity even at high molecular weight, owing to their globular structure and absence of entanglements.³⁸ Acrylated HBP were demonstrated to have significantly lower shrinkage and internal stress than standard acrylates.⁴³⁻⁴⁵ Schmidt *et al.*⁴⁶ at LTC have demonstrated twofold stress reduction and a simultaneous stiffness increase by a factor of 1.6 for a UV-curable polymer material based on acrylated HBP.

In combination with nanoparticles, the low viscosity of the HBP should be useful to postpone the liquid-to-solid transition (which compromises nanocomposite processing) to higher particle loadings. The rheology of nanoparticle suspensions in HBP has however not been studied, apart from the work on HBP/clay nanocomposites carried out at LTC.³²

1.1 OBJECTIVE AND CHALLENGES

The objective of this thesis was to investigate the process-structure-property relations of UV-curable HBP/silica nanocomposites, with particular attention paid to the interplay of conversion, shrinkage and stress build-up. A schematic drawing of the interplay of parameters and properties is shown in Figure 1-2.

These nanocomposites were expected to demonstrate improved mechanical properties, thermal stability, and reduced coefficient of thermal expansion over their unreinforced equivalents. In order to evaluate the potential of these materials for the application to high-precision nano-structured devices, the goal was to fabricate a nano-scale grating by low-pressure UV-nanoimprint lithography; these nanogratings were then supposed to be applied in wavelength-interrogated optical sensors⁴⁷.

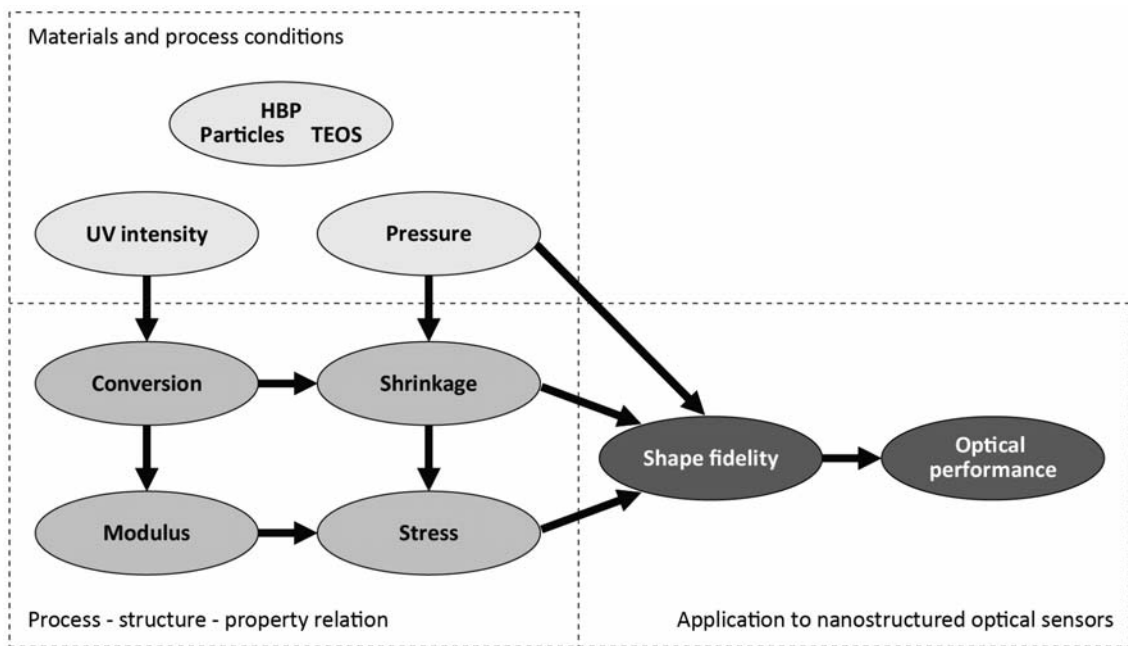


Figure 1-2 Interplay between composition, process conditions and materials properties, and influence on the shape fidelity of nano-devices.

The three main challenges that were identified in this project were:

- to produce highly filled transparent nanocomposites, due to the liquid-to-solid transition resulting from the high specific surface area of the filler;
- to determine the shrinkage and stress dynamics in the extremely fast polymerizing UV-curable systems; and
- to produce devices with structure in the nanometer scale, comparable to the size of the inorganic phase.

In order to approach these challenges, two different nanocomposite processing routes were evaluated. One was solvent-assisted mixing of a nanopowder with the HBP, and the other was the *in situ* formation of the inorganic phase by condensation of an organometallic precursor (sol-gel processing) inside the polymer matrix. UV-hyphenated techniques were employed to monitor the fast evolving shrinkage and stress dynamics with high time resolution. Nano-sized gratings were then produced with the HBP/silica nanocomposites, and the shape fidelity and ultimate resolution of the gratings were investigated as a function of pressure and composition.

1.2 OUTLINE

A schematic outline of the thesis is shown in Figure 1-3. Chapter 2 presents a thorough review of the literature covering all relevant aspects to this work. Chapter 3 details the hyperbranched polymer and different inorganic powders that were chosen for the UV-curable nanocomposites.

In a first step, the rheological and glass transition behavior of the nanocomposites was investigated and the results and their analysis form Chapter 4. The rheological analysis was of great importance for the future production of high-fidelity nanostructures.

In a second step, the kinetics of network formation and the occurrence of gelation, which determines the internal stress of the material, were analyzed in the form of time-intensity-transformation diagrams, as detailed in Chapter 5.

In view of the application of these materials to high-precision devices, the dynamics of shrinkage and internal stress build-up during photo-polymerization and the thermo-mechanical properties of the cured material are important to understand and are addressed in Chapter 6.

The processing and resulting properties of dual-cured hybrid sol-gel nanocomposites are described in Chapter 7 and the results are compared to the nanocomposites prepared by conventional mixing.

As both types of nanocomposites showed highly interesting thermo-mechanical properties and low stress, these materials were then applied to the production of nanostructures and optical sensors and the results are discussed in Chapter 8. Chapter 9 concludes the work and provides an outlook to future research interest.

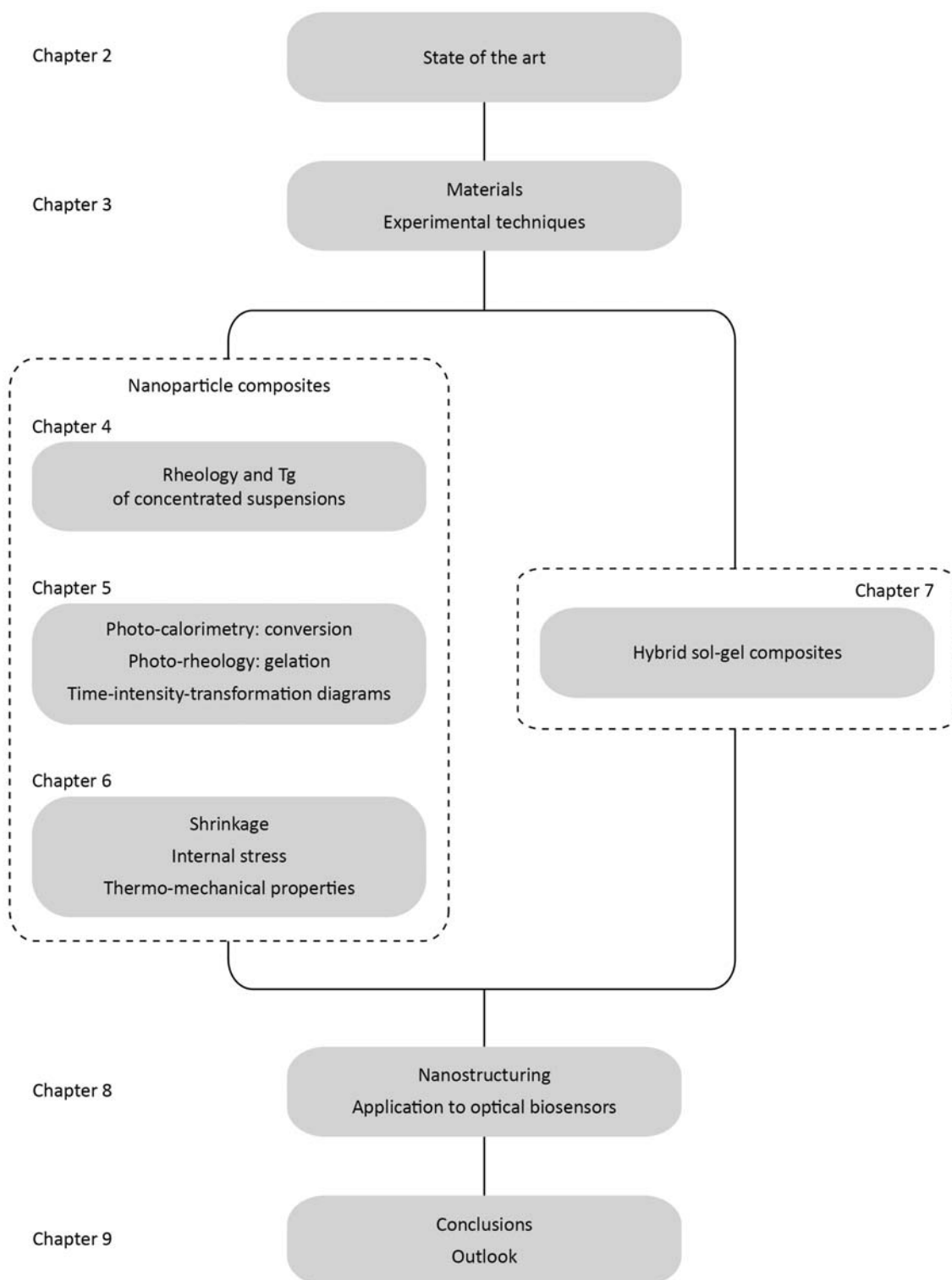


Figure 1-3 Outline of thesis.

2 STATE OF THE ART

2.1 POLYMERIZATION SHRINKAGE AND INTERNAL STRESS

Internal stress in polymers is a consequence of shrinkage,⁴⁸⁻⁵⁴ which occurs, for example, during solidification as a result of solvent evaporation, phase transformation, chemical reaction and coalescence, or from thermal expansion mismatch, e.g., with a substrate. In acrylates volume shrinkage due to polymerization reaction can be as high as 20%.⁵⁵ Polymerization shrinkage values of 6.9% for an epoxy resin⁵⁶, 8% for SU8⁵⁷, and 9.3% for PDMS⁵⁸ were reported. If the shrinkage is constrained, e.g., by a rigid substrate or reinforcement, the shrinkage will cause internal stresses to arise.

The origin of polymerization shrinkage is attributed to a change in interatomic spacing between molecules. Before polymerization, monomer molecules are about 4 Å apart. During polymerization, the interatomic spacing is replaced by single covalent bonds of about 1.5 Å length.^{55,59,60} Hence, shrinkage and stress are directly related to conversion (Figure 2-1).^{61,62}

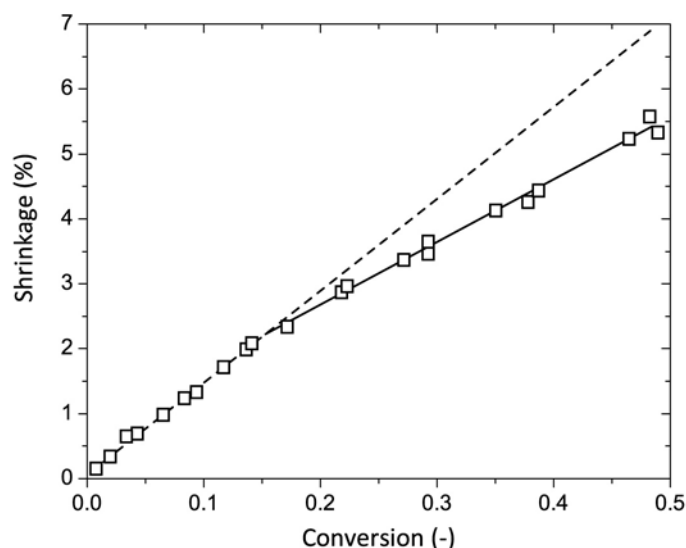


Figure 2-1 Relationship between shrinkage and conversion during the photo-polymerization of hydroxy-ethyl-bisphenol A-dimethacrylate. Figure adapted from⁶³.

2.1.1 Strategies for Shrinkage and Stress Reduction

Several approaches enable to reduce, counteract, or even suppress shrinkage. Low-shrinkage materials are based on large molecular weight monomers,^{55,64} which contain only few functional groups per volume, and hence only form few intermolecular bonds. The drawback of such materials is, however, the increase in viscosity and related processing difficulties following the empirical Mark Houwink equation:

$$[\eta] = x \cdot M^{a_{MH}} \quad 2.1$$

where $[\eta]$ is the intrinsic viscosity, M is the molecular weight, x and a_{MH} are constants for a given polymer with a_{MH} between 0.65 and 0.75 for linear random-coil polymers.⁶⁵

Various formulations that polymerize or copolymerize without shrinkage or even with expansion in volume have been studied.⁶⁶⁻⁶⁸ Spiroorthocarbonates, for example, expand their volume by as much as 10% during polymerization, due to the release of their initially compact structure by a ring-opening reaction.⁶⁹

Thermoplasts that phase separate with the crosslinking phase, so called “low-profile” additives, are also known to reduce the polymerization shrinkage.⁷⁰ Microvoids, which increase the overall volume, are formed as the mixture cools down from the process temperature, due to the differential thermal shrinkage between the phases.

Hyperbranched polymers⁴⁰ (HBP), which will be discussed in detail in Section 2.2, also exhibit low shrinkage and residual stress. And thanks to their globular structure and absence of entanglements, they show low Newtonian viscosities even at high molecular

weight. A 30% stress reduction was reported upon addition of 14 wt% epoxy-functionalized HBP in an epoxy resin.⁴⁵ This was due to increased relaxation capacity of the epoxy network during crosslinking and a stress concentration mechanism at the epoxy/HBP interface. The increased relaxation capacity was attributed to a delay in modulus build-up of the HBP compared to the epoxy resin. Schmidt *et al.*⁴⁴ found an optimum ratio of an acrylate resin with an acrylate-functionalized HBP to reduce the residual stress and simultaneously increase the Young's modulus above the level of the pure components.

Scott *et al.*⁷¹ reported a crosslinked polymer that, upon exposure to light, exhibited stress and/or strain relaxation. This was achieved by reversible cleavage of the polymer backbone to allow chain rearrangement without mechanical property degradation.

The introduction of a non-shrinking inorganic phase into the polymer matrix is a further route to reduce the overall shrinkage.^{20,24,64,68} 64% shrinkage reduction was achieved upon addition of 53 vol% inorganic particles.²⁰ Especially in dental restorative practice, composite resins are commonly used to reduce microcracks at the tooth/resin interface and related postoperative problems.⁷²⁻⁷⁴ However, in the case of highly filled dental composites an increase in stiffness of the material also increased the internal stress.²⁶ Replacing the silane-treated filler, which provides chemical bonding between the two phases, with untreated filler, reduced the polymerization stress by 25%.⁷⁵ Fillers also have an influence on the double-bond conversion, which will be discussed in Section 2.3.

Another common strategy to reduce stress is the adjustment of the temperature cycle of the cure with the attempt to relax stress at high temperatures.^{76,77} For example, in a conventional epoxy system no stresses developed during the reaction and subsequent cool-down above the glass transition temperature T_g . It was only when the temperature dropped below T_g that stress started to build up.¹³ In acrylates, on the other hand, considerable stress developed already during the polymerization reaction above T_g .¹³

In UV curing, which is usually conducted at room temperature, thermal stresses are negligible and would in fact result from exothermic effects. UV intensity cycles⁷⁸, in particular a combinations of initial slow polymerization (at low UV intensity) and then fast polymerization (at high UV intensity), the so called "soft-start"^{79,80} cure, was used to further reduce polymerization stress.

The sample geometry also plays a role in determining the level of internal stress, as it depends on the ratio of bound to unbound surface.^{72-74,81-83} Furthermore, stress

relaxation can take place through the formation of surface instabilities, as discussed in the following section.

2.1.2 Surface Instabilities

The mechanism of wrinkle formation (Figure 2-2) in curing coatings has been investigated in several studies.⁸⁴⁻⁹⁰ It was found that a depth-wise gradient in cure from the exposed surface of a coating inwards is a prerequisite for the formation of wrinkles. The surface layer of the coating solidifies first and emerges as a surface skin above a still liquid underlayer. Subsequently, in-plane compressive stress has to be generated in the surface skin, which then buckles out of plane and creates wrinkles.

The compressive stress in the surface layer can have different origins, e.g., from diffusion of unreacted monomer of the underlayer into the crosslinked skin and subsequent swelling⁸⁷, solvent absorption⁹¹, differential thermal expansion^{92,93} or shrinkage of the underlayer⁹⁴.

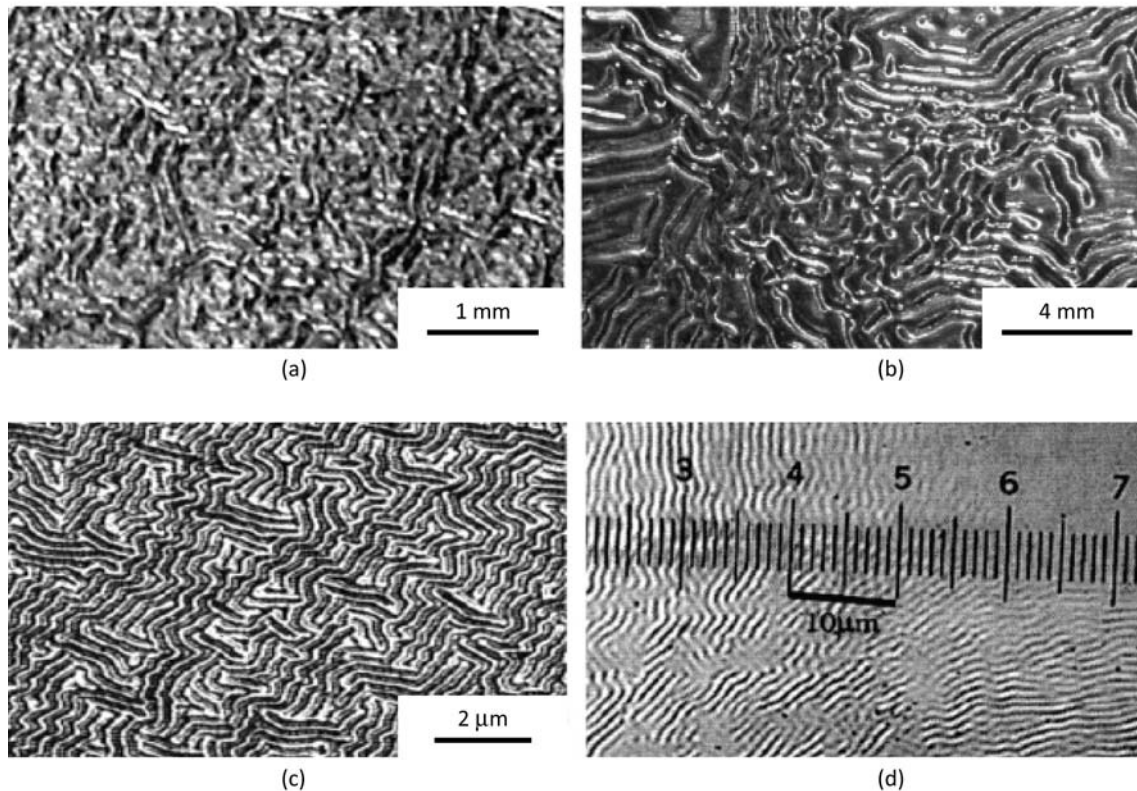


Figure 2-2 (a) Epoxy-based powder coatings, (b) liquid applied alkyd coating, (c) thin layer of metal deposited on hot elastomeric substrate by chemical vapor deposition, put in compression by cooling, and (d) compressively strained SiGe film on BPS glass, patterns formed during annealing. Figure taken from⁸⁷.

It was found that the wrinkle wavelength depended on the thickness and modulus of the surface skin, the in-plane compressive stress generated in the skin at the onset of wrinkling, as well as the time for complete gelation of the coating.^{84,87} In terms of viscosity it was stated that 10 Pa·s was an upper limit for wrinkling to occur.⁹⁵

Another possible wrinkle mechanism was established by Luciani *et al.*⁸⁶, who claimed that the subsurface material underwent a more rapid cure than both the surface layer and the layer in contact with the substrate. In the surface layer the curing reaction was inhibited by oxygen from the atmosphere, and in the layer in contact with the substrate the UV intensity was reduced, due to light absorption by the coating. If the stress relaxation through wrinkle formation is hindered by the rigidity of the material or a rigid substrate, high internal stresses build up. Therefore, Luciani's wrinkled coatings showed much lower internal stress and better long-term stability than non-wrinkled coatings. It is also possible to quantify residual stress in thin (<1 μm) polymer films via surface wrinkling.⁹⁶

Hierarchically wrinkled coatings^{97,98} were produced by stretching a viscoelastic film and modifying its surface by ultraviolet/ozone treatment. The mismatch in the equilibrium state of the skin and the substrate provoked wrinkling. Buckling instability patterns were also seen under mechanical in-plane compression of nanomembranes⁹⁹ and due to phase separation.^{100,101}

2.2 HYPERBRANCHED POLYMERS

HBP belong to the family of dendritic polymers, which are characterized by a highly branched structure and multiplicity of reactive chain-ends.⁴⁰ Dendrimers⁴² are produced in an iterative sequence of reaction steps, in which each additional iteration leads to a higher generation material, as shown in Figure 2-3.

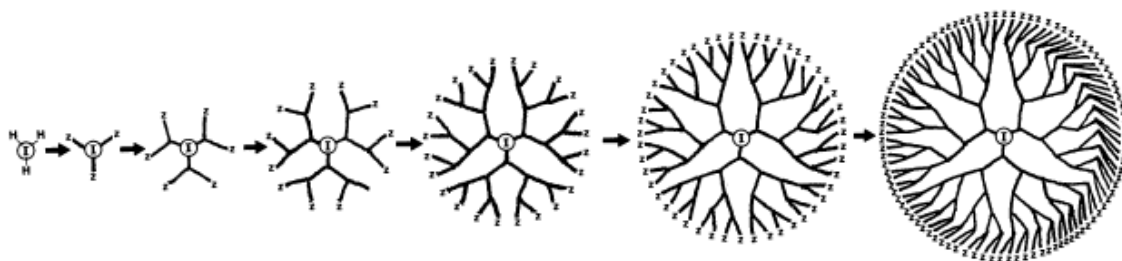


Figure 2-3 Stepwise synthesis of a dendrimer. Figure taken from¹⁰².

The first example of an iterative synthetic procedure towards well-defined branched structures has been reported as “cascade synthesis”¹⁰³ and in the early 1980s dendrimers were investigated thoroughly by Tomalia^{102,104} and Newkome¹⁰⁵.

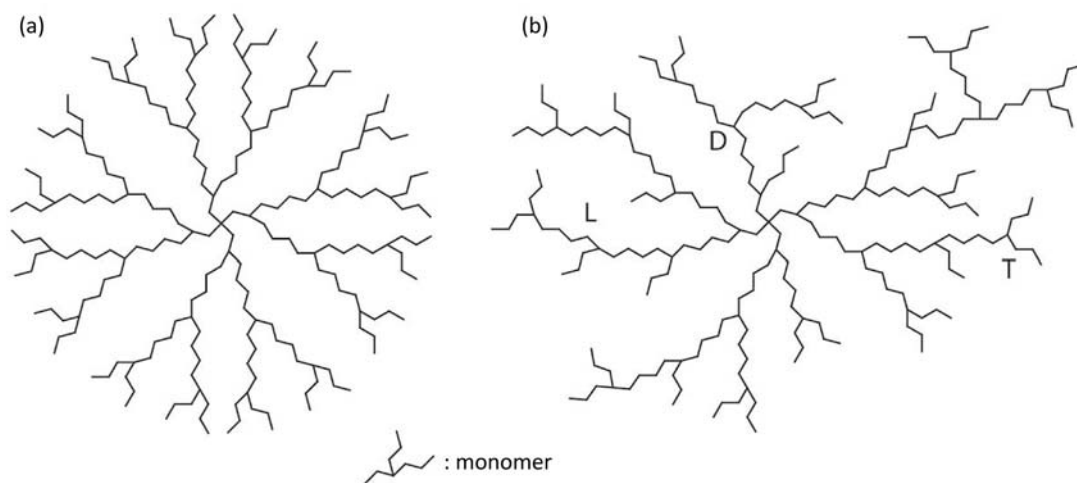


Figure 2-4 (a) Dendrimer and (b) hyperbranched polymer. L = linear, D = dendritic, T = terminal unit.

Dendrimers present perfect structural symmetry, a degree of branching D_B (Equations 2.2 and 2.3) equal to 1, and a precise number of end-groups. On the other hand, HBP are less perfectly branched and their structure is intermediate between those of linear polymers and dendrimers (Figure 2-4). They are synthesized in a one-step process by polycondensation of an A_2B monomer that contains two reactive groups of type A and one of type B.¹⁰⁶⁻¹⁰⁸ The functional groups A and B are selected in such a way that they react with each other to form a covalent bond. This process is very rapid compared to the stepwise synthesis of dendrimers, but leads to a D_B smaller than 1 (usually around 0.6),¹⁰⁶ because some of the A groups remain unreacted, leading to the incorporation of linear segments within a globular ensemble. The DB is calculated according to Fréchet¹⁰⁸ or Frey¹⁰⁹:

$$D_{B, \text{Fréchet}} = \frac{N_D + N_T}{N_D + N_L + N_T} \quad 2.2$$

$$D_{B, \text{Frey}} = \frac{2N_D}{2N_D + N_L} \quad 2.3$$

where N_D , N_L , N_T are the number of dendritic, linear and terminal units, respectively. Dendrimers exhibit properties that are unlike those of all other families of macromolecules, e.g., a maximum in intrinsic viscosity as a function of molecular weight

(Figure 2-5).³⁹ In general they have significantly lower viscosities than linear polymers of the same molecular weight.¹¹⁰ When polyether dendrimers were compared with their linear isomers, differing features became obvious after the 5th generation.¹¹¹ The hydrodynamic volume of the dendrimer was 30% smaller than that of its linear analogue, due to the more compact globular structure. Moreover, the dendrimer was completely amorphous and soluble in a variety of organic solvents, whereas the linear analogue was highly crystalline and poorly soluble in THF, acetone and chloroform.

Despite the imperfect branching, the globular structure of the HBP leads to similar rheological properties as the dendrimers, i.e., they exhibit low viscosity at high molecular weight.^{65,112} The Mark-Houwink parameters (Equation 2.1) a_{MH} were found to be between 0.3 and 0.4 or less.⁴¹ As the viscosity is related to the intermolecular interactions, it strongly depends on the nature of the functional groups.³⁸ The low viscosity of HBP in combination with their availability through simple processes, makes them an attractive low-cost alternative to the rather expensive dendrimers.

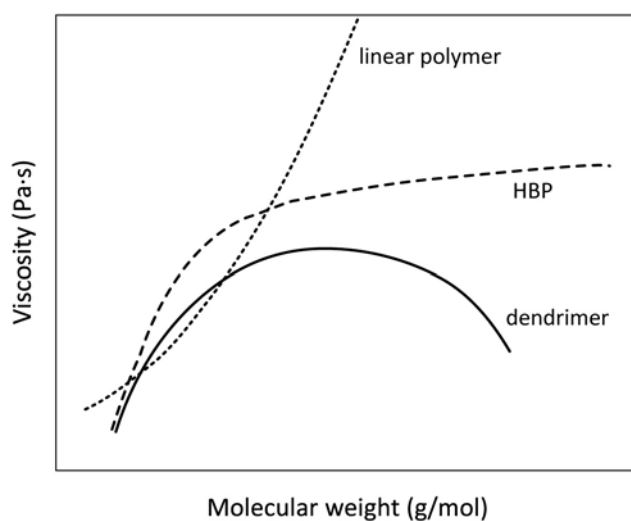


Figure 2-5 Viscosity of dendrimers, hyperbranched polymers and linear polymers as a function of molecular weight.

Applications of dendrimers and HBP include low viscosity toughening additives to thermosets,^{45,113-115} which don't affect the thermo-mechanical properties, as this is usually the case for rubber toughened resins.^{116,117} HBP were also used in composite materials,^{21,32,118-120} where they are claimed to facilitate filler dispersion.^{43,121,122} In clay nanocomposites they promoted exfoliation of the clays and stabilized the exfoliated structure after drying.²⁵ The globular structure, combined with a large number of polar

end-groups, and the relatively hydrophobic core prevented the molecules from collapsing onto the clay layers.¹²³

Dendrimers were used to encapsulate guest molecules into their internal cavities.^{124,125} The slow diffusion out of the “dendrimer box” enabled controlled release of drugs¹²⁶ or fragrances¹²⁷. Due to their high reactivity, dendrimers are also interesting materials for catalysts, with the advantage that the molecules are readily recoverable after the reaction from the solvent streams by ultrafiltration methods.¹²⁸

The surface chemistry of the HBP is easily adjustable and makes them versatile additives.^{65,110,129-134} For example, fluorinated¹³⁵ and alky-functionalized¹³⁶ HBP increased the hydrophobicity, thermal stability, and solvent resistance, when added to a resin. UV-curable HBP¹³⁷⁻¹⁴¹ have attracted interest due to their very fast polymerization reaction.

2.3 PHOTO-POLYMERIZATION

Photo-induced polymerization with UV light is an efficient method for the generation of highly crosslinked polymers from multifunctional monomers.^{17,142-144} It is used extensively for the ultrafast drying of printing inks, varnishes and protective coatings⁸⁶, the latter being utilized for the protection of virtually any substrate such as wood, plastics, metal, glass, optical fibers, leather, paper, and fabrics.^{145,146} It has also found extensive applications for adhesives and dental restorative formulations.^{68,79,147}

2.3.1 Free-Radical and Cationic Polymerization

For the UV curing process a small amount of a photosensitive initiator^{80,148} is added to the monomer liquid. During irradiation with UV light this photoinitiator is transformed into free-radicals or a cation that are able to initiate the polymerization and crosslinking reaction. The free-radical process has commercial predominance, because it is cheaper, better known and a big variety of monomers with high reactivity are on the market. Cure rates for cationic polymerization tend to be slower than for free-radical systems.¹⁴⁹ Nevertheless, the cationic process presents some advantages over the free-radical process. These are in particular the lack of oxygen inhibition^{150,151}, lower cure shrinkage, and the generally less toxic and irritant monomers.^{133,135} An overview of the characteristics of free-radical and cationic polymerization is given in Table 2-1.

Table 2-1 Overview of characteristics of free-radical and cationic UV curing.⁴⁶

	Free-radical	Cationic
Materials	e.g., acrylates	e.g., epoxies
Growth	chain growth	step growth
Oxygen inhibition	sensitive	not sensitive
Cure speed	very high	medium
Shrinkage	high	low
Conversion at gelation	1-15%	30-70%
Skin irritation by monomers	high	low

UV-curable monomers are stable in the dark. Upon switching on the light, polymerization starts immediately and at high rate. This easy external control of the reaction start is very convenient for production. In the case of free-radical polymerization, the reaction occurs only in illuminated areas, which enables the generation of high resolution images for the production of printing plates, optical discs and microcircuits. Cationic polymerization is also called “living” polymerization, because once initiated, it continues in the dark.¹⁵²

2.3.2 Kinetics of Photo-Polymerization

High molecular weight monomers have the advantage to crosslink at a relatively low light dose, allowing for low photoinitiator concentration, weak light source and/or faster line speed. Therefore, HBP were investigated in several studies as photo-polymerizable resins^{16,129,132,153,154} or additives^{130,133,135,136} for the production of highly crosslinked materials.

The polymerization behavior and kinetics were modeled in numerous studies based on the phenomenological autocatalytic model (Figure 2-6a).¹⁵⁵⁻¹⁵⁸ This model is described in more detail in Chapter 5. Autoacceleration occurs during the initial stage of polymerization, when the mobility of the radical species becomes restricted due to the formation of a polymer network. This affects mainly the termination step, which becomes diffusion controlled, thus leading to an increase of the radical concentration and hence of the polymerization rate. Autodeceleration is generally observed in the later stages of the polymerization reaction, i.e., when the propagation reaction becomes diffusion controlled. The decreased mobility of the propagating radical and the unreacted monomers leads to a

slow-down of the polymerization reaction. Eventually, the reaction stops due to vitrification before complete conversion is achieved.

Many parameters on the cure kinetics of photo-polymers were investigated. It was concluded that the conversion rate increased with increasing UV intensity, photoinitiator concentration, functional group or monomer concentration, and temperature.¹⁵⁹⁻¹⁶⁴ The ultimate conversion also increased as the curing temperature was raised,¹⁶⁵ because the final stage of the reaction was diffusion controlled.

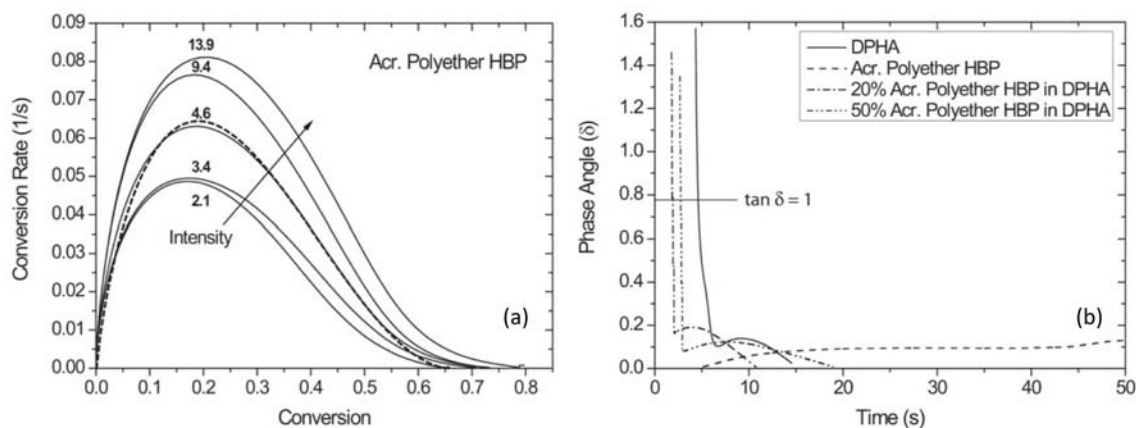


Figure 2-6 (a) Double bond conversion rate as a function of conversion measured by photo-DSC. The dotted line represents the fit of the autocatalytic model. Figure taken from¹⁶. (b) Phase angle as a function of polymerization time measured by photo-rheology. Figure taken from⁴⁴.

For the dependence of the ultimate conversion on the UV intensity different studies showed inconsistent results. For example, it was shown that higher UV intensity led to higher conversion^{16,159}, while in other studies it was found that using the same energy level (intensity · polymerization time) the same conversion was achieved.^{79,147,166} In the first case, the trend was explained with the fact that under certain conditions the polymerization shrinkage created non-equilibrium volume conditions, i.e., the specific volume was bigger than the equilibrium value. The resulting excess volume allowed higher mobility and diffusivity to the reacting species than they would have had at the equilibrium. As the conversion level, at which the reaction would have stopped (if the system were at equilibrium), was approached, the excess volume allowed for further reaction and the maximum conversion increased.

Multifunctional acrylates can crosslink so readily that even at low conversion tightly crosslinked microgels¹⁶⁷⁻¹⁷² can form, that are still soluble in the polymer liquid. The more the formation of microgels is favored, the more the formation of rigid network is delayed. The process of solidification is shown in Figure 2-7.

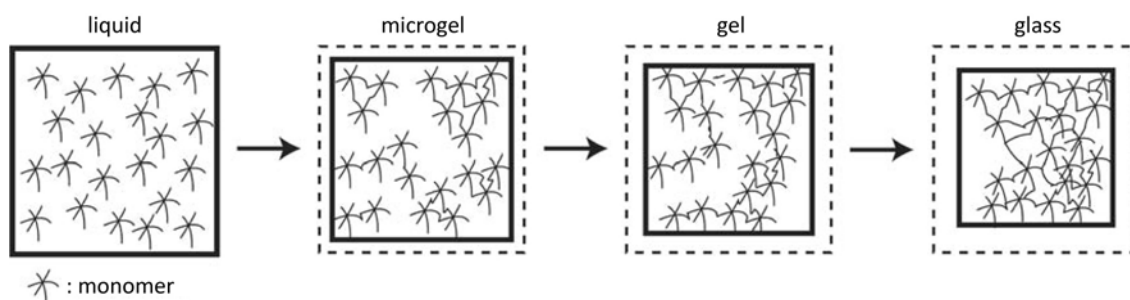


Figure 2-7 Schematic of gel formation with previous formation of microgel structure. The conversion of the monomer into a glassy solid is accompanied by volume shrinkage. Figure taken from⁴⁶.

2.3.3 Shrinkage and Stress in UV-Curable Polymers

As shrinkage is related to conversion, in the case of photo-polymers it may also be related to UV intensity. In some cases, polymerization contraction was found to increase with UV intensity,^{173,174} whereas in other cases, exothermic temperature rise expanded the volume and reduced the shrinkage at high intensities.¹⁷⁵

In all those cases, high intensities lead to high conversion rates in photo-polymers, equivalent to high temperatures in thermosetting polymers.¹⁷⁶ The conversion rate is an important factor with respect to volume relaxation and shrinkage dynamics. When the relaxation time of the forming polymer becomes too long to follow the volume change induced by crosslinking, the volume is no longer at its equilibrium. This is also the case after vitrification⁶³, where the polymer passes from a rubbery to a glassy state. Chain movements are restricted after vitrification (i.e., the relaxation time is very high) and shrinkage is no longer able to keep up with conversion, hence excess volume is generated. Despite the excess volume, significant stresses rise after vitrification,^{44,76,174,177} due to the increased elastic modulus of the material in the glassy state. Moreover, the excess volume allows additional mobility for the reactive chain ends, leading to higher ultimate conversion,¹⁴³ and hence higher ultimate stress. Shrinkage that occurs before the gel point, defined as the moment when a 3-dimensional network first spans throughout the entire material volume, is compensated by flow and does not induce stress.⁷⁹

To understand the dynamics of shrinkage and stress, it is crucial to understand the interplay between conversion, conversion rate, volume relaxation and structure build-up (gelation, vitrification).

2.3.4 Gelation, Vitrification and Time-Intensity-Transformation Diagrams

Three criteria are generally used to determine the occurrence of gelation: i) from photo-rheology^{178,179} experiments as the crossover of the storage and loss moduli,¹⁸⁰ i.e., when the tangent of the phase angle δ is equal to 1 (Figure 2-6b), ii) as the point, where the phase angle is independent of the frequency,¹⁷⁸ or iii) as the maximum in the conversion rate *versus* conversion curve (Figure 2-6a) derived from photo-DCS experiments.

Vitrification is also determined by photo-rheology when $\tan(\delta)$ as a function of curing time goes through a maximum,^{178,181} or as a departure from the diffusion-controlled kinetic behavior.¹⁶ In the case of epoxies, vitrification is a distinct event, occurring separately from gelation. In the acrylates vitrification starts immediately after gelation, the two events being sometimes hardly distinguishable, and lasts until the end of the reaction.⁴⁹

Time-intensity-transformation (TIT) diagrams^{44,182} are analogous to the time-temperature-transformation diagrams^{181,183,184} for thermosetting resins. They were elaborated by combining conversion data with the occurrence of gelation and vitrification, and present a tool to choose the optimum processing conditions to achieve low polymerization stress. The investigation of the influence of filler on conversion, gelation and vitrification, and the compilation in TIT diagrams, is an objective of the present work.

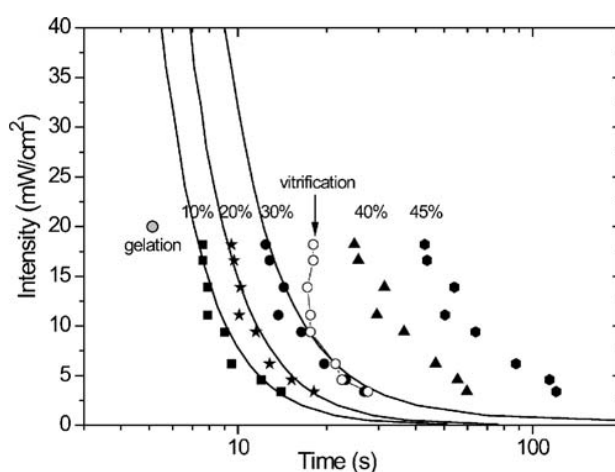


Figure 2-8 Time-intensity-transformation diagram for an acrylated hyperbranched polymer. Figure taken from⁴⁴.

2.3.5 Influence of Filler on Reaction Kinetics

UV curing is also widely used for the curing of composite components.¹⁸⁵ In many cases the same autocatalytic model as for the unfilled resins could be used to describe the cure behavior of composites.¹⁸⁶⁻¹⁸⁸ However, different studies led to different conclusions about the influence of the filler on the conversion rate and maximum conversion. Three scenarios were found in literature:

Firstly, the filler did not affect the degree of conversion^{20,188,189} and the reaction rate was the same as for the pure resin.¹⁹⁰ If the filler was produced by sol-gel processing prior to polymerization, the presence of unreacted precursor slowed down the reaction, but did not affect the final conversion.¹⁹¹

Secondly, nanocomposites with TiO₂ in epoxy acrylate showed decreased polymerization rate in comparison with the pure resin, because the TiO₂ particles strongly absorbed the UV light.¹⁹² In another study the conversion was reduced with the filler, which was claimed to be because reacting monomer adsorbed on the filler surface and was less mobile.¹⁹³ Similarly, fillers slowed down the reaction rate, due to lower reactivity of the functional groups grafted to the particles.^{194,195} Silica filler was also shown to decrease the time for gelation and vitrification to occur.¹⁹⁶

In the third case, filler particles accelerated the reaction rate of UV-curable acrylate systems, which was claimed to be due to the synergistic effect of silica nanoparticles during the photo-polymerization process, which also led to higher ultimate conversion.^{187,197} Montmorillonite clay increased the polymerization rate, because the ions in the organically modified clay catalyzed the curing reaction. In that case the conversion behavior deviated from the autocatalytic model.¹⁹⁸

2.4 COMPOSITES

The use of particulate materials for enhancement of polymer properties dates back to the earliest years of the polymer industry. Initially used as extending agents to reduce the cost of polymer-based products, fillers were soon recognized to overcome the limitations of polymers, such as low stiffness and low strength, and to improve their thermo-mechanical properties. A strong correlation between filler volume and elastic modulus¹⁹⁹⁻²⁰², compressive yield stress²⁰³, scratch resistance²⁰⁴, thermal stability^{191,205,206}, glass transition temperature²⁰⁷⁻²⁰⁹, coefficient of thermal expansion²¹⁰⁻²¹², as well as optical²¹³⁻²¹⁹ and physical properties like gas permeation²²⁰⁻²²⁴ was demonstrated. More

and more, composites are used as photoresists with high etch resistance²²⁵⁻²²⁷, thermally imprintable resists²²⁸, and as resist for UV-imprinting²²⁹⁻²³⁴ of dimensionally stable and high precision nanostructures.

Filler/matrix interfacial interactions play an important role in determining the thermo-mechanical properties of a composite.²³⁵⁻²³⁸ Fillers that are treated to improve wetting show better scratch resistance than untreated fillers.^{23,239,240} The interfacial interactions also dominate the rheological behavior of nanocomposite melts.²⁴¹⁻²⁴⁴ Hence, numerous studies can be found on the surface modification of fillers.²⁴⁵⁻²⁴⁹

2.4.1 Nanocomposites

The properties of composites with filler dimensions ranging from micrometer to a few millimeters do not profoundly depend on the size of the fillers. If filler dimensions are decreased down to a few nanometers, the effect on properties such as thermal stability^{250,251} and reinforcement²⁵²⁻²⁵⁵ becomes much more important. This is a consequence of the extremely large specific interfacial area and very short distance²⁵⁶ between reinforcing particles.

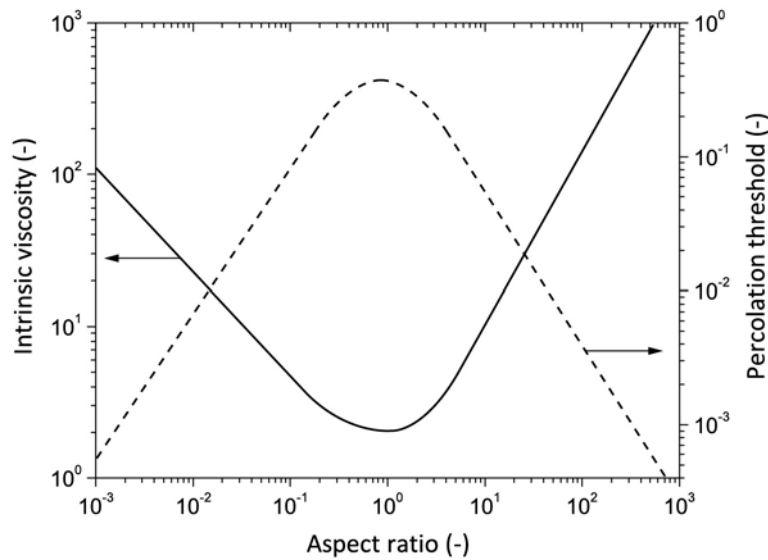


Figure 2-9 Percolation threshold and intrinsic viscosity as a function of filler aspect ratio. Figure adapted from²⁵⁷.

The last two decades have seen the emergence of so called nanocomposites, where the filler has at least one dimension in the nanometer range. The three families of discrete particle composites that have attracted most attention are carbon nanotube

composites^{211,258-261}, clay nanocomposites²⁶²⁻²⁶⁶, and spherical inorganic particle composites^{254,267-269}, of which amorphous SiO₂ particle composites are the most common.

Various models have been developed to predict the mechanical properties of carbon nanotube composites²⁷⁰, clay composites²⁷¹, or spherical particle composites^{272,273}. Amongst many others, models for the CTE²⁷⁴⁻²⁷⁶, tensile creep behavior²⁷⁷, filler/matrix interface formation²⁷⁸, and dielectric properties²⁷⁹ have been established. The shape of the particles^{257,280}, and in particular the aspect ratio, is an important factor that determines the percolation threshold and resulting rheological behavior (Figure 2-9).²⁸¹⁻²⁸⁴

Already small quantities of nanofillers can have a considerable effect on reinforcement. For example, addition of 0.1% of carbon nanotubes into an epoxy had a measurable effect on reinforcement²⁸⁵ and 10% of carbon nanotubes in polystyrene increased the storage modulus by 49%.²⁸⁶ Another advantage of nanocomposites is their transparency to visible and UV light, the latter being especially important if photopolymerization is used.

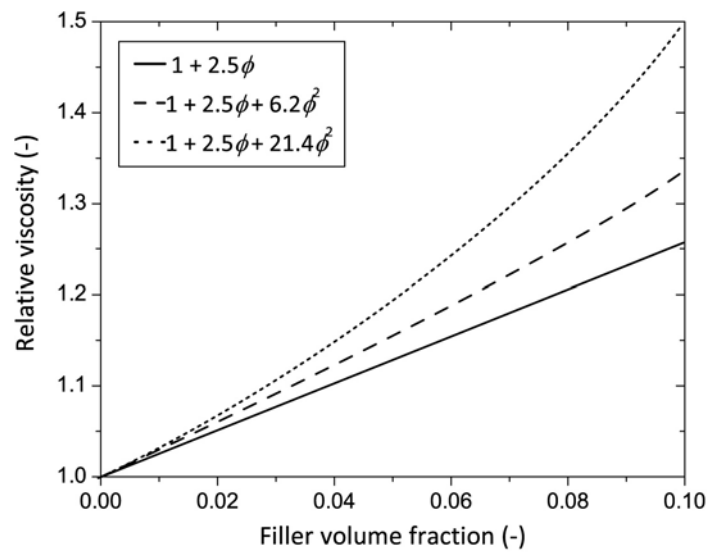


Figure 2-10 Relative viscosity of dispersions of spherical particles. Einstein model for the dilute regime (filler fraction < 0.02, solid line). Models for the semi-dilute regime (filler fraction > 0.02) considering the interparticle interaction in good solvents (dashed line) and poor solvents (dotted line). Figure adapted from²⁵⁷.

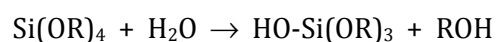
However, the claimed benefits of nanocomposites rely on a good dispersion of the particles, which is usually associated with processing problems. In fact, small amounts of nanoparticles drastically alter the viscoelastic properties of the material, transforming the liquid-like polymer into a solid-like composite paste.^{30,31,33,269,287,288} The liquid-to-solid transition is a major challenge for nanocomposite processing and is often overcome with the use of solvents.

For microfillers, the critical volume fraction, beyond which the viscosity diverges towards infinity, is $\phi^* \approx 0.64$ for random close-packed spherical particles at low shear rate and $\phi^* \approx 0.7$ at high shear rate.²⁸⁹ For nanoparticles the liquid-to-solid transition was found to occur at a particle fraction as low as 10%.^{284,290} Several studies concluded that this low ϕ^* was observed for strong interfacial interactions, which resulted in an immobilized layer of polymer adsorbed on the surface of the particles, and in confinement effects between particles.^{31,243,291} The degree of immobilization as well as the thickness of the immobilized layer was correlated to the affinity between matrix and particles. Due to the high specific surface area of nanoparticles, the fraction of immobilized matrix can be quite large, hence the strong increase in viscosity, exceeding by far the one predicted by classic models (Figure 2-10). As an example, a 200-fold increase in viscosity was found when 3.4 wt% fumed silica was added to a cyanate ester.²⁶⁷ Similar findings were reported for entangled²⁹² and non-entangled²⁹³ polymer melts. The presence of an immobilized polymer layer near the particle surface was also suggested from changes in the glass transition temperature of less than 100 nm thick supported polymer films,²⁹⁴⁻²⁹⁶ of which the equivalence with nanocomposites was established by Bansal *et al.*²⁹⁷ For both, supported thin films and polymer nanocomposites a gradient in T_g in the interfacial region and the suppression of physical aging was proposed.²⁹⁸⁻³⁰⁰

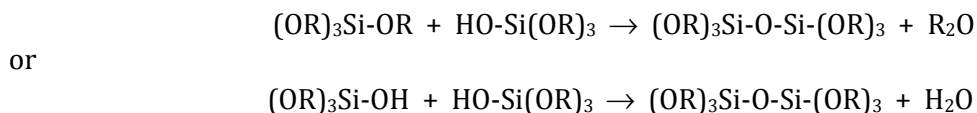
A solution to overcome processing problems of nanocomposites due to the high viscosity is the use of an organometallic liquid precursor, to form the inorganic phase *in situ* in the polymer matrix, as will be elaborated in the following section.

2.4.2 Hybrid Sol-Gel Composites

Sol-gel processing describes the synthesis of an inorganic phase from a liquid organometallic precursor. Metal alkoxides in the form of $M(OR)_4$, where M is usually Si or Ti, are popular precursors because they react readily with water. The most common silica precursor is tetraethyl orthosilicate (TEOS, Figure 3-8a), where $R = CH_2CH_3$, but also other ligands are possible.³⁰¹ The first reaction step is hydrolysis, where hydroxyl ions attach to the metal atoms, as in the following reaction:



Two partially hydrolysed molecules can link together in a condensation reaction, such as:



Silicon alkoxides are not very reactive, but their reaction rates can be adjusted by using acid, base or nucleophilic catalysts.³⁰² The reaction of the titanium alkoxides, on the other hand, is difficult to control.

Sol-gel processing was initially only used for the formation of inorganic monolithic structures or hard films.³⁰³⁻³⁰⁵ However, this process suffered from drawbacks such as crack formation in coatings, brittleness of sols or high sintering temperatures necessary for complete densification. These limitations were overcome by adding organic modifiers³⁰⁶ to the inorganic network to promote the elasticity of the gel. It was shown that only 5% of star alkoxy silane molecules (Figure 2-11) into the inorganic network during sol-gel synthesis substantially improved the toughness, with a Young's modulus within a factor of 2 of that of the inorganic glass. The modified glass showed much higher energy to break and compression strength.³⁰⁷

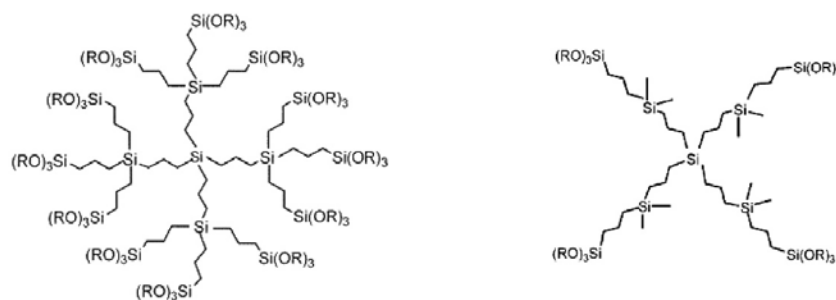


Figure 2-11 Two examples of a star alkoxy silane molecule, varying in number of the reactive alkoxy silane groups. Figure taken from³⁰⁷.

For sol-gel processing of organic/inorganic hybrids the monomer and a liquid organometallic precursor are mixed in the liquid state, allowing for a very homogeneous distribution of the reactants on a molecular level. Good dispersions have been obtained using *in situ* sol-gel^{302,308-311} formation of inorganic particles inside the polymerized matrix, in particular in the case of SiO_2 ^{312,313} or TiO_2 ^{314,315}.

The pH plays an important role in determining the morphology of the forming silica phase. At $pH \leq 2$ hydrolysis is faster than condensation, leading to fine silica particles, whereas at higher pH the particles aggregated.³¹⁶ If a low pH is combined with the use of a coupling agent, a very fine silica structure (2-5 nm), intertwined with the polymer network is expected.^{35-37,317,318} In Figure 2-12 the two different morphologies are sketched.

A coupling agent is a molecule that contains different functional groups that allow on one hand the copolymerization with the organic matrix, and on the other hand the condensation with the silica network. An example of a coupling agent used for the radical polymerization of acrylates is shown in Figure 3-8b. The addition of the coupling agent induces covalent bonds between the organic and inorganic phase, which is crucial to obtain a high performance material. The coupling agent also reduces the size of the inorganic domains by pinning the inorganic phase to the matrix, therefore preventing macroscopic phase separation.^{34,319}

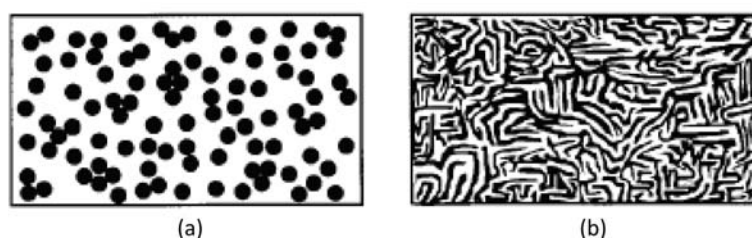


Figure 2-12 Schematisation of composites prepared by (a) mixing of the polymer with a nanopowder and (b) sol-gel process using a coupling agent. Figure taken from³⁷.

Manufacturing output of sol-gel-based materials is compromised by the processing conditions such as condensation time (up to 24 h³²⁰) and temperature (around 80°C). Long cure times are required when applying such coatings to thermoplastic substrates with low heat tolerance. Another issue is shrinkage during drying or from evaporation of byproducts. Drying shrinkage can be minimised by working without solvents and by minimising the amount of water engaged in the hydrolysis reaction.³⁰⁹

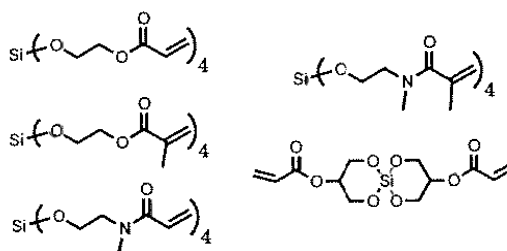


Figure 2-13 Sol-gel precursors for low-shrinkage composites. Figure taken from³¹¹.

Another approach is the use of tetraalkyl orthosilicate derivatives that contain polymerizable alkoxide groups in place of the standard ethoxide groups.³¹¹ During hydrolysis and condensation these four equivalents of polymerizable alcohols are liberated and then incorporated into the polymer network. Hence, no byproducts are

evaporated and large scale shrinkage is avoided. A few examples of such low-shrinkage sol-gel precursors are shown in Figure 2-13.

Sol-gel processing has been used also in combination with hyperbranched polymers^{121,191,315,321} and UV polymerization^{191,194,322}.

2.5 NANOSTRUCTURES

The production of nanostructures can be achieved by two different strategies. With the “bottom up” approach the nanostructure self-assemble into the required shape from smaller elements. The nanostructuring of solid-state materials is more often done by “top down” lithography, starting from a monolithic piece of material. Typically, this employs a polymer resist layer that is sensitive to light of a certain wavelength and etch resistant in the transfer step. A pattern is transferred from a mask to the resist by imprinting or energetic particle (electron, photon, ion) exposure, and from the resist to the underlying layer by etching. The etching step, which can be done dry (by sputtering) or wet (chemically), is the time-limiting step in the total lithography process.

2.5.1 Nanostructures in Biosensors

For many current applications in the point-of-demand (outside laboratory) and point-of-care (near patient) fields biochemical substances in a gas or liquids have to be measured with high resolution. A salient example is the monitoring of antibiotics in liquid food (e.g., milk), due to the misuse of antibiotics in animal industry, with the risk of bacteria resistance also in humans.³²³⁻³²⁵

Integrated optics is one well-known technique for the detection of (bio-)molecules and has been used for many years. Optical sensors include uniform grating couplers³²⁶⁻³²⁸, chirped grating couplers³²⁹, surface plasmon resonators³³⁰⁻³³², resonant mirrors³³³, and Young interferometers³³⁴. The sensitivity of such devices strongly depends on the precision of the coupling and resonator functions. Both are realized using nano-scale grating patterns (Figure 2-14), for which dimensionally stable materials such as glass are often selected, in spite of high fabrication cost. Polymers are thus increasingly used as a low-cost alternative.^{5,6}

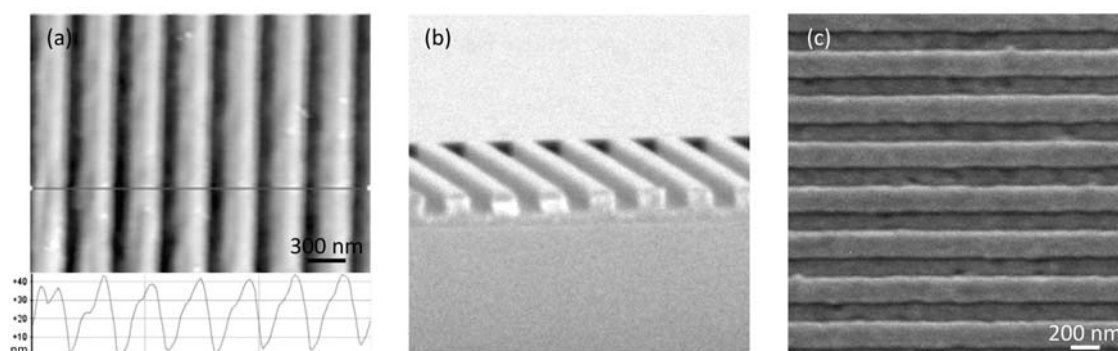


Figure 2-14 Examples of nanostructures in biosensors. (a) Polycarbonate grating for surface plasmon resonance, produced by laser interference⁵, (b) epoxy resin Bragg grating filter, period: 515 nm, depth: 200 nm, produced by soft lithography⁶, and (c) PMMA grating for coupled waveguide surface plasmon resonance, produced by reactive ion etching³³⁰.

2.5.2 Nanostructuring of Polymers

Polymer nanostructures are produced with the same “top down” process used for the resist patterns as described above, without the need of the time-consuming etching of an underlying substrate. Hence, the process is faster and cheaper than the structuring of solid-state material. Table 2-2 lists the various lithography methods available to date. The resolution of the pattern depends on the type of exposure³³⁵, and is basically limited by the wavelength of the radiation. Exposure types include UV light, X-ray, electron or ion beam.

Table 2-2 Characteristics of the different lithography methods. (+) = favorable, (–) = less favorable.

Method	Minimum resolution	Cost	Throughput
Ultraviolet light lithography	500 nm	+	+
X-ray lithography	50 nm	–	+
Electron beam lithography	5-10 nm	–	–
Ion beam lithography	10 - 50 nm	–	–
Laser interference lithography	20 nm	+	+
Atomic force microscope lithography	10-20 nm	–	–
Nanoimprint lithography	5 nm	+	–
UV-nanoimprint lithography	5 nm	+	+

Other nano-patterning methods include atomic force microscope lithography³³⁶, focused ion beam lithography³³⁷ or “bottom up” approaches such as block copolymer micelle nanolithography³³⁸, direct imprinting techniques³³⁹⁻³⁴², and others^{28,343-346}.

Nanoimprint lithography (NIL) was first reported by Chou^{347,348} and is nowadays a well established contact lithography technique. The principle is based on the mechanical modification of a thin polymer film with a stamp containing a nano-pattern. NIL allows for low-cost and high-throughput production of nano-patterns and devices with sub-10 nm resolution.⁸ If combined with fast UV polymerization it is the most rapid and cost-effective replication process.^{18,19} However, the stresses that arise from the polymerization process may cause instabilities in the produced pattern.^{349,350}

3 MATERIALS AND METHODS

3.1 MATERIALS

3.1.1 Hyperbranched Polymer

The hyperbranched polymer (HBP) studied was a 3rd generation acrylated polyether with an average acrylate functionality of 29. Its structure is shown in Figure 3-1. The molecule is derived from a 3rd generation hyperbranched polyether polyol (Boltorn® EO3000, Perstorp AB, Sweden) with a theoretical functionality of 32. It was synthesized by ring-opening polymerization of 3-ethyl-3-(hydroxymethyl)oxetane³⁵¹ and terminated with ethylene oxide to increase flexibility. The acrylation was carried out according to conventional preparation of acrylic esters by condensation of the polyol with acrylic acid and the acrylate group concentration was determined by bromine titration³⁵². Synthesis, acrylation and bromine titration were done by Perstorp AB, Sweden.

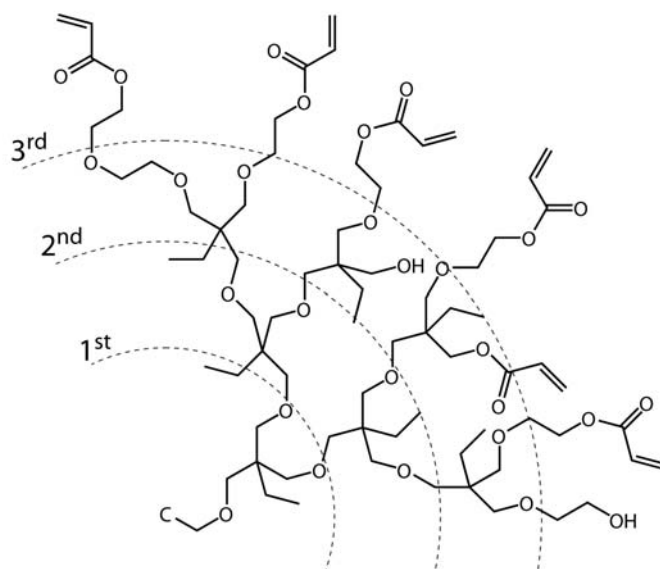


Figure 3-1 Structure of the hyperbranched acrylate monomer studied. The three ring segments represent the three generations. C denotes the tetrafunctional core atom from which four branches grow out. Only one sample branch is shown.

Although synthesis led to imperfect branching and significant polydispersity, the HBP preserved the essential features of dendrimers, that is, high end-group functionality, globular architecture and low viscosity. Dipentaerythritol hexaacrylate (DPHA, Sigma-Aldrich, Figure 3-2) is a standard acrylate resin and was used for comparison. Some structural properties are listed in Table 3-1.

Table 3-1 Structural properties of HBP and DPHA. The number of acrylate functions per monomer, the molecular weight and the acrylate group concentration are taken from the specifications of the supplier.

Property	Unit	HBP	DPHA
Theoretical functionality		32	6
Actual functionality		29	5.5
Mass molecular weight M_w	g/mol	7976	524
Number molecular weight M_n	g/mol	3577	
Acrylate group concentration	mmol/g	4	10.5
Degree of branching (Fréchet, Eq. 2.2)		0.41	n.a.

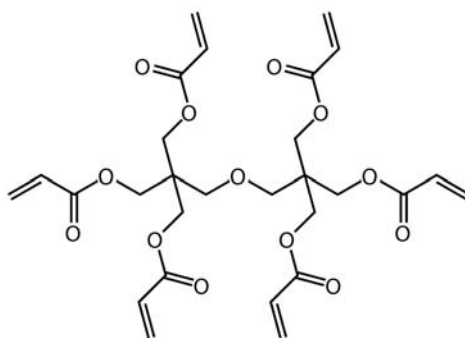


Figure 3-2 Structure of dipentaerythritol hexaacrylate (DPHA). In reality, one of the acrylate groups can be replaced by an OH function.

3.1.2 Photoinitiator

1-hydroxy-cyclohexyl-phenyl-ketone (Irgacure® 184, Ciba Specialty Chemicals, Figure 3-3) was used as a photoinitiator at a concentration equal to 1 wt%. The absorbance spectrum in acetonitril for different concentrations is shown in Figure 3-4.

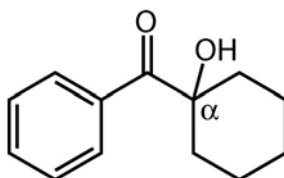


Figure 3-3 Photoinitiator 1-hydroxy-cyclohexyl-phenyl-ketone. Cleavage occurs at the α position.

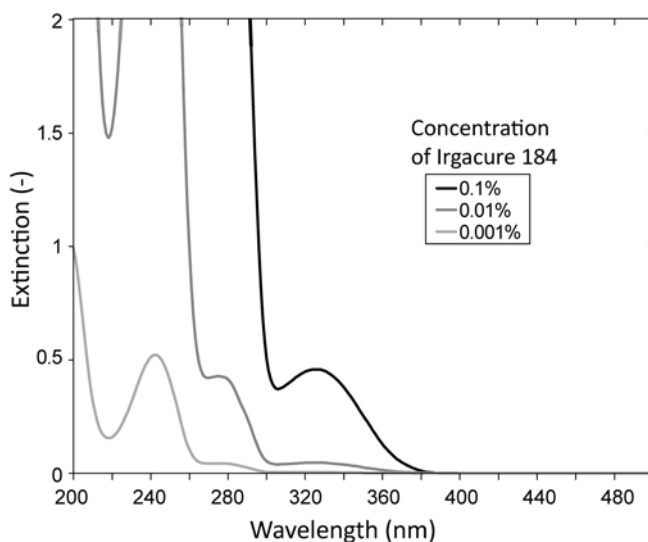


Figure 3-4 Extinction spectrum of Irgacure 184 in acetonitril for different concentrations. Figure adapted from the technical datasheet from Ciba Specialty Chemicals.

Irgacure® 184 is well soluble in acrylates and has a relatively low efficiency in the spectrum of the employed UV lamp. According to the Beer-Lambert equation, the intensity $I(z)$ absorbed at a depth z is:

$$I(z) = I_0 \left(1 - e^{-2.3 \varepsilon_t [PI] z} \right) \quad 3.1$$

where I_0 is the incident intensity, $[PI]$ is the photoinitiator concentration and ε_t the molar extinction coefficient found to be equal to $74 \text{ L} \cdot \text{mol}^{-1} \text{cm}^{-1}$ at 313 nm for Irgacure® 184.¹⁴⁸ Figure 3-5 shows the absorption calculated according to Equation 3.1 as a function of photoinitiator concentration and coating thickness. For a photoinitiator concentration of 1 wt% ($0.0563 \text{ mol} \cdot \text{L}^{-1}$) and a film thickness of 100 μm (this thickness is representative of the sample geometry in photo-DSC, photo-rheology, interferometry and beam bending analysis) only 9% of the UV light was absorbed at 313 nm wavelength. This should assure a relatively homogeneous cure, i.e., at a similar rate, throughout the sample thickness.

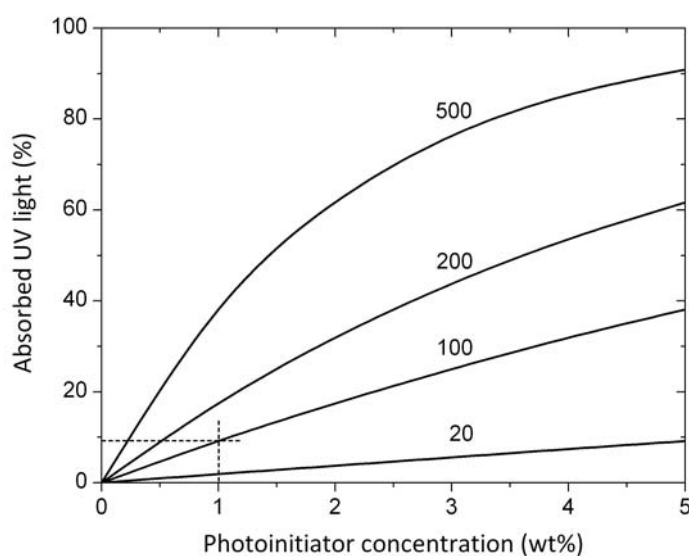


Figure 3-5 Absorption of UV light as a function of photoinitiator (Irgacure® 184) concentration for different coating thicknesses (μm as indicated).

3.1.3 Silica Nanopowder

Two kinds of nanoparticles were used. Highlink® Nano G502-31 (Clariant) is a suspension of 30 wt% monodispersed amorphous SiO_2 nanoparticles in isopropanol. These organosols were found slightly more hydrophobic than aqueous silica sols.³⁵³ The mean particle diameter is 13 nm (BET measurements gave a size of 12 nm³⁵³). With the density $\rho = 2.11 \text{ g/cm}^3$ this corresponds to a specific surface area of about $220 \text{ m}^2/\text{g}$. Aerosil® R7200 (Degussa) is an amorphous fumed SiO_2 nanopowder with a specific surface area of about $150 \text{ m}^2/\text{g}$. The average primary particle size is 12 nm, though particles are fused into aggregates as shown Figure 3-6. The particle surface is treated

with methacrylsilane, which chemically bonds the particles to the HBP network during photo-polymerization.^{240,246} The methacrylate group concentration was 0.637 mmol/g and was calculated from the carbon content of the powder that was taken from the specifications of the supplier. The surface chemistry of the Highlink (HL) and Aerosil (AS) particles is sketched in Figure 3-7.

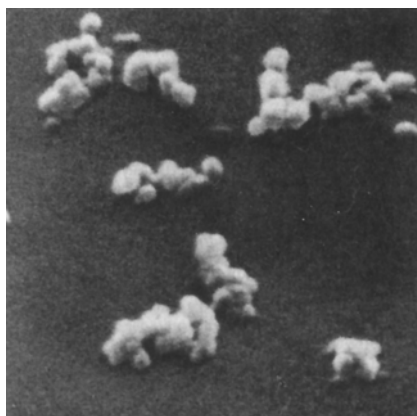


Figure 3-6 SEM image of gold-coated Aerosil® D150 silica particle aggregates. The primary particle size is 14 nm. Figure taken from³⁵⁴.

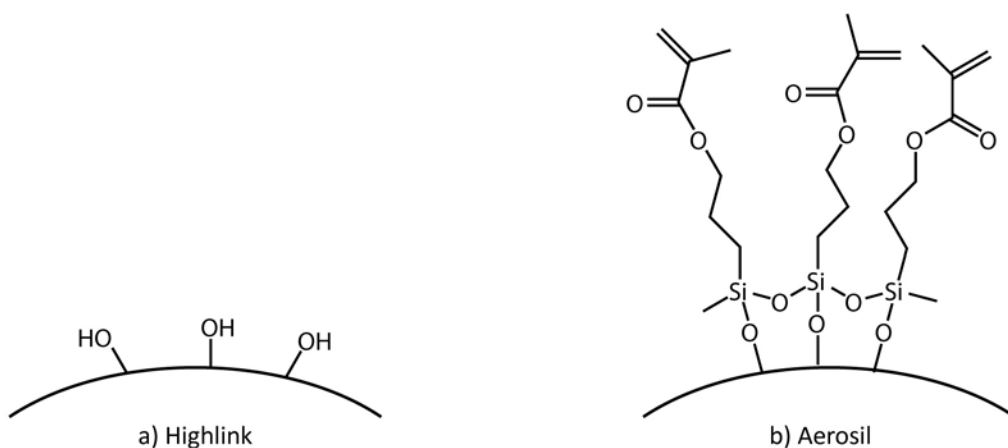


Figure 3-7 (a) Silanol HL surface and (b) silylated AS surface (three methacrylsilane molecules are shown).

3.1.4 Precursor and Coupling Agent for Sol-Gel Process

Tetraethyl orthosilicate (TEOS, Sigma-Aldrich) was used as a precursor for the formation of SiO₂ by the sol-gel process³⁰². Methacryloxy(propyl)trimethoxysilane (MEMO, Sigma-Aldrich) was used as a coupling agent. The chemical structure of both reactants is shown in Figure 3-8. The coupling agent has the ability to chemically bond to the matrix

during photo-polymerization and to condensate into the SiO₂ network, thereby chemically linking the two phases together.³⁴

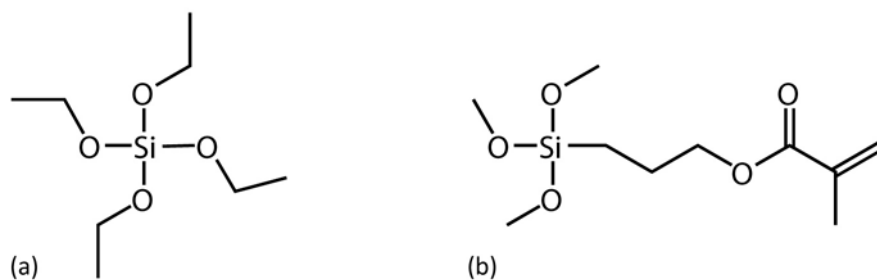


Figure 3-8 Chemical structure of (a) tetraethyl orthosilicate (TEOS) and (b) methacryloxy-(propyl)trimethoxysilane (MEMO).

3.1.5 Sample Preparation

The photoinitiator was dissolved in the HBP while stirring at 70°C in an oil bath for 30 min. Following references to HBP will always refer to the mixture of HBP with 1 wt% photoinitiator.

Highlink Composites

The HL suspension was mixed with the HBP and stirred for 30 min at room temperature. The solvent was removed at 40°C under vacuum until no more weight change was recorded. Composite samples with SiO₂ volume fraction from 5 to 25% were produced.

Aerosil Composites

The AS powder was dispersed in isopropanol (ratio 1:3 by weight) and processed 10 · 30 s with ultrasound (400 W, Digital Sonifier, Branson) to disagglomerate the agglomerates. The AS suspension was then mixed with the HBP for 30 min at room temperature. The solvent was removed at 40°C under vacuum until no more weight change was recorded. Composite samples with SiO₂ volume fraction from 5 to 25% were produced.

Sol-Gel Composites

HBP, MEMO, TEOS and 1 M HCl in water were mixed together in this order. Acidic conditions favor the formation of a fine silica microstructure.³¹⁶ After each step the mixture was stirred at room temperature until homogenization was visually observed. After addition of the last compound the mixture was stirred for 30 min. The amount of

TEOS was calculated assuming 100% conversion of the precursor into SiO_2 . The amount of coupling agent was calculated to give a concentration of 10% methacrylic groups within acrylic groups. The conversion of the silanol groups into SiO_2 was also assumed to be 100%. The amount of H_2O was calculated to give a molar ratio of H_2O to ethyl groups equal to 1:2. Condensation of the inorganic phase was done at 80°C for 4 h. Photopolymerization of the HBP network was done either before, after or during condensation, as will be explained in detail in Chapter 7.

3.2 EXPERIMENTAL METHODS

3.2.1 UV Lamp

The same UV lamp with a 200 W high pressure mercury bulb (OmniCure 2000, Exfo, Canada) in combination with a liquid light guide was used to polymerize the HBP materials in all experiments. The light intensity on the sample was measured using a spectrometer (Sola-Check, Solatell, UK) over the range of 270 to 470 nm. The spectrum of the UV lamp is shown in Figure 3-9.

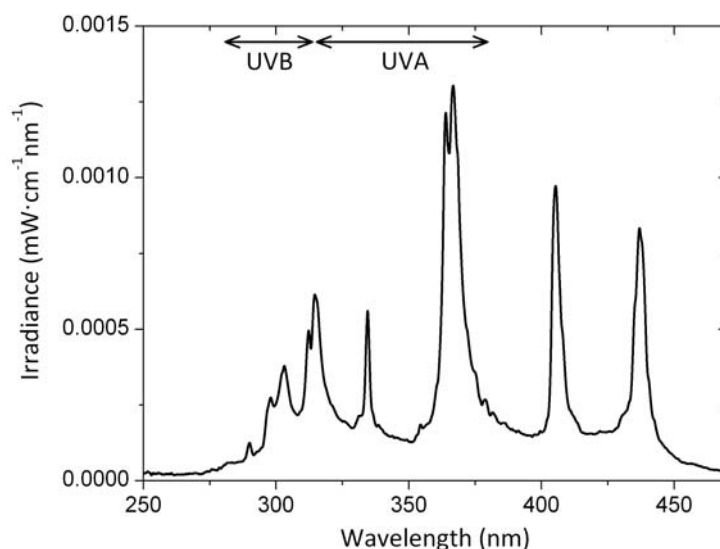


Figure 3-9 Spectrum of the OmniCure 2000 UV lamp.

3.2.2 UV-VIS Absorption

Absorption measurements were done on a UV/VIS/NIR spectrometer (Lambda 19, Perkin Elmer) at 1 nm/s in the range of 200 to 600 nm. HBP nanocomposite films with thickness of $100 \pm 5 \mu\text{m}$ were observed in transmission.

3.2.3 Thermo-Gravimetric Analysis (TGA)

The SiO₂ weight content in HL and AS composites and sol-gel hybrid materials and their thermal stability were measured in a TGA (SDTA851^e, Mettler Toledo). The weight loss was recorded while the samples were heated from ambient temperature to 800°C at 10 K/min.

3.2.4 Rheology

Oscillatory shear measurements of the uncured material were carried out on a strain-controlled rotational rheometer (ARES, Rheometrics Scientific), equipped with a temperature-controlled oven. For the HBP and the composites containing HL and AS a cone-plate geometry with a diameter of 25 mm, a cone angle of 0.1 rad and a gap of 0.051 mm was used. Under certain conditions the measured torque was below the sensitivity of the rheometer (0.2 g·cm). In this case, a cone-plate geometry with a diameter of 50 mm, a cone angle of 0.04 rad and a gap of 0.051 mm was used. Due to the low viscosity of the mixtures containing the sol-gel precursor, measurements were done with a couette geometry using a cylinder diameter of 25 mm, cylinder length of 32 cm and wall space of 1 mm. The strain was ensured to be in the linear viscoelastic range at any frequency and temperature, i.e., between 0.1 and 30% depending on the composition. The linear viscoelastic range was determined from strain sweep data conducted at a frequency of 100 rad/s at different temperatures.

3.2.5 Photo-Rheology

To monitor the stiffness build-up during photo-polymerization and to determine the onset of gelation, photo-rheological experiments were conducted on a stress-controlled rotational rheometer (AR2000, TA Instruments). A schematic drawing is shown in Figure 3-10. The samples were tested between two parallel plates of diameter 20 mm. The lower plate was made of quartz, through which the light reached the sample. A gap size of 100 μm and a frequency of 10 Hz were used. For the sol-gel samples a chamber was placed around the plates to prevent evaporation. All experiments were conducted at ambient temperature in air. The onset of illumination was synchronized with the rheological data acquisition by sending an electrical signal to the acquisition system while switching on the

lamp. The sampling rate was twice the oscillation frequency, hence 20 points/s. The limitations of the instruments were reached when the shear modulus was around 6 MPa.

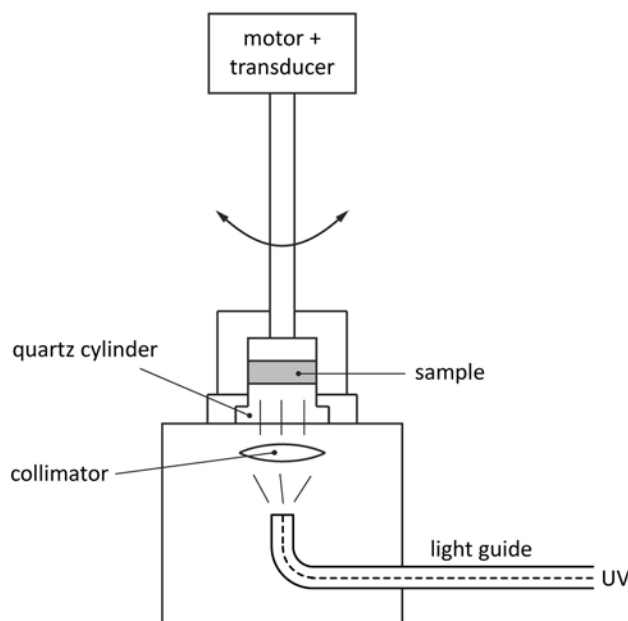


Figure 3-10 Schematic drawing of the AR2000 photo-rheology set-up.

3.2.6 Differential Scanning Calorimetry (DSC)

The glass transition temperature T_g of the composites in the polymerized state was determined by means of DSC (Q100, TA Instruments). The DSC was calibrated using sapphire and indium standards. Heating-cooling-heating cycles were conducted with a heating and cooling rate of 10 K/min between -20 and +70°C for the polymerized samples. The sol-gel samples were heated up to 100°C. 10-15 mg sample was put into a crimped aluminum pan and the T_g was determined from the second heating stage at the midpoint of the transition step.

3.2.7 Modulated Differential Scanning Calorimetry (MDSC)

The influence of the silica nanoparticles on the glass transition of the material in the unpolymerized state was investigated by means of MDSC, where a sinusoidal temperature modulation was superposed to classic DSC temperature ramp. Temperature modulated DSC scans were performed with the Q100 DSC apparatus. An *ad hoc* calibration for heat capacity measurements was performed according to the manufacturer's instructions. 10-15 mg sample was put into crimped aluminum pans and the reversing and non-

reversing components of the heat capacity were recorded in the range between -90 and -35°C. Cooling from the ambient temperature to -90°C and subsequent heating to -35°C were done at the same rate of 1 K/min. A thorough investigation of the optimum parameters that was done prior to the experiments is described in Appendix B.

3.2.8 Photo Differential Scanning Calorimetry (PHOTO-DSC)

The kinetics of the polymerization reaction was analyzed with the Q100 DSC apparatus. The photo-calorimetric accessory allowed illumination of the sample and the reference independently. The cell was sealed with a quartz window that let the UV light pass onto the open aluminum sample pans. Neutral filters were used for experiments at low UV intensity. Measurements were carried out at room temperature. The residual temperature increase of the sample, due to the irradiation from the lamp, was less than 1°C. The heat of polymerization was recorded as a function of time and the double bond conversion α was calculated according to Hoyle and Pappas¹⁴⁹ from the total heat of reaction H_{total} calculated by integrating the exothermic peak.

$$\alpha = \frac{H_{\text{HBP}}}{H_{100\%}} = \frac{H_{\text{total}}/m_{\text{HBP}}}{[AG] \cdot \Delta H_{\text{AG}}} \quad 3.2$$

where H_{HBP} is the heat of reaction per gram of HBP, H_{total} is the heat of reaction per gram of sample as measured from the DSC, $H_{100\%}$ is the theoretical heat for 100% double bond conversion of the HBP, m_{HBP} is the weight fraction of HBP, $[AG]$ is the concentration of acrylate groups in the HBP and ΔH_{AG} is the energy of the acrylate double bond equal to 86.31 kJ/mol³⁵⁵. Equation 3.2 is valid for the α of HBP and the HL composites. For the AS and the sol-gel composites the heat of reaction of the methacrylate groups has to be taken into account. The energy of the methacrylate double bond is 54.89 kJ/mol³⁵⁵ and it was assumed that all methacrylate groups of the coupling agent and on the AS surface reacted during the photo-polymerization reaction.

3.2.9 Shrinkage: Photo-Interferometry

Polymerization shrinkage during photo-polymerization was monitored real-time using a Michelson interferometer. This method, which was proposed by de Boer⁶³ to measure shrinkage during fast polymerization with an adequate time resolution, was developed and adapted to photo-polymerizing coatings at LTC. A detailed description of

this measurement method can be found in the PhD thesis of Schmidt⁴⁶. A schematic drawing of the experimental set-up is shown in Figure 3-11.

A 100 μm thick layer of sample was spread on a laboratory glass slide using a doctor blade. The reaction chamber was flushed with nitrogen. The onset of illumination was synchronized with the data acquisition by sending an electrical signal to the acquisition system while switching on the UV lamp. A typical sampling frequency was 200 Hz. The linear shrinkage S_L was calculated according to the following Equations:

$$S_L = \frac{N_{MM}\Delta h_c}{h_{c,fi} + N_{MM}\Delta h_c} \quad 3.3$$

$$\Delta h_c = \frac{\lambda}{4n_c(t)} = \frac{635 \text{ nm}}{4n_c} \quad 3.4$$

where N_{MM} is the number of maxima and minima of the interferometer curve as shown in Figure 3-12. Δh_c is the thickness change between a maximum and a minimum, $h_{c,fi}$ is the final thickness of the coating, λ is the wavelength of the laser, n_c is the refractive index of the coating, and t is the time. n_c was a function of conversion but changed by less than 2%⁴⁶ and was therefore considered to be constant. The refractive index was measured with a standard refractometer and the final thickness of the sample was measured with a profilometer (alpha-step 200, Tencor Instruments). The volumetric shrinkage S_V is related to the linear shrinkage S_L as:

$$S_V = 3S_L - 3S_L^2 + S_L^3 \approx 3S_L \quad 3.5$$

This simplification holds, since the linear shrinkage is usually smaller than 10%. The accuracy of the shrinkage measurement was approximately 10%.

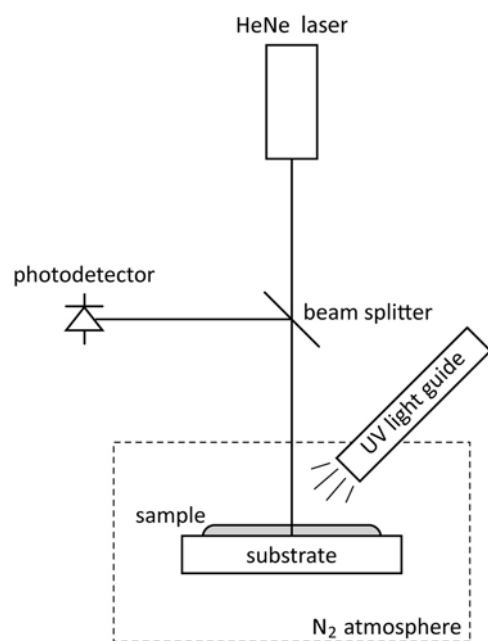


Figure 3-11 Experimental set-up for measuring polymerization shrinkage.

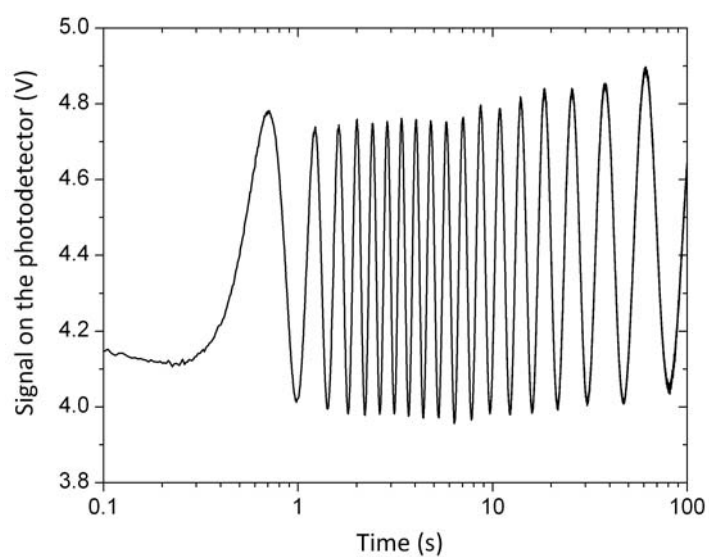


Figure 3-12 Typical laser intensity measured at the photodetector during UV exposure.

3.2.10 Internal Stress: Beam Bending

The in-plane stress of coatings was determined from the curvature of coated aluminum beams and calculated according to the models of Stoney³⁵⁶ and Inoue³⁵⁷. The model of Stoney assumes that the coating thickness is negligible and does not include the coating modulus. The model was used for the time resolved calculation of internal stress σ_i , because the Young's modulus of the coating was not known at any given time:

$$\sigma_i = -\frac{E_s h_s^2}{6r h_c} \quad 3.6$$

where E_s is the Young's modulus of the substrate, h_c and h_s are the thickness of the coating and substrate, respectively, and r is the radius of curvature of the beam. The model of Inoue is more refined and includes correction for in-plane strain. It also takes into account the Young's modulus of the coating. The model of Inoue was used to calculate the stress of the cured material.

$$\sigma_i = -\frac{E_s h_s^2}{6r h_c} \left(\frac{(1-uq^2)^3(1-u) + (uq(q+2)+1)^3 + u(uq^2+2q+1)^3}{2(1+q)(1+uq)^3} \right) \quad 3.7$$

$$\text{with } u = \frac{E_c}{E_s} \text{ and } q = \frac{h_c}{h_s} \quad 3.8$$

where E_c is the Young's modulus of the coating. A layer of sample with a thickness of about 100 μm was applied to a 280 μm thick aluminum strip. The strip had the dimensions 200 mm \cdot 5 mm and was completely covered by the sample. It was placed on the bearings inside the reaction chamber that was flushed with nitrogen. A schematic drawing of the experimental set-up is shown in Figure 3-13.

The maximum tolerable deflection for the aluminum beam to remain in the linear elastic range (0.2%) was 20 mm. The radius of curvature was calculated as:

$$r = \frac{4g^2 + L}{8g} \approx \frac{L^2}{8g} \quad 3.9$$

where L is the distance between the bearings (150 mm) and g is the deflection that was measured with a capacitive displacement sensor. To promote the coating adhesion the surface of the aluminum beam was treated with methacrylsilane. For this purpose, H_2O was mixed with isopropanol in the ratio 1:1 and the pH was adjusted to 3.5 using nitric acid. 3 wt% of a methacrylsilane compound (A174 silane, GE Silicones) was added and the

solution was stirred for 1 h. The aluminum beams were immersed in the solution for 30 s, then rinsed with water and dried with compressed air.

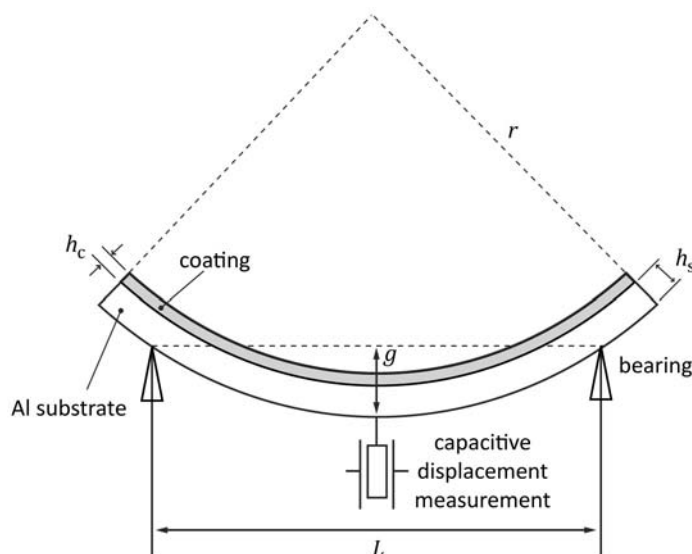


Figure 3-13 Experimental beam bending set-up to measure internal stress.

3.2.11 Dynamic Mechanical Analysis (DMA)

The viscoelastic properties of the polymerized material were measured in a DMA (Q800, TA Instruments) under axial oscillatory deformation at a frequency of 1 Hz during heating from room temperature up to 150°C at a rate of 10 K/min. Samples with a thickness of 400 μm were cut in strips of 20 mm in length and 3 - 5 mm in width.

3.2.12 Thermo-Mechanical Analysis (TMA)

The coefficient of thermal expansion (CTE) of the polymerized composites was measured by means of TMA (402, Netzsch). Samples with a thickness of 400 μm were cut in strips of approximately 4 mm in width and 10 mm in length. The strips were grooved on one end and mounted to a stable cross-section in the shape of a cross (see example in Figure 3-14). This allowed testing the CTE under compression. A constant force of 20 g was applied, and it was checked that this load did not induce creep in the material. The resulting stress could not be calculated, because the sampler had the shape of a half-sphere and the exact area of contact could not be determined. Dilatation of the sample was recorded as a function of temperature during cooling from ambient temperature to -70°C and during heating from -70 to 150°C. Cooling and heating were done at a rate of 5 K/min.

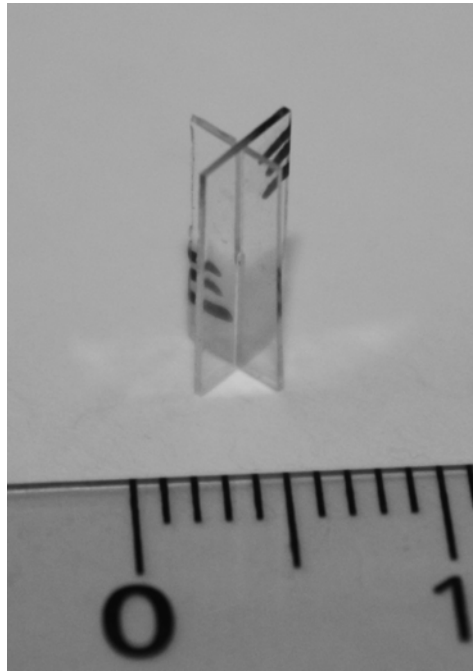


Figure 3-14 Cross shaped sample to measure the coefficient of thermal expansion under compression.

3.2.13 Transmission Electron Microscopy (TEM)

The microstructure of the nanocomposites was investigated by TEM (Philips/FEI, CM20 at 200 kV and CM12 at 120 kV). The samples were embedded in an epoxy resin (Epoxy resin medium kit, Fluka) and cut with a diamond knife on a microtome (Ultracut E, Reichert-Jung) to 40 nm thick slices, then put on a carbon coated grid.

3.2.14 Surface Roughness: Profilometer

The surface roughness R_a of the material was measured using a profilometer (alpha-step 200, Tencor Instruments) over a length of 80 μm at a scan speed of 5 $\mu\text{m/s}$ and an average was calculated over at least five R_a measurements.

3.2.15 Atomic Force Microscopy (AFM)

The topography of the nanogratings was analyzed by AFM (Multimode II, Veeco) in contact mode using a silicon nitride tip with a spring constant of 0.06 N/m. 512 scans were recorded over a length of 2 μm .

3.2.16 Nuclear Magnetic Resonance (NMR)

The condensation of the inorganic phase was measured by solid-state ^{29}Si -NMR (Avance 400, Bruker). The spectra were obtained at 59.62 MHz and the solid samples were ground prior to analysis. NMR spectra were deconvoluted using Gaussian fits in terms of Q_i where $i = 2, 3, 4$ correspond to the number of siloxane bridges bonded to the silicon atom of interest. The condensation state was calculated according to³⁷:

$$\Omega = \sum_{i=2}^4 \frac{i}{4} Q_i = \frac{1}{2} Q_2 + \frac{3}{4} Q_3 + Q_4 \quad 3.10$$

4 RHEOLOGICAL BEHAVIOR AND IMMOBILIZED POLYMER FRACTION OF CONCENTRATED HBP/SILICA SUSPENSIONS

It is often observed that the addition of very small particles has a high impact on the rheology of a polymer, with the emergence of a liquid-to-solid transition above a concentration threshold and associated processing problems. The HBP with Newtonian viscosity was expected to postpone the concentration threshold, thus enabling high particle loading. In this chapter the influence of particle surface chemistry and particle morphology on the microstructure, liquid-to-solid transition and glass transition behavior of HBP/SiO₂ suspensions was investigated.

4.1 MICROSTRUCTURE

Figure 4-1 shows the microstructure of the two types of cured nanocomposites. Polymerized HL composites remained completely transparent, while AS composites showed a slightly milky appearance at high filler level. The composites containing HL particles were true nanocomposites, where the inorganic phase was monodispersed in the HBP matrix. In contrast, the AS powder could not be completely disagglomerated during the ultrasound treatment. Image analysis revealed that the average agglomerate size for the AS suspension was 120 nm, with a very large size distribution. The volume fraction of SiO₂ in the agglomerates (ϕ_{agg}) was found to be equal to 55% at 5% SiO₂. For higher silica fractions image analysis was difficult, due to overlapping agglomerates, but ϕ_{agg} did not seem to change significantly.

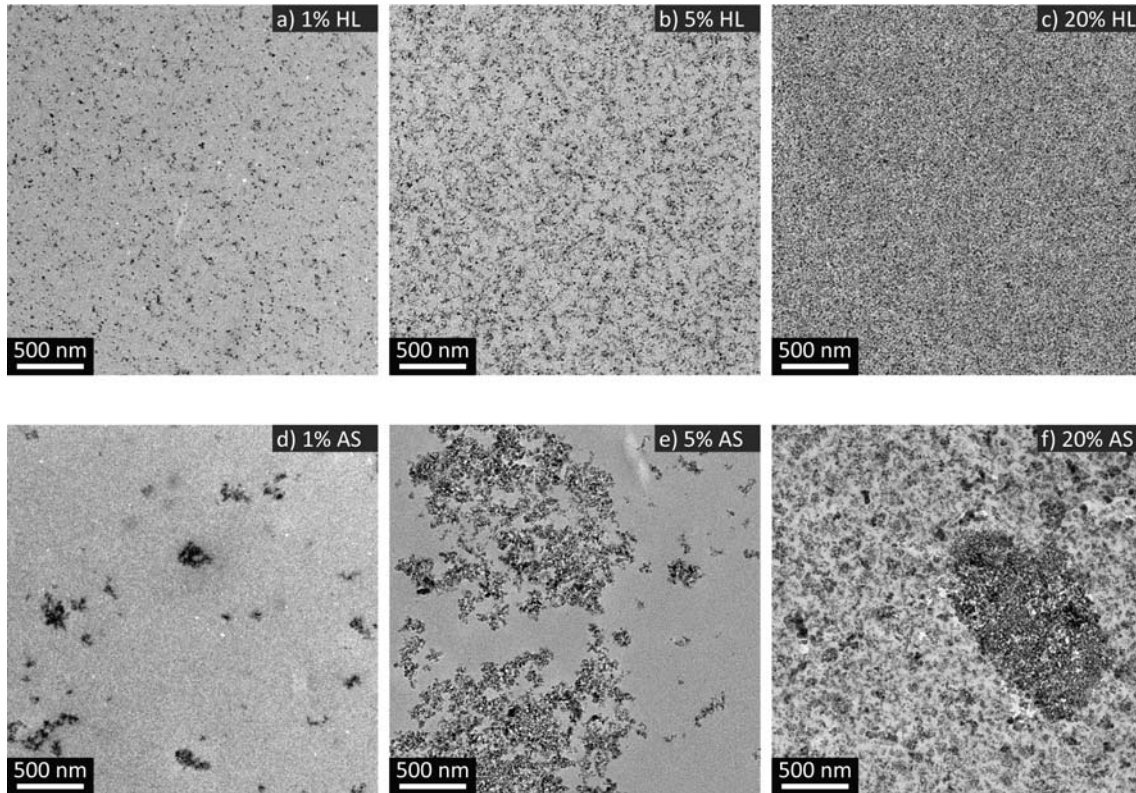


Figure 4-1 Transmission electron micrographs of HL and AS composites at 1, 5 and 20% filler fraction.

4.2 INFLUENCE OF NANOFILLER ON RHEOLOGICAL BEHAVIOR

Figure 4-2 depicts the viscosity as a function of angular frequency ω and SiO₂ volume fraction ϕ for the HL and AS suspensions in the HBP. The pure HBP showed Newtonian behavior with viscosity independent of frequency over the investigated range.

The viscosity increased with increasing filler fraction with shear thinning becoming apparent at $\phi = 5\%$ for HL and at $\phi = 10\%$ for AS. Shear thinning was the result of an increase in relaxation time with respect to the pure polymer. The increase in viscosity as well as the shear thinning behavior with increasing filler fraction was much more pronounced for HL than for AS. At a volume fraction of 10%, well-dispersed HL increased the HBP viscosity at 0.1 rad/s by more than 5 orders of magnitude. At 25% the increase reached 8 orders of magnitude, whereas it was 1000 times less for agglomerated AS. Such huge increases in viscosity by far exceeded previously reported data for concentrated suspensions of hard spheres in Newtonian fluids^{293,358,359}, which implies that the HBP presented a very strong affinity with the HL silica sol, and to a lesser extent with silylated AS particles. These results demonstrate the considerable influence of the interfacial interactions and dispersion state of nanoparticles on the viscosity of concentrated HBP suspensions.

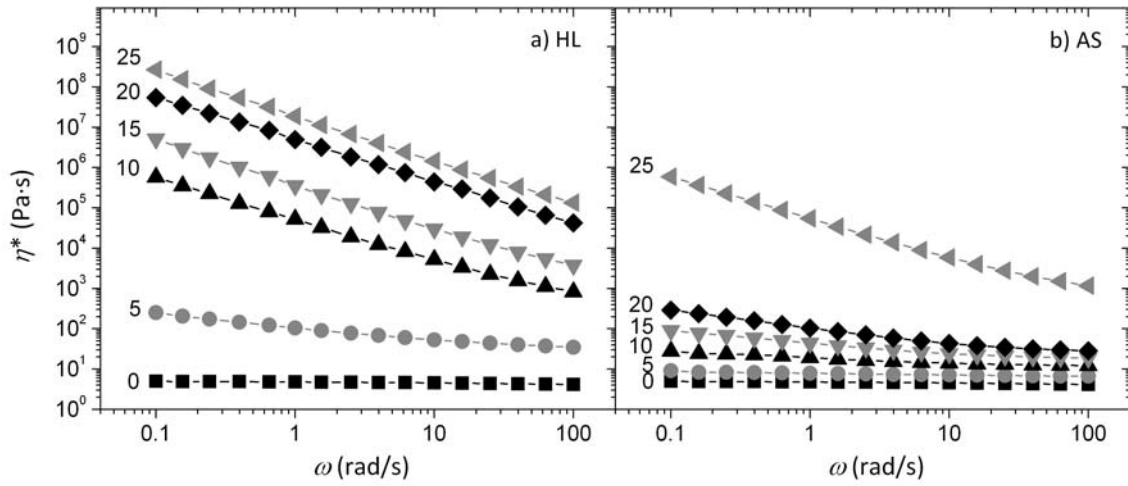


Figure 4-2 Viscosity of HBP/silica suspensions as a function of angular frequency ω and particle volume fraction from 0 to 25% (as indicated).

Shear thickening was not detected in the investigated frequency domain. This phenomenon results from a temporary hydrodynamic clustering of compact groups of particles formed as shear forces drive them into contact.³⁶⁰ Shear thickening was reported to occur above a critical shear rate, usually in the range of 1 to 10 s⁻¹, where short-range lubrication forces dominate the observed viscosity increase.³⁶¹ The critical shear rate $\dot{\gamma}_{\text{crit}}$ corresponds to a critical Péclet number $Pe_{\text{crit}} = 6\pi\eta_m\dot{\gamma}_{\text{crit}}r^3/k_B T$ (η_m is the viscosity of the continuous phase, i.e., the matrix, r is the particle radius, k_B is the Boltzmann constant, and T the absolute temperature) larger than several 10.³⁶² A minimum strain amplitude is also required for suspensions to shear thicken.³⁶³ Shear thickening of AS suspensions in

polypropylene glycol was indeed found to occur at dynamic shear rates $\gamma_0\omega$ (where γ_0 is the strain amplitude and ω is the frequency) above 10 s^{-1} .³⁵⁴ The investigated HBP/SiO₂ suspensions were tested at shear rates below 3 s^{-1} , i.e., below the critical conditions (Pe_{crit} was smaller than 0.15 in the case of HL and smaller than 21 in the case of AS aggregates, which again is below the critical condition for shear thickening, $Pe > 100$, even at the highest investigated shear rate of 3 s^{-1}).

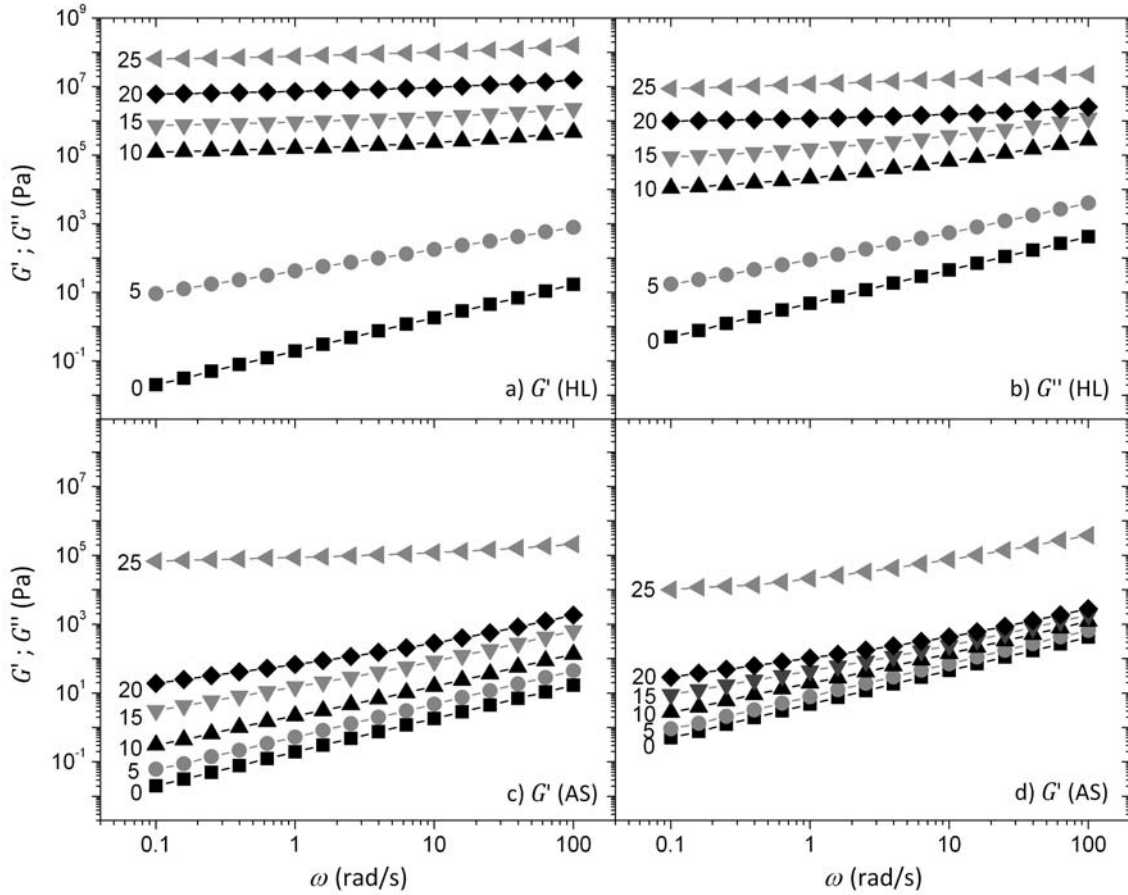


Figure 4-3 Storage and loss moduli of HBP/silica suspensions as a function of angular frequency ω and particle volume fraction from 0 to 25% (as indicated).

Figure 4-3 shows the complex shear moduli G' and G'' as a function of frequency and SiO₂ fraction for the two types of suspensions. For the pure polymer, G' and G'' were both approximately proportional to ω , indicating that HBP was not exactly a Newtonian fluid for which $G' = 0$ and $G'' \sim \omega$. However, since $G^* = \eta^* \cdot \omega = \sqrt{G'^2 + G''^2}$ was dominated by G'' , the HBP can be considered as a viscoelastic liquid with Newtonian-like behavior. At increasing SiO₂ fraction the scaling progressively evolved towards that for an elastic solid.

Assuming that the low strain rheological response was dominated by a single relaxation time η_∞^*/G_0^* , where $G_0^*(\phi)$ is the limiting modulus as $\omega \rightarrow 0$ and $\eta_\infty^*(\phi)$ is the

limiting viscosity as $\omega \rightarrow \infty$, the dimensionless quantities G^*/G_0^* and η^*/η_∞^* were described by a single master curve, when plotted against the dimensionless frequency $\omega \cdot \eta_\infty^*/G_0^*$:

$$\frac{G^*}{G_0^*} = 1 + \left(\frac{\eta_\infty^* \omega}{G_0^*} \right) + \kappa \left(\frac{\eta_\infty^* \omega}{G_0^*} \right)^\Gamma \quad 4.1$$

$$\frac{\eta^*}{\eta_\infty^*} = 1 + \left(\frac{\eta_\infty^* \omega}{G_0^*} \right)^{-1} + \frac{1}{\kappa} \left(\frac{\eta_\infty^* \omega}{G_0^*} \right)^{-\Gamma} \quad 4.2$$

where κ and Γ are parameters. This scaling was used by Rodlert *et al.*³² based on Lin's³⁶⁴ model for steady state shear thinning particle suspensions, to which belong the investigated nanocomposites.

Since no plateau values for $G_0^*(\phi)$ and $\eta_\infty^*(\phi)$ could be observed for the shear thinning mixtures in the investigated frequency range, the corresponding values at $\omega = 0.1$ rad/s and $\omega = 100$ rad/s, respectively, were chosen and the limiting data was called $G_{0.1}^*$ and η_{100}^* . The reduced data is shown in Figure 4-4 together with the fitted Equations 4.1 and 4.2 using $\kappa = 1.09$ and $\Gamma = 0.47$. These values are very close to the values that Rodlert found for HBP/clay nanocomposites. Interestingly, Equations 4.1 and 4.2 account well for both suspension families. It is therefore inferred that the rheological data of any suspension may be expressed entirely in terms of the parameters $G_{0.1}^*$ and η_{100}^* .

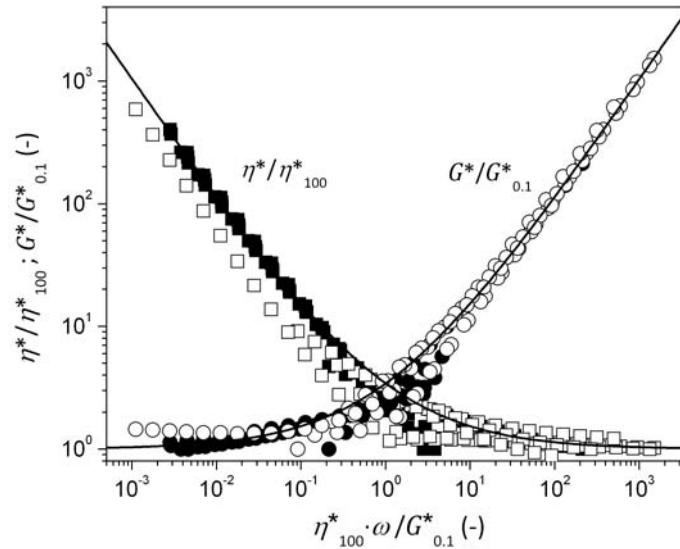


Figure 4-4 Superposition of reduced rheological data *versus* reduced frequency. Empty symbols: AS, full symbols: HL. The solid lines represent Equations 4.1 and 4.2 with $\kappa = 1.09$ and $\Gamma = 0.47$.

Figure 4-5 shows the influence of the temperature T on the viscosity of HBP and HBP/particle suspensions in so called Arrhenius coordinates. As temperature increased,

the viscosity of the suspensions was reduced, due to the temperature dependence of the HBP viscosity. For both types of particles this trend became less pronounced with increasing fraction, indicating that the suspensions became independent of the matrix viscosity and that a temperature-independent rigid network had formed.³² As was already noticed in Figure 4-2, the HL suspensions became considerably stiffer than the AS suspensions with increasing particle fraction.

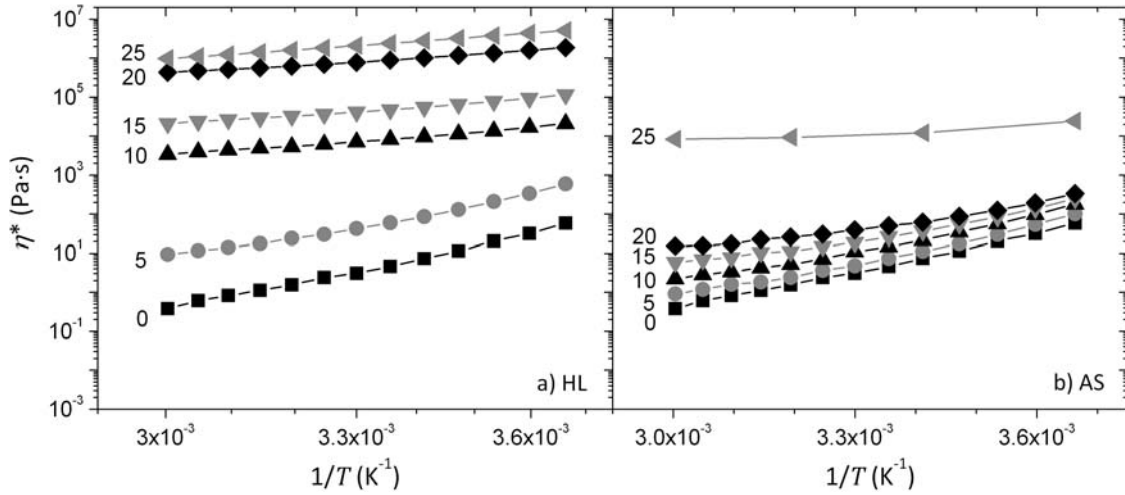


Figure 4-5 Viscosity of HBP/silica suspensions at $\omega = 6.28$ rad/s as a function of inverse temperature and particle volume fraction from 0 to 25% (as indicated).

A further insight into the viscoelastic properties of the HBP/silica suspensions was obtained from stress relaxation experiments. Figure 4-6 shows the stress τ resulting from the application of a 1% shear deformation. The residual stress corresponds to the yield stress of the material,³⁶⁵ i.e., the minimum stress necessary to deform a yield stress fluid. The scatter at low filler fraction was due to the sensitivity limit of the rheometer. The stress and relaxation time both increased with increasing filler fraction, which was consistent with the emergence of shear-thinning shown in Figure 4-2. A power-law relaxation behavior was moreover evident, especially for HL suspensions with an exponent equal to -0.13 for all concentrations beyond 10%. The present evidence for self-similar dynamics implies that the concentrated HBP/silica suspensions behave as a network-type fluid, similar to elastomers³⁶⁶ and entangled ring-type polymers³⁶⁷.

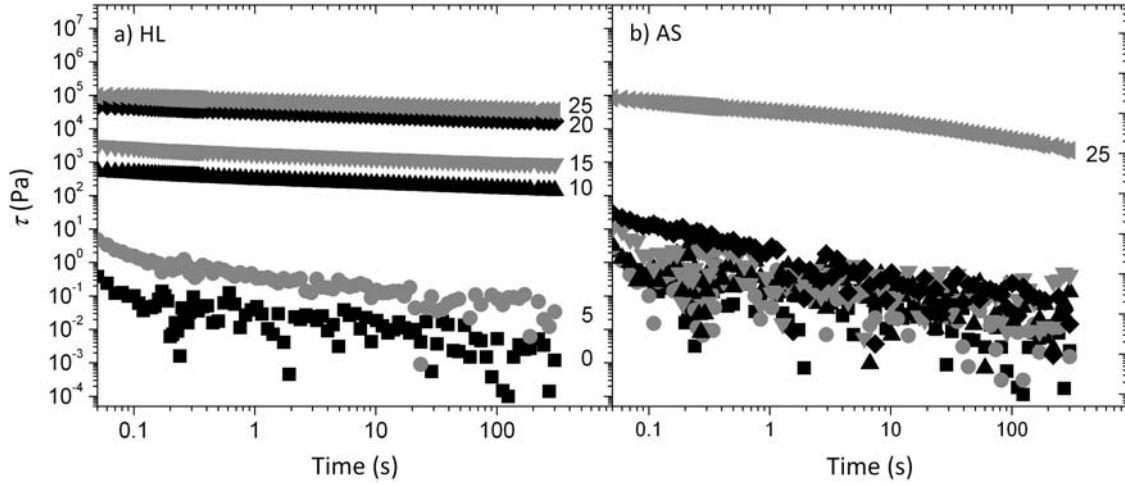


Figure 4-6 Stress relaxation under 1% shear deformation for HBP/silica suspensions as a function of time and particle volume fraction from 0 to 25% (as indicated).

4.3 INFLUENCE OF NANOFILLER ON GLASS TRANSITION BEHAVIOR

The glass transition behavior of HL and AS composites was analyzed using temperature modulated DSC scans. The MDSC protocol is detailed in Appendix B. The reversing heat capacity as measured included the contributions of the HBP and the silica. The contribution of the HBP phase $C_{p,\text{HBP}}$ was obtained from a mass balance:

$$C_{p,\text{HBP}} = \frac{C_{p,s} \cdot m_s - C_{p,\text{SiO}_2} \cdot m_{\text{SiO}_2}}{m_{\text{HBP}}} \quad 4.3$$

where $C_{p,s}$ and C_{p,SiO_2} are the reversing heat capacities of the sample and the amorphous silica, respectively, m_s is the total mass of the sample, and m_{SiO_2} and m_{HBP} are the masses of the silica and the HBP, respectively. The heat capacity values for silica as a function of temperature were obtained from tabulated data³⁶⁸. Figure 4-7 shows the reversing heat capacity curves for the HBP phase in HL and AS suspensions. It is evident that the transition step height decreased with increasing filler fraction and the transition was shifted to higher temperatures. Both effects were more pronounced for the HL. The non-reversing heat capacity was not measured for the AS suspension, due to uncontrolled cooling conditions. For comparison, the reversing heat capacity of composites containing micro-sized silica particles was measured (Figure 4-8). No significant influence of the micro-silica on the transition step height was observed.

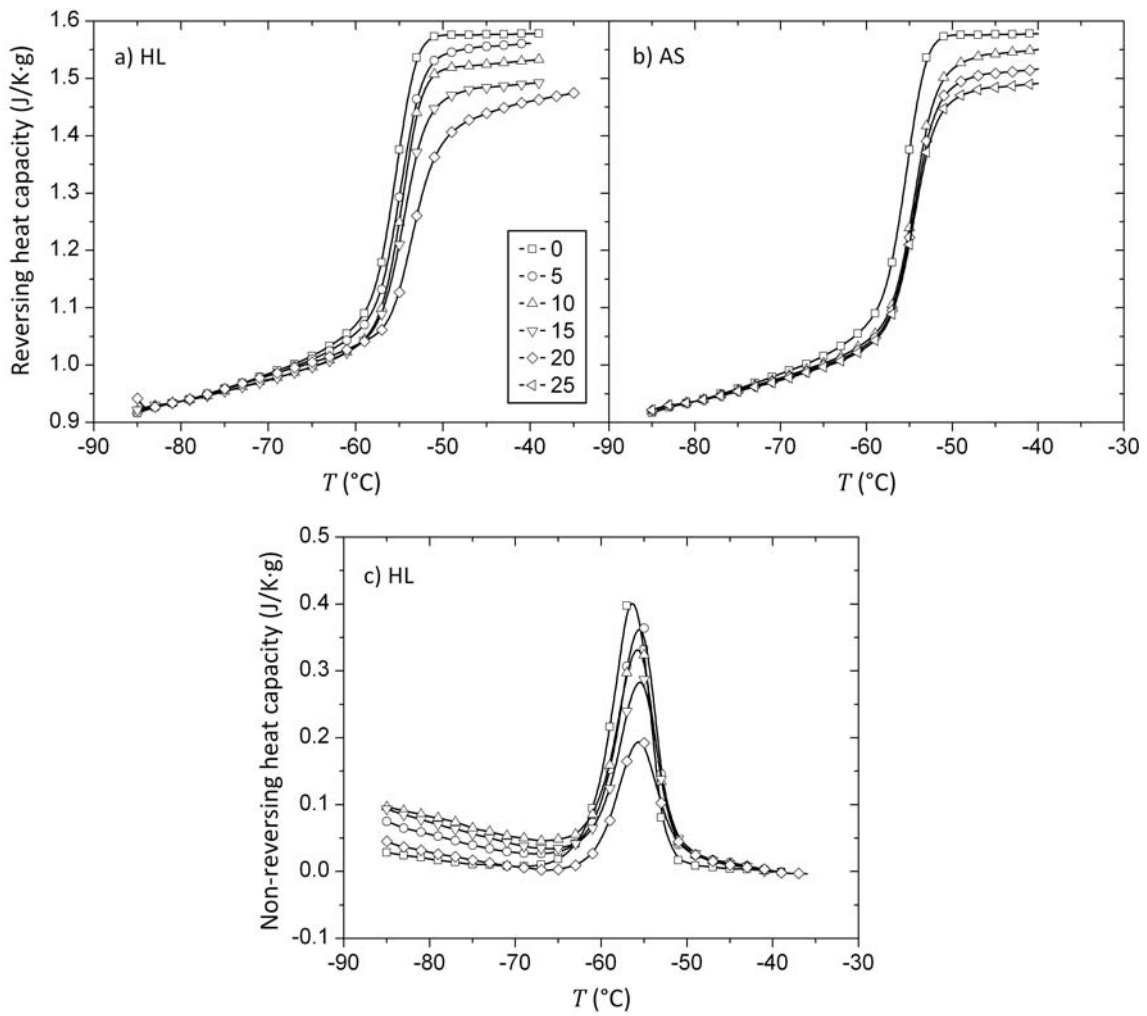


Figure 4-7 Reversing heat capacity measurements on HBP/silica suspensions containing (a) HL and (b) AS, and (c) non-reversing heat capacity for HL suspensions as a function of temperature T and particle volume fraction from 0 to 25% (as indicated). The non-reversing heat capacity was set to zero in the rubbery state.

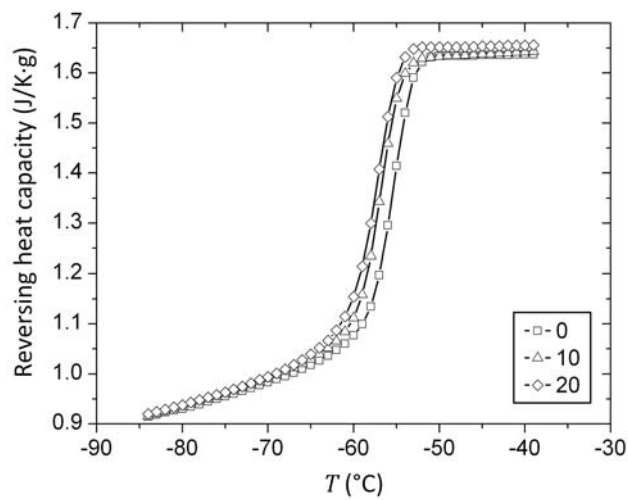


Figure 4-8 Reversing heat capacity measurements on HBP/silica suspensions containing micro-sized silica particles as a function of temperature T and particle volume fraction from 0 to 20% (as indicated).

The glass transition temperature T_g was determined at the inflection point of the curves and the values are reported in Table 4-1. The T_g of the HL suspensions progressively increased with filler volume fraction ϕ , whereas for the AS suspensions the T_g was constant but higher than that of the HBP. It was verified that these changes were not due to differences in heat transfer properties of the material with different SiO_2 fraction. In that case the T_g would have changed strongly as a function of heating rate. Instead, only marginal shifts were observed when the heating rate was increased from 1 to 5 °C/min.

Table 4-1 Glass transition temperature T_g , reversing heat capacity step ΔC_p at T_g , and enthalpy relaxation strength ΔH_r (non-reversing peak height) for HL, AS and micro- SiO_2 suspensions at different filler fractions.

	HL suspensions			AS suspensions		micro- SiO_2 suspensions	
SiO_2 (vol%)	T_g (°C)	ΔC_p (J/K·g)	ΔH_r (J/K·g)	T_g (°C)	ΔC_p (J/K·g)	T_g (°C)	ΔC_p (J/K·g)
0	-55.8	0.542	0.41	-55.8	0.542	-55.8	0.542
5	-55.2	0.508	0.36				
10	-54.6	0.484	0.33	-54.7	0.506	-57.2	0.529
15	-54.5	0.454	0.28				
20	-53.5	0.411	0.19	-54.6	0.467	-57.8	0.563
25				-54.6	0.451		

4.4 LIQUID-TO-SOLID TRANSITION

The results from rheological and calorimetric experiments are synthesized in the composite Figure 4-9, which represents different facets of the liquid-to-solid transition of the HBP/silica suspensions. Figure 4-9a shows the tangent of the phase angle $\tan(\delta) = G''/G'$, obtained from Figure 4-3, that is a measure for the elasticity of the fluid. $\tan(\delta) = 1$ was used to define the transition from a viscoelastic liquid to a viscoelastic solid, which is comparable to physical gelation, where the particles show strong enough interactions with each other to form a 3-dimensional network. For the HL suspensions, the liquid-to-solid transition occurred at $5\% < \phi < 10\%$, after which the dependence of $\tan(\delta)$

on the solid phase fraction was weak. Hence, at $\phi = 5\%$ the solid nanoparticles formed a network, which conferred to the material a rather elastic behavior. The decrease in $\tan(\delta)$ for the AS suspensions was more gradual, and the liquid-to-solid transition occurred only at $\phi > 20\%$. The same critical volume fractions also appeared when looking at the activation energy E_A for viscous flow, reproduced in Figure 4-9b. These values were calculated from a linear fit of $\ln(\eta^*)$ versus $1/T$ shown in Figure 4-5, where an Arrhenius behavior was evident. For the pure HBP, E_A was equal to 61 kJ/mol. For HL suspensions, the activation energy dropped at $5\% < \phi < 10\%$, then became almost independent of ϕ . Hence, at $\phi = 5\%$ the viscosity of the composite became independent of the matrix viscosity and therefore independent of the temperature. For AS suspensions, the activation energy decreased gradually with the particle fraction and reached the value of the HL plateau at $\phi = 25\%$. A similar decrease in activation energy with filler fraction was found by Rodlert *et al.*²¹ A further indication of the liquid-to-solid transition was derived from the stress data (Figure 4-6) after a relaxation time of 300 s, and is shown in Figure 4-9c. According to Jing *et al.*³⁶⁹ a liquid is considered to be a yield stress fluid, if the residual stress is higher than 1 Pa. For the HL suspensions, this was the case for $\phi > 5\%$, whereas AS suspensions reached the yield limit only at $\phi > 20\%$.

Figure 4-9d shows the change in heat capacity $\Delta C_{p,HBP}$ at T_g , which was determined as the distance between the two tangents before and after the transition in Figure 4-7a,b. In the glassy state the tangent was taken between -80 and -70°C and in the rubbery state between -48 and -38°C. The error on the $\Delta C_{p,HBP}$ was estimated to be 4-5%. For both suspensions $\Delta C_{p,HBP}$ decreased with increasing amount of silica. This reflects a decrease in the polymer mobility, that was due to the interaction with the particles, as will be discussed in the following section. This effect is more pronounced for the HL suspensions than for the AS suspensions. The liquid-to-solid transition is not visible in the $\Delta C_{p,HBP}$ behavior. That is, because a thermal effect, instead of a mechanical effect, was measured in the latter case.

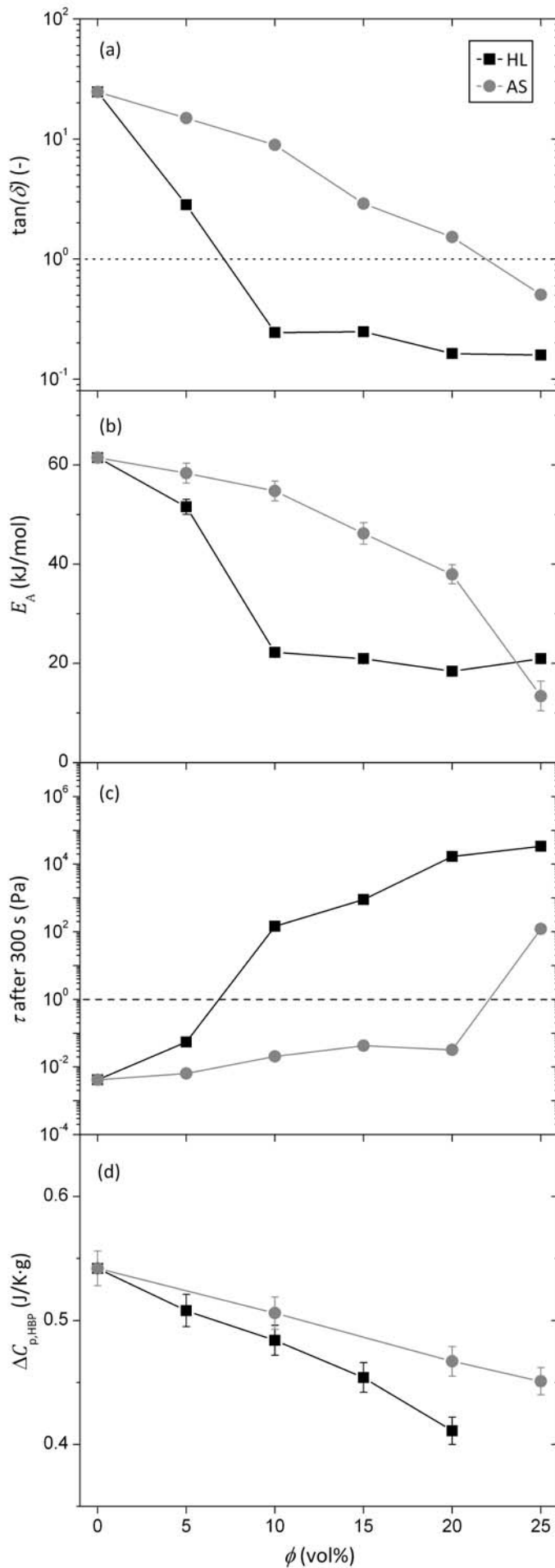


Figure 4-9 (a) Tangent of the phase angle of HBP/silica suspensions vs. particle volume fraction at $\omega = 6.28$ rad/s, the dotted line represents the liquid-to-solid transition, (b) activation energy for viscous flow, (c) stress after 300 s of relaxation, the dashed line separates the yield-stress fluids from the non-yield-stress fluids, and (d) change in heat capacity at T_g .

4.5 IMMOBILIZED POLYMER IN HBP/SILICA SUSPENSIONS

4.5.1 Viscosity Increase and Effective Particle Fraction

The huge increase in viscosity of the present HBP suspensions (Figure 4-2), especially for well-dispersed silica sols, and related early gelation was somehow surprising, as the low viscosity non-entangled HBP was expected to maintain also a low suspension viscosity. The viscosity of particle suspensions has been analyzed and modeled since early studies made by Einstein³⁷⁰, as summarized in the review of Bicerano *et al.*²⁵⁷ Three different concentration regimes are usually identified for particle suspensions.

In the dilute regime with non-interacting particles the viscosity of the suspension is often described in terms of virial expansions (i.e., power series) of the particle volume fraction ϕ .³⁷⁰ Hence, the viscosity becomes proportional to ϕ in the limit $\phi \rightarrow 0$. Classic models for dilute suspensions were established for particles of sizes larger than several micrometers.^{268,371,372} However, these models often underestimate the viscosity of nanocomposites, including the present materials, by several orders of magnitude, because they do not take into account the very large specific surface area of the particles and possible polymer-particle interactions.

The semi-dilute regime is defined to include the broad range of volume fractions between which the interparticle interactions first become appreciable, and at which they begin to predominate. The “crossover volume fraction” defines the transition between the dilute and the semi-dilute regimes and occurs at $\phi = 1 - 2\%$ for spherical particles.²⁵⁷ The model of “sticky spheres”³⁷³ takes into account the short range attractive interactions between particles in the semi-dilute regime.

A suspension is defined as concentrated for volume fractions greater than the geometric percolation threshold ϕ_c .²⁵⁷ Motions in dispersions with $\phi > \phi_c$ are necessarily collective, but the suspension continues to be fluid-like until interparticle interactions cause contacting particles to become stuck into a rigid array. At a certain particle fraction $\phi^* > \phi_c$ the necessity for collective motions becomes strong enough to cause a transition from a highly viscous fluid to a true solid, for which the viscosity is infinite. The fraction ϕ^* can be considered equal to the maximum packing fraction $\phi_{cp} = \pi/\sqrt{18} = 0.7405$ for close-packed and $\phi_{rcp} \approx 0.64$ for random close-packed monodisperse spheres²⁸⁹, and decreases rapidly with increasing particle anisotropy. For the semi-dilute and concentrated regime up to ϕ^* an asymptotic relationship between the relative viscosity η_r and ϕ was proposed

by Krieger and Dougherty (so called “hard sphere” model³⁷¹) and is frequently used^{293,358,359,362,374,375}:

$$\eta_r = \frac{\eta}{\eta_{\text{HBP}}} = K \left(1 - \frac{\phi}{\phi^*} \right)^{-\psi} \quad 4.4$$

where η and η_{HBP} are the viscosities of the HBP/silica suspension and HBP, respectively, K is related to the virial expansion of ϕ and varies between 0.88 and 1,³⁷² and the exponent $\psi = [\eta]\phi^*$, where $[\eta] = 2.5$ is the intrinsic viscosity for suspensions of spheres³⁷⁶, or $\psi = 2$. The latter value, based on analogies between hydrodynamics and electrostatics,³⁷² was used in the present work. Equation 4.4 is compared with the experimental data in Figure 4-10 using $\phi^* = \phi_{\text{rcp}} = 0.64$ and $K = 1$, and found to underestimate by far the measured increase in viscosity for the two types of HBP/silica suspensions.

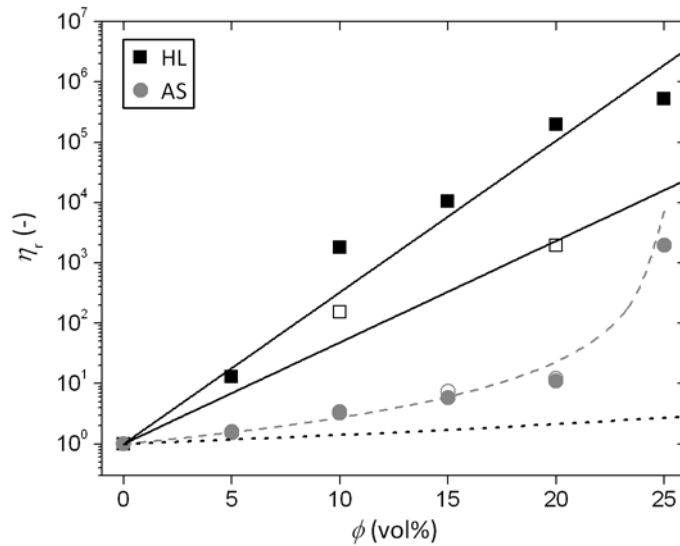


Figure 4-10 Reduced viscosity of HBP/silica suspensions (full symbols) and DPHA/silica suspension (empty symbols) at $\omega = 6.28$ rad/s as a function of particle fraction. The dotted line represents Equation 4.4 with $K = 1$, $\psi = 2$ and $\phi^* = 0.64$, the dashed line represents Equation 4.7 with $a = 3.3$ nm, $r = 9.1$ nm and $\phi^* = 0.64$, and the solid line represents Equation 4.10 with $A = 29$ for the HBP/HL suspensions and $A = 19$ for the DPHA/HL suspension.

4.5.2 Modeling of AS Suspensions

To account for the actual increase in viscosity, an adsorbed and confined HBP layer on the surface of the particles was postulated. Immobilized layers were reported to increase the hydrodynamic radius of the particles in proportion with the radius of gyration of the molecules.²⁹³ The impact of an immobilized polymer layer on the rheological properties of polymer/particle suspensions was described in earlier

studies.^{243,291,377} If one assumes that, under shear deformation, this layer moves with the particle, it has to be regarded as a contribution to the disperse phase, thus it increases the solid volume fraction to an effective fraction ϕ_{eff} . For a given immobilized layer thickness, the immobilized volume scales with the specific particle surface area and was expected to be larger for the HL case compared to the AS case.

Equation 4.4 was inverted to calculate ϕ_{eff} for both types of suspensions from the experimental viscosity data (using $K = 1$, $\psi = 2$ and $\phi^* = 0.64$). The results are shown in Figure 4-11 for the investigated range of frequencies.

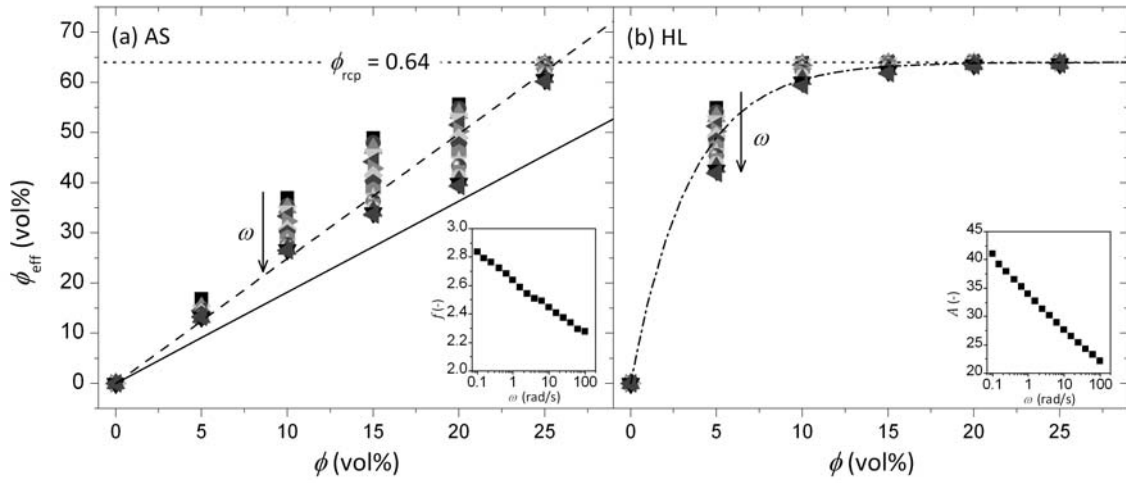


Figure 4-11 Effective particle fraction ϕ_{eff} as a function of real particle fraction ϕ calculated from suspension viscosity data using Equation 4.4 with $K = 1$, $\psi = 2$ and $\phi^* = 0.64$, for frequencies ω in the range of 0.1 to 100 rad/s. The solid line in Figure 4-11a shows ϕ_{eff} calculated from the actual volume fraction of particles in AS agglomerates (55%). The dashed line in Figure 4-11a is a fit of Equation 4.5 at $\omega = 6.28$ rad/s with adjustable factor f , the dash-dotted line in Figure 4-11b is a fit of Equation 4.9 at $\omega = 6.28$ rad/s with adjustable factor A . The insets show the logarithmic dependence of the factors f and A on the frequency.

For AS suspensions, ϕ_{eff} increased approximately linearly with ϕ , reaching the packing limit $\phi^* = \phi_{\text{rcp}} = 0.64$ at the highest investigated fraction $\phi = 0.25$. The present ϕ_{eff} values are comparable with those obtained for various nanoparticle suspensions in PEG, depending on the molecular weight of the polymer.^{378,379} The large increase in effective volume was partially due to the fact that the agglomerates were not dense accumulations of particles, but diffuse aggregated structures of chemically bonded primary particles, where the space was infiltrated with HBP. Therefore the agglomerate “particles” were considered as composites themselves with a 55% solid volume fraction. In other words, a suspension containing 5% silica contained 9% agglomerate particles. However, ϕ_{eff} was still higher than the calculated volume fraction of agglomerates (solid line in Figure

4-11a), and this was argued to result from an immobilized layer at the particle surface. The effective volume fraction was thus described as:

$$\phi_{\text{eff}} = f \cdot \phi \quad 4.5$$

where f is a proportionality factor. Assuming that the immobilized layer formed a continuous shell of constant thickness a on the surface of the particles, geometric considerations led to the following expression for the effective volume fraction ϕ_{eff} :

$$\phi_{\text{eff}} = \phi \left(1 + \frac{a}{r} \right)^3 \quad 4.6$$

where r is the radius of the particles. In the case of AS, two values of particle radius were considered: 6 nm (radius of the primary particles in the aggregates) and 9.1 nm. The latter radius was calculated from the known specific surface S (150 m²/g) and density ρ (2.2 g/cm³) of the AS powder as $3/(\rho \cdot S)$.

Substituting ϕ by ϕ_{eff} in Equation 4.4 (using $K = 1$ and $\psi = 2$) provides an expression for the relative viscosity of concentrated suspensions of particles surrounded by an immobilized layer:

$$\eta_r = \left(1 - \frac{\phi}{\phi^*} \left(1 + \frac{a}{r} \right)^3 \right)^{-2} \quad 4.7$$

This approach disregards the fact that the AS particles were agglomerated, which is discussed in a later paragraph. As also shown in Figure 4-11a, the proportionality factor f was found to decrease linearly with $\log(\omega)$. Since f is a function of agglomerate dimensions (Equations 4.5 and 4.6), this finding confirms the importance of the particles on the emergence of shear-thinning behavior of the suspensions (Figure 4-2). Equation 4.7 was fitted to the measured viscosity data at $\omega = 6.28$ rad/s with adjustable confined layer thickness a . The result shown in Figure 4-10 was obtained with $a = 2.2$ nm ($r = 6$ nm) or $a = 3.3$ nm ($r = 9.1$ nm). The fitted values of a for all frequencies are shown in Figure 4-12a and found to lie in the range of 2 to 5 nm, which is similar to the value of 5 nm found for PEO on silica particles.²⁹¹ At $\phi_{\text{eff}} = \phi^*$, the layer thickness a should be comparable to half of the mean free space d between nearest neighbor particles, calculated according to Tewari *et al.*²⁵⁶:

$$d = \langle H_1 \rangle - 2r = r \left(K_1 \left(\frac{3\phi}{4\pi} \right)^{-1/3} \left[1 + B_1 \left(\frac{\phi}{\phi_{\text{cp}}} \right)^{2/3} \right] - 2 \right) \quad 4.8$$

where $\langle H_1 \rangle$ is the distance between the cores of first nearest neighbor particles, $K_1 = 0.554$, $B_1 = 1.062$ and $\phi_{cp} = \pi/\sqrt{18}$ is the highest volume fraction for close-packed spheres. Equation 4.8 should be considered as an approximation for the case where the particles are aggregated and not isolated spheres. The half distance $d/2$ is plotted as a function of ϕ in Figure 4-12 and compared to the immobilized layer thickness values. For AS suspensions the half distance between particles rapidly decreased with increasing particle fraction, whereas the layer thickness was roughly independent of the volume fraction. In any case both values were of comparable magnitude, the differences resulting from the idealization of the actual heterogeneous microstructure shown in Figure 4-1.

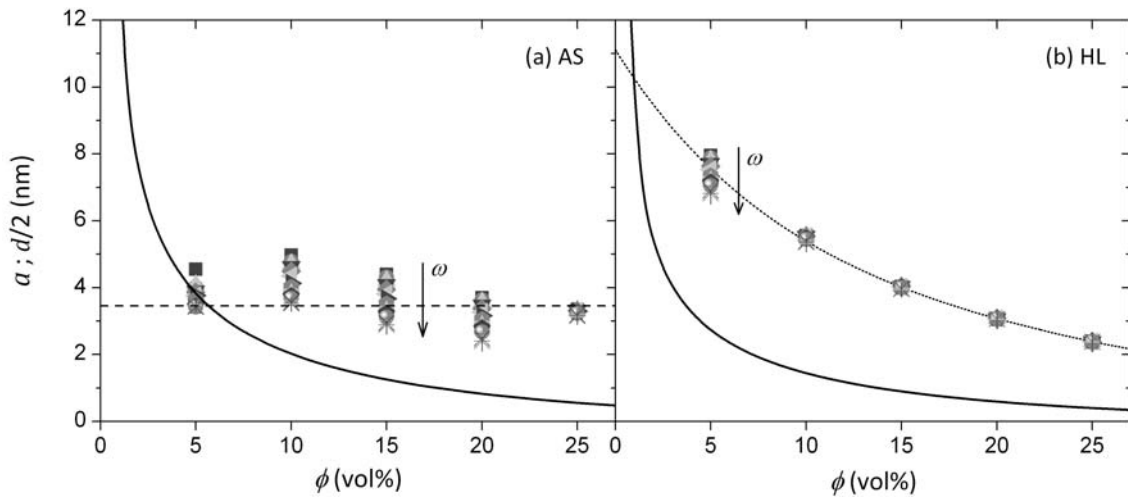


Figure 4-12 Confined layer thickness a (symbols) and half of the mean free space between particles $d/2$ (solid lines) as a function of (a) AS particles (using $r = 9.1$ nm) and (b) HL particle fraction ϕ , for frequencies ω in the range of 0.1 to 100 rad/s. The dashed line is the value of the immobilized layer thickness at $\omega = 6.28$ rad/s ($a = 3.3$ nm). The dotted line represents Equation 4.11 at $\omega = 6.28$ rad/s (with $r = 6.5$ nm, $\phi^* = 0.64$ and $A = 29$).

4.5.3 Modeling of HL Suspensions

In the case of the well-dispersed HL suspensions, ϕ_{eff} increased very rapidly with increasing ϕ (Figure 4-11b), reaching the packing limit $\phi^* = \phi_{rcp} = 0.64$ at a fraction as low as 10%. Similar results were reported for polyvinylidene fluoride nanocomposites.^{284,290} The dependence of the ratio ϕ_{eff}/ϕ on ϕ invalidated the “hard sphere” approach, and the effective particle fraction was fitted with an exponential form:

$$\phi_{eff} = \phi^* (1 - e^{-A\phi}) \quad 4.9$$

where the factor A was found to be proportional to $\log(\omega)$ (inset in Figure 4-11b). Substituting Equation 4.9 to the fraction ϕ in Equation 4.4 (using $K = 1$ and $\psi = 2$) leads to

an exponential dependence of the relative viscosity of HL suspensions on the particle volume fraction:

$$\eta_r = e^{2A\phi} \quad 4.10$$

Equation 4.10 was fitted to the measured viscosity data at $\omega = 6.28$ rad/s with adjustable factor A as shown in Figure 4-10. As in the AS agglomerate case, the effective volume fraction ϕ_{eff} of the HL suspensions was related to the actual fraction ϕ through an immobilized layer of thickness a , assumed to fully cover each single silica particle of radius r (Equation 4.6). The value of a was then calculated as a function of ϕ from the viscosity data at all investigated frequencies, using Equations 4.6 and 4.9:

$$a = r \left[\left(\frac{\phi^* (1 - e^{-A\phi})}{\phi} \right)^{1/3} - 1 \right] \quad 4.11$$

As shown in Figure 4-12b for $\omega = 6.28$ rad/s, the layer thickness a for the HL case decreased with filler fraction similarly to the distance between particles, and was independent of frequency except at 5% particle fraction. This result implies that it was the entire HBP volume, rather than a layer of finite thickness, which was immobilized. This is also why the calculated layer thickness was higher than the half distance between nearest neighbor particles. The idea of a gelled suspension at particle volume fraction larger than 5% is supported by the transition in $\tan(\delta)$, activation energy and stress relaxation behavior shown in Figure 4-9. The equilibrium thickness of the confined layer on the HL particles at a volume fraction of 5% was around 7.5 nm.

4.5.4 Discussion on the Exponential Scaling of the Viscosity

An exponential dependence of the viscosity on the volume fraction of solid matter in solution was first proposed by Arrhenius.³⁸⁰ It was suggested again later by Thomas, based on the work of Eyring.^{381,382} In the concentrated regime, a considerable rearrangement of particles must occur, when the suspension is sheared. Eyring proposed an exponential form for the probability of a particle transfer from one shear plane to another. The exponential scaling was observed in various particle suspensions,^{383,384} which was argued to result from the deformable nature of the particles including the adsorbed layer, so that the “hard sphere” approach was no longer applicable. Interestingly, similar findings were reported for the low shear behavior of dendrimer solutions^{385,386}, gelling systems (exponential scaling with crosslink density³⁸⁷) and microgel suspensions^{388,389}. In this

broad diversity of systems the exponential scaling was attributed to the deformable nature of the spherical molecules, with either a hard shell around a soft core (dendrimers) or a star-like microgel structure.

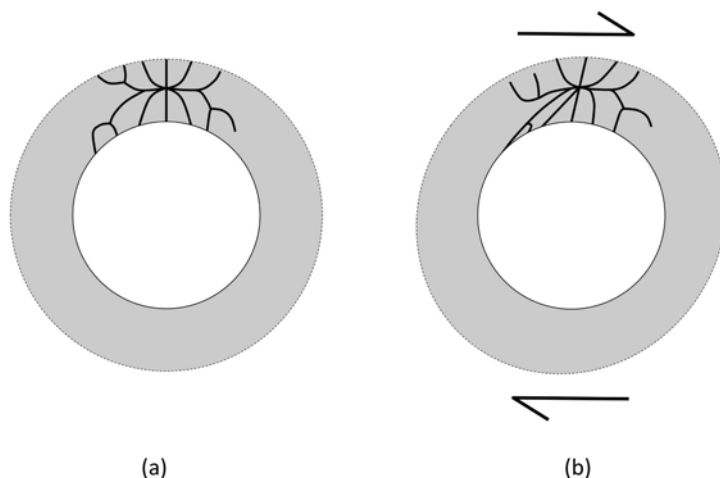


Figure 4-13 Immobilized shell of crosslinked molecules on a silica particle (a) at equilibrium and (b) under shear, leading to the observed exponential dependence of the concentrated suspension viscosity with particle volume fraction.

The exponential model thus appears to be specific of concentrated suspensions of particles with a shell of crosslinked molecules bound to the particle surface, so that i) they stay attached, and ii) show elastomer type deformation when the suspension is sheared as sketched in Figure 4-13. These two conditions were met in the case of the HL suspensions. The prevalent interaction between the silanol groups on the surface of the particles and the acrylated chain ends of the HBP was H-bonding³⁹⁰, which was stronger than the intermolecular interactions between adjacent HBP molecules. H-bonds were observed for nanocomposites containing untreated silica particles and polymer matrices with carbonyl groups using various methods (FTIR, NMR and DSC^{391,392}). The deformation of the H-bonded HBP was also restricted, if more than one branch was attached to the particle surface, leading to an elastomeric rather than a viscous response and to self-similar dynamics (Figure 4-6).³⁶⁶ The average thickness of the shell was found to be equal to 7.5 nm, which is comparable to the equilibrium radius of the single 3rd generation HBP molecule (4-5 nm^{115,393}). Since entanglement between such molecules can be disregarded, this result provides evidence of strong repulsive interactions between particles, resulting from the pinning of the molecules on the silica particles.²³ One may also expect that, due to strong affinity of the HBP and the silanol surface of the silica particles, the globular HBP were squeezed together and align perpendicularly on the particle surface to form a dense, star-like arrangement around the particles. The two conditions required for the

exponential scaling were tested with suspensions of HL in DPHA. The affinity of this small, star-like molecule with the silanol surface of the HL particles was similar to that of the acrylated HBP. The relative viscosity increase of HL suspensions in DPHA is depicted in Figure 4-10. In spite of limited amount of data, it is evident that the viscosity increased far beyond the “hard sphere” prediction. The application of the exponential model leads to a thinner immobilized shell (3.5 nm) than for the HBP, which again compares with the size of the smaller DPHA molecule.

If one of the above two conditions for the exponential scaling is not met, then the “hard sphere” behavior is observed. This was the case for a number of suspensions with strong interfacial interactions, but which did not fulfill the second condition of crosslinking.²⁹¹ This was also the case of the AS suspensions in HBP, which did not fulfill the first condition of strong interactions since only intermolecular interactions were present between the methacrylate group of the silane (covalently attached to the silica surface³⁹⁴) and the acrylated chain ends of the HBP. The average thickness of the shell was found to be equal to 3.3 nm. The relative viscosity of suspensions of AS in DPHA is also shown in Figure 4-10 and found to be almost identical to that of the HBP/AS case, with resulting shell thickness also close to 3.3 nm. The concurrence of the relative viscosity of AS suspensions in two different acrylate liquids, leading to the same shell thickness, suggests that the methacrylsilane, rather than the dispersion state, was the main factor that controlled the viscosity of the AS suspensions.

The present work confirms the major influence of particle surface chemistry and resulting interfacial interactions on the rheological behavior of concentrated suspensions of nanoparticles.

4.5.5 Calorimetric Aspects of Polymer Immobilization

A gradient in the glass transition temperature in the immediate vicinity of solid surfaces was reported to be the result of immobilization of the polymer. In the case of nanoparticles with very high specific surface, the immobilized polymer fraction can be important.²⁹⁸⁻³⁰⁰ Such effects have been studied also by calorimetry.³⁹⁵

The decrease in $\Delta C_{p,HBP}$ at T_g (Figure 4-9d) with increasing silica fraction reflects a decrease of the polymer mobility due to its interaction with the particles. Similarly, the enthalpy recovery peak ΔH_r , evident in the non-reversing data (Figure 4-7c), decreased

with increasing silica fraction, which implies a progressive suppression of physical aging also resulting from the immobilization of the glass-forming phase.

It was assumed that a fraction of the HBP was totally immobilized in the vicinity of the particle. What happens at the transition is beyond the purpose of this work. The actual physical state in the vicinity of the particle was simplified in the form of a solid shell of constant thickness as sketched in Figure 4-14.

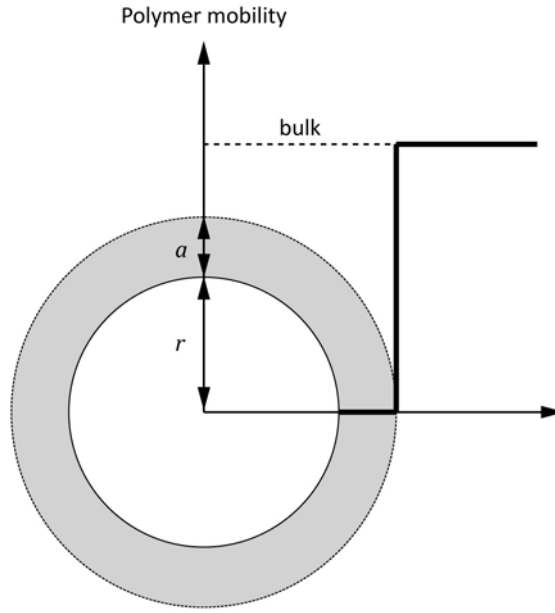


Figure 4-14 Sketch of the immobilized polymer shell of thickness a on the particle surface and corresponding mobility (thick solid line).

The immobilized volume fraction ϕ_{imm} was calculated assuming equal densities of the mobile and immobilized HBP³⁹⁵:

$$\phi_{\text{imm}} = 1 - \frac{\Delta C_{\text{p,HBP}}}{\Delta C_{\text{p,HBP}}^0} \quad 4.12$$

where $\Delta C_{\text{p,HBP}}$ is the reversing heat capacity step at T_g of the HBP fraction in the suspensions and $\Delta C_{\text{p,HBP}}^0$ is the reversing heat capacity step at T_g of the pure HBP. This approach is analogous to the calculation of a rigid amorphous fraction in semi-crystalline polymers proposed by Sargsyan *et al.*³⁹⁵ As shown in Figure 4-15, the immobilized HBP fraction was found to be proportional to ϕ for both suspensions, but higher in the case of HL. The thickness a of the immobilized shell around individual particles was calculated assuming that all particles have the same radius r :

$$a = r \left(\left(1 + \frac{\phi_{\text{imm}}}{\phi} \right)^{1/3} - 1 \right) \quad 4.13$$

With $r = 6$ nm for the HL and $r = 9.1$ nm for the AS, the average thickness of the immobilized shell was independent on ϕ and equal to 1.9 ± 0.1 nm for the HL and 1.7 ± 0.3 nm for the AS particles, as shown in Figure 4-16.

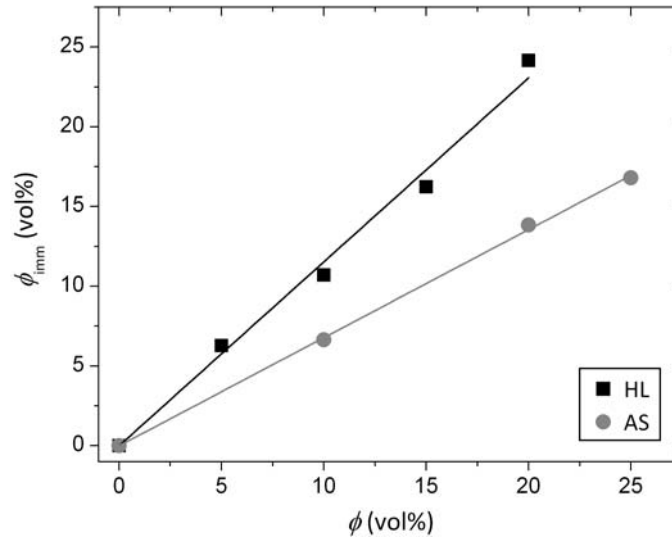


Figure 4-15 Immobilized HBP volume fraction ϕ_{imm} as a function of filler fraction ϕ for HL and AS suspensions.

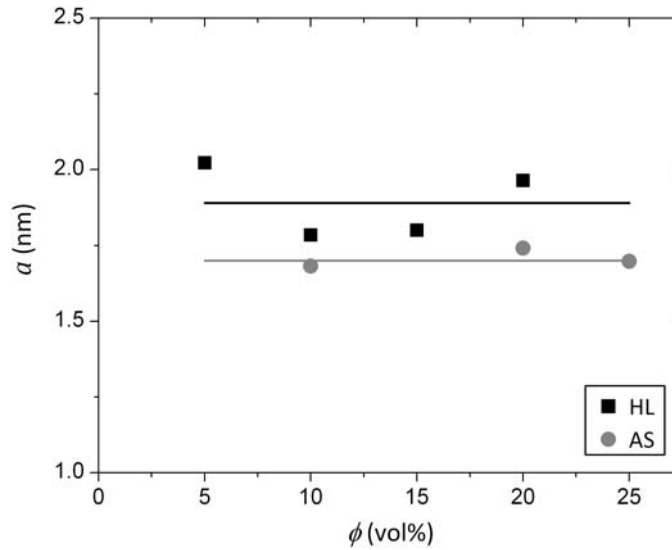


Figure 4-16 Immobilized shell thickness a as a function of filler fraction ϕ for HL and AS suspensions.

4.5.6 Discussion

A vast amount of literature was devoted to the interactions between polymer molecules and inorganic surfaces. In the case of nanocomposites with a very large specific surface of the filler, such interactions are expected to substantially influence the properties of the polymer phase. However, contradictory results were frequently reported for the influence of particles on the T_g .³⁹⁶ For example, the same epoxy resin that formed an immobilized layer on Al_2O_3 particles did not do so on SiO_2 particles.^{397,398} In poly(vinyl acetate)/ SiO_2 nanocomposites there was no evidence that the local segment dynamics of chains adjacent to the filler differed from the bulk matrix.³⁹⁹ However, for PMMA/ SiO_2 nanocomposites, a broadening of the glass transition was observed, attributed to hydrogen bonding between the matrix and the filler.^{391,392}

These contradictory results can in fact be reconciled, when the nature of the polymer/particle interaction is clarified. For PMA-based nanocomposites it was shown that silica surface treatment, where the OH groups were substituted by trimethylsilyl groups, led to intermediate immobilization effects between that of untreated silica and the bulk polymer.³⁹² The degree of grafting and the size of the surface functionalizing molecules strongly influenced the thermal behavior, relaxation dynamics and viscosity in unentangled polymers.⁴⁰⁰ Small molecules used for surface treatment behaved as “dry brushes” with respect to the host polymer, the T_g of which decreased and the viscosity only weakly depended on ϕ . On the contrary, large molecules wetted the surrounding polymer and led to increased T_g , relaxation times and viscosity. These effects could be very large at filler fractions as low as 3 wt%. It was moreover observed that if the polymer had comparable or lower degree of polymerization (DP) with respect to the grafted molecules, the T_g of the nanocomposite was increased, and when the DP was higher, the opposite effect was observed.²³⁵

The markedly different degree of immobilization for the HL and AS suspensions confirmed the importance of the particle surface chemistry and resulting interfacial interactions. A tentative sketch of the interfacial structure for the investigated systems is depicted in Figure 4-17. In the case of HL particles with silanol groups on the surface, the prevalent interaction with the acrylated chain ends of the HBP is H-bonding³⁹⁰, which is stronger than the intermolecular interactions between adjacent HBP molecules. The immobilized shell should be constituted within one monolayer of HBP. The average thickness of the shell on the HL particles was found to be equal to 1.9 nm, which was indeed half to the size of the HBP molecule.

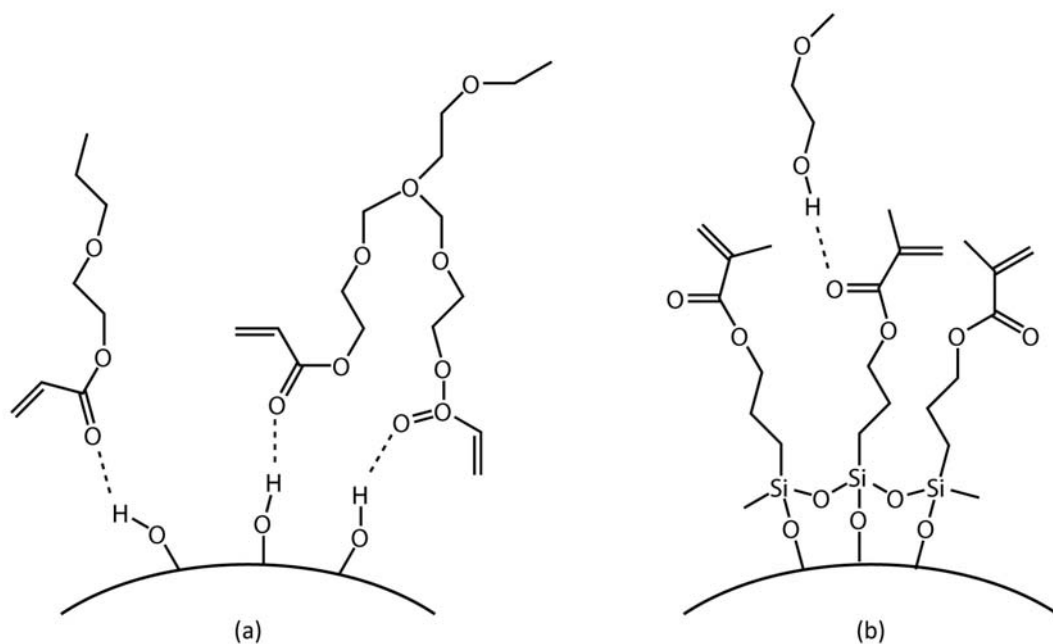


Figure 4-17 Tentative interactions in immobilized shells around a silica particle. (a) H-bonding between the acrylated HBP (the ends of three branches of the molecule are depicted) and the silanol surface of a HL particle, (b) covalent bonding of the methacrylsilane to the AS particle and H-bonding with one HBP branch.

In the case of the methacrylsilane treated AS particles, the silane molecule was covalently attached to the silica surface by hydrolysis and condensation reactions.³⁹⁴ The Si-O covalent bond was, again, stronger than the intermolecular interactions between the methacrylate group of the silane and the acrylated chain ends of the HBP. Additional H-bonds might also have been present between the methacrylate groups and residual OH groups of the HBP. The average thickness of the shell was found to be equal to 1.7 nm, which was slightly higher than the length of the methacrylsilane (≈ 1 nm). This value corresponds to the extended configuration of the silane, favored by the small difference in solubility parameters between the acrylate and methacrylate functions.⁴⁰¹

Besides surface chemistry effects, the curvature of the surface may also influence the extent of immobilization. Harton *et al.*⁴⁰² showed that for the same system the thickness of the bound layer was equal to 1 nm in case of 15 nm diameter nanoparticles, and became equal to 5 nm in the case of thin films on flat surfaces. As the particle size increased from 13 nm in HL to 18.2 nm in AS, this is expected to play a role in the case of good silica dispersion in the HBP.

A further indication of the existence of an immobilized layer is the fact that for systems with quite different morphologies rheological and calorimetric approaches both led to an immobilized layer thickness that was independent on the filler fraction. With purely hydrodynamic interactions between the particles, the interacting volume per

particle would be close to zero at low filler fraction and become very important as particles come into close contact. This would in fact not be consistent with our finding of a constant interacting volume per particle. The calorimetric results are quite different from the rheological results for the immobilized layer thickness. This was expected, since the molecular scale relevant for shear viscosity and heat capacity are also different. In any case, the results are in qualitative agreement, with a higher immobilized layer thickness for the HL suspensions than for the AS suspensions. The liquid-to-solid transition below 10% of silica for the HL suspension is consistent with the higher immobilized HBP fraction with respect to AS suspensions, where this transition occurred above 20% of silica. These results underline the important role played by interfacial interactions in nanocomposite materials.

4.6 SUMMARY

The analysis of the rheological and glass transition behavior of agglomerated and well-dispersed concentrated nanocomposite suspensions of silica in an acrylated HBP, using both untreated and silylated particles, led to the following conclusions:

- A liquid-to-solid transition systematically occurred for concentrations lower than the maximum packing fraction ($5\% < \phi < 10\%$ for HL, $20\% < \phi < 25\%$ for AS). This was attributed to the presence of an immobilized polymer layer on the surface of the particles, resulting in an effective particle fraction higher than the real fraction. The average thickness of this layer was equal to 3.3 nm for AS and 7.5 nm for HL particles.
- In the case of agglomerated silane-treated silica with weak intermolecular interactions with the HBP, the classic “hard sphere” model for concentrated suspensions was validated using a constant immobilized layer thickness. In the case of well-dispersed suspensions of untreated silica H-bonded with the HBP, an exponential increase of the viscosity with the particle fraction was derived.
- The existence of an immobilized HBP layer around the particles was confirmed by calorimetry.

5 PHOTO-CALORIMETRY, PHOTO-RHEOLOGY AND TIME-INTENSITY-TRANSFORMATION DIAGRAMS

The addition of nanoparticles was found to dramatically increase the viscosity of the HBP suspensions, which may greatly compromise the processability of the HBP nanocomposites. The objective of this chapter is to explore the dynamics of the structure-property relation during photo-polymerization. Attention is paid to the kinetics of network formation and to the viscoelastic property build-up of the composites. This information should be useful to generate time-intensity-transformation diagrams similar to the ones compiled by Schmidt *et al.*⁴⁴

5.1 PHOTO-CALORIMETRIC ANALYSIS

5.1.1 Conversion and Conversion Rate

Figure 5-1 shows the double bond conversion as a function of time and UV intensity for HBP and composites containing HL and AS. After the reaction took off, the conversion increased rapidly and then slowed down again, until a plateau value was reached. The induction time depended on the UV intensity and was attributed to the formation of initiator-derived radicals and the inhibiting effect of dissolved oxygen. The final conversion of the HBP was 73%, which was reduced to 65% and 72% for the composites with 20% HL and AS, respectively.

In all cases, two main polymerization stages were identified. These were already observed for other acrylate systems, including HBP,¹⁶ and for silica nanocomposites.¹⁹⁷ At the beginning of the reaction, a sharp increase in the rate of polymerization was evident, which corresponded to autoacceleration. Due to the increasing viscosity, the mobility of the long-chain radical species was reduced; hence, two radical species were less likely to approach each other and recombine. Consequently, the rate constant for termination dropped, and the rate of polymerization increased.

Initiation and propagation were barely affected by the increased viscosity of the reactive mixture, because the mobility of the small monomers was still high. During the second stage, which started after going through a maximum rate of conversion, the reaction rate dropped quicker than would be expected due to the consumption of monomers only (autodecceleration). The overall reaction then became purely diffusion controlled. Because the cure temperature was above the ultimate T_g of the cured materials (Chapter 6.5), a third stage, controlled by vitrification, could not be identified in any of the mixtures.¹⁶

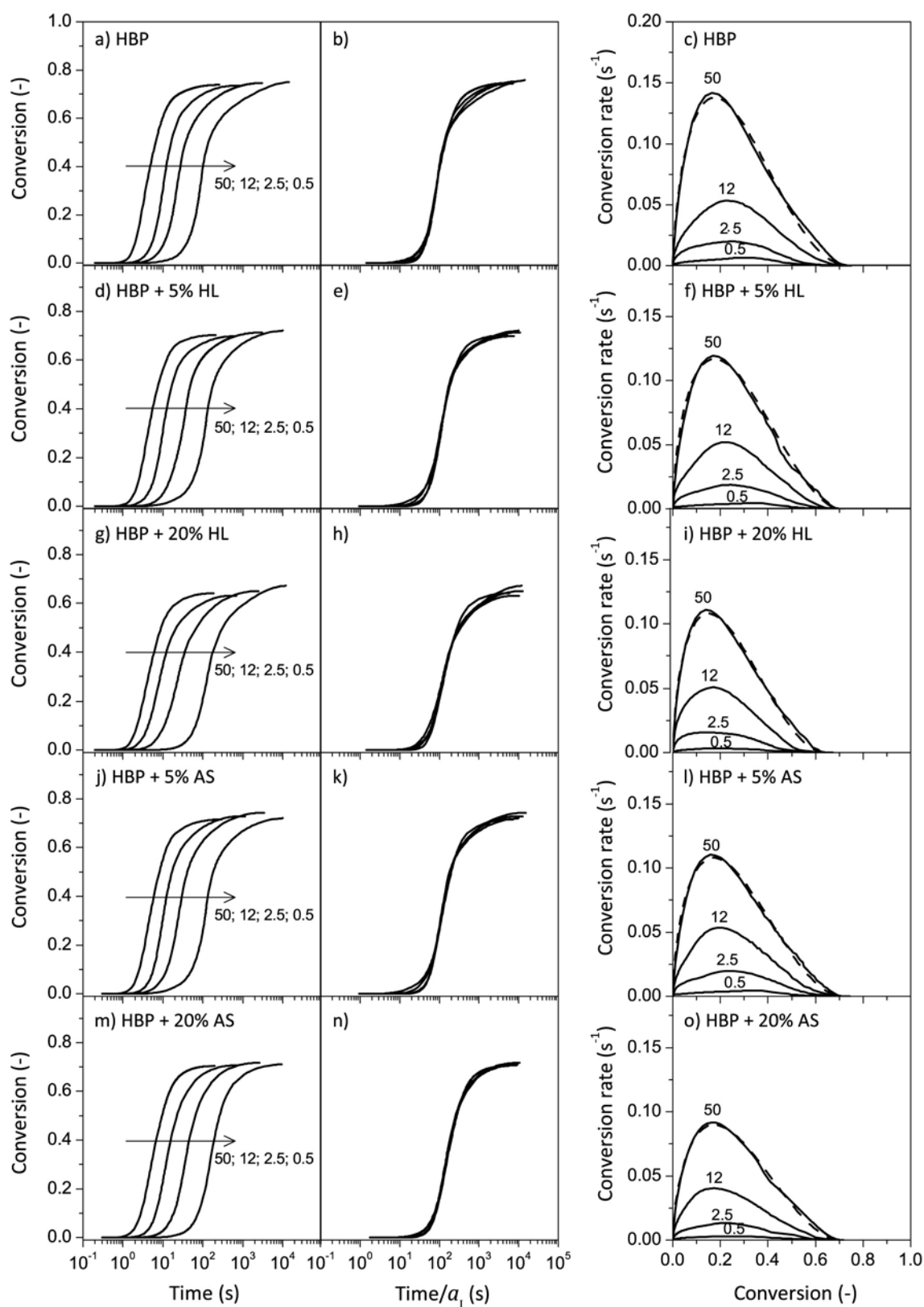


Figure 5-1 Conversion vs. time (left column), time-intensity superposition (middle column) and conversion rate vs. conversion (right column) for HBP and composites containing HL and AS at 5 and 20% filler fraction, polymerized at different intensities (mW/cm^2 as indicated). The autocatalytic model is compared with the conversion rate data for an intensity of 50 mW/cm^2 (dashed line).

5.1.2 Time-Intensity Superposition

It is evident that the intensity did not influence the maximum conversion of the HBP and the composites. This result is contradictory to the results reported by Schmidt *et al.*¹⁶ and Lecamp *et al.*¹⁵⁹, who found that conversion increased at higher intensities. The reason is in fact due to the different choices of limits for the integration of the heat flow with time. In the present case, the DSC peak was integrated from the time the lamp was switched on until the time when there was no longer any measurable change in the heat flow by DSC, whereas Schmidt defined the conversion reaction to be completed, when the heat flow reached 1/100th of its maximum value.¹² By choosing the same integration criteria as Schmidt, the influence of the intensity on the maximum conversion also became apparent.

The time-intensity superposition principle may be written as:

$$\alpha(t_1, I_1) = \alpha(t_0, I_0) \Leftrightarrow t_1 = \frac{t_0}{a_1} \quad 5.1$$

where α is the conversion, t is the time, I is the irradiation intensity and a_1 is the time-intensity shift factor. The validity of this approach was demonstrated by Corcione *et al.*⁴⁰³ for the photo-polymerization of non-vitrifying epoxy-based resin.

For the HBP and HL and AS composites a single master curve was obtained by a horizontal shift of the conversion *versus* time curves at different intensities according to Equation 5.1. The shift factors were determined using the data at 0.5 mW/cm² as reference, therefore the shift factor at 0.5 mW/cm² is unity. The shifted curves are shown in Figure 5-1b,e,h,k,n. For the HBP and the composites, the time-intensity superposition holds well between 0.1 and 0.6 conversion. The discrepancy in the initial part of the curves may be explained with a delay in the measurement of the evolved heat by the DSC, which is emphasized at the high intensities when the heat flux was higher. The filler content did not affect the shift factors, which showed power-law dependence on the intensity (Figure 5-2):

$$a_I = a_0 \cdot I^b \quad 5.2$$

where a_0 is the proportionality factor and b is the exponent equal to 0.7 ± 0.02 .

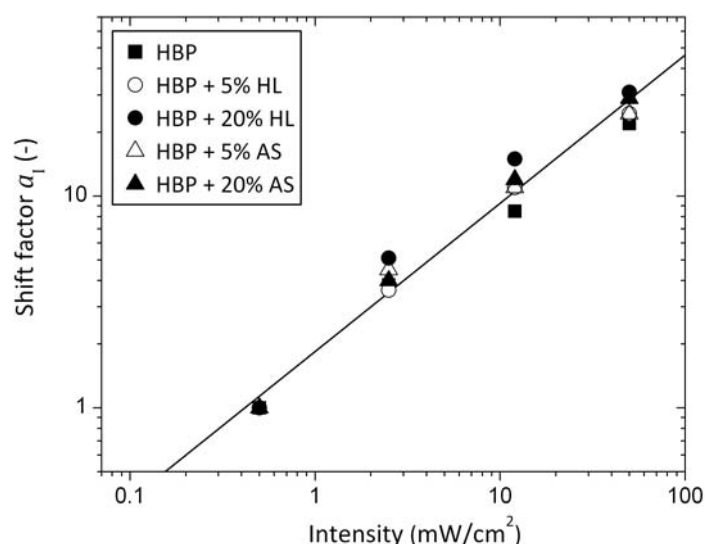


Figure 5-2 Time-intensity-shift factor for HBP and composites containing 5 and 20% HL and AS. The power-law fit is represented by the continuous line.

5.1.3 Influence of Silica Particles on Conversion

Figure 5-3 depicts the ultimate conversion for all materials investigated. It is evident that the maximum conversion in HL composites decreased with the filler volume fraction ϕ (11% reduction at $\phi = 20\%$) compared to HBP, whereas the final conversion of the AS composites was nearly independent of ϕ (1.5% reduction at $\phi = 20\%$).

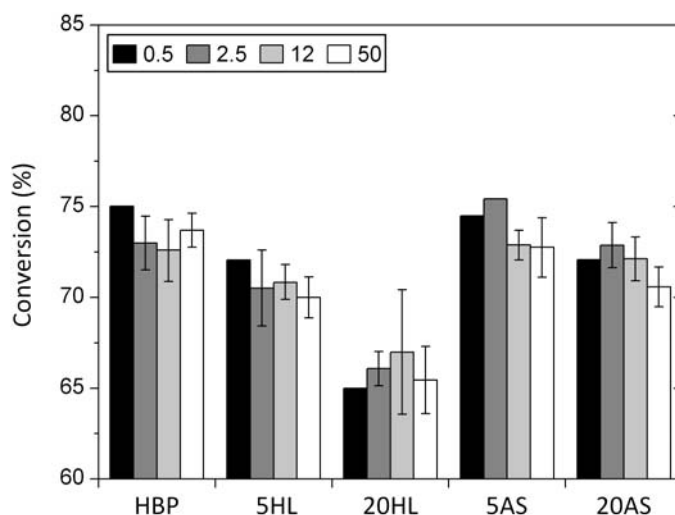


Figure 5-3 Maximum conversion for HBP and composites containing 5 and 20% HL and AS at different intensities (mW/cm² as indicated).

The observed reduction of the maximum conversion on addition of a filler was also found by Harsch *et al.*¹⁹³ for composites based on epoxy resin and SiO₂ particles. On the contrary, Cho *et al.*¹⁹⁷ showed that the formulations containing silica nanoparticles gave

higher exothermic peaks and ultimate conversion, as well as a shorter induction time. They suggested that silica particles behaved as an effective flow or diffusion-aid agent for the photo-polymerization process. However, this phenomenon was unlikely, because the viscosity of the composite increased with filler loading, thus reducing the mobility of the reacting species. UV absorption measurements showed slightly improved transparency for the HL composites than for HBP in the range of 250 to 500 nm (Figure 5-4). Therefore, light scattering due to nanoparticles could be excluded as a source of decreased conversion. The increased transparency of the HL composites was due to their reduced refractive index compared with that of the HBP, hence increased Fresnel transmittance coefficient T_r according to⁴⁰⁴:

$$T_r = \frac{4n_m}{(n_m + 1)^2 + \kappa_m^2} \quad 5.3$$

where n_m and κ_m are the refractive and extinction indices of the material, respectively. The refractive index of the composite is a function of the refractive indices of the HBP ($n_m = 1.49 - 1.5$ measured with a standard refractometer) and SiO_2 ($n_m = 1.46$ at 500 nm²¹³) and often behaves according to the rule of mixture.^{213,217} The refractive index of the composite containing 20% of HL was found to be equal to 1.481. The extinction index is negligible for the considered materials in the visible range. The transmittance of the nanocomposite at 500 nm was equal to 96.24% according to Equation 5.3, which was higher than that of the HBP, found to be in the range of 96.0 to 96.1%.

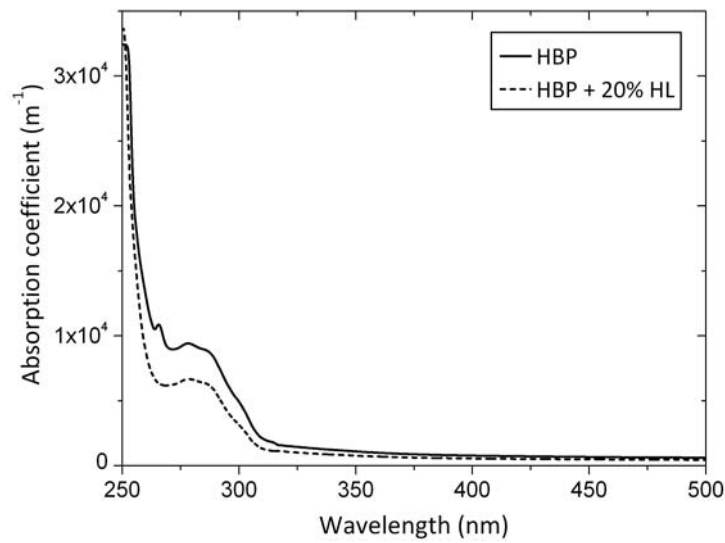


Figure 5-4 UV absorption of cured HBP and a composite containing 20% HL.

5.2 CONVERSION MODELING

One phenomenological model successfully applied to UV curing of acrylates and acrylate composites is the autocatalytic model^{155,189,405}:

$$\frac{d\alpha}{dt} = k\alpha_r^m(1 - \alpha_r)^n \quad 5.4$$

with

$$\alpha_r = \frac{\alpha}{\alpha_{\max}} \quad 5.5$$

where α is the conversion at any time, α_{\max} is the maximum conversion, k is the rate constant, m is the autocatalytic exponent, and n is the reaction order. The autocatalytic exponent takes into account the autoacceleration, i.e. the immobilization of the polymer chains in the forming network due to an increase in viscosity, which prevents recombination of the polymer radicals, resulting in a drop of the termination rate. This model was derived from the autocatalytic Kamal model⁴⁰⁶, which was developed for the thermal cure of polyesters. Although photoinitiated polymerization is autoaccelerated and not autocatalyzed, the shape of the curves were the same and the model was applied to describe these reactions in a purely phenomenological way. The curves obtained with the autocatalytic model for an intensity of 50 mW/cm² are shown in Figure 5-1c,f,i,l,o. The rate constant k was modeled assuming power-law dependence of the UV intensity:

$$k = k_0(\phi) \cdot I^\beta \quad 5.6$$

where k_0 is a factor that depends on the filler fraction ϕ , and I is the UV intensity. The exponent β is related to the termination mechanism. For $\beta < 0.5$, primary radical termination is predominant, i.e., the reaction of an initiator radical with a radical site on the evolving polymer. For $\beta = 0.5$, second order termination is predominant, i.e., the reaction of two radical polymer sites. For $0.5 < \beta < 1$, first-order termination, i.e., trapping of the radical end in the forming network or recombination with oxygen, and second-order termination happen in parallel. For $\beta = 1$, first-order termination is predominant.⁴⁰⁷

5.2.1 Influence of Intensity

The rate constant of the HBP and the composites strongly depended on the intensity (Figure 5-5a). The intensity exponent β (Figure 5-6) was found to be in the range of 0.6 to 0.8, which indicates that first-order and second-order termination mechanisms occurred

simultaneously. In contrast, the work of Schmidt *et al.*¹⁶ and Timpe *et al.*¹⁶³ gave values for β smaller than 0.5, indicating that primary radical termination was predominant. The degree of branching D_B of the acrylated HBP used by the former authors was equal to 0.35, which is lower than that in the present work (0.41). A lower D_B implies that additional reactive sites are less accessible and in fact are available for radicals trapping, leading to β smaller than 0.5. First-order termination includes the reaction of radicals with oxygen. Therefore, higher amounts of dissolved oxygen could also have been the reason for the higher β values in the present case. The addition of a filler increased β , but did not change the termination mechanism.

The reaction order n and the autocatalytic exponent m were independent of the intensity (Figure 5-5b). The reaction order was around 0.7 and the autocatalytic exponent around 2, so that the overall reaction order ($m + n$) was ≈ 2.7 . This is close to the reaction order 3, which was found in a previous study on dimethacrylate oligomers.¹⁵⁶

The conversion at maximum conversion rate α'_{\max} increased towards lower intensities, as seen in Figure 5-5c. An increase in conversion at α'_{\max} is comparable with a shift of gelation to a higher conversion. Microgelation^{167,172} is the formation of macromolecules that are no longer soluble in the unreacted monomer liquid. At this stage, conversion proceeds in a macroscopic liquid state, in which shrinkage stress does not build up. Low intensities seemed to favor the formation of microgels and therefore increased the conversion at α'_{\max} . The same result was found by Neves *et al.*⁷⁹ for the photo-polymerization of acrylate composites. In this case and in the present case, lower viscosities were maintained during longer times, when lower intensities were used, which favored increased conversion before macroscopic gelation. Anseth *et al.*³⁵⁵ found the opposite trend and explained this with delayed volume shrinkage at higher intensities, which subsequently led to higher final conversion. This was not observed in the present work, where the final conversion was independent of UV intensity (Figure 5-3). A shift of gelation towards higher conversion allows the material to relax more shrinkage stress, which is favorable for the production of low-stress materials.

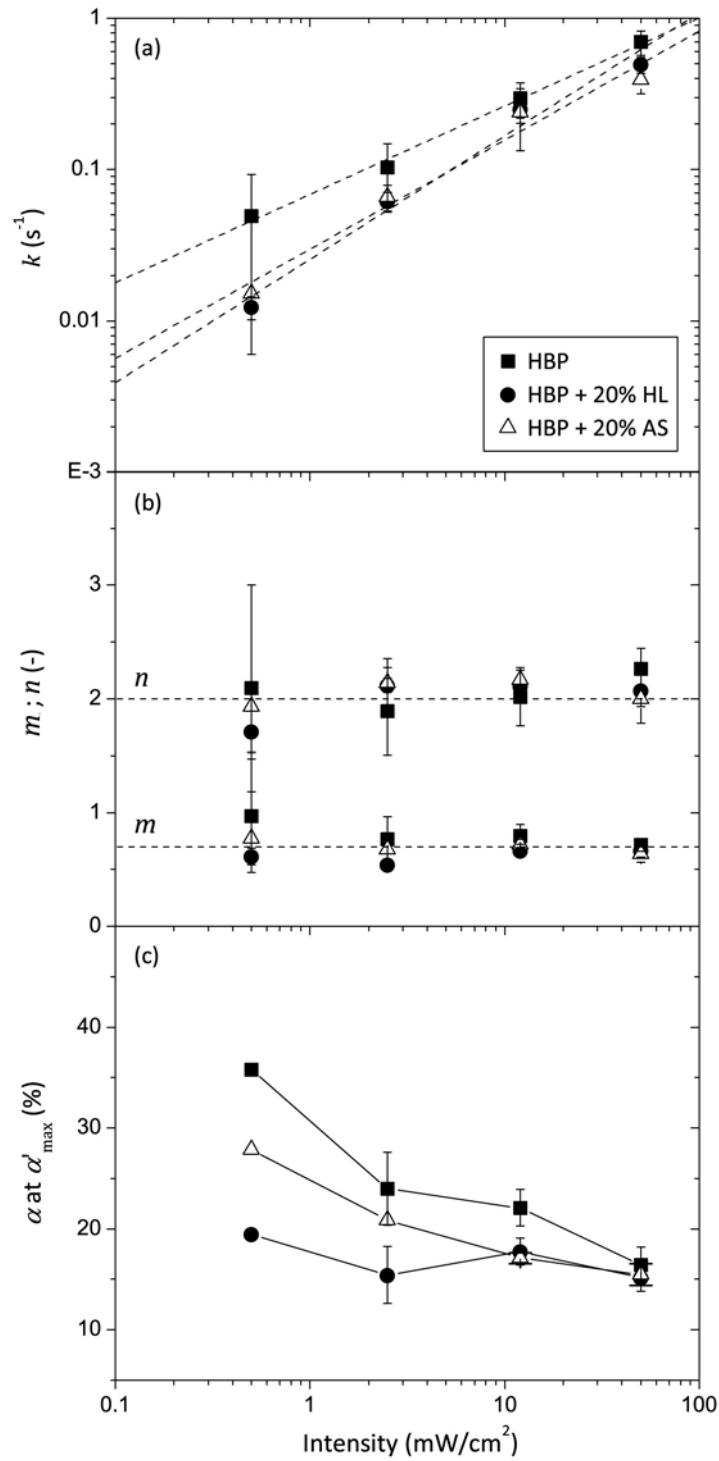


Figure 5-5 (a) Rate constant k , (b) autocatalytic exponent m and reaction order n , and (c) conversion α at maximum conversion rate α'_{\max} as a function of intensity for HBP and composites containing 20% HL and AS.

It is evident from Figure 5-6 that the values obtained for the intensity exponent β of the rate constants match the previously mentioned intensity exponent b of the time-intensity-shift factor. In fact, assuming that the kinetic law chosen to model the photopolymerization (Equation 5.4) is correct, one can write, at constant temperature:

$$\frac{d\alpha}{d\alpha_r^m(1-\alpha_r)^n} = k(I)dt \quad 5.7$$

Integration of this equation leads to:

$$\int \frac{d\alpha}{d\alpha_r^m(1-\alpha_r)^n} = \int k(I)dt = k(I) \cdot t \quad 5.8$$

If $\alpha(t_0, I_0) = \alpha(t_1, I_1)$, then, as the left side of Equation 5.8 only depends on α , it follows that:

$$k(I_0) \cdot t_0 = k(I_1) \cdot t_1 \quad 5.9$$

Substituting the power-law dependence of k in Equation 5.6 into Equation 5.9 one finds that:

$$k_0 \cdot I_0^\beta \cdot t_0 = k_1 \cdot I_1^\beta \cdot t_1 \Rightarrow t_1 = I_0^\beta \cdot \frac{t_0}{I_1^\beta} \quad 5.10$$

Comparing this equation to Equation 5.2, one can easily see that b must be equal to β , as it has been found for the photo-polymerization of HBP and HBP nanocomposites, as well as for composites based on fluorinated acrylates⁴⁰⁸. This result also points out that the radiation dose equivalence principle that was postulated by several authors^{79,147} and can be expressed as:

$$\text{Property} = F(t \cdot I) \quad 5.11$$

is not applicable in this case. In fact, to have the same conversion it is the product $(t \cdot I^\beta)$ that must be constant. It therefore descends that those systems, for which bimolecular or primary radical termination ($\beta < 1$) are predominant, may not abide by the radiation dose equivalence law. As monomolecular termination ($\beta = 1$) is favored by the restriction of the movement of the macroradicals, due to high viscosity and dense network formation, small monomers with low functionality and low viscosity are likely to highly deviate from the radiation dose equivalence principle. A further confirmation is given by the curing behavior before vitrification of DPHA (dipentaerythritol hexaacrylate), a monomer with low viscosity and fairly low functionality, for which Schmidt *et al.*¹⁶ found predominant primary radical and bimolecular termination with $\beta = 0.35$, and for which we found that the shift factor b was ≈ 0.32 . These results are in agreement with the finding of Feng and Suh⁴⁰⁹, who found that the power dose equivalence principle was respected in the case of monomolecular termination ($\beta = 1$), while for bimolecular termination ($\beta = 0.5$) it was not.

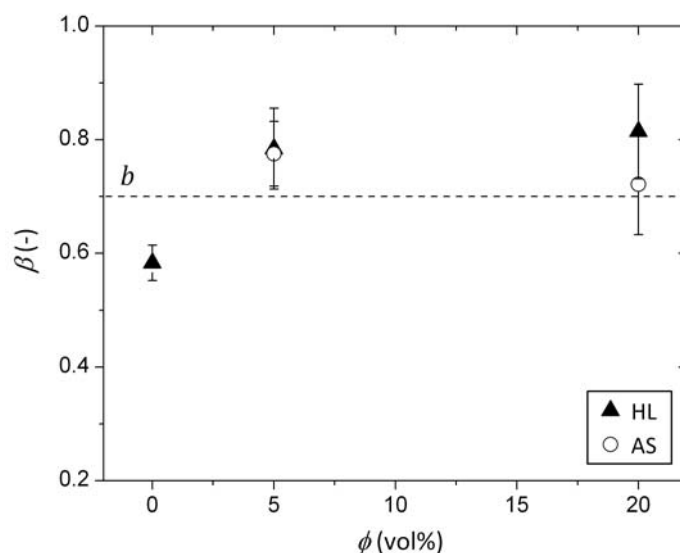


Figure 5-6 Intensity exponent β for HL and AS composites at different filler fraction ϕ . The dashed line represents the intensity exponent b of the time-intensity-shift factor.

5.2.2 Influence of Composition and Nanostructure

The rate constant marginally decreased with filler fraction (Figure 5-7a), in contrast with the large influence of UV intensity shown in Figure 5-5a. The mobility of the reacting species was, therefore, only weakly influenced by the considerable increase in viscosity of the nanocomposite suspension reported in Chapter 4. The reaction order n and the autocatalytic exponent m were independent of the filler fraction for all composites (Figure 5-7b). Because n and m were also independent of the intensity within experimental scatter, the conversion state of all materials investigated is fully described by the change of one single intensity and filler fraction dependent rate constant k . HL and AS composites showed reduced conversion at α'_{\max} compared with HBP (Figure 5-7c), particularly at low intensities. As pointed out earlier, the conversion at α'_{\max} is related to gelation of the material. The increased viscosity of the composites due to the nanofiller reduced the mobility of the reacting species, leading to early gelation of the surrounding polymer and eventually reducing the final conversion. This effect was more pronounced for HL composites owing to their considerably higher viscosity, resulting from the improved dispersion state of the nanoparticles compared with AS composites. Interestingly, the dispersion state of the nanocomposites did not significantly influence the rate constant or the overall reaction order. However, better dispersion led to earlier gelation, especially at low intensities, and lower ultimate conversion, with probable consequences in terms of stress build-up.⁴⁴

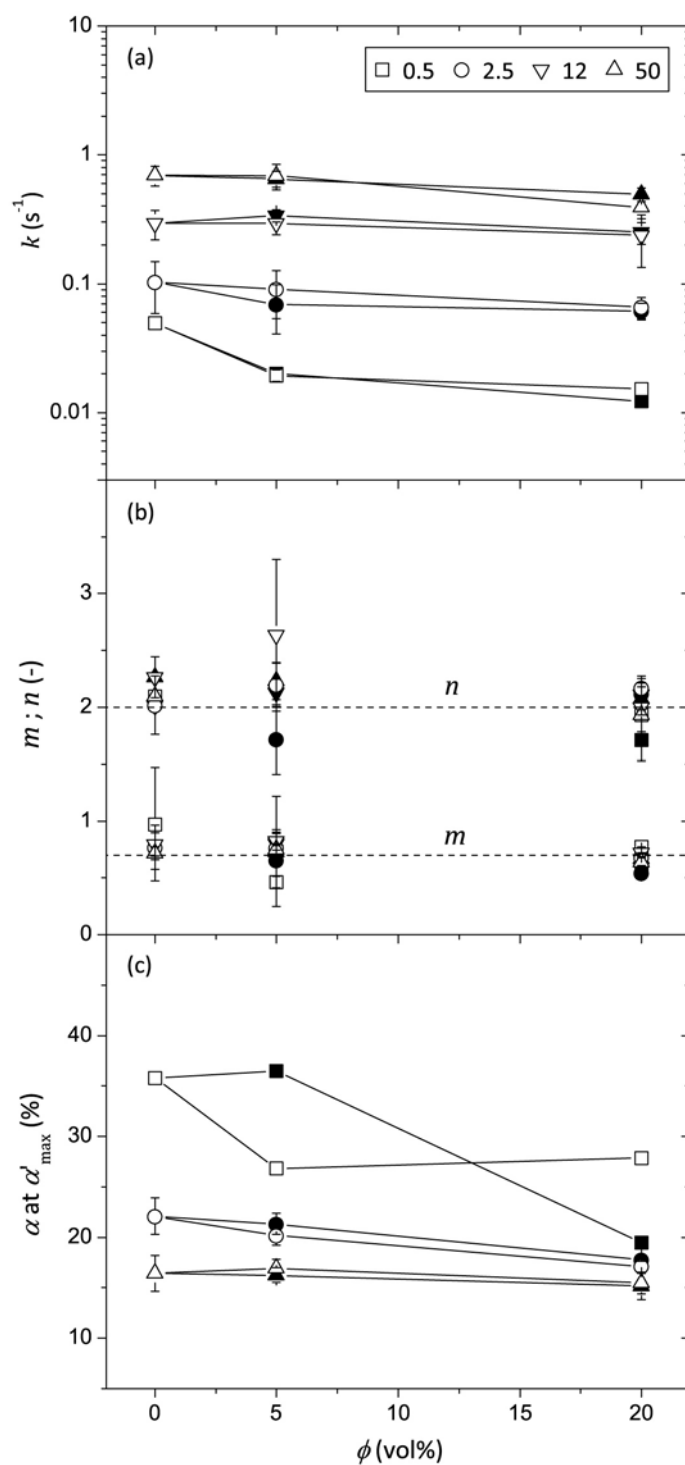


Figure 5-7 (a) Rate constant k , (b) autocatalytic exponent m and reaction order n , and (c) conversion α at maximum conversion rate α'_{\max} as a function of filler fraction ϕ for HBP and composites containing HL (full symbols) and AS (empty symbols) at different UV intensities (mW/cm² as indicated).

5.3 PHOTO-RHEOLOGICAL ANALYSIS

5.3.1 Modulus and Phase Data

The influence of intensity and composition on the complex modulus G^* and the phase angle δ between loss and storage moduli are shown in Figure 5-8. At time $t = 0$ the UV lamp was turned on. After a few seconds G^* increased rapidly over several orders of magnitude until it finally reached a plateau, due to the limits of the rheometer (approx. 6 MPa). At higher intensities, the stiffness onset, after which the stiffness increased rapidly, was shorter and the stiffness built up faster. The time at the stiffness onset for the HBP and composite containing 20% HL and AS is compared in Figure 5-9. The stiffness onset was defined as the crossover of the tangents as shown in Figure 5-8c. The stiffness build-up occurred generally later for the composites than for the HBP.

Figure 5-8b depicts the phase angle δ as a function of UV illumination time for HBP. At $t = 0$ and during the induction period the HBP remained viscous ($\delta = \pi/2$), and then δ dropped rapidly due to gelation and increasingly elastic behavior of the material. Gelation corresponds to the transition from a viscous liquid to a viscoelastic solid. Two criteria are generally used to demine the occurrence of gelation: i) at the crossover of storage and loss moduli, expressed in $\tan(\delta) = 1$, or ii) at the point, at which the phase angle is independent of the frequency.¹⁸⁰ In the following discussion, the time at $\tan(\delta) = 1$ will be used as the gelpoint criterion. The drop in δ was delayed, when lower intensities were used. The plateau value of δ after the transition was not reliable, due to the limits of the rheometer.

At $t = 0$, the AS composite (Figure 5-8d) did not show viscous, but liquid viscoelastic behavior ($\delta \approx 1$), due to the interaction with the silica particles. For the HL composite at 20% silica (Figure 5-8d), the elastic contribution to the shear strength was higher than the viscous contribution. This means that the material behaved like a viscoelastic solid also in the non-polymerized state, i.e. the material was in a physically gelled state, due to the presence of the particles. A liquid-to-solid transition was confirmed in the range of 5 to 10% filler fraction for the HL composites and in the 20 to 25% range for the AS composites from rheological analysis in the unpolymerized state, as was discussed in Chapter 4.

Vitrification, occurring when the T_g of the curing material becomes equal to the reaction temperature and defined as a peak in the $\tan(\delta)$ versus time curve,¹⁸¹ was not observed in HBP nor in any of the composites. This correlates with the finding that T_g was equal to 9°C for the HBP and the HL and AS composites, independent of the filler fraction,

which means that all investigated materials were in the rubbery state at room temperature.

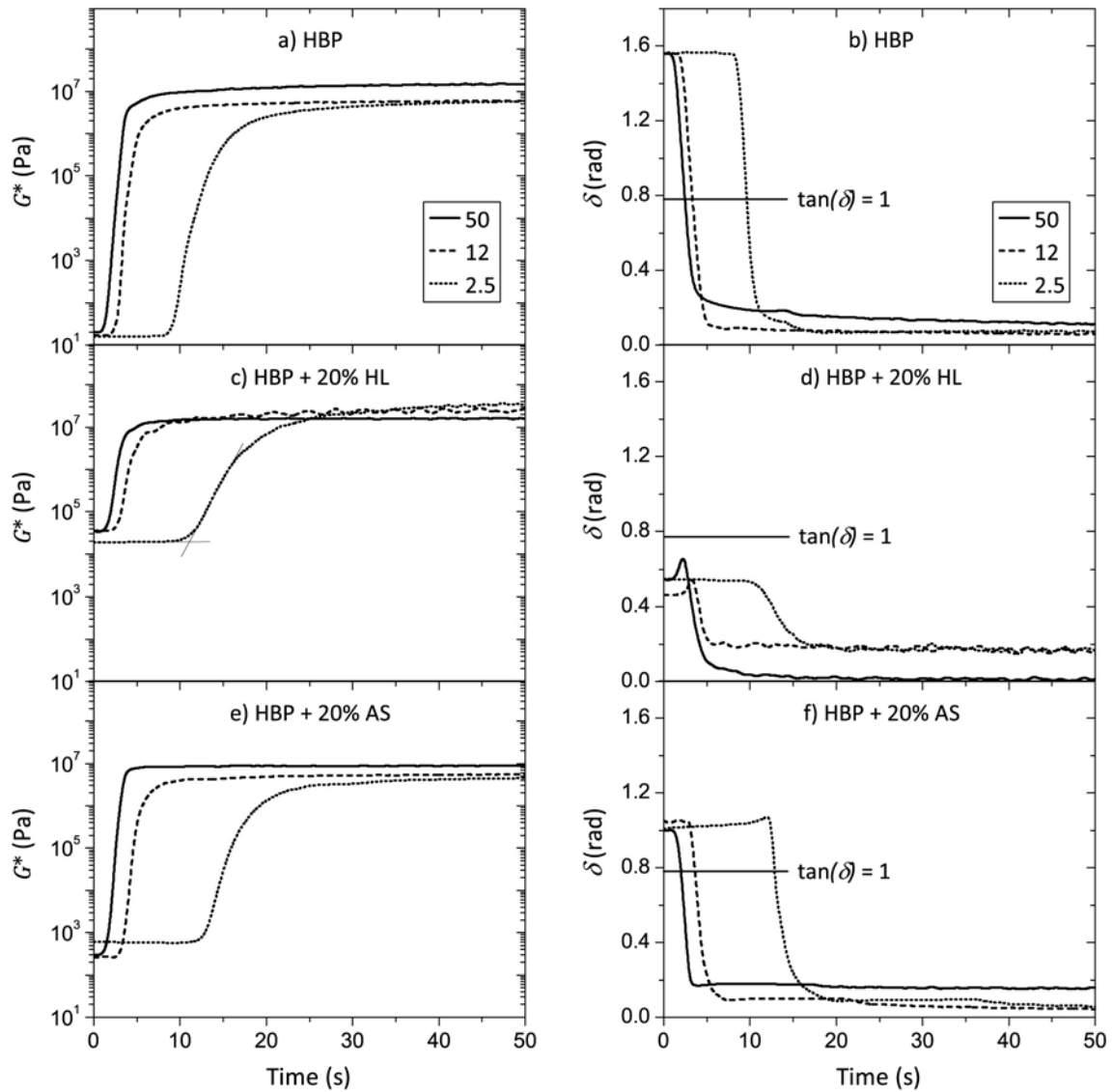


Figure 5-8 Evolution of the complex shear modulus G^* (left column) and the phase angle δ for HBP and composites containing 20% HL and AS, polymerized at different UV intensities (mW/cm² as indicated).

5.3.2 Influence of Intensity

The stiffness onset occurred later than the conversion onset (induction time, during which the initiator radicals are consumed by oxygen dissolved in the monomer), as shown in Figure 5-9. This is also demonstrated in Figure 5-10, where G^* is plotted against the conversion data obtained under the same UV conditions, and G^* was delayed with respect to conversion. This was due to the formation of microgels, the existence of which was

prolonged at low intensities and during which conversion proceeded in a macroscopic liquid state.

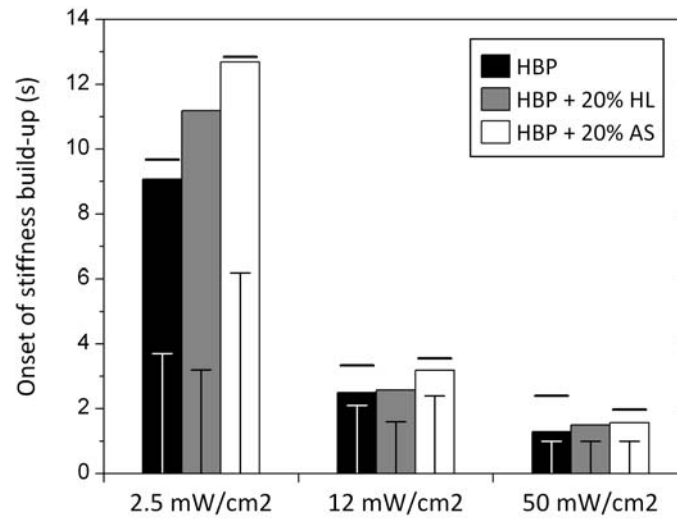


Figure 5-9 Stiffness onset for HBP and composites containing 20% HL and AS for three different intensities. The horizontal lines represent the time at gelation and the drop lines represent the induction time for conversion.

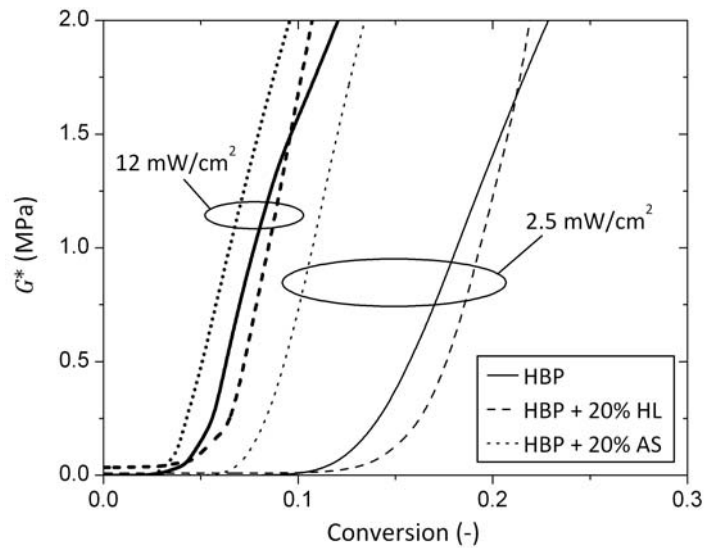


Figure 5-10 Shear modulus G^* as a function of conversion for HBP and composites containing 20% HL and AS at two different intensities.

Figure 5-9 shows that for the HBP polymerized at 50 mW/cm² the gelpoint was reached at 2.4 s, and considerably later for lower intensities, e. g. at 9.7 s at an intensity of 2.5 mW/cm². This result suggests that high intensities were very effective in reducing the initial liquid-like stage and the overall polymerization time. The time-intensity superposition (Equation 5.1) was also applied to the gelation time. A shift factor with power-law dependence on the intensity and an exponent b equal to 0.55 ± 0.09 was found,

which is close to the exponent determined from the conversion data. A strong correlation is evident between gelation and the onset of the stiffness build-up. This is because the formation of a 3-dimensional network is necessary for the material to bear mechanical load.

5.4 TIME-INTENSITY-TRANSFORMATION DIAGRAMS

The conversion data and modeled iso-conversion curves for HBP and composites containing 20% HL and AS were combined with structural information (i.e., gelation) in the form of time-intensity-transformation diagrams, depicted in Figure 5-11. It is clear that the intensity had a considerable influence on the conversion. The iso-conversion curves, derived from the autocatalytic model, reproduced the measured conversion data up to 50% conversion. For conversion higher than 50%, the model predicted shorter polymerization times than those measured. Schmidt *et al.*¹⁶ attributed the deviation from the autocatalytic model to vitrification. However, in the current case no vitrification occurred. The deviation of the model from the measured data was the result of the simplification of the intensity and composition dependence on one single parameter $k(I, \phi)$, i.e. with m and n independent of I and ϕ . This simplification only holds true up to 50% conversion.

For very high intensities the iso-conversion lines should become vertical, since there is a maximum intensity, beyond which the reaction does not accelerate further.⁴¹⁰ This is because the reaction kinetics are no longer controlled by the initiation rate, but only by the diffusion rate of the reactive species. For systems with high initiation efficiency, the saturation intensity can be as low as 30 mW/cm².⁴¹⁰

Figure 5-11 shows that the intensity dependence of conversion and gelation are different, especially for the HBP, as represented by the different slopes of the iso-conversion and the gelation lines. For the HBP and to a little extent for the AS composite, gelation was shifted to higher conversions, when lower intensities were used, this effect being more pronounced for the HBP than for the AS composite. This trend was already noticed from the delayed stiffness onset with respect to conversion (Figure 5-10) and the increased α at α'_{\max} (Figure 5-5c), which is also shown in the TIT diagrams. The delayed gelation at lower intensities was presumably due to favored formation of microgels^{167,172}. This delayed formation of rigid network is an important factor to reduce internal stress.

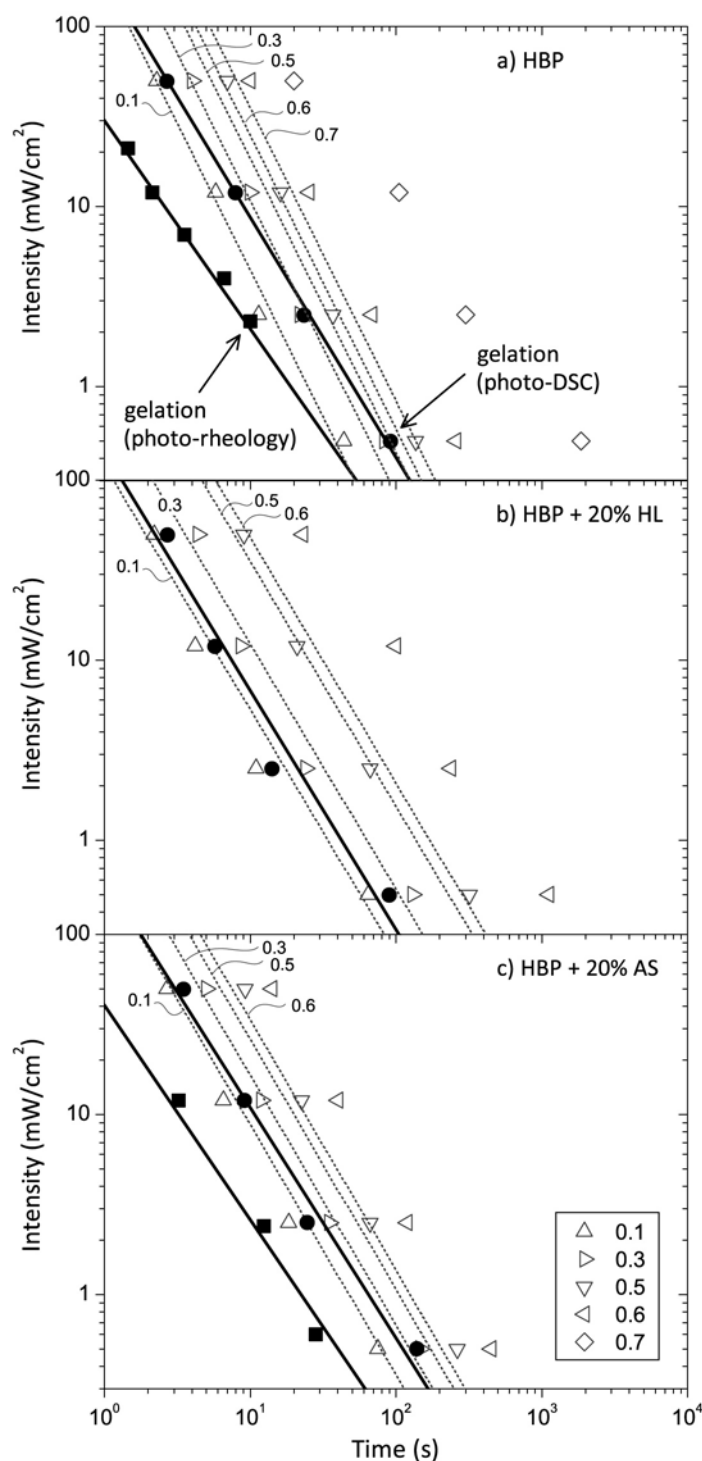


Figure 5-11 Time-intensity-transformation diagram of (a) HBP and composites containing (b) 20% HL, and (c) 20% AS. The empty symbols represent the conversion data as measured, the dotted lines represent the iso-conversion curves, derived from the autocatalytic model. The full symbols represent the occurrence of gelation, determined from photo-rheology (squares) and from photo-calorimetry (circles). The solid lines are the power-law fits of the intensity with the gelation time.

Gelation determined from calorimetric analysis occurred considerably later, i.e. at higher conversion, than if determined from photo-rheology. As an example, for the HBP, gelation was determined between 16 and 35% conversion (depending on the intensity) from calorimetry, while it occurred already before 10% conversion for all intensities

according to photo-rheological analysis. The latter result was confirmed in a similar photo-rheological study on hyperbranched acrylates.⁴⁴

For the HL composites, only calorimetric gelation could be identified, since the material was in a physically gelled state for $\phi > 5\%$. Calorimetric gelation occurred between 10 and 20% conversion, independent of the UV intensity, which is generally later than in the HBP and the AS composites, especially at low intensities. This early gelation implies, that internal stresses should be high in the HL composites. Interestingly, the stiffness build-up as a function of conversion (Figure 5-10) indicates delayed gelation for the HL composite with respect to the HBP and the AS composite. This behavior, on the other hand, should be favorable for the reduction of internal stress.

5.5 SUMMARY

The influence of UV intensity and of nano-sized SiO₂ particles on the photopolymerization behavior of an acrylated HBP was investigated. The analysis of the experimental data is summarized as follows:

- A time-intensity superposition was postulated. The shift factors were independent on the filler content, but showed power-law dependence on the intensity with an exponent equal to 0.7.
- An autocatalytic model was used to analyze the experimental conversion data. The reaction rate showed power-law dependence on the intensity, with exponents in the same range as those of the shift factor. This demonstrates that the radiation dose equivalence principle is not applicable for the photo-polymerization of these compounds.
- The ultimate conversion was found to be lower by 11% for the composites compared to the pure HBP. This effect was emphasized in the case of good dispersion of the silica particles, attributed to the increased viscosity of the suspension and therefore reduced mobility of the reacting species.
- The photo-curing behavior was also investigated in terms of stiffness build-up and gelation. Time-intensity-transformation diagrams were established combining conversion data with the occurrence of gelation. They showed that low intensities were able to delay the gelation with respect to conversion.

6 SHRINKAGE AND STRESS DYNAMICS AND THERMO-MECHANICAL ANALYSIS

Internal stress in materials is a consequence of dimensional changes, including chemical shrinkage and thermal contraction, combined with the build-up of elastic properties. Addition of a filler is effective to reduce shrinkage²⁰ and stress²⁴, but not always, due to increased stiffness²⁶. In the case of photo-polymerization, the role of the UV intensity in the shrinkage and stress build-up is not well established. The present chapter aims at clarifying these points, paying attention to the influence of UV intensity and inorganic phase. The thermo-mechanical properties of the HBP nanocomposites will also be presented.

6.1 SHRINKAGE DYNAMICS

Figure 6-1 shows the linear polymerization shrinkage as a function of polymerization time for HBP and HL and AS composites at different UV intensities. The

final shrinkage was roughly 4.5%, except in the case where 20% HL was added to the HBP. In that case, the shrinkage was reduced down to approximately 3%. At higher intensity the change in volume took off earlier, corresponding to a shorter induction time for conversion, and the shrinkage proceeded faster according to the faster polymerization reaction (Chapter 5).

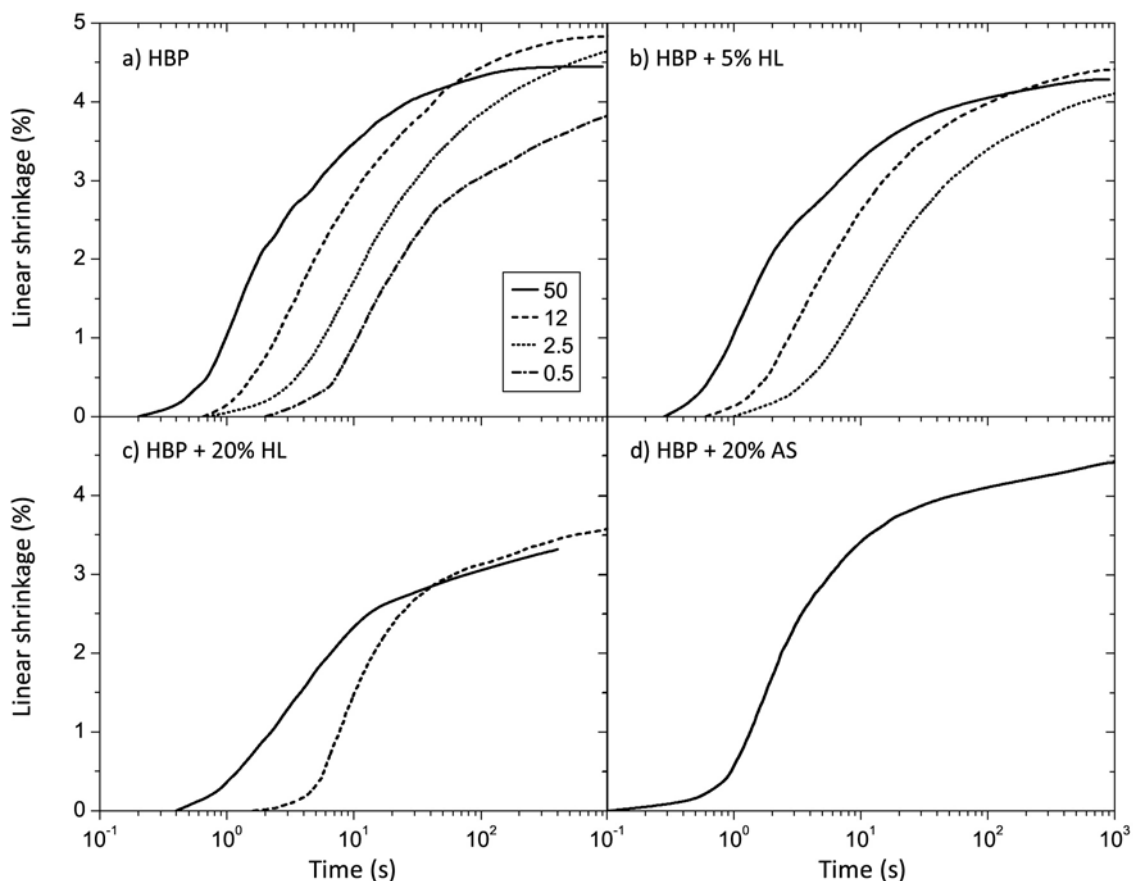


Figure 6-1 Linear shrinkage as a function of polymerization time for (a) HBP and composites containing (b) 5% HL, (c) 20% HL, and (d) 20% AS at different UV intensities (mW/cm² as indicated).

In order to determine the relation between shrinkage and conversion, the linear shrinkage is plotted as a function of conversion for three different UV intensities in Figure 6-2a. Conversion was measured as a function of time using photo-DSC (Chapter 5) and at the same UV intensities used for the shrinkage measurements. A markedly non-linear behavior with three stages is evident, which is quite different from the expected linear behavior of non-vitrifying systems⁶³ (Figure 2-1). In the first stage, the shrinkage reaction occurred ahead of conversion reaction up to $\alpha = 5$ -10%. In the second stage, shrinkage occurred linearly with advancing conversion until stage three, where the material continued to shrink, while the conversion almost came to a halt.

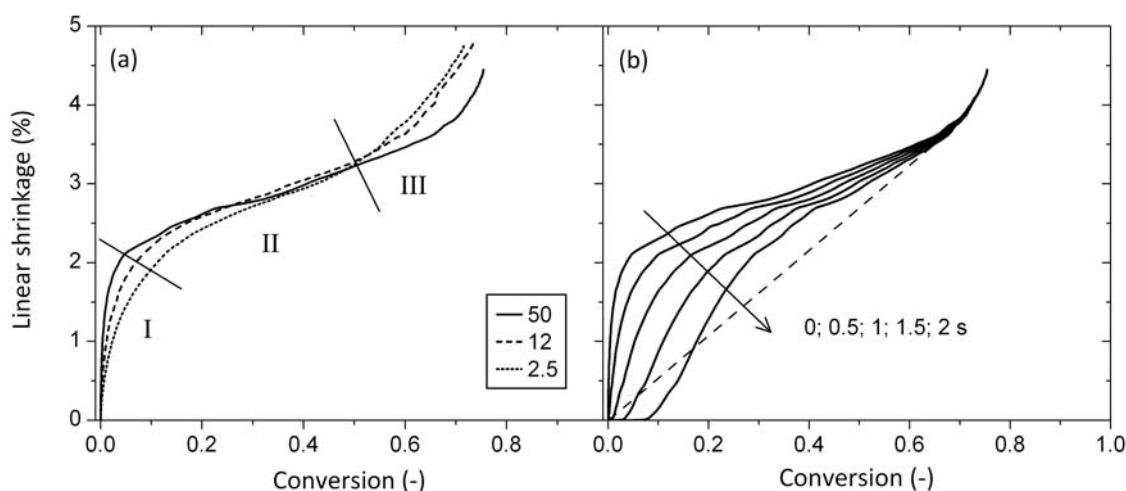


Figure 6-2 Linear shrinkage as a function of conversion for (a) HBP at three different intensities (mW/cm^2 as indicated) and (b) at $50 \text{ mW}/\text{cm}^2$ under the assumption that conversion measurements were delayed by 0.5 to 2 s. The dashed line represents the linear relationship according to de Boer⁶³.

The first stage, where shrinkage is ahead of conversion, was believed to be an artifact. It presumably resulted from a detection delay of the DSC compared with the interferometer. While interferometry is an extremely fast acquisition method, the measurements in the DSC depend on the heat transfer through the sample and through the sample holder assembly. To visualize the influence of this delay, the shrinkage measurements were shifted in time by 0.5 to 2 s, as shown in Figure 6-2b. If the delay was chosen larger than 1 s, the tendency of the curve was inversed and the shrinkage finally lagged behind conversion. FT-IR *in situ* interferometry could overcome this problem and give a better insight into the shrinkage *versus* conversion behavior.

Figure 6-3 shows that the final shrinkage was independent of intensity within experimental scatter. It was found in earlier studies that the ultimate shrinkage increased with conversion, due to increased degree of crosslinking and extent of cyclization.^{173,174} However, this explanation was not applicable to the current case, with conversion independent of intensity (Chapter 5). Stansbury *et al.*¹⁷⁵ observed a reduction of shrinkage at high intensities, resulting from exothermic effects that allowed the network formation to take place in a more expanded state. In the present case, no significant shrinkage reduction was observed at higher intensities, in spite of temperature rise of 7°C at $12 \text{ mW}/\text{cm}^2$ and 14°C at $50 \text{ mW}/\text{cm}^2$ during the photo-polymerization reaction.

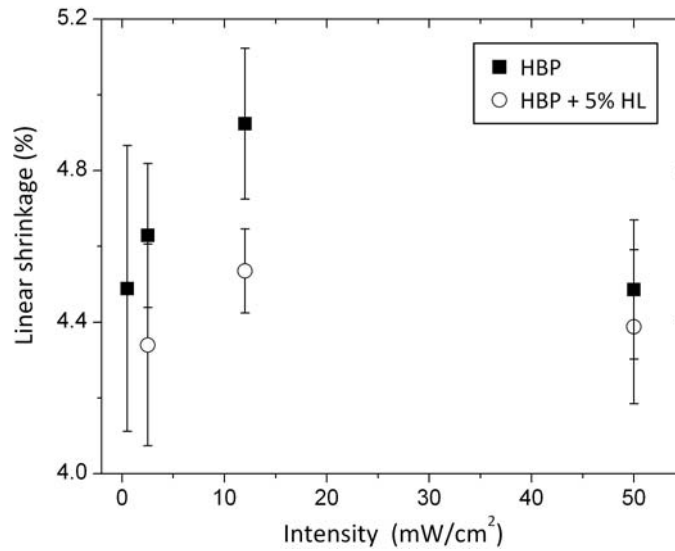


Figure 6-3 Linear shrinkage as a function of UV intensity for HBP and a composite containing 5% HL.

Figure 6-4 plots the overall shrinkage of the composites as a function of filler volume fraction ϕ . The shrinkage of the composite containing 20% HL was reduced by $26 \pm 14\%$ compared to the pure HBP, therefore the rule of mixture was obeyed within experimental scatter:

$$S_{\text{comp}} = S_{\text{HBP}}(1 - \phi) \quad 6.1$$

where S_{comp} and S_{HBP} are the linear shrinkage of the composite and the HBP, respectively. Figure 6-5 demonstrates that shrinkage was in fact related to conversion.^{55,59,60,67} This explains why AS composites (with higher final conversion) on average shrank more than HL composites (with lower final conversion) at 50 mW/cm². Assuming that conversion and shrinkage are linearly related, which was observed for non-vitrifying systems⁶³, one writes:

$$S_{\text{comp}} = S_{\text{HBP}} \frac{\alpha_{\text{comp}}}{\alpha_{\text{HBP}}}(1 - \phi) \quad 6.2$$

where α_{comp} and α_{HBP} are the conversion of the composite and the HBP, respectively. The experimental scatter was too high to test the accuracy of Equation 6.2. With 20% filler loading, combined with intensity increase from 12 to 50 mW/cm² an overall shrinkage reduction of 33% from 4.9% down to 3.3% shrinkage was achieved. This is a promising result for the production of dimensionally stable devices.

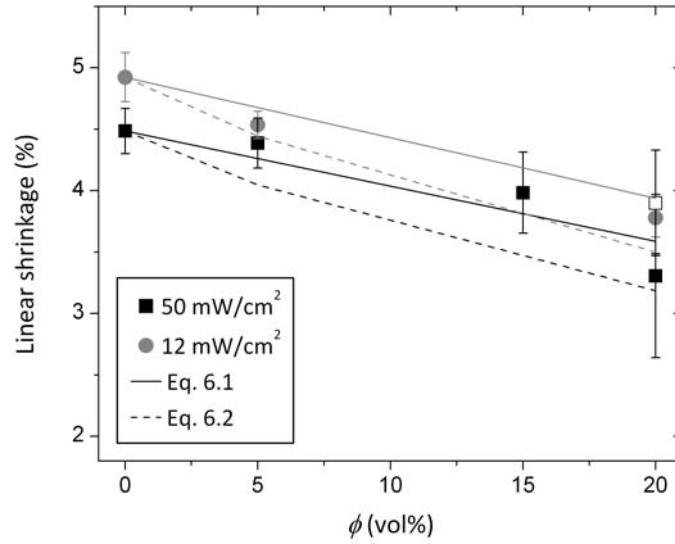


Figure 6-4 Linear shrinkage of HL (full symbols) and AS (empty symbol) composites as a function of filler fraction ϕ for two different intensities. The lines represent the calculated shrinkage from two different models.

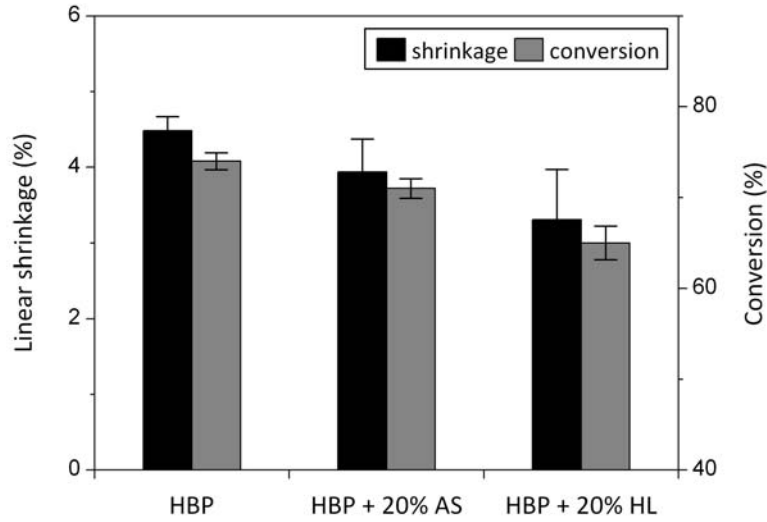


Figure 6-5 Final conversion and linear shrinkage at 50 mW/cm² for HBP and composites containing 20% HL and AS.

6.2 SHEAR MODULUS DYNAMICS

Figure 6-6 shows the shear modulus G^* as a function of conversion. The shear modulus of the cured material could not be measured with the photo-rheometer and was instead calculated from DMA data using the following equation:

$$G^* = \frac{E^*}{2(1-\nu)} \quad 6.3$$

where E^* is the Young's modulus and is ν the Poisson ratio. If it was assumed that $\nu = 0.3$, G^* was calculated to be approximately 500 MPa for the HBP, 800 MPa for

composites containing 20% AS, and 1200 MPa for composites containing 20% HL. At room temperature the materials were above their T_g , so that G^* should be proportional to the crosslink density, hence to the conversion:

$$G^* = \frac{Nk_B T}{V} = \alpha k_B T \quad 6.4$$

where N is the number of crosslinks per volume V and $k_B = 1,38 \cdot 10^{-23}$ J/K is the Boltzmann constant. This relationship is, however, only true for a homogeneously crosslinking material. As mentioned before, the formation of microgels occurred before gelation in the HBP and the composites, leading to a heterogeneous microstructure, with microgel particles in a liquid matrix. Therefore, no linear behavior between G^* and α was observed before gelation. However, a linear relationship was expected after gelation, when a 3-dimensional network started to form, but this was neither the case. Presumably, a still inhomogeneous distribution of crosslink density immediately after gelation led to the non-linear behavior. In fact, an approximately power-law dependence of G^* on the conversion was observed between gelation and 20 to 30% conversion.

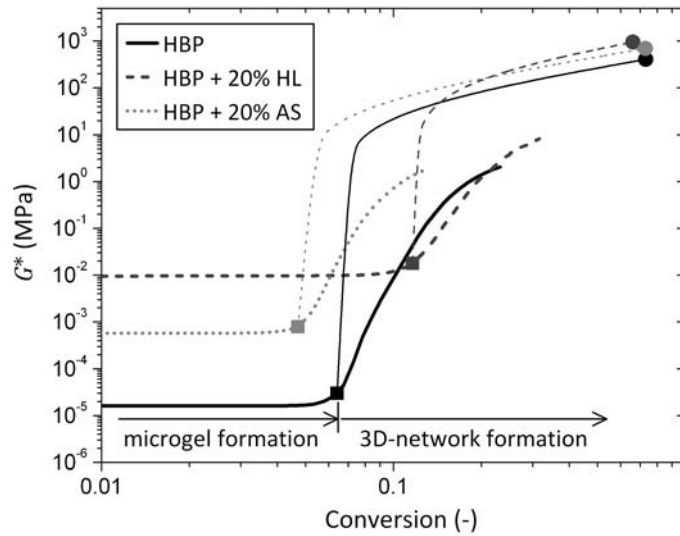


Figure 6-6 Shear modulus G^* as a function of conversion at 2.5 mW/cm². The thin lines represent the theoretically linear dependence (in a log-log plot) of G^* on the conversion after gelation (squares). The circles are the moduli calculated using Equation 6.3.

Figure 6-7 shows the shear modulus G^* as a function of linear shrinkage. As the rheometer was not capable to follow G^* beyond a few MPa, the values of G^* were interpolated with the final G^* calculated from Equation 6.3. As G^* showed power-law dependence on the conversion after gelation, a power-law relationship was also chosen for

the interpolation. The same power-law fitted well with the experimental data after the stiffness onset, which is also related to gelation.

The internal stress was determined by integrating G^* with the shrinkage, i.e. as the area under the curve in Figure 6-7, and found to be around 2 MPa for the HBP, 2.7 MPa for the AS and 5.5 MPa for the HL composites at 20% filler fraction.

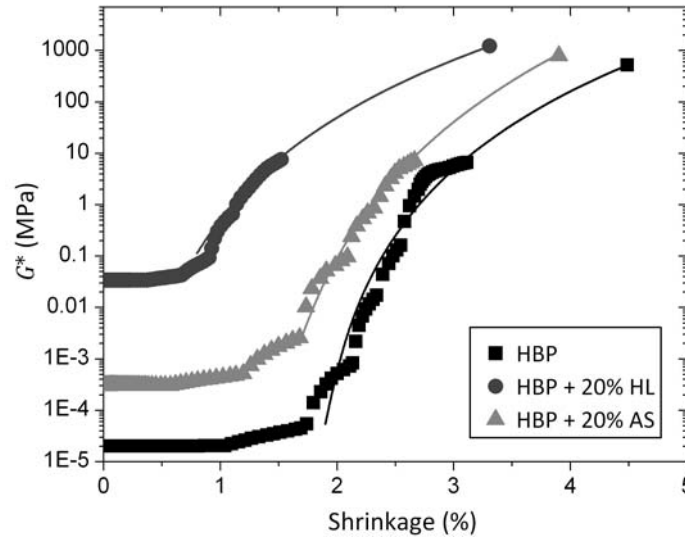


Figure 6-7 Shear modulus G^* as a function of shrinkage for HBP and HBP composites containing 20% HL and AS at 50 mW/cm². The experimental data are plotted up to 8 MPa, from where they are extrapolated with a power-law to the values calculated from Equation 6.3.

6.3 INTERNAL STRESS DYNAMICS

Figure 6-8 shows the evolution of internal stress σ_i as a function of time. The modulus-independent model of Stoney (Equation 3.6) was used to calculate the stress, because the Young's modulus was not known throughout the polymerization reaction. The stress onset was delayed, if lower intensities were used, and the stress built up slower, correlating to the longer induction time and slower reaction rate (Chapter 4). It was found that higher intensities led to higher stress. Schmidt *et al.*⁴⁴ found the same trend and attributed it to higher ultimate conversion at higher intensities, which was not the case in the present study. The intensity dependence was considered as an artifact and related to the limitations of Stoney's model, which does not include the modulus of the coating. In reality, the modulus depended on the composition as well as on the intensity, as will be shown in Section 6.5. The HL composites showed higher internal stresses than the pure HBP.

Figure 6-8 also shows the stress calculated from the integration of the modulus $G^*(t)$ with the shrinkage $S_L(t)$, which predicted a slower stress build-up, than was measured by beam-bending experiments. It is believed that the modulus independent model of Stoney generally overestimated the internal stress level.

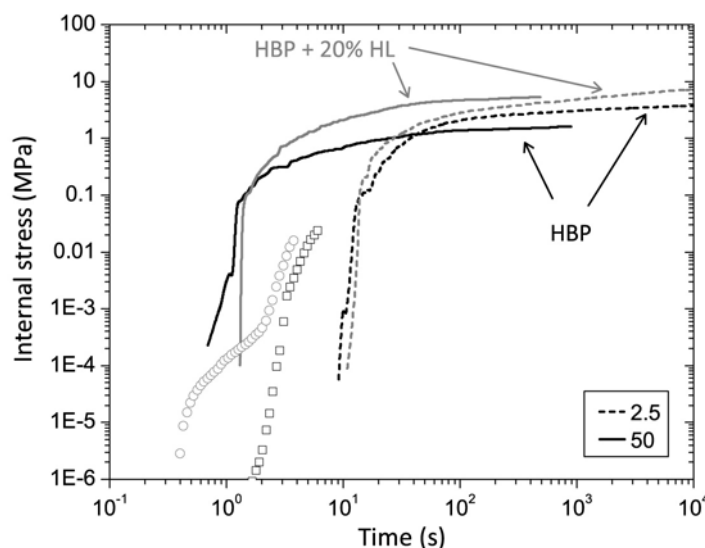


Figure 6-8 Internal stress as a function of time. The lines are the stresses calculated from the model of Stoney at two different intensities (mW/cm^2 as indicated). The symbols are the stresses calculated from the integration of $G^*(t)$ with $S_L(t)$ at $50 \text{ mW}/\text{cm}^2$ for HBP (squares) and a composite containing 20% HL (circles).

Figure 6-9 shows the evolution of internal stress σ_i as a function of conversion and shrinkage. The onset of stress was delayed in terms of conversion, if lower intensities were used (Figure 6-9a), which confirms the delay in gelation at lower intensities. At high intensities, stress built up instantly with conversion, and then increased moderately and linearly until almost the end of the reaction. At a conversion close to the ultimate conversion, the stress increased strongly and the stress level was nearly doubled. Such strong stress increase would normally be expected at vitrification. Wen *et al.*¹⁷⁷ defined vitrification as the point, when the stress exceeded the linear extrapolation of the early reaction by 0.1 MPa. Following this approach, the conversion at vitrification was found to be around 70% for HBP and 50% for the composite containing 20% HL at $2.5 \text{ mW}/\text{cm}^2$. However, since vitrification was not apparent in photo-DSC and photo-rheological experiment, the sharp increase in stress at the end of the reaction was presumably due to volume relaxation process lagging behind network formation. This was already observed for the shrinkage as a function of conversion (Figure 6-2), and Figure 6-9b demonstrates that shrinkage and stress were indeed nearly linearly related.

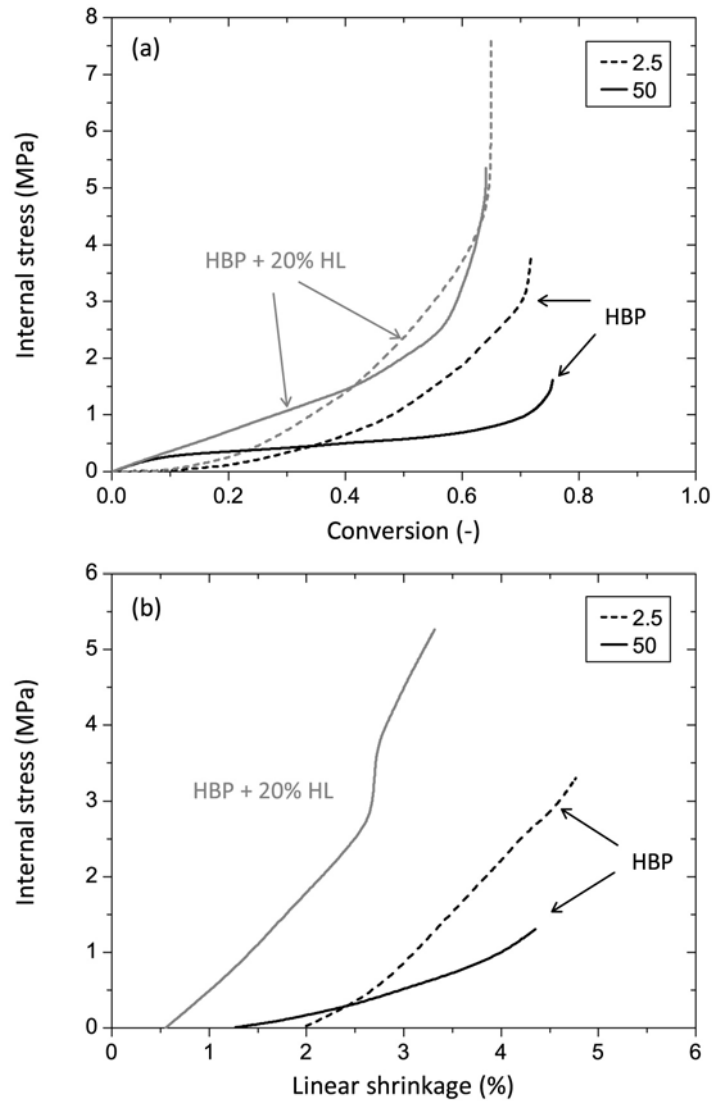


Figure 6-9 Internal stress, calculated from the model of Stoney, as a function of (a) conversion and (b) linear shrinkage for HBP and a composite containing 20% HL, polymerized at two different intensities (mW/cm² as indicated).

The model of Inoue (Equation 3.7) takes into account the modulus of the coating and should therefore give more accurate stress values. Figure 6-10 shows the ultimate internal stress of HBP and HL composites, calculated from the model of Inoue, as a function of intensity and filler fraction. In contrast to the model of Stoney, the stress by Inoue was independent of the intensity. The stress level depended strongly on the filler fraction. A linear relationship between stress and filler fraction was observed, in spite of reduced shrinkage. The same trend was also found elsewhere.²⁶ It appears that the greater stiffness of the more heavily filled materials played a major role in determining the amount of polymerization stress. AS composites had the same internal stress as HL composites, despite their increased polymerization shrinkage. This was due to the reduced Young's modulus, as will be shown in Section 6.5.

The results were in good agreement with the stress values calculated from the integration of the curve in Figure 6-7, except for AS composites, where the discrepancy was due to the large experimental error of the AS shrinkage data (10%).

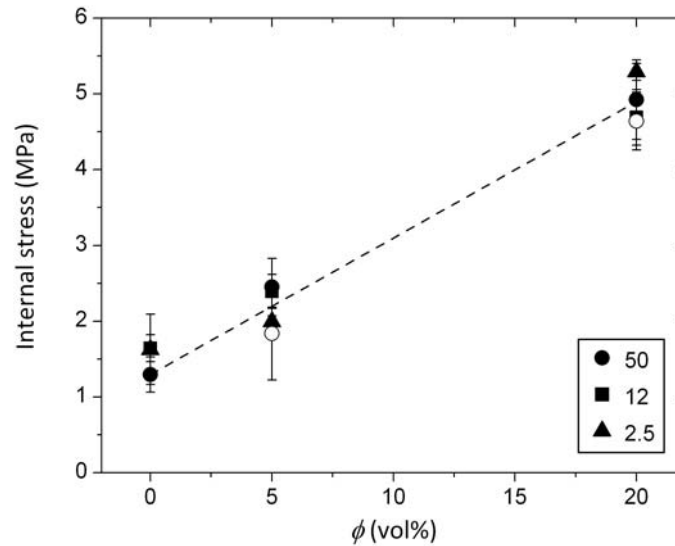


Figure 6-10 Internal stress determined from beam bending experiments, using the model of Inoue, for HBP composites as a function of filler fraction ϕ at different intensities (mW/cm² as indicated). Empty symbols: HL; full symbols: AS.

6.4 STRESS RELAXATION BY SURFACE WRINKLING

Surface instabilities during polymerization of coatings, such as surface wrinkles^{86,87}, are the result of compressive stress relaxation. In view of the application of polymers in micro- and nanostructures, wrinkling is to be avoided, since the wavelength and amplitude of such wrinkles are usually in the same size-range as the structures to be produced.⁹⁷ It has been found that, for wrinkles to form, an in-depth conversion gradient needs to be present. This means that the surface layer solidifies first, while a still-liquid underlayer remains.⁸⁴⁻⁸⁸ Subsequent polymerization shrinkage of the underlayer puts the surface layer under compressive stress.

Three model experiments were conducted to determine the influence of absorption and conversion gradient on the surface roughness on 100 μm thick HBP nanocomposite coatings, as sketched in Figure 6-11:

- “Top”: illumination from above the coating using a UV transparent substrate
- “Bottom”: illumination from below the coating through a UV transparent substrate
- “Mirror”: illumination from above the coating using a UV reflecting substrate

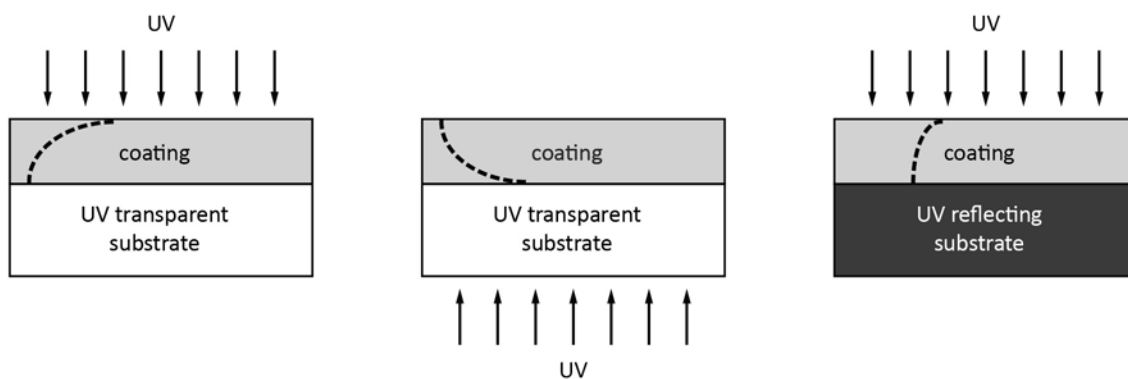


Figure 6-11 Three model experiments with asymmetric conversion gradient. The dashed curves represent the different conversion profiles, which control the stress dynamics and surface formation mechanisms.

No micro-sized surface wrinkles were observed by optical microscopy for any of the three conditions and visual inspection showed glossy surfaces in all three cases. Figure 6-12 shows the average surface roughness R_a for HBP polymerized at 2 and 50 mW/cm². The error bars correspond to the standard deviation of a minimum of five profilometer scans on different positions of the same sample. *Top*, *bottom* and *mirror* stand for the three types of illumination as described above.

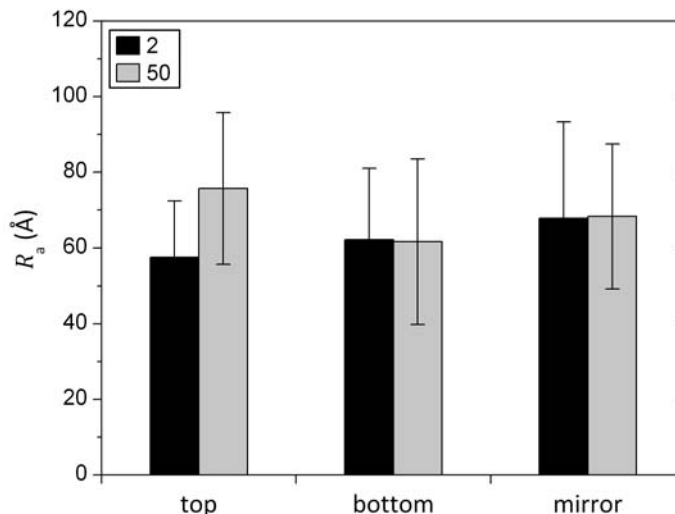


Figure 6-12 Surface roughness R_a of HBP polymerized from different directions at two different intensities (mW/cm² as indicated).

The measured roughness was in the nanometer range, with no significant difference between the three illumination conditions. Hence, no stress relaxation by out-of-plane deformation took place. In all cases, the approximate period of the surface roughness was in the micrometer range, leading to a nanoscopically flat surface, as is sketched in Figure 6-13. Hence the quality of the nano-pattern to be produced should not be compromised.

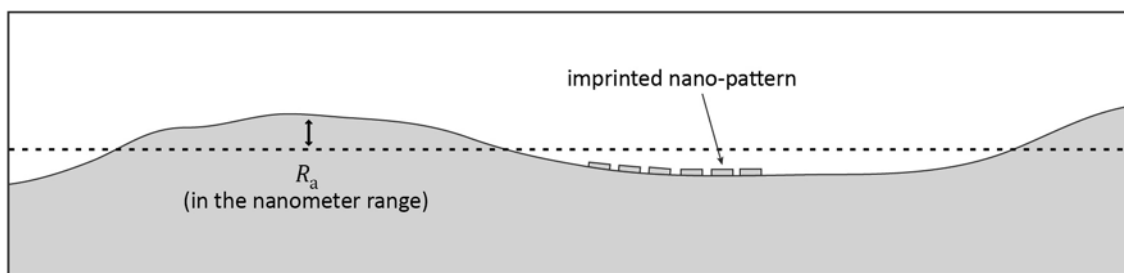


Figure 6-13 Surface roughness in the nanometer range does not compromise the nano-pattern, because of the large approximate period of the roughness.

A more pronounced wrinkling effect was expected at lower intensities, due to slower reaction and increased gradient of cure in the sample.⁴⁶ This was, however, not the case. Two possible explanations were identified for the absence of surface wrinkles. Firstly, the low levels of internal stress did not cause enough driving force for surface wrinkles to occur. Secondly, the very rapid and homogenous conversion throughout the thickness of the sample led to an insufficient conversion gradient.

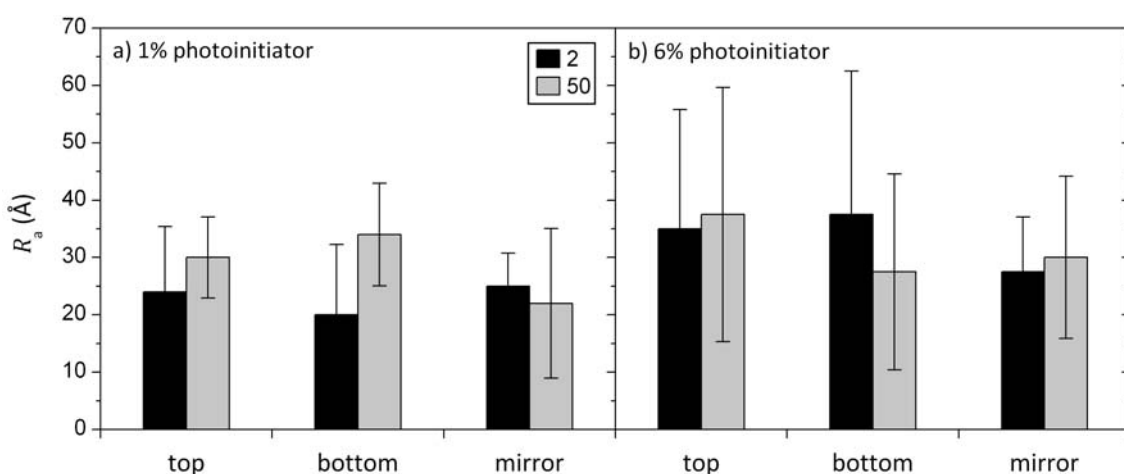


Figure 6-14 Surface roughness R_a of DPHA containing (a) 1% and (b) 6% photoinitiator and polymerized from different directions at two different intensities (mW/cm² as indicated).

Surprisingly, under the same conditions the standard acrylate DPHA, which exhibits two times higher internal stress⁴⁴ than HPB, did not show any stress relaxation in the form of microscopic surface wrinkles either (Figure 6-14a). In order to increase the conversion gradient, the photoinitiator concentration was increased from 1 to 6%, with no significant effect on the surface roughness (Figure 6-14b).

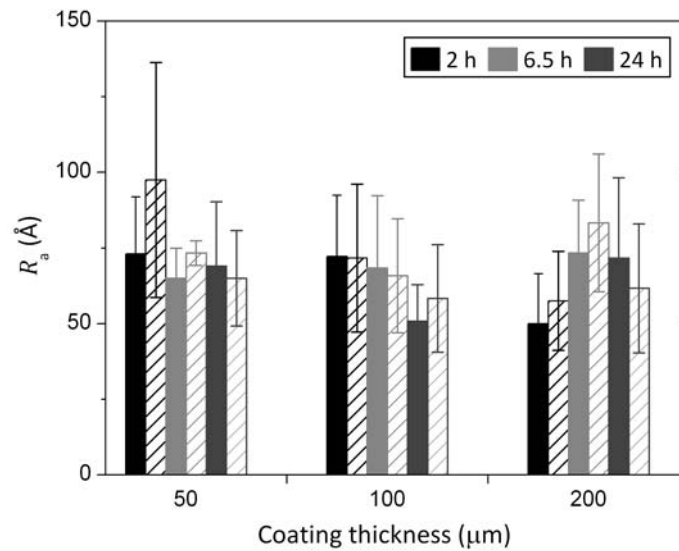


Figure 6-15 Surface roughness R_a of HBP coatings with different thicknesses polymerized at 50 mW/cm² in air after leveling at ambient pressure (filled columns) or reduced pressure (patterned columns). The leveling time is indicated.

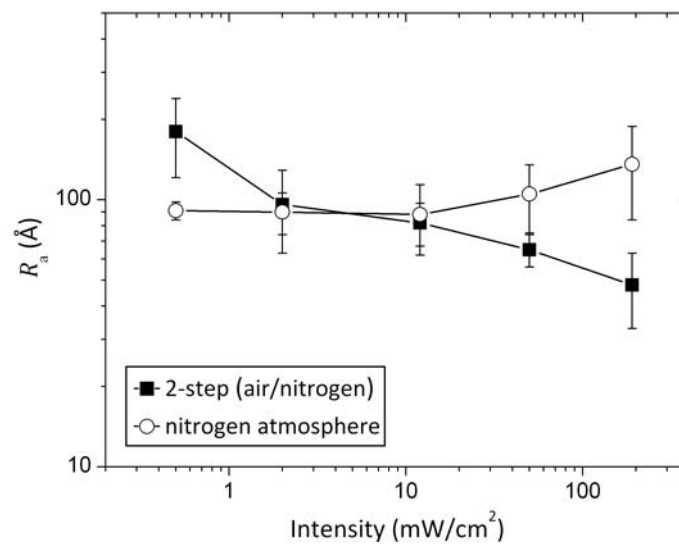


Figure 6-16 Surface roughness R_a of HBP as a function of UV intensity polymerized under nitrogen atmosphere and using 2-step polymerization.

In the UV-curable coatings investigated by Luciani *et al.*⁸⁶, surface wrinkles were only observed for polymerization in air. The presence of oxygen was necessary to inhibit the initiation and slow down the polymerization reaction. Moreover, a certain pre-polymerization leveling time was necessary for some evaporation phenomena to occur, the role of which they did not fully understand. Figure 6-15 shows the surface roughness of HBP coatings polymerized in air as a function of coating thicknesses, leveling times and pressure during leveling. Neither of these parameters combinations provoked macroscopic surface wrinkling or even had an influence on the surface roughness.

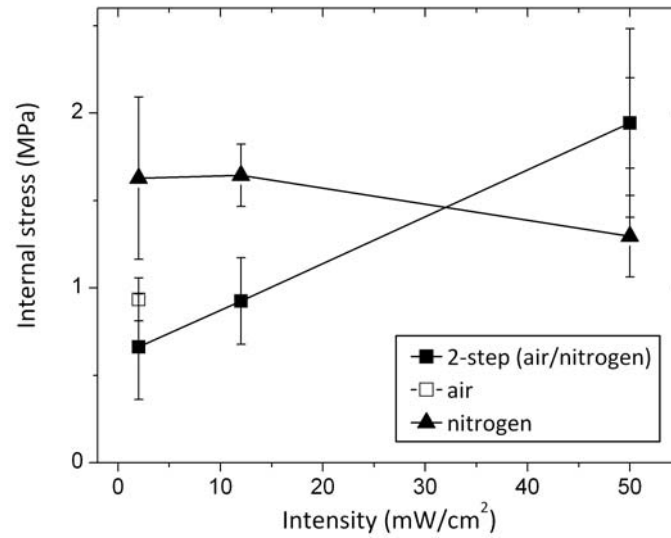


Figure 6-17 Internal stress of HBP as a function of UV intensity polymerized using 2-step process and in air with subsequent removal of the liquid surface layer.

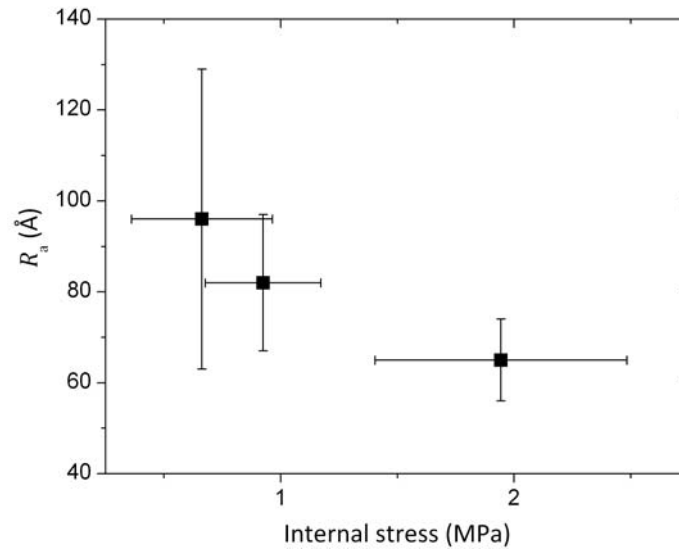


Figure 6-18 Surface roughness R_a as a function of internal stress for HBP polymerized using 2-step process.

In fact, oxygen inhibition was so strong in the layer exposed to the air, so that a thin surface layer of the coating did not polymerize and remained liquid. Hence, the top layer had to be washed off with acetone, and the roughness of the underlayer was measured.

Figure 6-16 shows the surface roughness of the HBP, where this liquid surface layer was not washed off, but polymerized in a second step under nitrogen. It was found that increased UV intensity reduced the surface roughness, if this 2-step polymerization was used. It was also found that the internal stress was also dependent on the UV intensity, when the 2-step polymerization was applied, and the same was true for HBP coatings polymerized under air with subsequent removal of the liquid surface layer (Figure 6-17).

Polymerization in inert atmosphere did not show a significant intensity dependence of the internal stress. Low intensities in combination with oxygen inhibition led to the conversion gradient necessary for the relaxation of in-plane stress in the form of increased roughness, as shown in Figure 6-18. Using the 2-step process, coatings with residual stress lower than 1 MPa were produced.

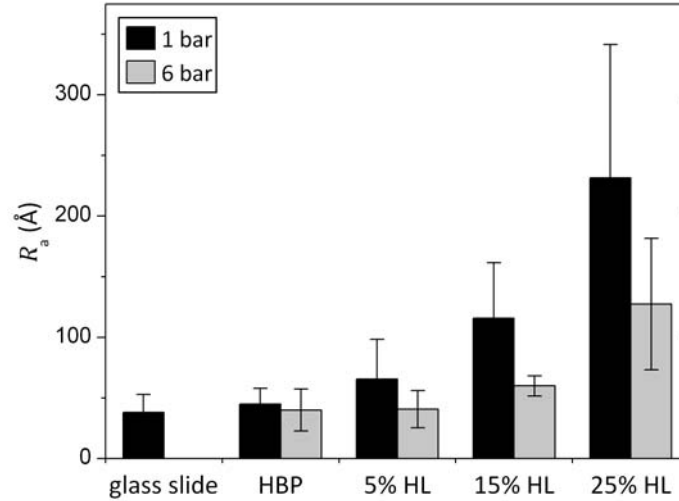


Figure 6-19 Surface roughness R_a of HBP composites as a function of HL filler fraction. Polymerization was done under compressive load (1 and 6 bar) between two glass slides.

In view of the application of HBP nanocomposites to structured devices using nanoimprint lithography, which will be addressed in Chapter 8, the surface roughness of HL composites was measured after polymerization under compression between two glass slides (Figure 6-19). The roughness was strongly dependent on the amount of silica in the nanocomposite, resulting from the increased viscosity, which prevented the elimination of air-bubbles in the coating volume. The roughness was reduced, if high pressure was applied.

6.5 THERMO-MECHANICAL PROPERTIES

6.5.1 Thermal Stability

Figure 6-20 shows the thermal stability of the HBP and the composites containing HL and AS. The HBP network was stable up to approximately 400°C, above which thermal degradation occurred in one step (one derivative peak). The thermal stability of the composites was marginally improved with the addition of SiO₂. The residue of the HBP was due to the formation of a non-volatile carbon char.¹⁹¹

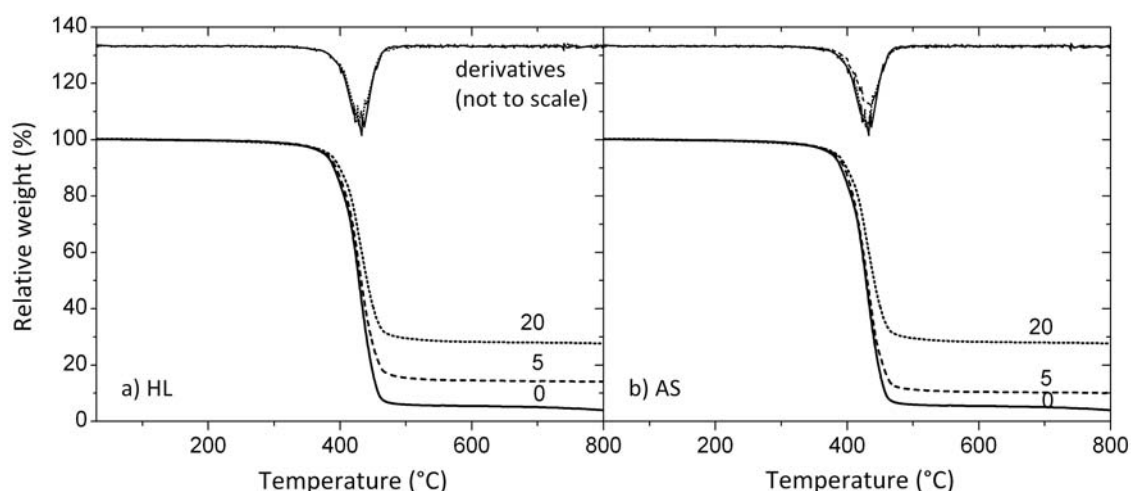


Figure 6-20 Relative weight and derivatives as a function of temperature for HBP and composites containing (a) HL and (b) AS at different filler fraction (vol% as indicated).

6.5.2 Glass Transition Temperature

The glass transition temperature T_g of the HBP monomer as measured with DSC was around -56°C. Upon polymerization the T_g , being a function of crosslink density, increased. Figure 6-21 depicts the transition temperature of the fully cured HBP and the composites containing 20% HL and AS, which was between 8 and 9°C for all investigated materials. This means that at room temperature the material was in the rubbery state, which confirms the photo-calorimetric and photo-rheological analyses, where no vitrification phenomena were detected. The T_g was independent of the UV intensity, which correlated with the ultimate conversion being independent of UV intensity. It was also independent on the filler fraction, which was found in earlier studies¹⁹⁶, and was attributed to little interfacial interaction between the filler and the resin. In the present case, rheological analysis of the nanocomposite suspensions showed rather important interfacial interactions, especially in the case of the well-dispersed HL composites. It is therefore

inferred, that the reduced conversion of the composites with respect to the HBP counteracted any increase in T_g resulting from strong interfacial interaction.

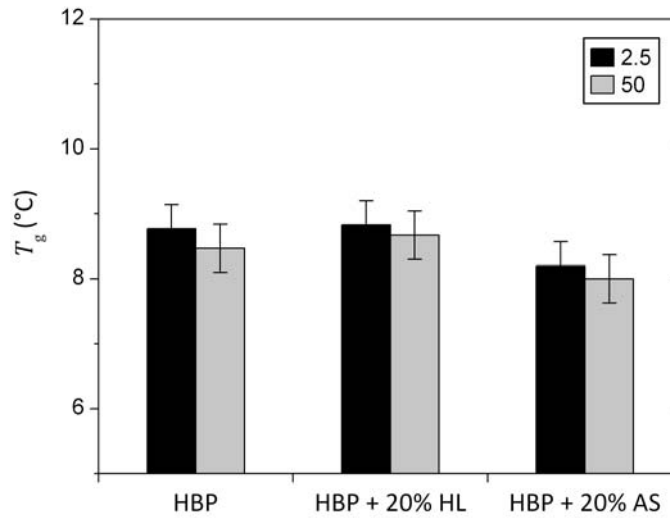


Figure 6-21 Glass transition temperature T_g of HBP and composites containing 20% HL and AS, polymerized at 2.5 and 50 mW/cm².

6.5.3 Dynamic Mechanical Analysis

Figure 6-22 shows the complex moduli and the phase angle δ that were recorded as a function of temperature for the HBP and composites containing 5 and 20% HL. The transitions from rigid glassy to soft rubbery behavior, defined as the maximum in $\tan(\delta)$,⁴¹¹ was very broad and occurred over a temperature range of about 100°C.

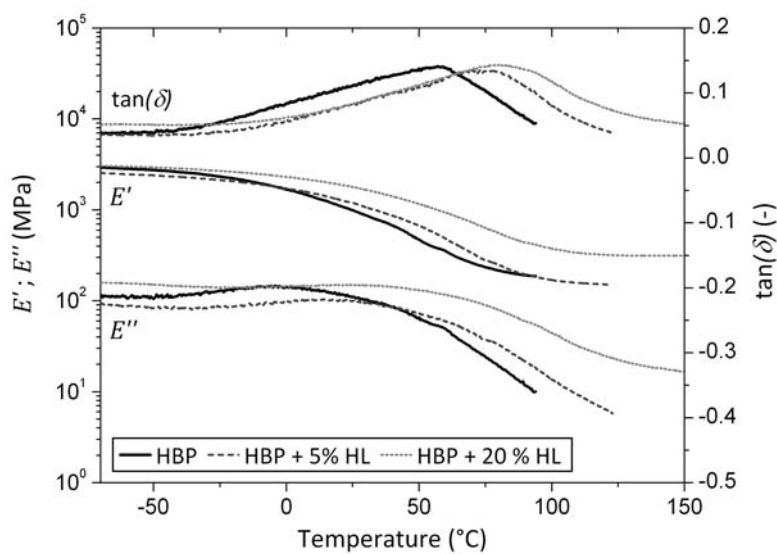


Figure 6-22 Complex moduli E' , E'' and tangent of the phase angle δ for HBP and HL composites at 5 and 20% filler fraction, polymerized at 12 mW/cm².

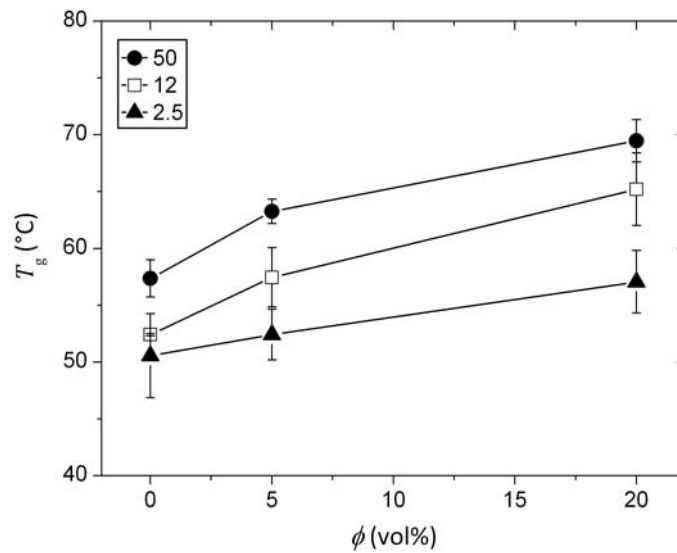


Figure 6-23 Glass transition temperature T_g determined by DMA for HBP/HL composites as function of filler fraction ϕ polymerized at different intensities (mW/cm^2 as indicated).

Figure 6-23 shows the temperature at the maximum in $\tan(\delta)$ for the HBP and composites containing HL and AS as a function of UV intensity and filler fraction. Contradicting to the glass transition temperature measured by calorimetry, this transition temperature increased with both, UV intensity and the filler fraction. The reason for this was that DMA measured a change in relaxation time,⁴¹¹ while the T_g in the DSC was determined from a change in the heat capacity.⁴¹² Therefore, the two transitions are not exactly comparable.

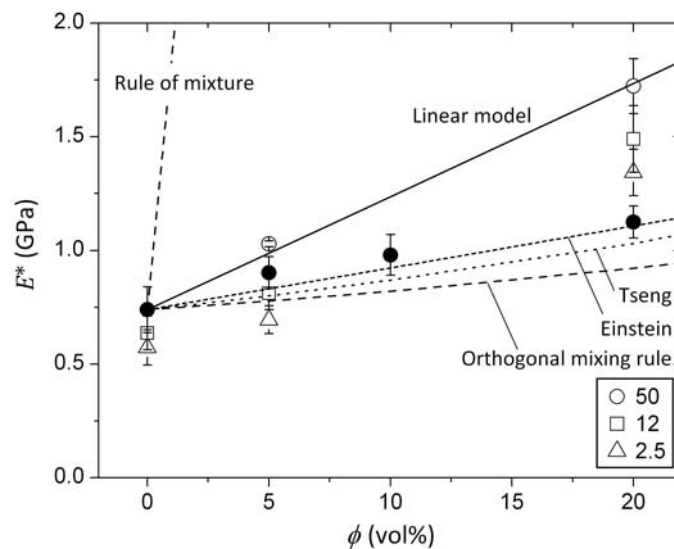


Figure 6-24 Tensile modulus E^* determined by DMA at 25°C as a function of filler fraction ϕ for HBP composites polymerized at different UV intensities (mW/cm^2 as indicated). Empty symbols: HL; full symbols: AS. The lines represent different models that were fitted to the data at $50 \text{ mW}/\text{cm}^2$.

Figure 6-24 shows the complex moduli at 25°C for the HL and AS composites as a function of UV intensity and filler fraction. Similar to the trend of T_g , an increase in E^* was observed with increasing UV intensity and filler fraction. The well-dispersed HL composites showed higher modulus than the agglomerated AS composites.

Different models were tested for the filler fraction dependence of the modulus. The rule of mixture (Equation 6.5), assuming that the two phases have the same Poisson ratio²⁷⁰, highly overestimated E^* , whereas the orthogonal mixing rule (Equation 6.6) underestimated E^* . The model of Tseng²⁷² was established especially for nanocomposites. It considers the effects of inter-particle interaction and performs a statistical averaging to the solution of the problem of two-nanoparticle interactions. This model though underestimated E^* by a factor of 3.5 for the HL composites and a factor of 1.5 for the AS composites. The model of Einstein (Equation 6.7) fitted well the AS data, but underestimated the HL data. Derived from the empirical model of Ishai²⁰³ for the dependence of the yield stress on the filler fraction, a linear model (Equation 6.8) was proposed for the HL data.

$$E = \phi \cdot E_f + (1 - \phi) \cdot E_m \quad 6.5$$

$$\frac{1}{E} = \frac{\phi}{E_f} + \frac{1 - \phi}{E_m} \quad 6.6$$

$$E = E_m (1 + 2.5 \cdot \phi) \quad 6.7$$

$$E = E_m + c \cdot \phi \quad 6.8$$

where E , E_f and E_m are the moduli of the composite, filler and matrix, respectively, and c is a proportionality constant.

6.5.4 Coefficient of Thermal Expansion

Figure 6-25 depicts representative coefficient of thermal expansion (CTE) data of the investigated materials as a function of temperature and for three different load levels. The influence of the load applied during the dilatometry experiment on the CTE data was negligible, i.e. creep did not occur. In all cases, three quasi-linear stages were identified. The transition between the first and the second stage correlated roughly with the glass transition temperature measured by DSC. The transition between the second and the third stage was close to the transition temperature measured by DMA.

In classic elastomers the transition occurs in one step accompanied by a 3-fold increase in CTE. In the HBP the CTE increased roughly by a factor of 3 from 40 to 120 ppm/K, but the hyperbranched structure comprised multiple relaxation times, leading to the observed broad transition.

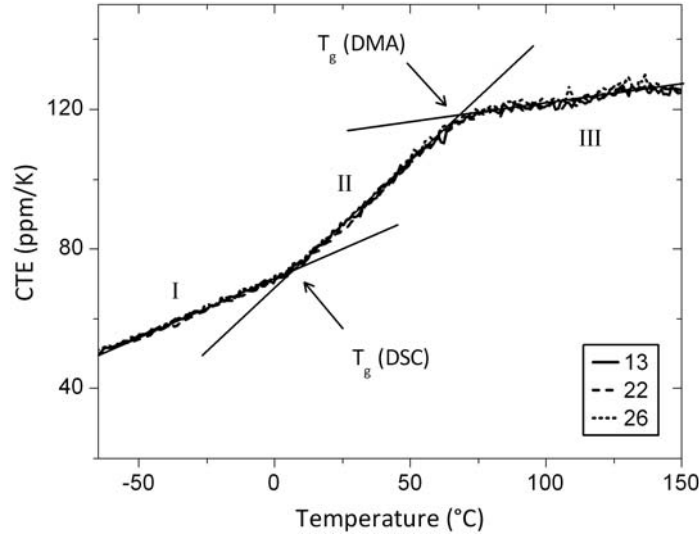


Figure 6-25 CTE as a function of temperature for a composite containing 20% HL measured under different compressive loads (cN as indicated).

Figure 6-26 shows the CTE at room temperature for the HBP and the composites as a function of UV intensity and filler fraction. Increased UV intensity slightly reduced the CTE, presumably due to the increased stiffness and T_g of the material. The addition of a filler was much, however, more effective in terms of CTE reduction.

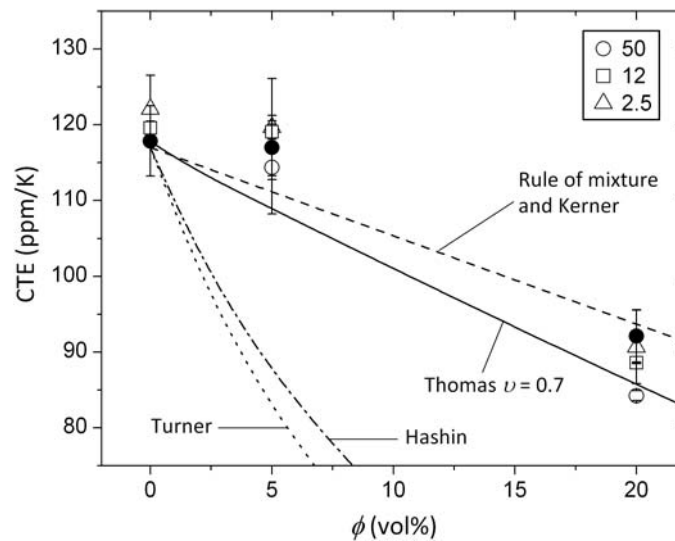


Figure 6-26 CTE as a function of filler fraction for composites containing HL and AS polymerized at different intensities (mW/cm² as indicated). Empty symbols: HL; full symbols: AS. The lines represent different models that were fitted to the data at 50 mW/cm².

Several models for the prediction of CTE of composites have been established and are compiled in the work of Chen²⁷⁵ and Hsieh⁴¹³. The linear rule of mixture (Equation 6.9), which considers the matrix as a liquid and assumes each phase to expand freely, and the more complex Kerner model (Equation 6.10) for spherical filler and perfect adhesion of the two phases, gave the same result. They both fitted quite well for low ϕ , but slightly underestimated the effect of the nanofiller at higher ϕ , in particular for the HL composites. However, based on the requirements of the Kerner model for perfect adhesion, it can be concluded that the adhesion between the two phases was quite good. The Turner model (Equation 6.11) and the Hashin^{212,276} model (Equation 6.12) highly underestimated the CTE of the composites. The Thomas model (Equation 6.13) is an empirical modification of the rule of mixture and was found to give the best fit to the experimental data of the HL composites at $\nu = 0.7$.

$$\chi_c = \phi \cdot \chi_f + (1 - \phi) \cdot \chi_m \quad 6.9$$

$$\chi_c = \phi \cdot \chi_f + (1 - \phi) \chi_m - (\chi_m - \chi_f) \phi (1 - \phi) \left(\frac{1}{K_m} - \frac{1}{K_f} \right) \left(\frac{\phi}{K_m} + \frac{1 - \phi}{K_f} + \frac{3G_m}{4} \right)^{-1} \quad 6.10$$

$$\chi_c = \frac{\chi_f \cdot \phi \cdot K_f + \chi_m (1 - \phi) K_m}{\phi \cdot K_f + (1 - \phi) K_m} \quad 6.11$$

$$\chi_c = \chi_f + (\chi_m - \chi_f) \frac{1/K_c - 1/K_f}{1/K_m - 1/K_f} \quad 6.12$$

$$\chi_c^\nu = \phi \cdot \chi_f^\nu + (1 - \phi) \cdot \chi_m^\nu \quad 6.13$$

where χ_c , χ_m and χ_f are the CTE of the composite, filler and matrix, respectively, G_m is the shear modulus of the matrix, K_c , K_m and K_f are the bulk moduli of the composite, matrix and filler, respectively, and ν is a parameter.

6.6 SUMMARY

The influence of UV intensity and SiO₂ particles on the shrinkage, modulus and resulting stress dynamics, as well as on the thermo-mechanical properties of HBP nanocomposites was investigated. The main results are summarized in Table 6-1 and compared with standard UV-curable resins.

- An overall linear shrinkage reduction of 33% down to 3% shrinkage could be achieved upon addition of 20% inorganic filler and using high intensities. Despite

the reduced shrinkage of the composites, which followed approximately the rule of mixture, the internal stress strongly increased with the filler fraction, due to the increased stiffness of the composites.

- Stress relaxation by surface wrinkling phenomenon was only observed for 2-step polymerization and was on the nanometer scale. However, with this method residual stresses as low as 0.66 MPa could be achieved.
- The addition of SiO₂ nanoparticles led to a very pronounced change in thermo-mechanical properties. The stiffness was increased by 133% up to 1.7 MPa for the HL and by 52% up to 1.1 MPa for the AS composites at 20% filler fraction. For the same composites the CTE was decreased by 28% and 21% down to 84 and 92 ppm/K, respectively.
- The glass transition temperature, as measured with calorimetry, was found to be independent of UV intensity and filler fraction and equal to 9°C. However, the transition in relaxation behavior, correlated with a transition from soft to glassy behavior, was shifted from 50 to 70°C upon addition of 20% HL and using high intensities.

Table 6-1 Comparison of different resins with the investigated HBP and HBP nanocomposites in terms of internal stress, stiffness, linear shrinkage and coefficient of thermal expansion.

Material	Stress (MPa)	Young's modulus (GPa)	Shrinkage (%)	CTE (ppm/K)
HBP	1.3	0.7	4.3	117
HBP (2-step)	0.66	0.5		
HBP + 20% HL	4.9	1.7	3.3	84
DPHA ⁴⁴ (UV acrylate)	6.7	3	7	
TMPTA ^{78,85} (UV acrylate)	3-15	2.4	11-15	
SU8 ^{57,77,414}	20-75	2.6 – 4.0	10	50

7 SOL-GEL HYBRID NANOCOMPOSITES

Hybrid nanocomposites derived by sol-gel processes motivate a large amount of research work, as reviewed by several authors.^{308,310,415,416} The low viscosity of the liquid organometallic precursor should help to overcome the processing problems of the particulate nanocomposites, the viscosity of which increased, due to the high specific surface area of the nanofiller. In this chapter, the sol-gel composites will be compared to the particulate nanocomposites in terms of rheological behavior, conversion state, thermo-mechanical properties and internal stress.

7.1 DUAL-CURE PROCESS

The dual-cure process involves a photo-polymerization and a condensation step, which were carried out using different sequences, as depicted in Figure 7-1. In all cases, condensation lasted in total 4 h. When the photo-polymerization was done before condensation (“UV first”, Figure 7-1a), the low viscosity of the HBP/precursor mixture

facilitated processability. However, during condensation high shrinkage occurred, due to the evaporation of byproducts, and the stress was released through cracking of the composite.

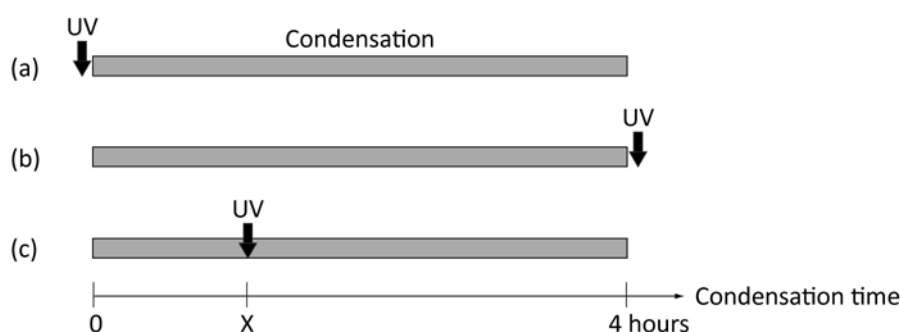


Figure 7-1 Three sequences of sol-gel composite dual-cure preparation. (a) Polymerization before condensation, (b) polymerization after completed condensation, and (c) polymerization after a few minutes of condensation.

Table 7-1 Advantages and disadvantages of two cases of dual-cure sol-gel processing

	Advantages	Disadvantages
Case (a): “UV first”: Condensation after photo-polymerization	Very fine silica network is ensured, due to the coupling agent that copolymerizes with the HBP network and prevents macroscopic phase separation. Low viscosity for processing.	Shrinkage from evaporation of byproducts in the rigid HBP network leads to internal stress and subsequent cracking. Poor adhesion of the composite on the glass substrate.
Case (b): “condensation first”: Condensation before photo-polymerization	Shrinkage from evaporation of byproducts occurs in liquid material, hence no internal stresses and no cracks. Condensation of siloxane groups with glass substrate leads to very good adhesion.	Rigid silica network builds up, high pressure is necessary for imprinting.

To avoid cracking the polymerization was done after completed condensation reaction (“condensation first”, Figure 7-1b). In this case, no shrinkage stress from evaporation built up, but the processability of the composite was greatly compromised, due to increased viscosity of the system. The advantages and limitations of these two cases are summarized in Table 7-1.

To benefit from the low viscosity for processing without cracking of the material, the photo-polymerization was done a few minutes after the condensation reaction had started (Figure 7-1c). A certain amount of byproduct could thus evaporate before a rigid network was formed and shrinkage stress could relax in the still liquid polymer.

The sol-gel composites remained completely transparent after photo-polymerization and subsequent condensation of the inorganic phase (Figure 7-2). Figure 7-3 shows TEM micrographs of sol-gel composites at 5 and 20% theoretical filler fraction ϕ_{th} , where condensation was done after photo-polymerization. No phase contrast could be seen in those images, presumably due to a very fine silica network. A structure size of 3 - 5 nm was found elsewhere.³⁵ Thanks to the coupling agent, which copolymerized with the organic matrix, the silica was linked to the HBP network and therefore prevented microscopic phase separation.

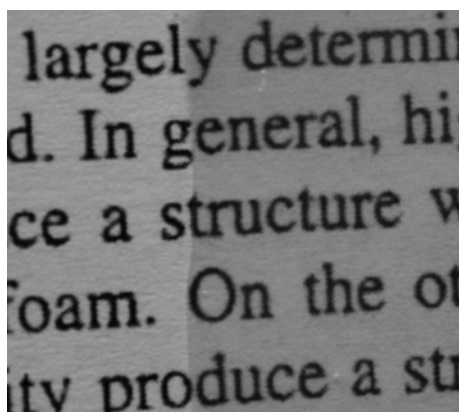


Figure 7-2 Transparent 100 μm sol-gel hybrid film containing $\phi_{th} = 20\%$. The composite film covers the right side of the image.

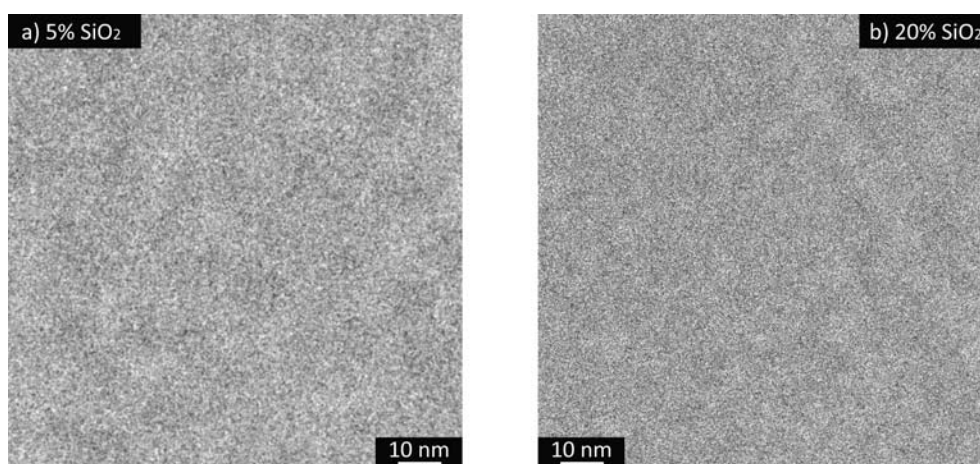


Figure 7-3 Transmission electron micrographs of sol-gel composites at a theoretical silica volume fraction of (a) 5% and (b) 20%.

Thermo-gravimetric analysis (Table 7-2) confirmed the presence of a non-volatile phase close to the theoretical amount of silica, if the HBP residue was subtracted. Non-volatile residues were also found in epoxy resins, where carbon char contents up to 8% were recorded.¹⁹¹

Table 7-2 Non-volatile residues from TGA for HBP/silica hybrid composites produced by sol-gel process.

Sample	HBP	$\phi_{th} = 5\%$	$\phi_{th} = 20\%$
Theoretical volume fraction of inorganic phase (%)	0	5	20
Theoretical weight fraction of inorganic phase (%)	0	8.7	31.1
Measured weight residue (%)	1.5	10.2	33.8
Calculated volume fraction ^(*) of inorganic phase (%)	–	4.5	19.3

(*) The weight residue of the HBP was subtracted from the residue of the composites.

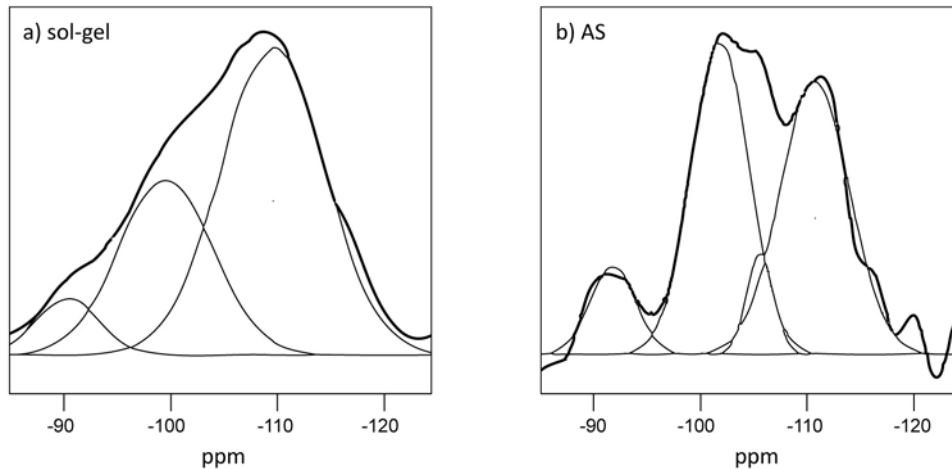


Figure 7-4 ²⁹Si-NMR data and deconvoluted peaks of (a) a sol-gel hybrid composite at 20% inorganic phase and (b) AS powder.

The presence of a silica phase was confirmed by solid state ²⁹Si-NMR (Figure 7-4). The deconvoluted spectra gave signals at approximately -92, -102 and -113 ppm. The position of the peaks was close to those described in other studies and corresponded to Q_2 , Q_3 and Q_4 species, respectively.^{37,417} The peak at -106 ppm in Figure 7-4b was believed to be a shift in Q_3 , due to impurities in the material. The condensation state Ω of the sol-gel silica was calculated (Equation 3.10) to be equal to 84%, with a majority of Q_4 species,

as opposed to 89% for the AS silica powder. The lower condensation state of the sol-gel silica was the result of the relatively low condensation temperature and of the acidic condensation condition.³⁷

Table 7-3 Corresponding amount of liquid reactants added to the HBP in order to produce the theoretical silica volume fraction ϕ_{th} through hydrolysis and condensation.

ϕ_{th} (vol%)	TEOS, MEMO, 1 M HCl in H ₂ O (vol%)
5	30
10	44
20	62

The rheological analysis was done on HBP solutions before polymerization and thermal condensation reaction. The solutions contained the necessary amount of TEOS, MEMO and 1M HCl in H₂O to produce the theoretical volume fraction of silica ϕ_{th} , assuming 100% condensation of the precursor and the coupling agent. Table 7-3 shows the corresponding total amount of reactants that was added to the HBP for each specific ϕ_{th} .

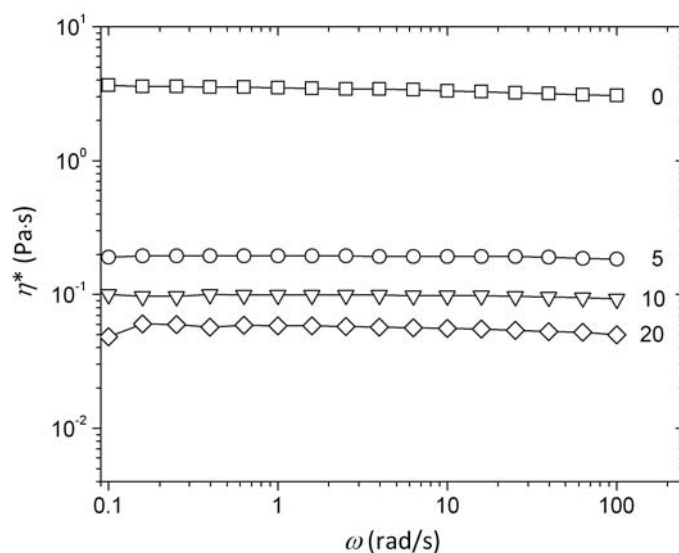


Figure 7-5 Viscosity η^* as a function of frequency ω for HBP solutions containing the corresponding amount of precursor to produce different fractions of silica ϕ_{th} (vol% as indicated).

Figure 7-5 shows the viscosity of the HBP and the HBP/precursor solutions. The pure HBP showed Newtonian behavior with viscosity independent of frequency in the investigated range. The viscosity decreased with increasing amount of precursor and the

Newtonian behavior was preserved. The reduction of the viscosity was due to the fact that the added precursors were low-viscosity liquids. HBP/precursor solutions to produce $\phi_{th} = 20\%$ showed more than 9 orders of magnitude lower viscosity at 0.1 rad/s than the HL composites at $\phi = 20\%$.

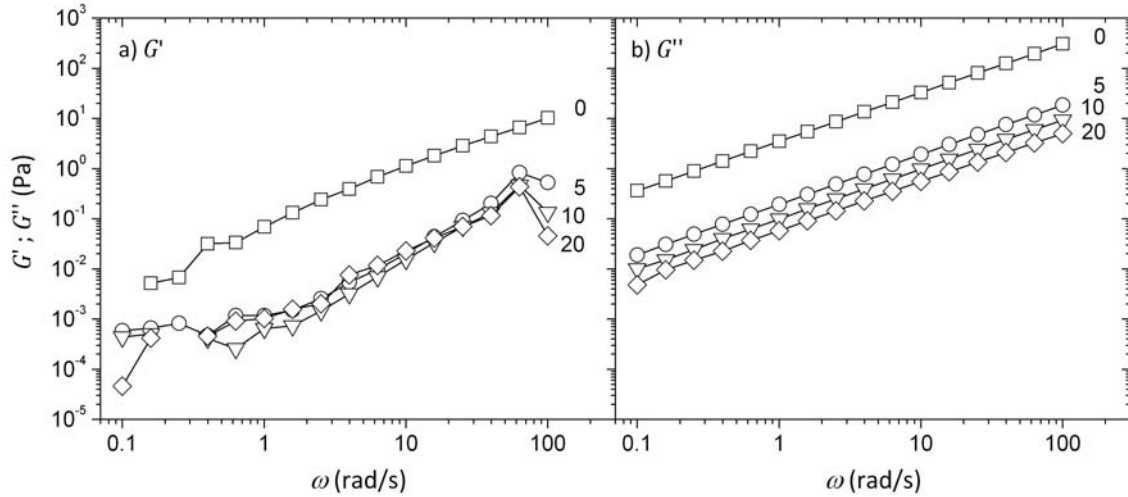


Figure 7-6 Shear moduli (a) G' and (b) G'' as a function of frequency ω for HBP/precursor solutions containing the corresponding amount of precursor to produce different fractions of silica ϕ_{th} (vol% as indicated).

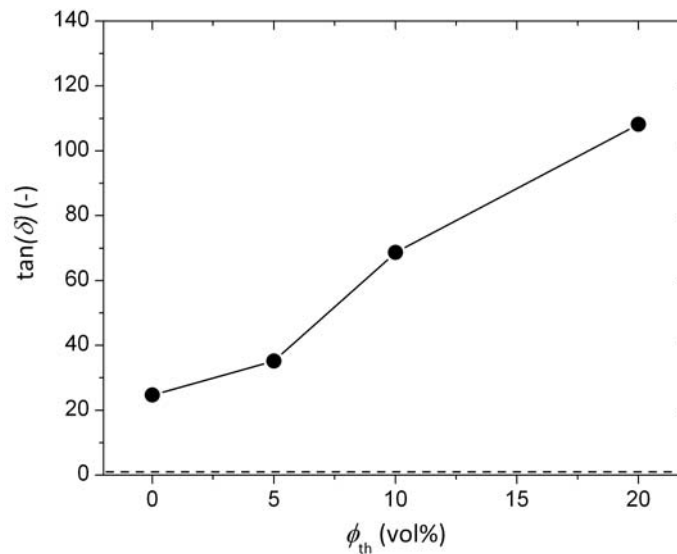


Figure 7-7 Tangent of the phase angle δ at $\omega = 6.28$ rad/s for HBP/precursor solutions containing the corresponding amount of precursor to produce different fractions of silica ϕ_{th} . The dashed line at $\tan(\delta) = 1$ represents the liquid-to-solid transition.

Figure 7-6 shows the complex shear moduli G' and G'' as a function of frequency and the corresponding amount of precursor to produce ϕ_{th} . For the pure polymer and the HBP/precursor solutions G' and G'' were both approximately proportional to ω , confirming their Newtonian-like behavior.

Figure 7-7 shows the tangent of the phase angle $\tan(\delta) = G''/G'$, obtained from Figure 7-6. It is obvious that the more precursor was added to the HBP, the more liquid the material became. Contrary to the particulate (HL and AS) composites, where the addition of a filler led to a more solid-like behavior, the addition of the precursor pushed the solution further away from the liquid-to-solid transition at $\tan(\delta) = 1$.

7.2 PHOTO-CALORIMETRIC ANALYSIS

The HBP solutions containing the liquid precursor were photo-polymerized before condensation of the inorganic phase (“UV-first”). Figure 7-8 shows the conversion curves, including the time-intensity transformation and the conversion rate data. The data was recorded at different UV intensities and for $\phi_{th} = 5$ and 20%.

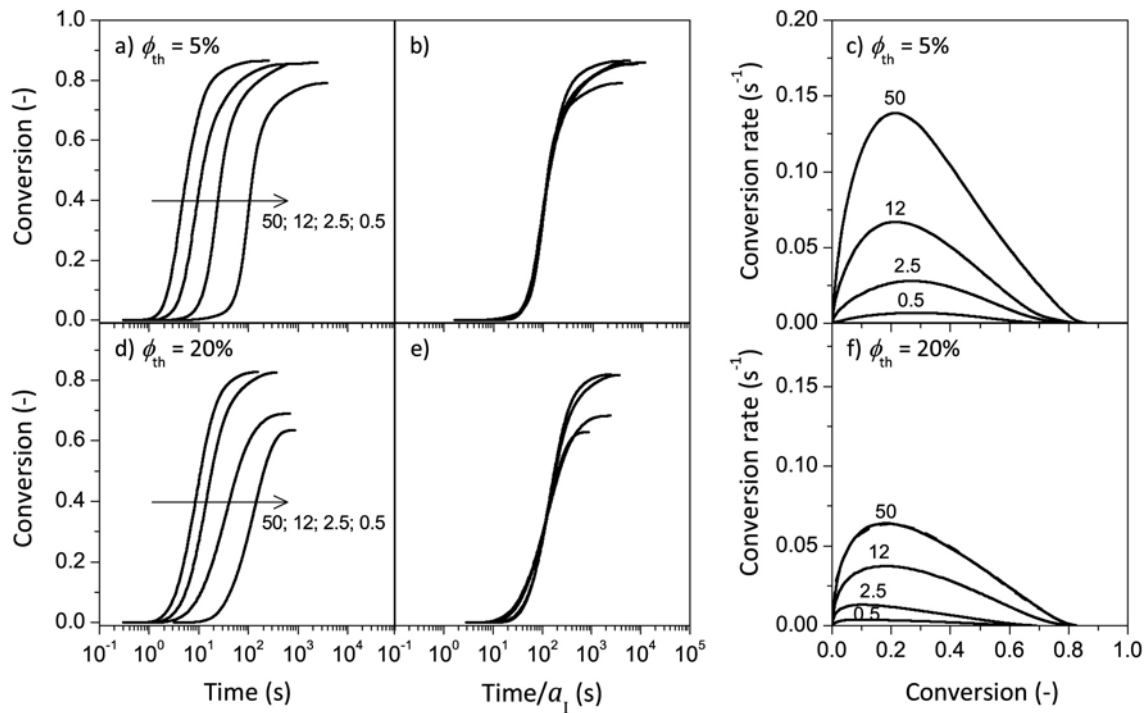


Figure 7-8 (left) Conversion as a function of time, (middle) time-intensity superposition, and (right) conversion rate as a function of conversion for HBP solutions containing the corresponding amount of precursor to produce $\phi_{th} = 5$ and 20%. The autocatalytic model is compared to the conversion rate data for an intensity of 50 mW/cm² (dashed line; nearly perfect overlap with experimental data).

Figure 7-10 shows the ultimate conversion of the HBP/precursor solutions, which was found to increase by 17% at $\phi_{th} = 5\%$. At higher precursor levels, the conversion became strongly dependent on the UV intensity. The conversion rate at low precursor levels was slightly higher than that of the HBP, and hence than that of the particulate

composites (Figure 5-1). At high precursor level, the conversion rate dropped even below the rate of the particulate composites. Li *et al.*³⁶ found that the conversion and conversion rate increased for sol-gel nanocomposites with respect to the particulate nanocomposites, though they did not compare them with the conversion of the pure resin. Other studies^{35,191} showed that the presence of TEOS as a sol-gel precursor did not influence the final conversion, but in some cases increased the rate of reaction.

At low precursor level the reduced viscosity and hence increased mobility of the radicals presumably provoked the increase in conversion rate and conversion. It was assumed that at higher precursor level the dilution of the reacting species became more important and led to the opposite trend in conversion rate. The marked intensity dependence of the conversion at high TEOS content was believed to be an artifact and attributed to evaporation of volatile precursor components.

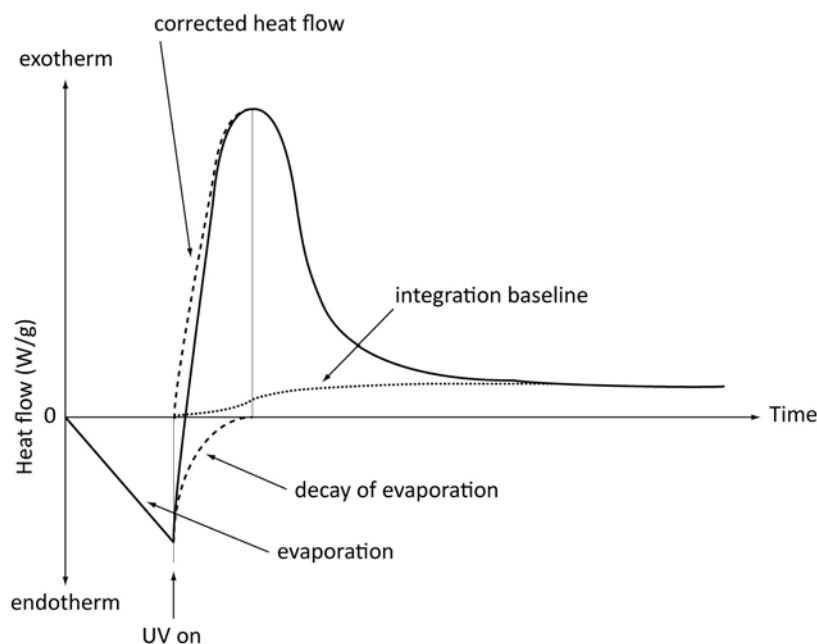


Figure 7-9 Correction of the heat flow, measured by photo-DSC, for the calculation of the conversion.

During photo-calorimetric experiments the endothermic heat flow from evaporation overlapped with the exothermic heat flow of the polymerization reaction, which greatly complicated the analysis of the DSC signal. A model was devised to account for the endothermic heat flow, using the following assumptions: (i) The heat flow decayed exponentially from the moment the lamp was switched on until the maximum heat flow (related to gelation) was reached. (ii) The absolute number of reacting groups in the solution remained unchanged, i.e., no evaporation of HBP and coupling agent occurred.

This was tested by gravimetric analysis of the pure constituents. The highest evaporation rate was found for H₂O.

The modeled endothermic contribution to the heat flow was then subtracted from the total heat of reaction, as shown in the schematic drawing in Figure 7-9. If the assumed exponential evaporation decay were too rapid with respect to the actual decay, this would result in an underestimation of the ultimate conversion and vice-versa. If evaporation of the coupling agent occurred, the conversion would increase.

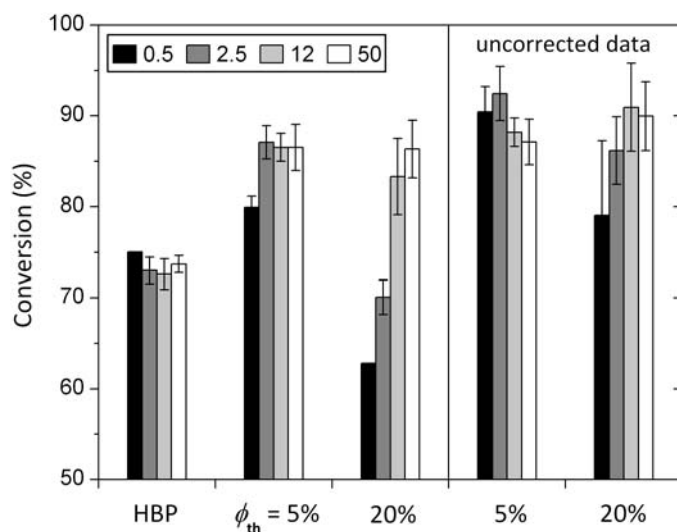


Figure 7-10 Ultimate conversion of HBP and HBP solutions containing the corresponding amount of precursor to produce $\phi_{th} = 5$ and 20%, photo-polymerized at different intensities (mW/cm² as indicated). Corrected and uncorrected data is shown for the composites.

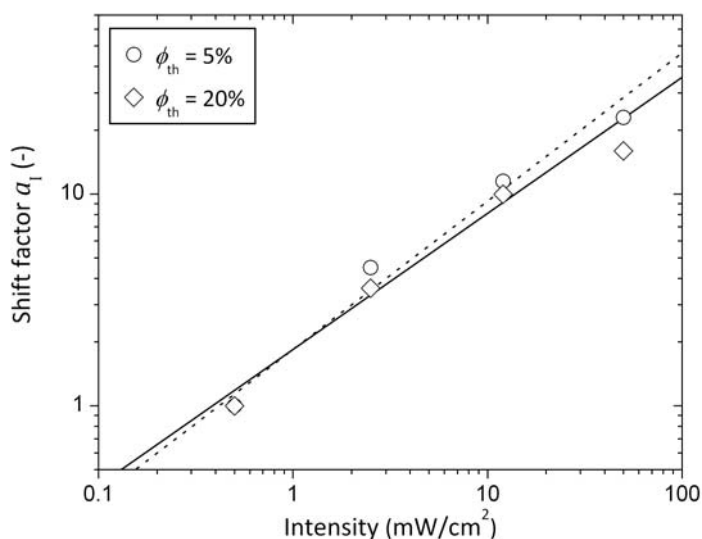


Figure 7-11 Time-intensity-shift factor with respect to the intensity of 0.5 mW/cm² for HBP solutions containing the corresponding amount of precursor to produce $\phi_{th} = 5$ and 20%. The solid line represents the fit of the shift factors, the dotted line is the fit of the shift factor for the HL and AS composites.

The time-intensity superposition was obeyed until conversion $\alpha = 0.7$ for low precursor levels and until $\alpha = 0.4$ for high precursor level, beyond which conversion became dependent on the UV intensity. The shift factors were determined using the data at 0.5 mW/cm^2 as reference, and were found to be in the same range as those of the HBP and the particulate composites, as shown in Figure 7-11, with an intensity exponent $b = 0.64 \pm 0.05$.

7.2.1 Autocatalytic Conversion Modeling

The autocatalytic model, described in detail in Chapter 5, was used to analyze the conversion data of the sol-gel composites. The fits shown in Figure 7-8 nearly perfectly overlap with the experimental data and the model parameters are regrouped in Figure 7-13. The rate constant depended on the amount of precursor in the HBP. At low precursor level, the rate constant was marginally increased with respect to the pure polymer, whereas at high precursor level it was reduced. In all cases, the rate constant strongly depended on the intensity (Figure 7-13). The intensity exponent β was found to be close to 0.6 (Figure 7-12), which indicates that first-order and second-order termination mechanism occurred simultaneously.

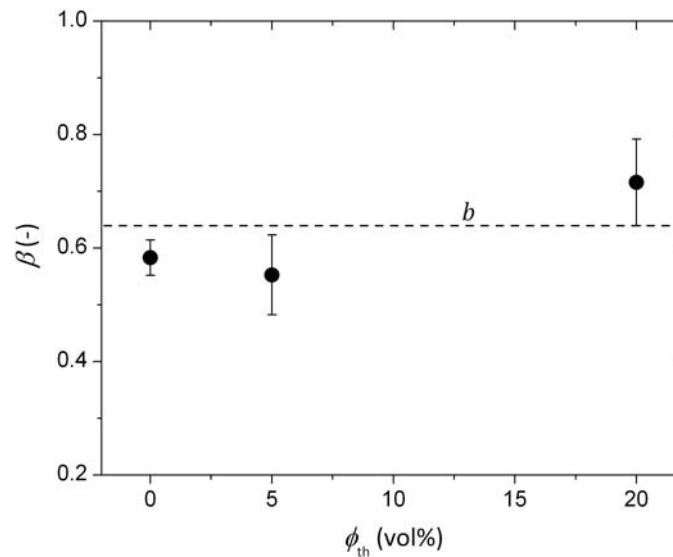


Figure 7-12 Intensity exponent β for HBP solutions containing the corresponding amount of precursor to produce ϕ_{th} . The dashed line represent the intensity exponent b of the time-intensity-shift factor.

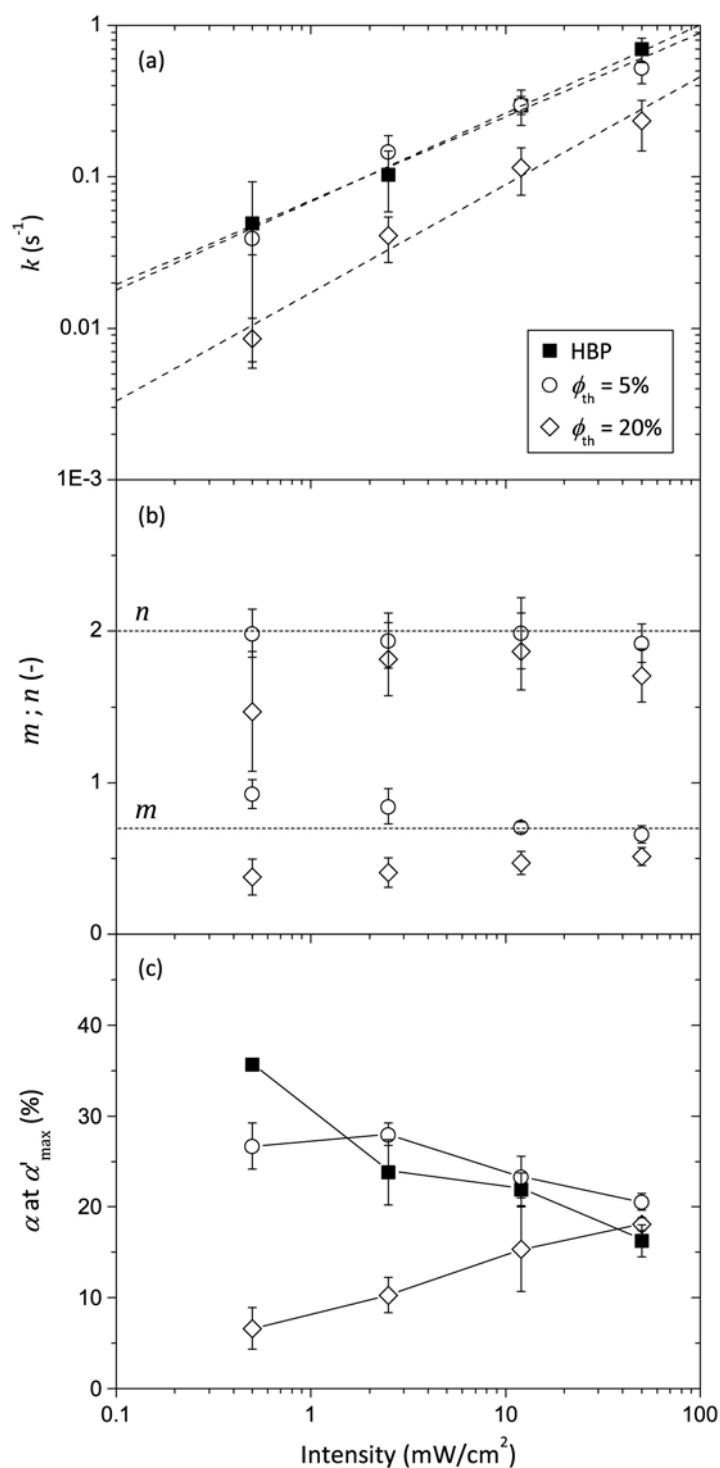


Figure 7-13 (a) Rate constant k , (b) autocatalytic exponent m and reaction order n , and (c) conversion α at maximum conversion rate α'_{max} as a function of intensity for HBP and HBP solutions containing the corresponding amount of precursor to produce $\phi_{th} = 5$ and 20%. The dashed lines represent the fit with the rate constant data. The dotted lines represent the average values for the HBP and the composites containing HL and AS.

Compared to the particulate composites, the termination mechanism were the same, with more emphasis on second-order termination for the sol-gel composites, particularly at low precursor level. Second-order being the reaction of two radical polymer sites, this

mechanism was presumably facilitated due to the reduced viscosity of the HBP/precursor solutions and hence increased mobility of the polymer chains.

It is evident, that also in the case of the sol-gel composites, the intensity exponent β for the rate constant was the same as the intensity exponent b for the shift factor. This confirms that for those systems, for which bimolecular or primary radical termination ($\beta < 1$) are predominant, the radiation dose equivalence law ($t \cdot I$) is not valid and should in fact be rewritten to $(t \cdot I^\beta)$.

The reaction order n and the autocatalytic exponent m were independent on the intensity (Figure 7-13b), and the same as for the HBP and the particulate composites within experimental scatter. This means that the conversion state of the sol-gel composites, the particulate composites and the pure HBP is fully described by the change of one single intensity and filler/precursor loading dependent rate constant $k(\phi, I)$.

For low precursor levels, the conversion α at maximum conversion rate α'_{\max} was generally higher than for the HBP, and increased towards lower intensities (Figure 7-13c). The lowest intensity measured presented an exception to this trend, correlating with the drop in conversion at this intensity. As pointed out earlier, the conversion at α'_{\max} is related to gelation of the material. The reduced viscosity of the HBP/precursor solutions increased the mobility of the reacting species and was able to delay the gelation with respect to the pure polymer. Correspondingly, the HL and AS composites, both exhibiting considerably higher viscosity, gelled earlier than the HBP. It is therefore expected that stress will be lower in the sol-gel composites than in the HL and AS composites. At high precursor level the conversion at α'_{\max} decreased towards lower intensities, which correlates with the overall conversion being reduced at low intensities.

The composition and intensity both influenced the composite formation, which will have an impact on the stress formation. This is better visualized in the form of time-intensity-transformation (TIT) diagrams.

7.3 PHOTO-RHEOLOGY AND TIME-INTENSITY-TRANSFORMATION DIAGRAMS

Figure 7-14 depicts the evolution of the complex modulus G^* and the tangent of the phase angle δ during photo-polymerization for HBP solutions containing the corresponding amount of precursor to produce $\phi_{\text{th}} = 5$ and 20%. A cap was used to cover the parallel plate geometry in order to control the evaporation. At time $t = 0$ the UV lamp

was turned on. After a few seconds G^* increased rapidly over several orders of magnitude until it finally reached a maximum. At higher intensities the induction time, during which the material remained in a liquid-like state, was shorter and the stiffness built up faster. The induction time for the HBP solutions at low precursor level was comparable to that of the HBP (Chapter 4), but was significantly longer at higher precursor level. The same was true for the stiffness onset, which occurred earlier at low precursor level than at high precursor level. In the case of lower precursor level, a plateau value was reached at $G^* \approx 10$ MPa, which was due to the limitation of the photo-rheometer. However, for higher precursor levels, the plateau was at $G^* \approx 1$ MPa, which was the true shear modulus of the material. The reduced modulus of this HBP/precursor mixture with respect to the HBP and the particulate composites was due to the high amount of liquid precursor that was trapped in the polymerized HBP network, acting as a plasticizer. Nevertheless, the material became brittle and cracked.

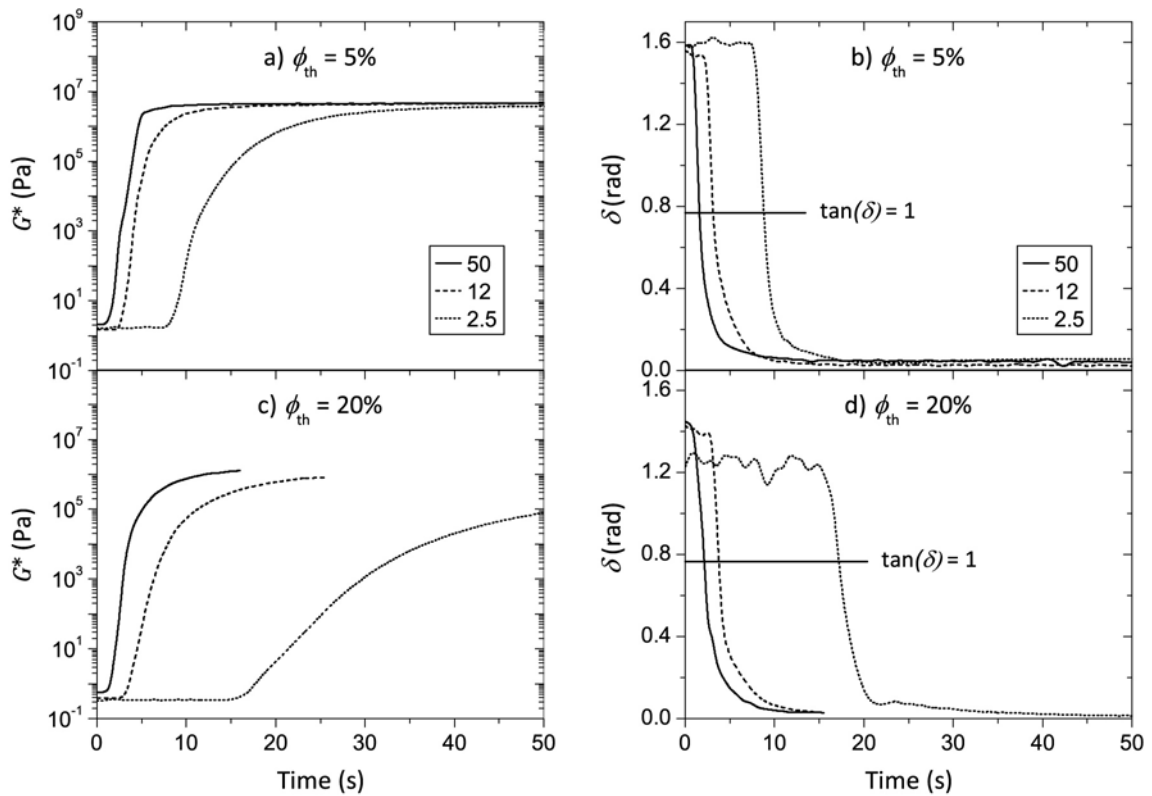


Figure 7-14 Evolution of the complex modulus G^* and the phase angle δ for HBP solutions containing the corresponding amount of precursor to produce $\phi_{th} = 5$ and 20%, photo-polymerized at different intensities (mW/cm^2 as indicated).

As expected, the phase angle of the low precursor mixture showed viscous behavior at $t = 0$. A few seconds after the UV light was turned on δ dropped rapidly, indicating increasingly elastic behavior of the material. The drop in δ and related gelation at

$\tan(\delta) = 1$ was delayed, when lower intensities were used, and occurred after the same time as in the HBP. For high precursor levels, the phase angle was smaller than for the pure HBP, which contradicts the data in Figure 7-7. The reason for this was the small tool geometry of the photo-rheometer in combination with the very low viscosity of the HBP/precursor solutions, which did not give a sufficient signal strength. To increase the signal, a high deformation outside the linear viscoelastic range was chosen, with the implication that the phase angle was underestimated. Corresponding to the delayed modulus build-up, the drop in δ occurred generally later for this HBP/precursor mixture than for the HBP and the particulate composites. Vitrification was not observed in the sol-gel composites.

The time-intensity-transformation diagrams in Figure 7-15 combines the photo-calorimetric and the photo-rheological data. The iso-conversion curves, as derived from the fit with the autocatalytic model, correlated with the measured conversion data within experimental scatter up to 70%. It is clear that the intensity had a considerable influence on the conversion.

In view of the desired reduction of internal stress, the occurrence of gelation with respect to conversion is essential. In the case of low precursor level, gelation was independent of intensity and below 10% conversion, if the photo-rheological data was considered. Gelation as determined from photo-calorimetric analysis appeared, however, to be intensity dependent and was delayed at lower intensities, similarly to HBP and the AS composites (Chapter 4). With high precursor level, gelation determined from photo-rheology was around 10% conversion and also independent of intensity, whereas calorimetric analysis showed delayed gelation at higher intensity. Based on this result, lower polymerization stress should be expected at higher intensities for the highly filled sol-gel composites, in contrast to the HBP and the particulate composites, for which lower stresses are expected at lower intensities.

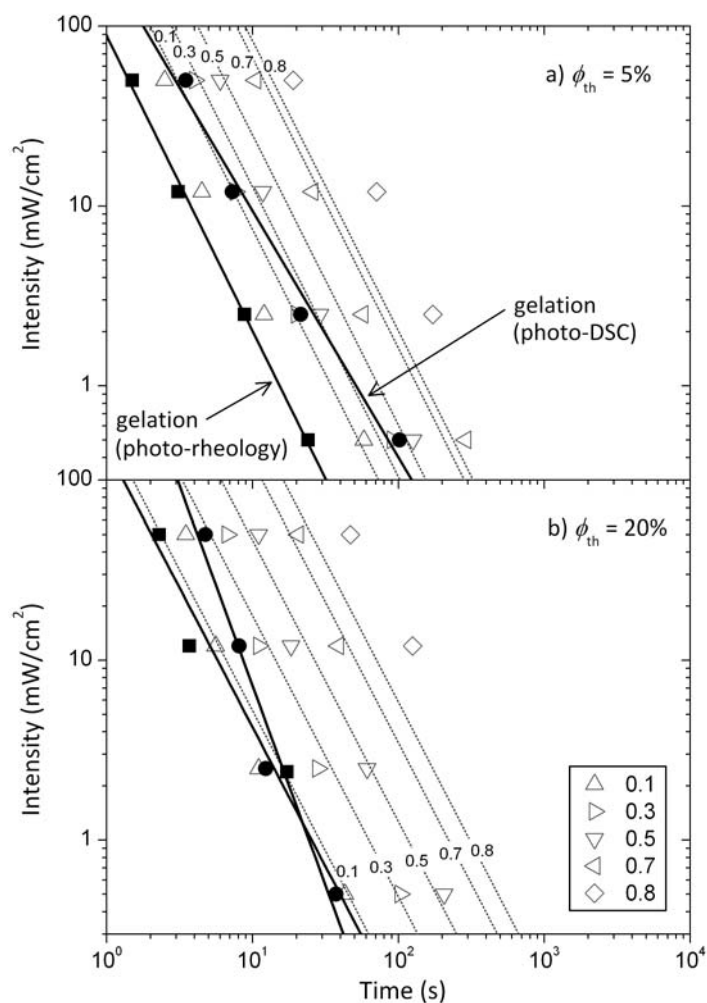


Figure 7-15 Time-intensity-transformation diagram of HBP solutions containing the corresponding amount of precursor to produce (a) $\phi_{th} = 5\%$ and (b) $\phi_{th} = 20\%$. The empty symbols represent the conversion data, the dotted lines represent the iso-conversion curves, derived from the autocatalytic model. The full symbols represent the gelation time, determined from photo-rheology (squares) and from photo-calorimetry (circles). The solid lines are the power-law fits of the intensity with the gelation time.

7.4 THERMO-MECHANICAL PROPERTIES AND INTERNAL STRESS

Figure 7-16 shows the thermo-gravimetric curve of the sol-gel composites. The weight loss at temperature $T < 400^\circ\text{C}$ was presumably due to evaporation of trapped side products or finalization of incomplete condensation.^{35,317} The more distinct weight loss at $T \approx 400^\circ\text{C}$, corresponding to the degradation of the polymer network, occurred at the same temperature as for the pure HBP. This is contradictory to the results of Amerio *et al.*³⁴, who found the degradation of the network to occur at higher temperatures for sol-gel composites with increasing silica content. They claimed that the polymer was protected by a layer of char, through which the oxygen could only penetrate by diffusion.

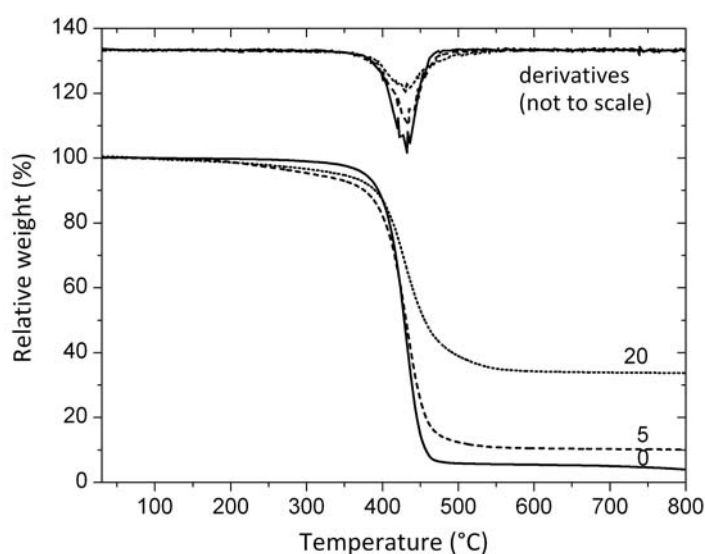


Figure 7-16 Relative weight and derivatives as a function of temperature for sol-gel composites photo-polymerized at 50 mW/cm^2 with different silica fractions ϕ_{th} (vol% as indicated).

Figure 7-17 shows that the dynamic moduli E^* for the sol-gel composites, with photo-polymerization done after condensation, were even higher than those of the HL composites. The modulus was proportional to ϕ_{th} , as was observed for the particulate composites. The high modulus of the sol-gel composites strengthens the assumption that the inorganic phase was in the form of a fine 3-dimensional silica network that was able to immobilize the surrounding polymer more effectively than the well-dispersed discrete particles. The processing sequence only had a minor influence, with a small increase in E^* the later the photo-polymerization was done (Figure 7-18).

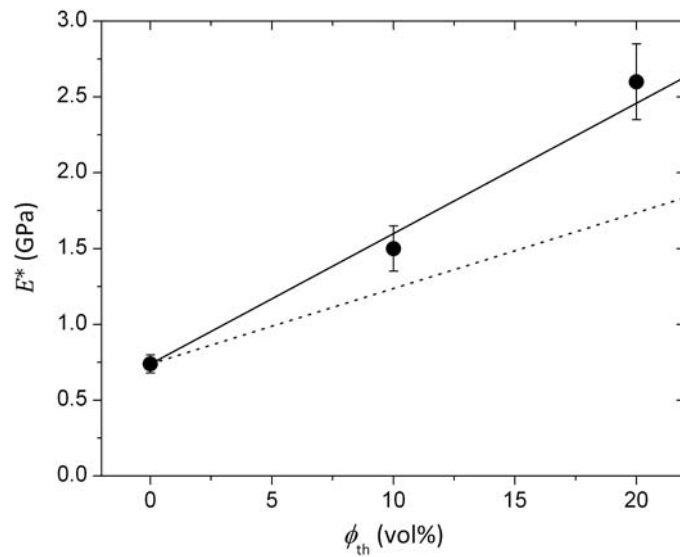


Figure 7-17 Dynamic modulus E^* for sol-gel composites photo-polymerized at 50 mW/cm² as a function of silica fraction ϕ_{th} . The solid line represents Equation 6.8, and the dotted line represents the fit of the model for the HL composites.

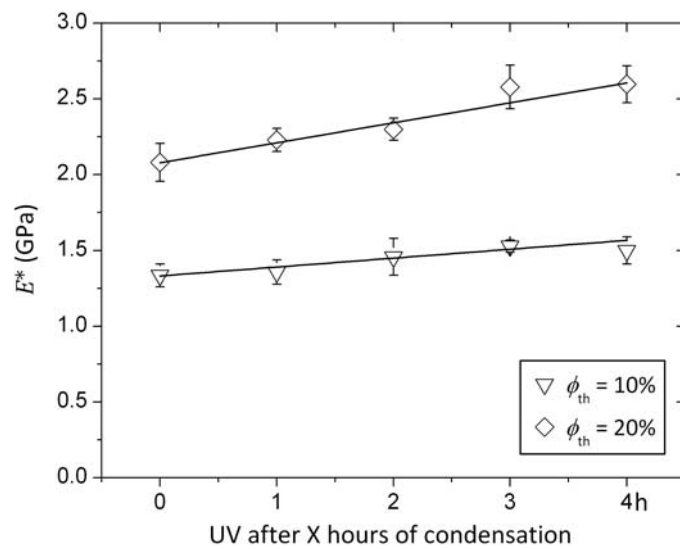


Figure 7-18 Dynamic modulus E^* for sol-gel composites photo-polymerized at 50 mW/cm² after different condensation periods.

Figure 7-19 shows the glass transition temperature T_g determined from dynamic mechanical analysis in comparison with the particulate composites. At $\phi_{th} = 20\%$ the T_g of the sol-gel composites was equal to 130°C, which was considerably higher than that of the HL composites (70°C).

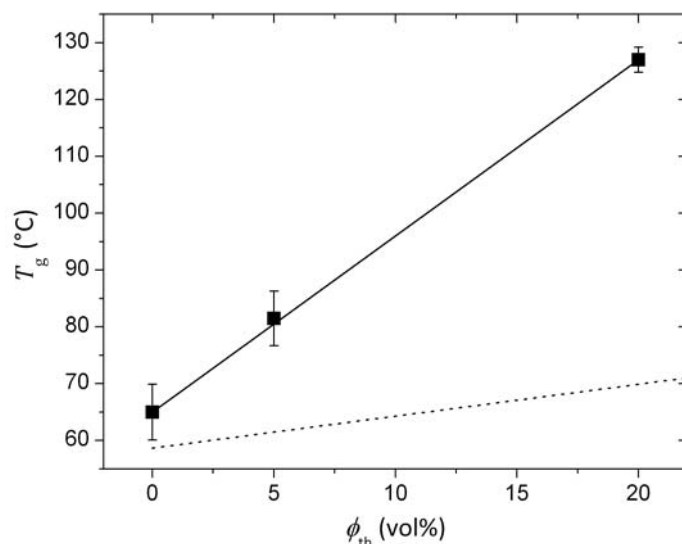


Figure 7-19 Glass transition temperature T_g determined by DMA for sol-gel composites as a function of silica fraction ϕ_{th} photo-polymerized at 50 mW/cm². The dotted line is the trend of the HL composites.

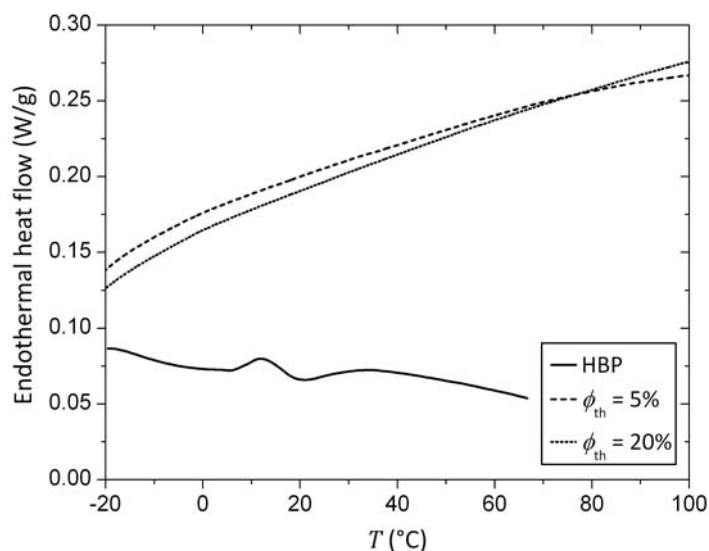


Figure 7-20 Endothermic heat flow as a function of time during heating at 10 K/min in the DSC for HBP and sol-gel composites at different silica volume fractions ϕ_{th} .

The glass transition temperature could not be determined from calorimetric experiments, since no step in the heat capacity was observed (Figure 7-20). This is generally related to complete immobilization of the polymer matrix by the inorganic phase. Again, this supports the earlier assumption of the silica being in the form of a fine network structure with very high specific surface area.

Correlating with the increased T_g and E^* , the coefficient of thermal expansion (CTE) as shown in Figure 7-21 was reduced by 46% at $\phi_{th} = 20\%$ with respect to the pure HBP. The reduction was by a factor of 1.6 more than for the particulate composites at the same filler fraction. The strongly improved thermo-mechanical properties makes the sol-gel

composites highly interesting materials for the production of dimensionally stable nanostructures.

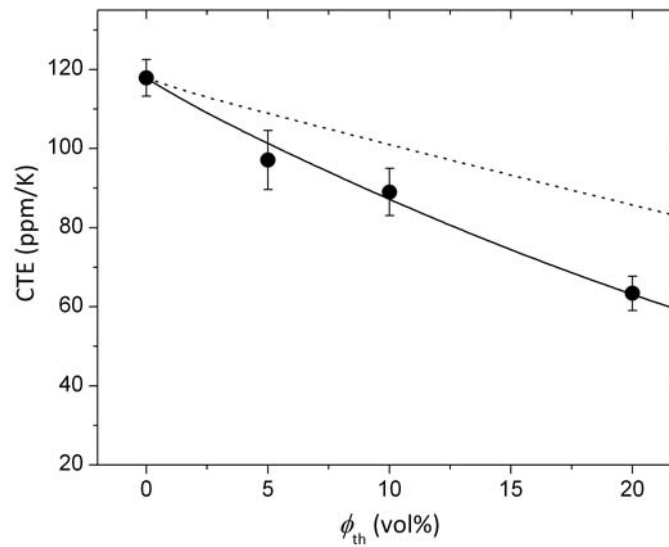


Figure 7-21 Coefficient of thermal expansion for sol-gel composites photo-polymerized at 50 mW/cm² as a function of silica fraction ϕ_{th} . The solid line represents the fit with the Thomas model ($\nu = 0.27$), the dotted line is the fit of the model for the HL composites ($\nu = 0.7$).

Figure 7-22 shows the residual stress of the sol-gel composites where photo-polymerized was done after 45 and 240 min of condensation. Calculations were done with Inoue's model, using the modulus values of the materials produced under the same conditions. If photo-polymerization was done before condensation, the internal stress could not be measured, due to cracking of the material.

It is evident that the stress doubled from $\phi_{th} = 0$ to 5%, beyond which it remained constant. No difference was observed between photo-polymerization after 45 or 240 min. At $\phi_{th} > 5\%$ considerably less stress developed for the sol-gel composites than for the particulate composites for a given amount of silica. As an example, at $\phi_{th} = 20\%$ stress reduction was by a factor of 2.2 was measured with respect to the particulate composites.

The reason for this was presumable that after 45 min the condensation was presumably incomplete, i.e. the precursor was only partially transformed into SiO₂. At that stage, the inorganic phase yet only showed reduced reinforcing effect, and the HBP was still swollen (i.e. plasticized) with liquid precursor. Therefore, polymerization shrinkage occurred in a less stiff material than was the case for the particulate composites, and shrinkage stress was able to relax. After photo-polymerization the condensation was completed, and only then the ultimate stiffness of the composite was built up.

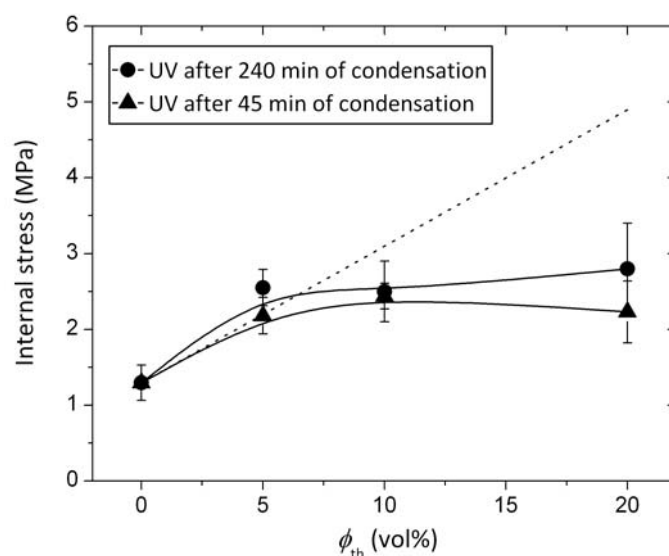


Figure 7-22 Internal stress determined from beam bending experiments, using the model of Inoue, for sol-gel composites as a function of silica fraction ϕ_{th} at 50 mW/cm². The dotted line represents the linear fit for the HL composites.

After 45 min of condensation, the precursor was completely transformed into solid SiO₂ and the byproducts were evaporated before the beginning of the photo-polymerization reaction. Therefore, similar reinforcing effect and stiffness could be expected for the sol-gel composites as for the particulate composites. The reason for the considerably reduced internal stress could therefore result from reduced polymerization shrinkage, which was not measured for these materials due to evaporation. As the silica was in the form of a fine inorganic network, shrinkage of the intertwined polymer was presumably restricted by the rigid inorganic network structure.

7.5 SUMMARY

Hybrid HBP/silica nanocomposites were prepared using a dual-cure process based on an *in situ* sol-gel method and photo-polymerization. The dual-cure process sequence was optimized to avoid premature cracking of the material due to excess evaporation. Comparison was done with nanocomposites prepared from mixing with a powder and the results are compiled in Table 7-4.

- All thermo-mechanically relevant properties were improved with respect to the pure HBP, e.g., at 20% silica fraction the stiffness was increased by a factor of 3.5, the glass transition temperature was increased by 63°C and the coefficient of thermal expansion was reduced by 46%. The internal stress for sol-gel composites

at 20% silica fraction was a factor of 2.2 smaller compared to the particulate counterpart.

- In view of the production of nanocomposite devices and in spite of much longer cycle times (4 h instead of 1 min for UV-curing only), due to the condensation step, the present low viscosity sol-gel composites offer improved processability, improved thermo-mechanical properties and lower internal stress compared to particulate composites. These properties resulted from a fine silica network that was able to immobilize the surrounding polymer in a more efficient way than the discrete particles.

Table 7-4 Comparison of sol-gel composites and particulate composites with 20% silica fraction. Values were taken at room temperature, where applicable.

HBP + 20% silica	η (Pa·s)	E^* (GPa)	CTE (ppm/K)	T_g (°C)	σ_i (MPa)
Sol-gel	$1.3 \cdot 10^{-2}$	2.6	63	127	2.2
HL	$2 \cdot 10^5$	1.7	84	69	4.9

8 NANOSTRUCTURING AND APPLICATION TO OPTICAL SENSORS

Hyperbranched polymers exhibit a high dimensional stability when applied to the fabrication of microstructures,^{414,418} due to their low polymerization shrinkage and low internal stresses. The addition of nanoparticles further reduced the polymerization shrinkage. However, it considerably increased the internal stress level. Moreover, solid particles with size comparable to nanostructures are likely to compromise the structure themselves. The objective of this chapter was to evaluate UV-curable HBP nanocomposites for rapid and cost-effective fabrication of stable nanostructured devices with very high precision, based on either SiO₂ nanoparticles or sol-gel processing. Nanogratings were produced using low-pressure UV-molding and the application of such nanogratings as wavelength-interrogated optical sensors¹ (WIOS) was evaluated.

8.1 UV-NANOIMPRINT LITHOGRAPHY PROCEDURE

Figure 8-1 sketches the nanoimprint lithography tool that was designed and built at the LTC. It consists of a 8 cm diameter cylindrical steel mold, equipped with a UV-transparent 3 cm thick quartz window. Pressure was applied using a pressure-controlled pneumatic movable stamp, to which the replication master was attached. Alignment accuracy was better than 0.02°.

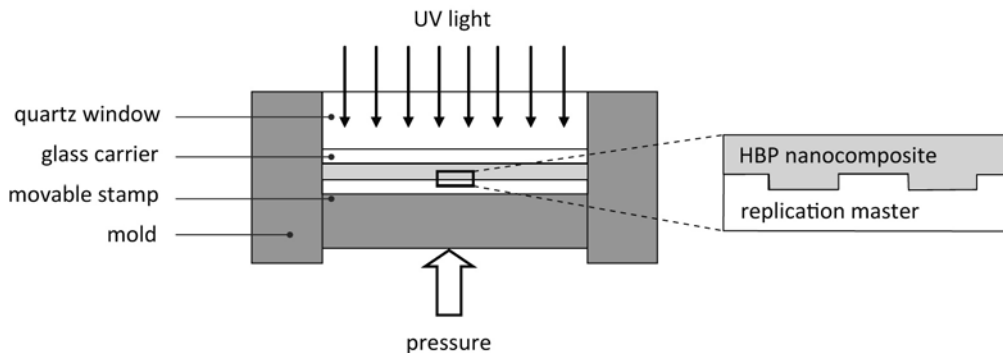


Figure 8-1 Schematic drawing of the UV-nanoimprint lithography tool.

The replication master was a dry etched glass grating (Figure 8-2) with a period of 360 ± 1 nm and a depth of 12 ± 1 nm. This particular grating structure is used in wavelength-interrogated optical sensors developed for immunoassay purposes, as described in the work of Cottier *et al.*⁴⁷ The material to imprint was dispersed on the master and covered with a glass slide, the surface of which was treated with a methacrylsilane compound for better adhesion of the polymer material (see procedure in Chapter 3.2.10). Pressure was applied while the material was photo-polymerized through the quartz window. Approximately 12% of the UV light was absorbed through the glass carrier. The UV intensities reported in the following were measured underneath the glass carrier, i.e. on the sample surface. After polymerization the pressure was released and the master was removed from the imprinted material attached to the glass carrier. Due to the 25° clearance angle of the glass grating, no special surface treatment was needed to help demolding.

In order to quantify the influence of the processing parameters on the fidelity of the imprinted gratings, the step height as well as the top and bottom dimensions as indicated in Figure 8-3 were compared. Each dimension was averaged over 5 repeating elements. The profile was calculated over approximately 500 AFM scan lines (Figure 8-2).

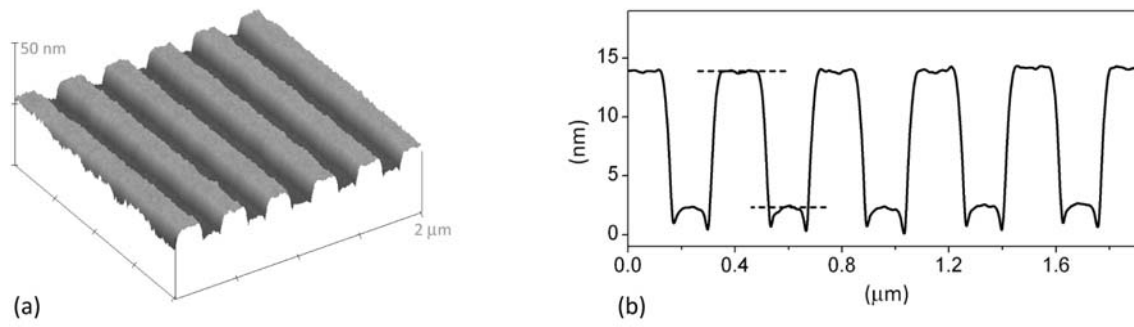


Figure 8-2 (a) AFM surface plot and (b) averaged profile over approximately 500 scans of the glass master grating. The troughs in the corners of the master grating resulted from the dry etching step during the production process. The step height was measured between the dashed lines.

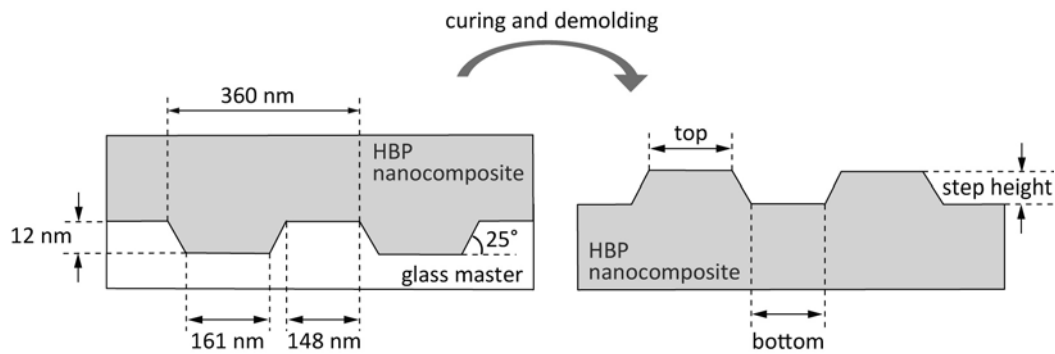


Figure 8-3 Dimensions of the master grating and nomenclature of the dimensions of the imprinted grating.

8.2 PROCESS INFLUENCES ON SHAPE FIDELITY OF HBP COMPOSITE NANOGRATINGS

8.2.1 Photo-Cured Grating Data

Figure 8-4 shows the averaged profiles of the photo-cured gratings for different UV illumination times t , UV light intensities I , pressures p and filler fractions ϕ . It is evident that good replication fidelity was achieved whatever the process conditions. After only 3 s of illumination at 25 mW/cm², or using a low intensity of 5 mW/cm², a stable grating structure was observed after lift-off of the master (Figure 8-4a,b). Even at the minimum pressure of 1 bar the grating was imprinted with good quality (Figure 8-4c). The grating structure was also properly imprinted in the HL and AS composites up to the highest filler content (Figure 8-4d). In all cases, the grating period was preserved (Figure 8-5), even when the gratings were removed from the glass carrier. The grating fidelity was better

than 98% as calculated from the standard deviation of the period of the imprinted grating from that of the replication master.

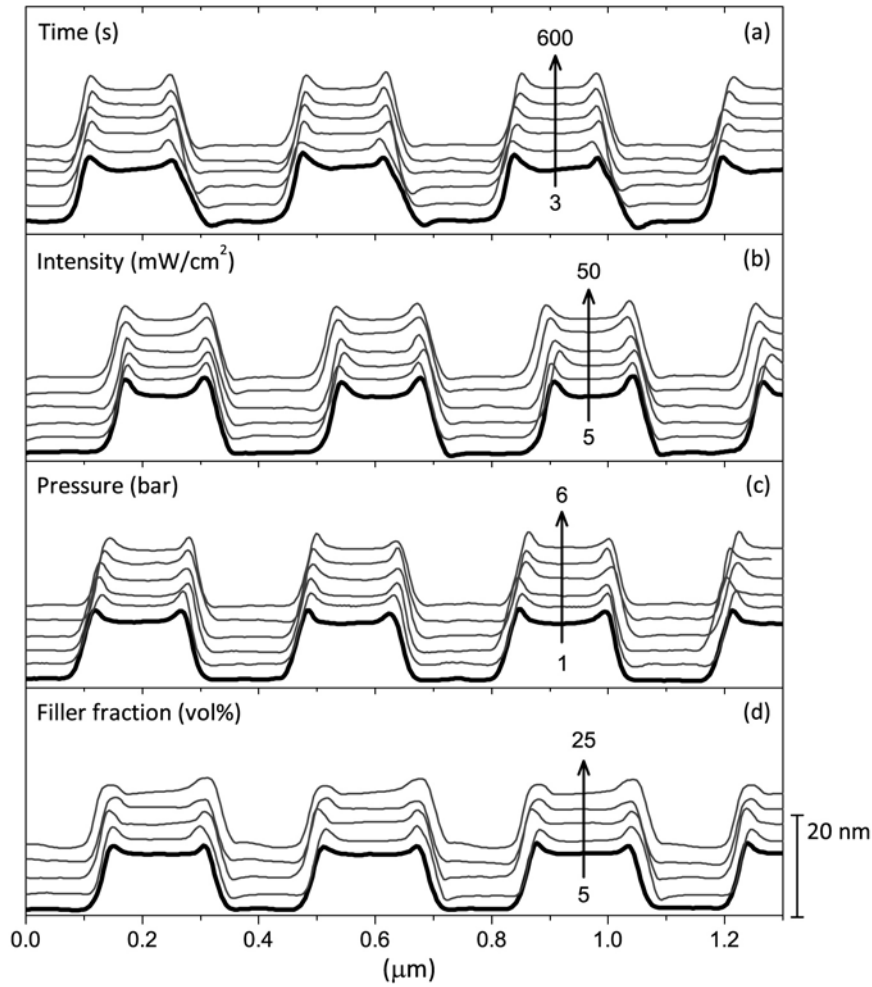


Figure 8-4 Averaged AFM profiles of HBP and nanocomposite gratings. Individual profiles are offset for legibility. (a) HBP gratings as a function of illumination time. $I = 25 \text{ mW/cm}^2$, $p = 5 \text{ bar}$. (b) HBP gratings as a function of UV intensity. $t = 600 \text{ s}$, $p = 5 \text{ bar}$. (c) HBP + 5% SiO_2 (HL) gratings as a function of pressure. $I = 60 \text{ mW/cm}^2$, $t = 90 \text{ s}$. (d) HBP composite gratings as a function of HL filler fraction. $I = 60 \text{ mW/cm}^2$, $t = 90 \text{ s}$.

A further insight into process influences on the shape fidelity is provided with the analysis of the grating geometry. Figure 8-6 shows the top and bottom dimensions as well as the step height for the same conditions as described above. When looking at the measured grating dimensions, it is evident that up to 10 s the step height remained constant within experimental scatter, and then decreased gradually (Figure 8-6a). The intensity did not influence the dimensions of the imprinted grating (Figure 8-6b). However, while the top and bottom dimensions correlated with the corresponding master dimensions, the step height was reduced by $4.3 \pm 1.3\%$ with respect to the master step height. Pressure levels ranging from 1 to 6 bar were applied to HBP nanocomposites

containing 5% SiO₂. For both types of composite (HL and AS), the dimension of the bottom part was reduced and that of the top part was expanded with respect to the corresponding dimensions on the master. This interesting result is examined in the following section. Moreover, the step height of the imprinted grating was 9.4% smaller than the master step height (Figure 8-6c).

The bottom and top dimensions, as well as the step height, strongly depended on the amount of filler (Figure 8-6d). The same effect was observed for the thermal imprinting of composite resins.²²⁸ Similarly to the effect of pressure, the top part was expanding while the bottom part and the step height were reduced. The clearance angle of the grating did not systematically change and only varied within 6% of the clearance angle of the master grating. The “ears” on the grating edges became less sharp, but the surface finish of the gratings was not compromised by the presence of the silica. No difference was observed between HL and AS composites.

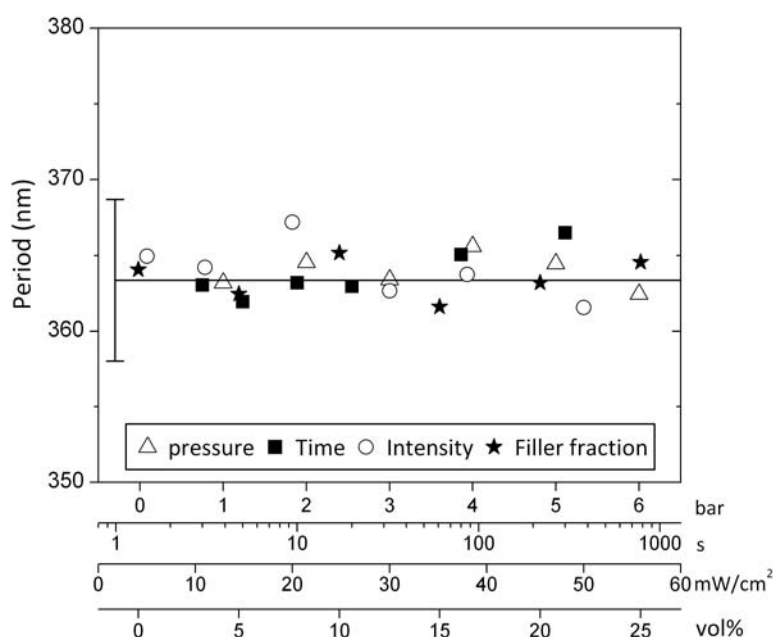


Figure 8-5 Grating period as a function of pressure, UV illumination time, UV intensity and filler fraction. The line with the error bar represents the period of the replication master.

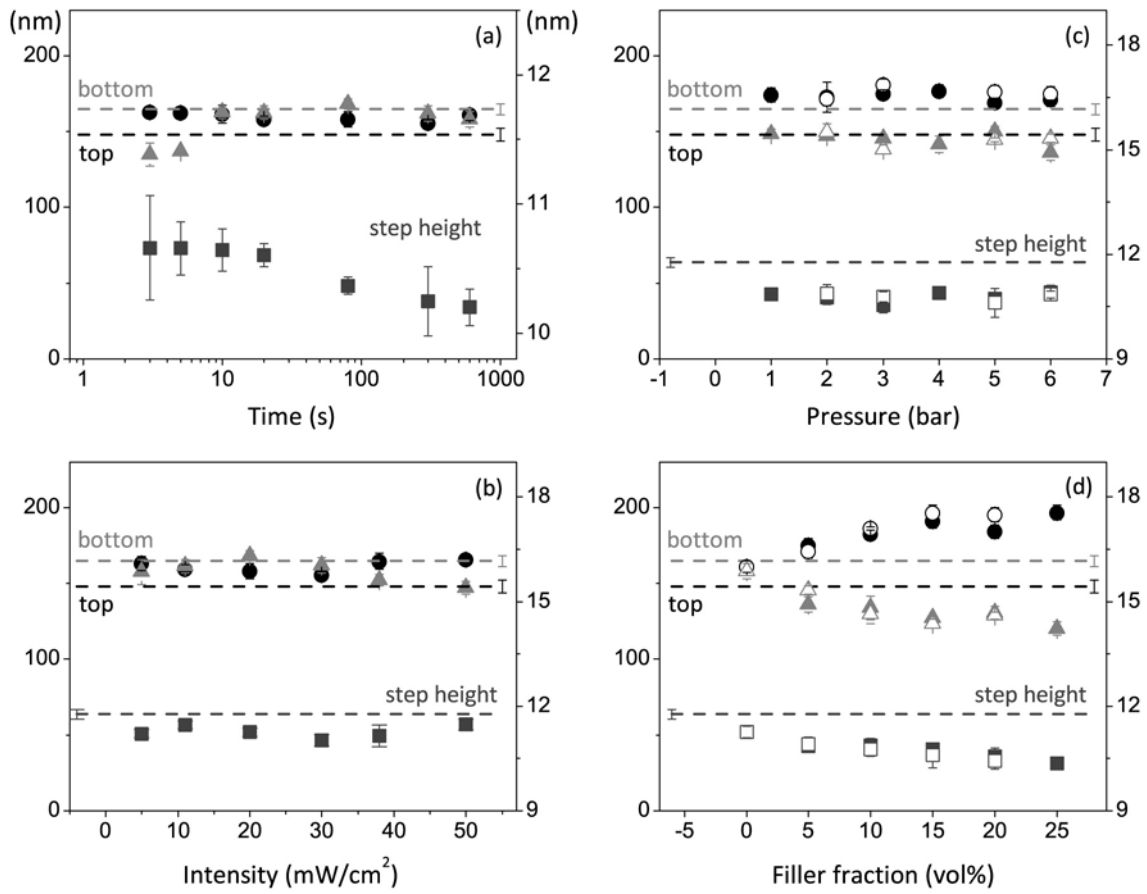


Figure 8-6 (a,b) HBP and (c,d) composite grating dimensions. Full symbols: HBP or HBP/HL composites; empty symbols: HBP/AS composites; circular symbols: top dimension; triangular symbols: bottom dimension; square symbols: step height. The dashed lines represent the dimensions of the replication master as labeled in the plot. (a) HBP grating dimensions as a function of illumination time. $I = 25 \text{ mW/cm}^2$, $p = 5 \text{ bar}$. (b) HBP grating dimensions as a function of UV intensity. $t = 600 \text{ s}$, $p = 5 \text{ bar}$. (c) HBP + 5% SiO_2 grating dimensions as a function of pressure. $I = 60 \text{ mW/cm}^2$, $t = 90 \text{ s}$. (d) HBP composite grating dimensions as a function of filler fraction. $I = 60 \text{ mW/cm}^2$, $t = 90 \text{ s}$.

It is remarkable, that at a pressure as low as 1 bar the grating structure was imprinted in nanocomposites containing up to 25% silica, despite the high viscosity that these materials exhibit. The period of the HBP nanocomposite gratings being equal to that of the replication master, this is a promising result for the production of polymer-based WIOS by nanoimprint lithography, because for good performance of the optical sensing devices, the period of the grating is the key parameter to control.⁴¹⁹ However, shrinkage of the step height occurred especially at high filler loading, and an unexpected lateral expansion of the grating walls was observed. These two phenomena resulted from the dynamics of structure build-up during cure of the polymer confined in the grating structure, including gelation and internal stress, as discussed in the next section.

8.2.2 Discussion on Process-Structure Relations

Gelation, being the transition between liquid and solid material, is an important parameter that determines the stability of the gratings. The gelpoint, as determined with photo-rheology (Chapter 5) from the crossover of storage and loss moduli, was found to occur at around 3 s for HBP at an intensity of 25 mW/cm². At that point, the double-bond conversion reached 15% and the shear modulus was approximately 1 MPa, hence the stability of the imprinted HBP grating after only 3 s of illumination (Figure 8-4a). The influence of gelation on the step height shrinkage is analyzed in Figure 8-7. The linear shrinkage, calculated from the reduction of the step height with respect to the step height at 3 s, was delayed in time by a factor of about 10, compared with the linear shrinkage determined by interferometry on flat HBP films. As polymerization set in, the equilibrium volume of the HBP reduced. In the absence of external pressure, voids would have immediately developed in the pits of the master grating. However, under constant external pressure the viscous material continued to fill the grating cavities. Only once the material had gelled, plastic flow was no longer possible and further polymerization shrinkage led to the observed reduction of the step height. While the gelpoint determined using photo-rheology was around 3 s, gelation determined by kinetic analysis (Chapter 5) occurred at 5 s for the current system. The latter result corresponded well with the moment after which the step height started to shrink.

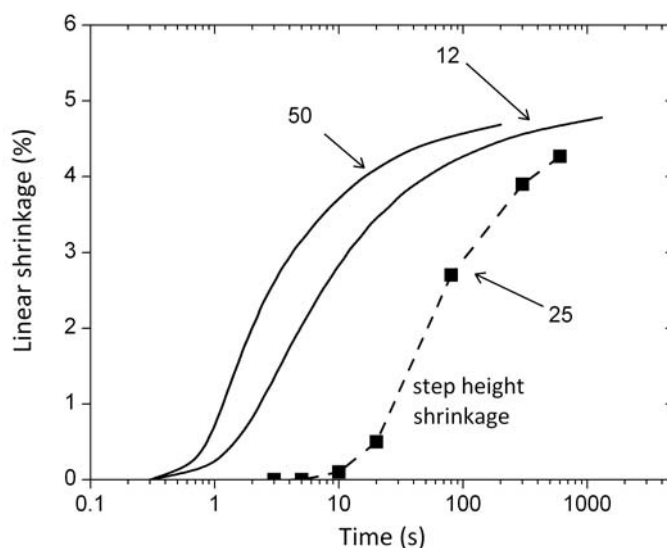


Figure 8-7 Linear polymerization shrinkage as a function of illumination time and intensity (mW/cm² as indicated) measured on HBP films (solid line) compared to the shrinkage as determined from the reduction in grating step height (squares and dotted line).

The average shrinkage of the fully polymerized gratings determined from the reduction in step height with respect to the master step height ($4.3 \pm 1.3\%$) was equal within experimental scatter to the linear shrinkage measured on flat films ($4.6 \pm 0.5\%$). The reason why the intensity did not influence the dimensions of the imprinted gratings was because the maximum conversion was independent of the UV intensity (Chapter 5).

A surprising result was the inversion of the bottom and top dimensions, which was evident when the pressure or the filler fraction was increased (Figure 8-6c,d). The sidewalls of the master were tilted by an angle of approximately 25° , the lateral dimensions of the grating were therefore a function of the step height, which in fact depended on the amount of silica in the composite. As an example, the step height of the imprinted grating containing 25% SiO_2 was reduced by 12% with respect to the master grating. This should have increased the top part by 6 nm, however, the real increase was 49 nm. The fact that the silica reduced the step height (Figure 8-6d) was surprising as well, since it had been shown that the presence of an inorganic filler reduced the overall polymerization shrinkage (Chapter 6.1).

The deviation of the top and bottom dimensions of the imprinted grating from the master dimensions was due to internal stress effects. Polymerization shrinkage and simultaneous stiffness build-up are the reason for internal stress build-up in polymer materials. Even though the presence of silica reduced the amount of polymerization shrinkage, the internal stress increased linearly with the filler fraction (Chapter 6.3), due to the increased stiffness of the composites (Chapter 6.5). The internal stress measurements as shown in Chapter 6.3 were done on flat films that were constrained in two dimensions by the substrate, i.e. under plane stress conditions. In the case of gratings, the constraints were in three dimensions, i.e. under hydrostatic conditions, hence higher stress levels are expected.^{81,82} After lift-off of the master, the stress relaxation led to the observed deformation of the grating.

Nanoparticles increased the stress within the grating structures, however, they did not compromise the surface quality, the reason for which was found to be a resin rich layer at the surface of the device (Figure 8-8). Deformation of the composite material under pressure led to exudation of the HBP phase, as often observed in case of compression molding of reinforced polymers in narrow geometries.⁴²⁰

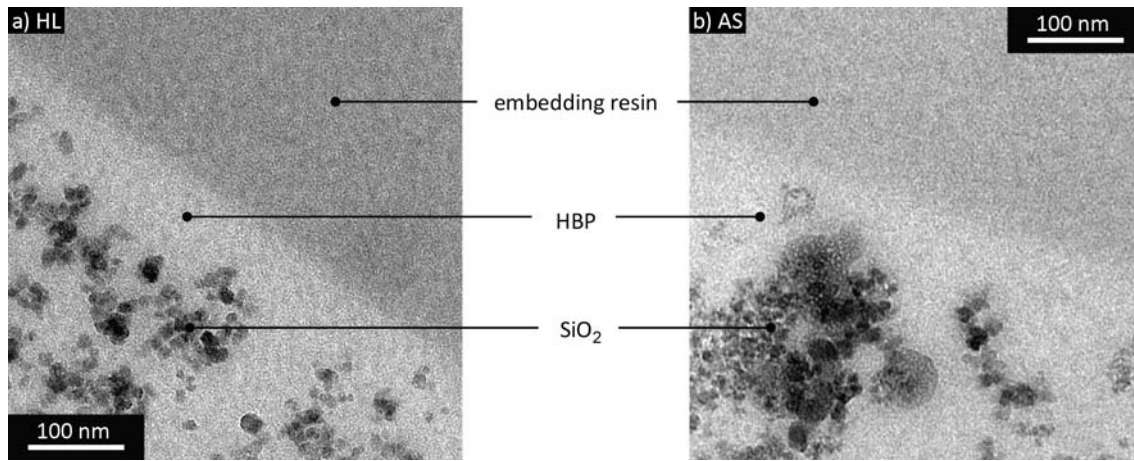


Figure 8-8 Transmission electron micrographs of grating surfaces of HBP nanocomposites containing 5% SiO₂ from (a) HL and (b) AS. A HBP resin rich layer at the surface of the grating is evident in both cases.

8.2.3 Summary of Grating Formation Process

To summarize, Figure 8-9 synthesizes a NIL process in the form of a 4-step sequence. In step 1 the composite paste was loaded on the replication master and upon application of pressure the material filled out the master grating cavities. At this stage, exudation of the polymer formed an approximately 100 nm HBP layer at the grating surface, thus ensuring a good surface quality. In step 2 the polymerization was initiated, shrinkage occurred in the entire volume of the composite, and the viscous material continued to fill the grating cavities under the constant applied pressure. In step 3 gelation occurred and plastic flow was no longer possible, thus further polymerization shrinkage led to reduction of the step height and internal stress started to build up. In step 4 the polymerization was completed and after release of the pressure the replicated grating was demolded and internal stresses could relax, resulting in the observed deformation of the grating structure.

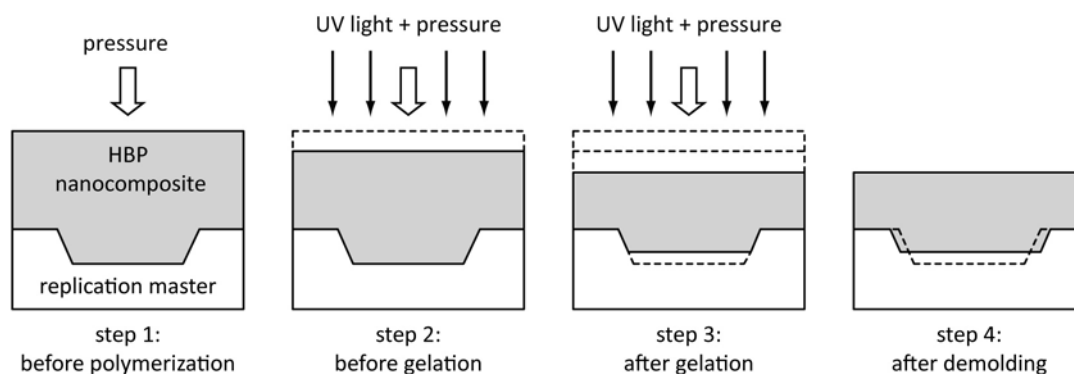


Figure 8-9 Schematic drawing the grating formation process during UV-NIL.

Considering that small changes in internal stress have a considerable influence on the geometry of a nano-pattern, the present low-stress HBP nanocomposites show immense advantage over commercial UV-curable acrylates, where the stress level goes up to 16 MPa^{78,85}. In the standard photo-resist SU-8, stresses are around 20 MPa⁵⁷ before and up to 75 MPa⁷⁷ after post-exposure bake. A further advantage for the production of stable nano-patterns is the reduced CTE (Chapter 6.5) for better thermal stability.

8.3 HYBRID SOL-GEL NANOGRATINGS

The sol-gel gratings were produced in a similar way as the particulate composite gratings. That is, the HBP solution was placed on a glass carrier and the master was pressed onto the sample, then the sample was illuminated with UV light while the pressure was kept constant. As already discussed in connection with the internal stress measurements on sol-gel hybrids in Chapter 7, a critical parameter to control in sol-gel composite processing was the timing of the photo-polymerization reaction with respect to the condensation reaction:

“UV first” (case (a)) systematically led to excessive deformation and cracking of the sample during condensation. Case (a) nanogratings could therefore not be analyzed and were unsuitable for the application to optical devices. “Condensation first” (case (b)) led to stable gratings, however with poor replication fidelity, as shown in Figure 8-10d. Another possibility that was explored was to perform the photo-polymerization reaction after a certain condensation time, and then continue the condensation to completion (case (c)). Total condensation time in all cases was 240 min. Figure 8-10 shows the averaged profiles of sol-gel composites prepared according to case (b) and case (c). The period was nearly preserved with a fidelity better than 95% (Figure 8-11). However, the step height progressively degraded and almost completely disappeared, when the condensation time before photo-polymerization increased.

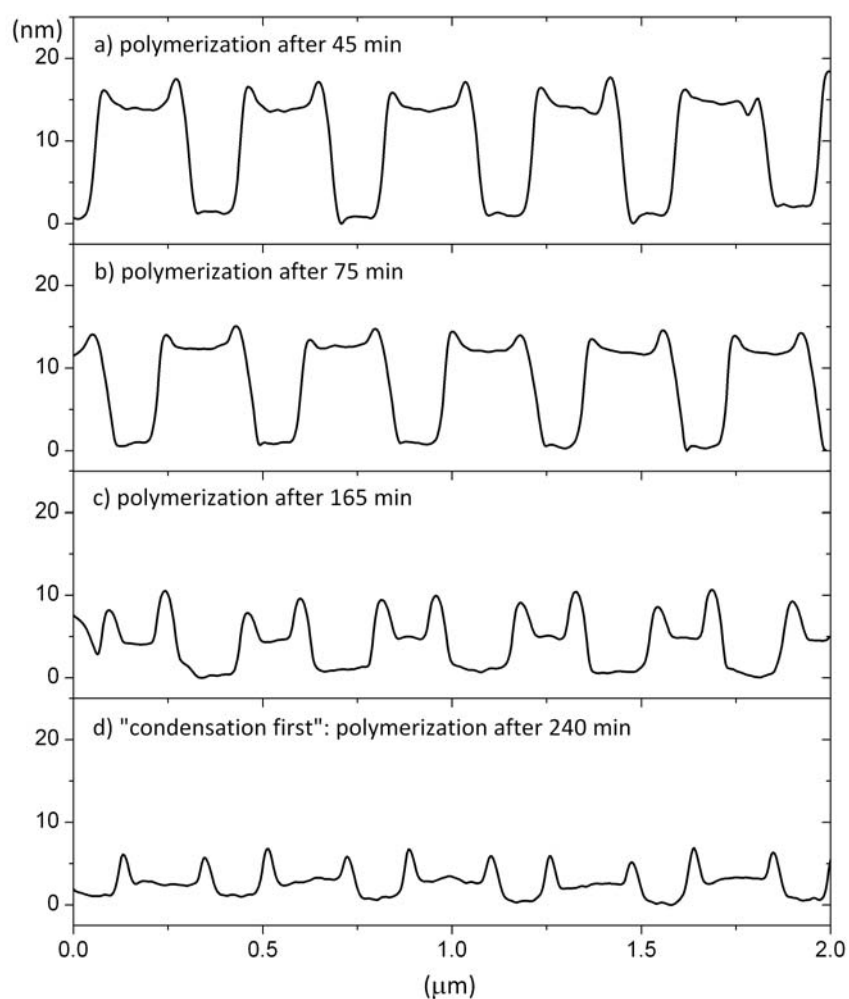


Figure 8-10 Averaged AFM profiles of sol-gel nanocomposite gratings at theoretical silica fraction $\phi_{th} = 25\%$ with photo-polymerization done after different condensation periods. In all cases the total condensation time was 240 min. $I = 50 \text{ mW/cm}^2$, $p = 6 \text{ bar}$, $t = 300 \text{ s}$.

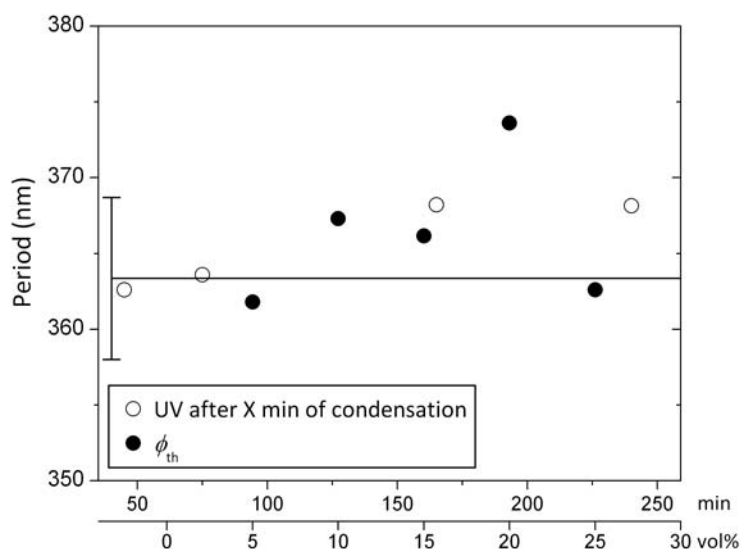


Figure 8-11 Grating period as a function of condensation time before photo-polymerization at $\phi_{th} = 25\%$, and as a function of theoretical filler fraction with photo-polymerization done after 45 min. The line with the error bar represents the period of the replication master.

Figure 8-12a shows the average step height measured from the same grating profiles. Again, it is obvious that the longer the initial condensation period, the smaller was the step height. The shape fidelity of the step height in case (b) was only 20%, giving an overall shape fidelity of about 19%. The reason for this was the high amount of silica that formed in the shape of a rigid 3-dimensional network and that could not be deformed with the maximum pressure of the NIL tool (6 bar).

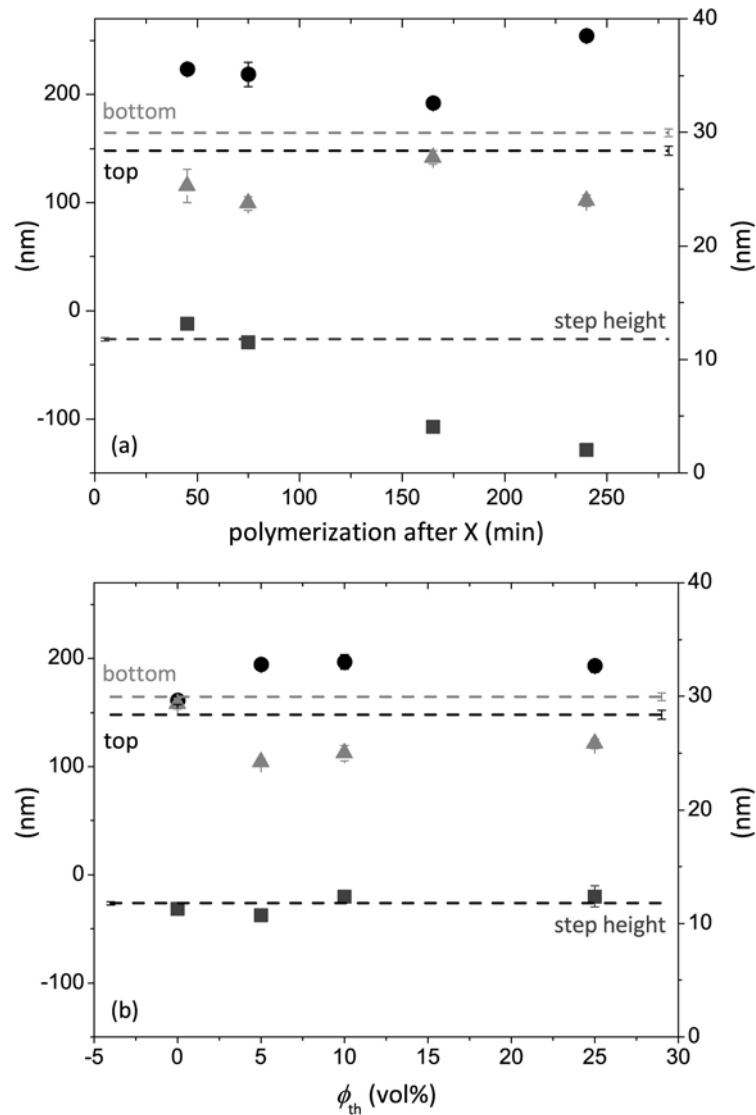


Figure 8-12 Grating dimensions for sol-gel nanocomposites as a function of (a) the length of the initial condensation period at silica fractions $\phi_{th} = 25\%$ and (b) at different silica fraction ϕ_{th} with photo-polymerization done after 45 min of condensation. Circular symbols: top dimension; triangular symbols: bottom dimension; square symbols: step height. The total condensation time was 240 min. $I = 50 \text{ mW/cm}^2$, $p = 6 \text{ bar}$, $t = 300 \text{ s}$.

After 45 min of condensation the composite had already relaxed an important amount of evaporation shrinkage stress, but the silica network was still sufficiently soft to be imprinted by the replication master at 6 bar. Hence, the step height was 12 nm, which

was equal to the master step height. Figure 8-12b shows the top and bottom dimensions as well as the step height for sol-gel composite gratings with different silica fractions ϕ_{th} , with photo-polymerization reaction performed after 45 min. It is evident that for $\phi_{th} \geq 5\%$ the top and bottom dimensions were constant, but deformed with respect to the master. Since the internal stress level was also constant for $\phi_{th} \geq 5\%$, these results confirm that the grating distortion was indeed a function of the internal stress level in the material. The scatter in the step height was because different masters were used with differences in step height up to ± 1 nm.

8.4 APPLICATION TO OPTICAL SENSORS

8.4.1 Detection Principle

The principle of wavelength-interrogated optical sensors is described in detail in the work of Wiki *et al.*¹ and summarized in Figure 8-13. The label free sensor contains an optical nanograting, through which a light wave is coupled into a high refractive index waveguide layer, to form a sensitive optical resonator. The resonance condition at which coupling occurs is interrogated with a vertical cavity surface emitting laser (VCSEL) at wavelength $\lambda = 763$ nm and tunable in the range of $\Delta\lambda = 2$ nm. The resonant coupling condition λ_r is very sensitive to minute changes in the refractive index, caused by the interaction of the analytical targets with receptors immobilized on the chip surface. The sensitivity of the device depends primarily on the period of the nanograting, the reason for which dimensional stability of the grating material is indispensable.

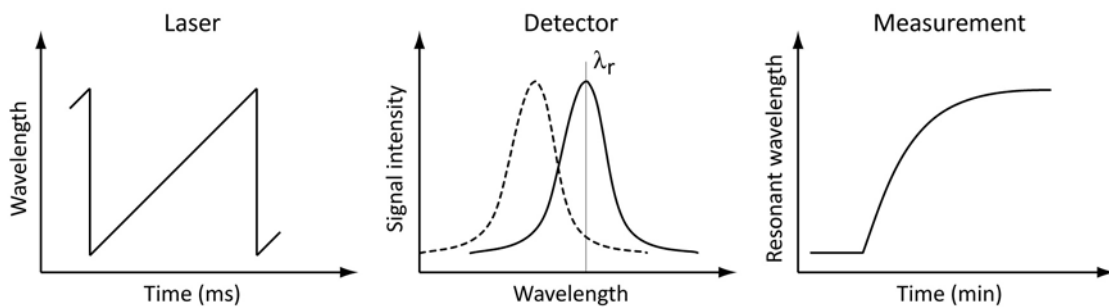


Figure 8-13 Label-free detection principle of the wavelength-interrogated optical sensor chip.

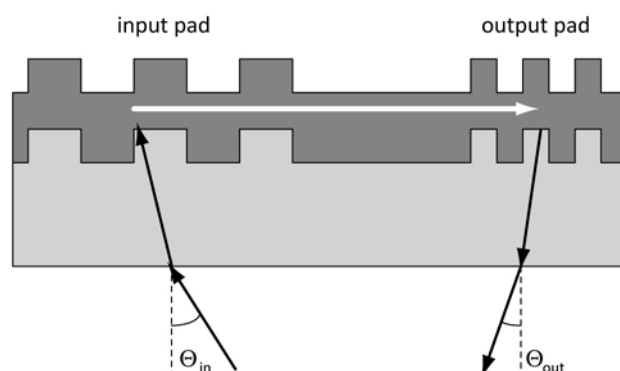


Figure 8-14 Cut through a dual period wavelength-interrogated optical sensor chip. The arrows indicate the path of the laser beam.

For the actual measurement, the input grating pad was illuminated through the transparent substrate with the tunable laser at a fixed angle θ_{in} (Figure 8-14). The guided mode was excited with maximum intensity, when the resonance condition λ_r was fulfilled. The light was then coupled out by the output grating and detected by a photodiode. The sensing of molecules is possible due to a shift in λ_r .

The detection accuracy of the WIOS is measured in g/m^2 , the reason for which larger (and heavier) molecules can be detected more easily. The detection limit of current WIOS devices is in the pg/mm^2 range. Using standards, it is possible to probe molecules in liquids with concentrations as low as a few ppb.³

8.4.2 HBP Composite WIOS

The HBP-based WIOS device contained adjacent grating pads with different periods (360 and 409 nm), as shown in Figure 8-14. This particular grating was reproduced using a nickel master giving imprinted gratings with less distinct edges. This was presumably due to a more roundish shape of the master, which was reproduced from a negative master by electroplating. An example of a HBP grating profile made from the nickel master is shown in Figure 8-15.

Titanium oxide films⁴²¹⁻⁴²³ of amorphous nature were deposited on the grating substrates by reactive DC magnetron sputtering in an argon/oxygen gas mixture and from a metallic titanium target (purity 99.99%). The thickness of the TiO_2 layer varied only by 1 nm within one batch. The average thickness over different batches was 141 ± 3 nm. The refractive index of the HBP and the TiO_2 layer at 763 nm was 1.486 and 2.03, respectively.

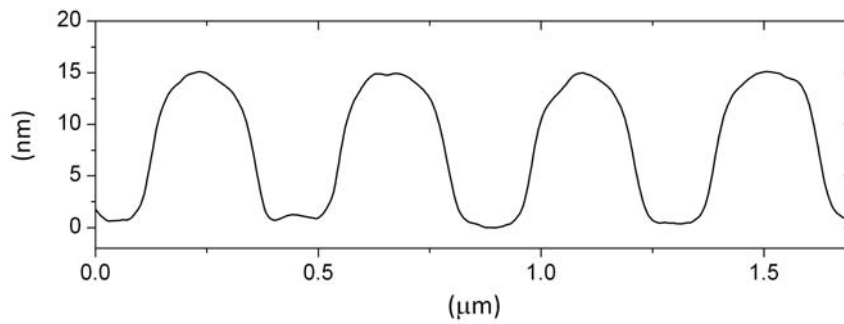


Figure 8-15 Profile of a HBP grating produced using a nickel shim master at 6 bar and 50 mW/cm².

To further facilitate the processing of the sensor device, thick HBP blocks with the same nanograting imprinted on the surface were produced without the need of a glass carrier, using a square shaped (1.7 · 1.7 mm²) and 1 or 2 mm deep mold. The device thickness did not caused problems for polymerization, as might have been expected from the absorption of UV light, i.e. the blocks were polymerized through the entire thickness. Visual inspection showed that after demolding the samples were mechanically stable in the sense that they did not macroscopically deform. However, these samples were unsuitable for the use as optical sensors, since residual porosity in the HBP volume diffused the laser light and the coupling signal was not distinguishable from the scattered light.

As light transmittance was shown to be higher for the nanocomposites than for the HBP (Chapter 5), the composite samples were expected to show reduced light scatter effect. However, the increased viscosity of the nanocomposites prevented the elimination of air bubbles, on which the light was then scattered. With increasing thickness the device appeared milky, due to residual porosity, this being the reason for the scatter of the laser light. The scattering effect was indeed stronger for the 2 mm sample than for 1 mm sample. Therefore, the use of cheap laser-transparent glass or plastic carriers was more favorable for the production of HBP and HBP nanocomposite WIOS.

8.4.3 Laser Coupling Test

Preliminary coupling tests were performed on the HBP composite gratings with a HeNe-laser at fixed wavelength $\lambda = 632.8$ nm and the coupling angle θ_{in} was recorded for transverse-electric (TE) and transverse-magnetic (TM) polarization. Coupling, as shown in Figure 8-16, was observed for all tested gratings, thus the functionality of the polymer-based gratings as a light coupler was proven. It was found that samples from the same TiO₂ deposition batch had the same coupling angle, independent of the substrate

composition, which correlates with the grating period being independent of the composition. In contrast, the coupling angle was very sensitive to TiO_2 thickness (Figure 8-17).

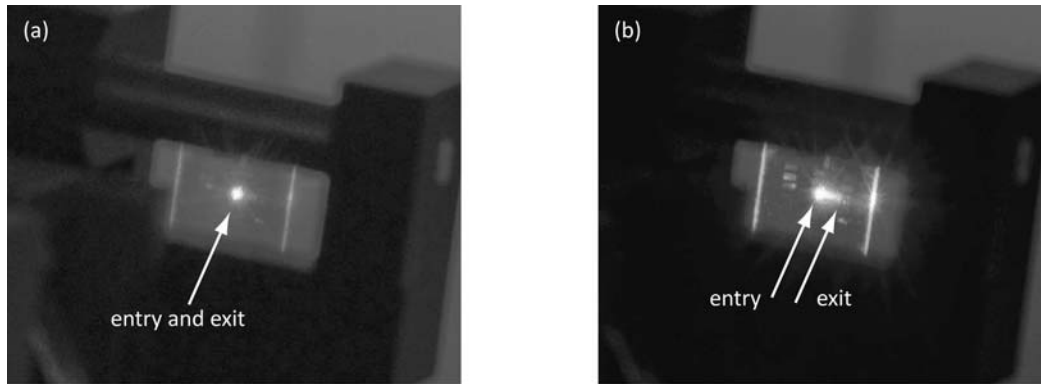


Figure 8-16 Optical performance test with (a) no coupling of the laser light, and (b) laser light coupling in and out at adjacent grating pads with light guidance in between.

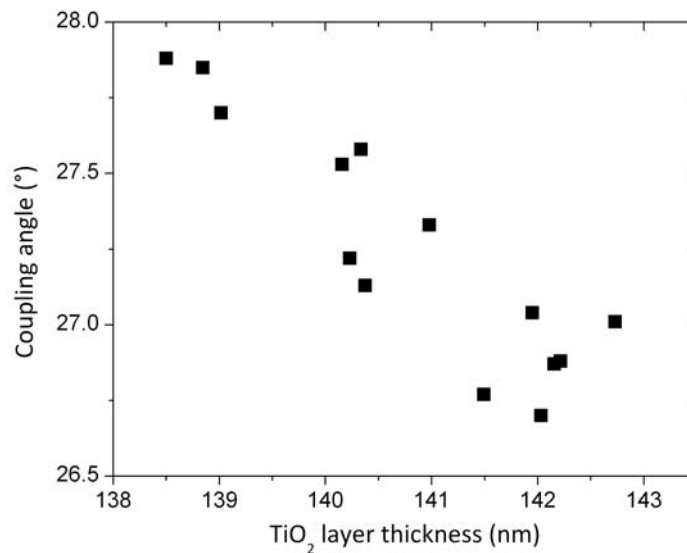


Figure 8-17 Dependence of the coupling angle on the TiO_2 layer thickness.

The functionality of WIOS chips based on TiO_2 coated HBP and HBP/ SiO_2 gratings was tested in an adjustable WIOS set-up¹. Therefore the sensor chip and laser were manually aligned to give the optimum signal. Figure 8-18 compares the resonant coupling signal of the tunable laser of the HBP and two HBP composites with that of the reference glass-based waveguide gratings. In all cases, the detected signal was strong, a proof that the HBP-based waveguide gratings had good optical properties in terms of coupling efficiency, waveguide propagation loss and grating reproducibility. The signal strength of the HBP sensor was basically the same as the standard high precision glass sensor, with only a small difference in peak height to full width half maximum (FWHM) value. The

signal strength of the composite sensors was, however, lower. The influence of the grating distortion shown in Figure 8-6 on the coupling efficiency was calculated to be less than 3%. It was thus concluded that the reduced laser signal was due to light scattering resulting from small air inclusions, entrapped during low-pressure processing of the highly viscous nanocomposite. Nevertheless, these devices were suitable for detection, since it is the position of the peak that determines the concentration of the analytical target.

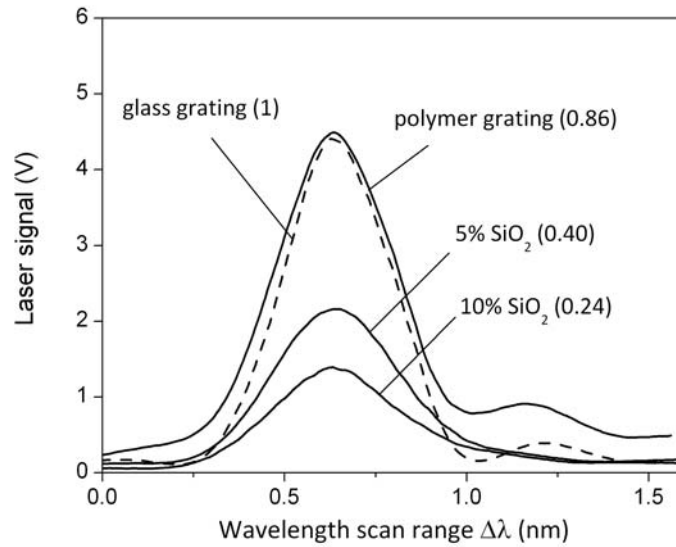


Figure 8-18 WIOS laser signal for the standard glass sensor (dashed line) and sensors made of HBP and composites containing 5 and 10% SiO₂ (HL). The numbers in parentheses are the signal height divided by the FWHM and normalized with respect to the glass grating.

8.5 IMMUNOASSAY

For the actual immunoassay the surface of the optical grating was functionalized with mouse immunoglobulin type G (IgG, JacksonImmunoResearch). The surface was washed first for 30 min with 10 mM phosphate buffered saline (PBS, Sigma-Aldrich), a buffer solution at pH 7.4 that is commonly used in biological research. Then the chamber was flushed with 0.5 µg/ml mouse IgG for 15 min, and washed again for 10 min with PBS. To cover the free surface between the attached antibodies, the system was then flushed with 1% bovine serum albumin (BSA, Sigma-Aldrich) for 10 min and subsequently washed with PBS until the signal peak position λ_r was stable.

After functionalization the chamber was infiltrated with different concentrations in the range of 1 to 100 µg/ml of the secondary antibody anti-mouse IgG (JacksonImmunoResearch), which would attach to the primary antibody mouse IgG immobilized on the

grating surface. The response signal of the HBP-based sensor and the reference glass-based sensor are compared in Figure 8-19. The curves are shifted for legibility. Interestingly, the novel HBP-based sensor gave the same response signal as the glass sensor. Based on this result, a detection sensitivity as high as ppb, which is relevant for the detection of liquid food contaminants, was demonstrated for the polymer-based sensor.

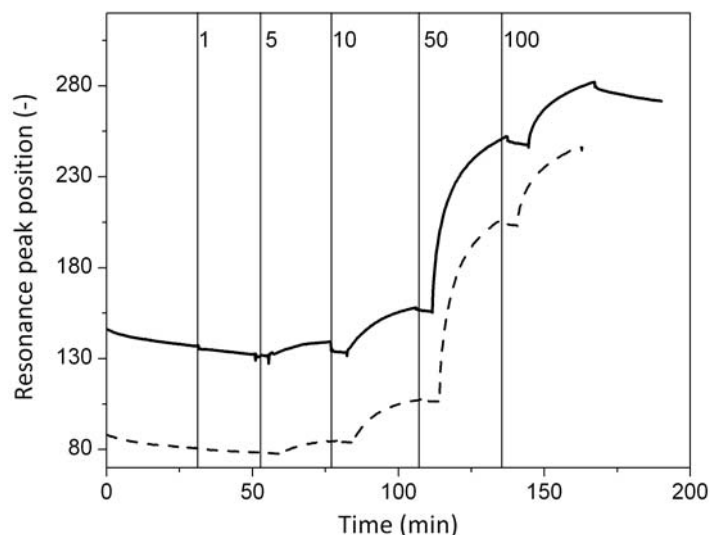


Figure 8-19 Detection test of anti-mouse IgG at different concentrations ($\mu\text{g/ml}$ as indicated) for a HBP-based sensor (solid line) and the reference glass-based sensor (dashed line). The sensors were previously functionalized with mouse IgG.

8.6 SUMMARY

Nano-sized gratings were produced from UV-curable acrylated HBP nanocomposites and sol-gel hybrids with up to 25% silica by nanoimprint lithography, and these gratings were used in optical sensors.

- A pressure as low as 1 bar and short process time of 3 s were sufficient to imprint a stable grating into the high viscosity particulate composite material. The period of the composite gratings was within 98% for the particulate composites and within 95% for the sol-gel hybrids with respect to the master period.
- Lateral distortion of the grating dimensions increased with the amount of silica, due to relaxation of stress, which built up after gelation and which was higher for the nanocomposites with high filler fraction.
- The laser coupling quality of WIOS devices based on HBP gratings coated with a high refractive index TiO_2 layer was found to be the same as the standard glass WIOS. An

immunoassay test with anti-mouse IgG proved an equivalent response signal of the HBP-based sensor and the glass-based sensor. Therefore the HBP-based WIOS represents a viable low-cost alternative to glass devices for label-free detection with very high sensitivity (a few ppb).

9 CONCLUSIONS

9.1 SUMMARY OF THE RESULTS

In the course of this thesis, UV-curable acrylated hyperbranched polymer nanocomposites were investigated in terms of suspension rheology, polymerization kinetics, shrinkage and internal stress, and their application for nanostructured optical devices. Two different processing routes (mixing with nanoparticles *versus* sol-gel processing with a liquid precursor), leading to different composite microstructures, were explored. Particular attention was paid to the influence of material variables, such as particle surface chemistry and concentration, and to process parameters, such as UV intensity and pressure.

Solvent-assisted mixing of the hyperbranched polymer with a SiO₂ nanopowder produced true nanocomposites, in which nanoparticles of 13 nm diameter (Highlink composites, HL) were monodispersed in the matrix. With the same method also composites containing agglomerates (Aerosil composites, AS), with a broad size distribution up to the micrometer range, were obtained. The *in situ* sol-gel route produced

a composite with a network-like silica phase, forming a very homogeneous structure at the nanometer scale. With the sol-gel route, the viscosity increase (which typically compromises nanocomposite processing) was overcome, since the low-viscosity precursor reduced the overall viscosity of the composite.

By contrast, the high specific surface area of the particulate composites (HL and AS) led to huge increases in the viscosity of the composite material, far beyond the prediction of classic models for concentrated suspensions of hard spheres. This phenomenon was attributed to a polymer layer immobilized on the particle surface. The existence of such a layer was confirmed by a liquid-to-solid transition that was visible in three different rheological aspects, i.e., in the $\tan(\delta)$, in the activation energy as well as in the yield stress behavior. The liquid-to-solid transition occurred in the range of 5-10 vol% for the HL and in the range of 20-25% for AS composites. The thickness of the immobilized layer was calculated to be around 7.5 nm on the HL particles and between 2 and 5 nm on the AS particles.

The existence of an immobilized HBP layer around the particles was also investigated via calorimetry in terms of heat capacity changes at the glass transition. By this method, the immobilized layer thickness was calculated to be just below 2 nm. In the case of the HL suspensions, untreated silica interacted via H-bonding with the HBP matrix, thereby partially immobilizing the first HBP molecular layer around the particles. For the AS suspensions, the immobilized layer corresponded roughly to the length of the methacrylsilane molecules used for the surface treatment.

A new model that included the confined polymer layer at the particle surface was developed. It predicted an exponential increase of the viscosity as a function of filler fraction. For the first time, the relevance of exponential scaling for HBP nanocomposite suspensions was demonstrated. The model is specifically for concentrated suspensions of particles with a shell of crosslinked molecules that are strongly bonded to the particle surface, so that they stay attached and show elastomer type deformation when the suspensions is sheared.

The photo-conversion behavior of all composites was analyzed using an autocatalytic model. With this model the influence of the composition and the UV intensity on the photo-polymerization behavior could be reduced to one single parameter, i.e., the rate constant. The reaction rate and ultimate conversion were found to be lower for the particulate composites with respect to the pure polymer, the reason for this being the

early gelation due to increased viscosity. The photo-polymerization of the sol-gel hybrids showed a higher conversion rate and ultimate conversion at low precursor level, due to the increased mobility of the reacting species in the low-viscosity mixture. At high precursor level, the conversion rate was considerably slowed down, and the ultimate conversion became intensity-dependent. This observation was attributed to an over-dilution of the HBP and possibly to evaporation effects.

A time-intensity superposition model was elaborated and tested with the HBP and the nanocomposites. The shift factors showed power-law dependence on the UV intensity with exponents equal to 0.7, independent of the SiO₂ content. It was demonstrated that this value corresponded to that of the power-law exponent of the intensity-dependence of the reaction rate (0.6-0.8). The present work also demonstrated that the radiation dose equivalence principle was not applicable for the photo-polymerization of compounds, in which bimolecular or primary radical termination was predominant.

Photo-rheological experiments allowed for the measurement of the shear modulus G^* and the occurrence of gelation from $\tan(\delta)$. The results of photo-calorimetric and photo-rheological studies were analyzed in the form of time-intensity-transformation diagrams, which clearly revealed a markedly different influence of the UV intensity on conversion and gelation. Curing at low UV intensity shifted the point of gelation to higher conversions. Hence, low UV intensities delayed the formation of a rigid network and prolonged the existence of microgels, during which conversion proceeded in a macroscopically liquid material, so that no shrinkage stress was built up. This delay in macroscopic gelation was the main factor for the low-stress behavior of HBP.

In the case of particulate composites, a 33% shrinkage reduction to 3% linear shrinkage was achieved with 20 vol% filler loading combined with an intensity increase from 12 to 50 mW/cm². By contrast, the internal stress linearly increased with the filler loading from 1.5 MPa for the pure HBP to 5 MPa for 20 vol% SiO₂, which was attributed to the increased stiffness of the composite material. The intensity did not influence the internal stress level. Nevertheless, the stress was a factor of 2 to 3 lower than in standard non-filled acrylic resins.

Microscopic surface wrinkling phenomena, as the result of stress relaxation, were not observed whatever the polymerization condition, such as gas atmosphere and coating thickness. The surface roughness was on a nanometer scale and only marginally dependent on the UV intensity, if polymerization was performed first in air and then in an

inert gas atmosphere. Using this two-step polymerization protocol in combination with low UV intensities, it was possible to reduce the level of internal stress to 0.7 MPa for the pure HBP.

In the case of sol-gel composites, all thermo-mechanically relevant properties were improved with respect to the pure HBP. At 20 vol% silica fraction, for example, the stiffness was increased by a factor of 3.5, the glass transition temperature was increased by 63°C, and the coefficient of thermal expansion was reduced by 45%. In all cases, the improvement was larger than for the particulate composites. This result suggests that the 3-dimensional inorganic network was able to immobilize the surrounding polymer in a more efficient way than the discrete particles. Moreover, the internal stress of the sol-gel composites at 20 vol% silica fraction was measured to be half of the one of their particulate counterparts.

Nano-sized gratings with a period of 360 nm and a step height of 12 nm were produced from the UV-curable acrylated HBP nanocomposites and sol-gel hybrids with up to 25 vol% silica by nanoimprint lithography in a rapid, low-pressure process using a glass master. A pressure as low as 1 bar and short process time of 3 s were sufficient to imprint a stable grating into the high-viscosity particulate composite material. The obtained gratings displayed a shape fidelity in terms of grating period better than 98%. Despite polymerization shrinkage, the step height remained constant until gelation, due to the viscous flow of the material under the applied pressure. After gelation, the step height was reduced over time until full conversion was achieved. The lateral dimensions of the grating expanded as a result of relaxation of the stress that built up after gelation. The expansion effect increased with the amount of particulate filler in the HBP up to 33% expansion for 20 vol% SiO₂, which was correlated with the increased level of internal stress in the nanocomposites. For the sol-gel composites, the expansion was 31% independent of the silica fraction, a result of a constant internal stress for these composites in the investigated silica fraction range. Pressure and UV light intensity did not influence the grating dimensions, provided that the maximum acrylate conversion was achieved. The surface quality of the grating was not compromised by the presence of the silica particles, due to the exudation of a surface layer rich in HBP resin.

The functionality of the nanogratings for light coupling was tested by incorporating them a wavelength-interrogated optical sensor. The laser coupling quality of this WIOS device, based on HBP gratings coated with a high refractive index TiO₂ layer, was found to

be the same as that of a standard glass-based WIOS. The presence of silica particles reduced the signal strength, due to propagation loss resulting from residual process porosity. Immunoassay tests with anti-mouse immunoglobulin type G (IgG) using a mouse IgG functionalized device proved an equivalent response signal of the HBP-based sensor and the glass-based sensor, with a detection limit in the ppb range.

9.2 MAIN ACHIEVEMENTS

The present work improved the understanding of the process-structure-property relations in UV-curable HBP nanocomposites. The results allowed to generate new materials with a unique combination of properties (improved thermo-mechanical properties, reduced shrinkage and internal stresses as low as 1 MPa).

Two new scaling relations were established to predict the behavior of nanocomposite suspensions during photo-polymerization and during shear deformation. Firstly, a time-intensity superposition principle was demonstrated with power-law dependence of the shift factor on the intensity, which invalidated the radiation dose equivalence principle for those materials. Secondly, exponential scaling of the viscosity with the filler fraction was found and attributed to an immobilized layer of crosslinked polymer on the surface of the particles.

The goal of this thesis was also to apply low-stress UV-curable hyperbranched polymer nanocomposites to the production of dimensionally stable, high-precision nanostructures. A proof of concept was demonstrated by integrating the produced nanogratings into optical sensors for the label-free detection of biomolecules. The novel polymer-based sensors showed excellent performance, with a sensitivity in the ppb range, equivalent to that of the standard ultrasensitive glass-based sensor.

The cost reduction achieved by the HBP-based material with respect to glass-based device nanostructures should be considerable if time, material cost, and reduced master wear due to low pressure imprinting, are considered. In conclusion, the HBP-based optical sensor represents a viable low-cost alternative to glass-based devices.

9.3 OUTLOOK

The reason for the very high viscosity of the nanocomposites was identified to be the large volume fraction of polymer immobilized on the inorganic particles. The influence of

the surface chemistry on this volume fraction was already explored by utilizing powders of different surface chemistry and dispersion. However, the experimental model should be further validated by identifying the respective influences of interface interactions and dispersion.

The sol-gel hybrids proved to be a valuable alternative to the particulate nanocomposites for the production of nanostructures. However, the condensation step was not investigated in terms of kinetics and activation energy, and needs further optimization for evaporation control. Mass spectrometry could give valuable information about the evaporation kinetics and the evaporating products.

The production of polymer-based WIOS includes the deposition of a high refractive index layer. This production step is still expensive and time-consuming, and it leads to internal stresses in the materials. This processing step may be avoided by the use of composite formulation with a through-thickness gradient in particle density, leading to a gradient in optical and mechanical properties.

Even though the polymer-based WIOS device showed the same performance in the detection of antibodies at different concentrations as the glass-based sensor, the ultimate detection limit of the devices has not yet been quantitatively determined. According to tests performed with the standard glass-based sensors, values in the ppb range are expected. Furthermore, the nanostructure of the WIOS device was reproduced with the HBP composites with very high replication fidelity. The WIOS structure is, however, rather shallow. However, high aspect ratio structures are required for example for the production of stencils⁴²⁴ or photonic integrated circuits⁴²⁵. It would thus be interesting to see which aspect ratios can be achieved with the HBP composites and using nanoimprint lithography.

APPENDIX A – LIST OF SYMBOLS AND ACRONYMS

SYMBOLS

symbol	unit	description
a	m	thickness of immobilized polymer layer
a_0	–	parameter
a_1	–	time-intensity-shift factor
a_{MH}	–	Mark Houwink exponent
A	–	parameter
$[AG]$	mol/g	acrylate group concentration
b	–	intensity exponent of the time-intensity-shift factor
B_1	–	constant (1.062)
c	–	parameter
$C_{p,HBP}$	J/(K·g)	reversing heat capacity of the HBP phase
$\Delta C_{p,HBP}$	J/(K·g)	reversing heat capacity change at T_g of the HBP fraction
$\Delta C_{p,HBP}^0$	J/(K·g)	reversing heat capacity change at T_g of the pure HBP
$C_{p,s}$	J/(K·g)	reversing heat capacity of the sample
$\Delta C_{p,s}$	J/(K·g)	reversing heat capacity change at T_g of the sample
C_{p,SiO_2}	J/(K·g)	reversing heat capacity of the SiO ₂ phase
d	m	mean free space between nearest neighbor particles
D_B	– or %	degree of branching
e	–	Euler's constant (≈ 2.718)
E	Pa	tensile modulus of the composite
E^*	Pa	complex tensile modulus
E'	Pa	tensile storage modulus
E''	Pa	tensile loss modulus
E_A	J/mol	activation energy
E_c	Pa	tensile modulus of the coating
E_f	Pa	tensile modulus of the filler
E_m	Pa	tensile modulus of the matrix
E_s	Pa	tensile modulus of the substrate
f	–	parameter
g	m	deflection

G^*	Pa	complex shear modulus
G'	Pa	elastic shear modulus
G''	Pa	viscous shear modulus
G_m	Pa	shear modulus of the matrix
G_0^*	Pa	limiting shear modulus as $\omega \rightarrow 0$
$G_{0.1}^*$	Pa	shear modulus at $\omega = 0.1$ rad/s
h_c	m	thickness of the coating
Δh_c	m	difference in coating thickness between maxima and minima
$h_{c,fi}$	m	final coating thickness
h_s	m	thickness of the substrate
ΔH_{AG}	J/mol	energy of acrylate double bond
H_{HBP}	J/g	heat of polymerization of the HBP fraction
ΔH_r	J/(K·g)	enthalpy relaxation strength
H_{total}	J/g	total heat of polymerization
$\langle H_1 \rangle$	m	distance between nearest neighbor particle cores
$H_{100\%}$	J/g	theoretical heat for 100% conversion
i	–	parameter
I	W/m ²	light intensity
I_0	W/m ²	incident light intensity
k	s ⁻¹	reaction rate
k_B	J/K	Boltzmann constant ($1,380650424 \cdot 10^{-23}$)
k_0	–	parameter
K	–	parameter
K_1	–	constant (0.554)
K_c	Pa	bulk modulus of the composite
K_f	Pa	bulk modulus of the filler
K_m	Pa	bulk modulus of the matrix
L	m	distance between bearings
m	–	autocatalytic exponent
m_{HBP}	g	mass of the HBP
m_s	g	mass of the sample
m_{SiO_2}	g	mass of the silica
M	g/mol	molecular weight
M_n	g/mol	number average molecular weight

M_w	g/mol	mass average molecular weight
n	–	reaction order
n_c	–	refractive index of the coating
n_m	–	refractive index of the material
N	–	number of crosslinks
N_D	–	number of dendritic units
N_L	–	number of linear units
N_{MM}	–	number of maxima and minima of the interferometer curve
N_T	–	number of terminal units
p	Pa	pressure
Pe	–	Péclet number
Pe_{crit}	–	critical Péclet number
$[PI]$	mol/L	photoinitiator concentration
q	–	ratio of coating and substrate thickness (h_c/h_s)
Q_i	–	condensation level of the silica atom
r	m	radius of curvature or radius of the particle
R_a	m	average surface roughness
S	m ² /g	specific surface
S_{comp}	– or %	linear shrinkage of the composite
S_{HBP}	– or %	linear shrinkage of the HBP
S_L	– or %	linear shrinkage
S_V	– or %	volumetric shrinkage
t	s	time
T	°C or K	temperature
T_g	°C or K	glass transition temperature
T_r	–	transmittance coefficient
u	–	ratio of coating and substrate moduli (E_c/E_s)
V	m ³	volume
V_f	–	volume fraction of the filler
V_m	–	volume fraction of the matrix
x	–	parameter
z	m	depth
α	– or %	conversion
α_{comp}	– or %	conversion of the composite

α_{HBP}	– or %	conversion of the HBP
α_{max}	– or %	maximum conversion
α'_{max}	–	maximum conversion rate
α_r	–	relative conversion ($\alpha_r / \alpha_{\text{max}}$)
β	–	intensity exponent of the rate constant
$\dot{\gamma}_{\text{crit}}$	s^{-1}	critical shear rate
γ_0	– or %	strain amplitude
Γ	–	parameter
δ	rad	phase angle between loss and storage moduli
ε_t	$\text{L}/(\text{mol}\cdot\text{m})$	molar extinction coefficient
η	$\text{Pa}\cdot\text{s}$	suspension viscosity
$[\eta]$	–	intrinsic viscosity
η^*	$\text{Pa}\cdot\text{s}$	complex viscosity
η_{HBP}	$\text{Pa}\cdot\text{s}$	viscosity of the HBP
η_{m}	$\text{Pa}\cdot\text{s}$	viscosity of the matrix
η_r	$\text{Pa}\cdot\text{s}$	relative viscosity (η/η_{HBP})
η_{∞}^*	$\text{Pa}\cdot\text{s}$	limiting viscosity as $\omega \rightarrow \infty$
η_{100}^*	$\text{Pa}\cdot\text{s}$	viscosity at $\omega = 100 \text{ rad/s}$
θ_{in}	rad	input angle
θ_{out}	rad	output angle
κ	–	parameter
κ_{m}	–	extinction index of the material
λ	m	wavelength
λ_r	m	resonant wavelength
ν	–	Poisson ratio
π	–	constant (≈ 3.14)
ρ	g/m^3	density
σ_i	N/m	internal stress
τ	Pa	stress
ν	–	parameter
ϕ	vol%	filler fraction
ϕ^*	vol%	maximum packing fraction
ϕ_{agg}	vol%	silica fraction in the agglomerates
ϕ_c	vol%	geometric percolation threshold

ϕ_{cp}	vol%	maximum packing fraction for close-packed spheres
ϕ_{eff}	vol%	effective filler fraction
ϕ_{imm}	vol%	immobilized polymer fraction
ϕ_{rcp}	vol%	maximum packing fraction for random close-packed spheres
ϕ_{th}	vol%	theoretical filler fraction in sol-gel composites
χ_c	K ⁻¹	coefficient of thermal expansion of the composite
χ_f	K ⁻¹	coefficient of thermal expansion of the filler
χ_m	K ⁻¹	coefficient of thermal expansion of the matrix
ω	rad/s	angular frequency
ψ	–	parameter
Ω	– or %	silica condensation state

ACRONYMS

AS	Aerosil
AFM	atomic force microscopy
BSA	bovine serum albumin
CTE	coefficient of thermal expansion
DPHA	dipentaerythritol hexaacrylate
DMA	dynamic mechanical analysis
DSC	differential scanning calorimetry
DP	degree of polymerization
F	function
HBP	hyperbranched polymer
HL	Highlink
IgG	immunoglobulin type G
MDSC	modulated differential scanning calorimetry
MEMO	methacryloxy(propyl)trimethoxysilane
NIL	nanoimprint lithography
NMR	nuclear magnetic resonance
PBS	phosphate buffered saline
PI	photoinitiator
TEOS	tetraethyl orthosilicate
TEM	transmission electron microscopy

TGA	thermo-gravimetric analysis
TMA	thermo-mechanical analysis
UV	ultra violet

APPENDIX B – MDSC PROTOCOL

The optimum experimental conditions in terms of scan rate, modulation amplitude and period were established with the pure HBP and with a 25% HL suspension. The principle of the modulated DSC is to superpose an oscillating sinusoidal temperature variation to the conventional DSC heating ramp. Theoretical description of this technique can be found elsewhere.^{426,427} The advantages of the MDSC are a high sensitivity to small transitions and the measurement of the heat capacity, which can be separated into reversing and non-reversing phenomena in one single measurement. Numerical simulations demonstrated that the choice of modulation parameters, such as heating/cooling rate and the oscillation period, is critical to obtain exploitable results. The glass transition temperature T_g was found to depend on the modulation period and cooling rate.⁴²⁸⁻⁴³¹ The step in the heat capacity at T_g , which corresponds to the glass relaxation, strongly depends on the modulation period, but less on the scan rate.⁴³² Therefore, long periods and slow scan rates are advised to obtain good estimates of the heat capacity step at T_g and the enthalpic relaxation.

The study in Chapter 5 focused on the reversing heat capacity curves $C_{p,s}$. Slow scan rates ($< 5\text{ }^{\circ}\text{C}/\text{min}$) were used for minimum baseline steepness and to obtain high oscillation amplitudes. According to TA instrument, a minimum of 4 to 5 complete oscillations must take place during the transition at T_g . Figure B-1 shows the reversing heat capacity curves of HBP and the composite containing 25% HL, obtained with a period of 100 s, an amplitude of $\pm 1^{\circ}\text{C}$ and scan rates of 1, 2 and $5\text{ }^{\circ}\text{C}/\text{min}$. At higher scan rate, the curves were shifted towards higher temperatures and the reversing heat capacity steps $\Delta C_{p,s}$ at T_g decreased. The same trend was observed in other studies.^{431,432} Figure B-2 shows the scans for the same materials obtained at a scan rate of $1\text{ }^{\circ}\text{C}/\text{min}$, amplitude of $\pm 1^{\circ}\text{C}$ and oscillation periods between 60 and 120 s. With increasing oscillation period, the reversing heat capacity curves were shifted towards lower temperature and the $\Delta C_{p,s}$ at T_g strongly increased. This trend was also observed in other studies.⁴²⁸⁻⁴³² The oscillation amplitude was varied between ± 0.5 and $\pm 1^{\circ}\text{C}$, and did not lead to significantly different results.

The curves for the HL composites in Figure B-1 and B-2 were not normalized with respect to the HBP mass, because only qualitative information was required.

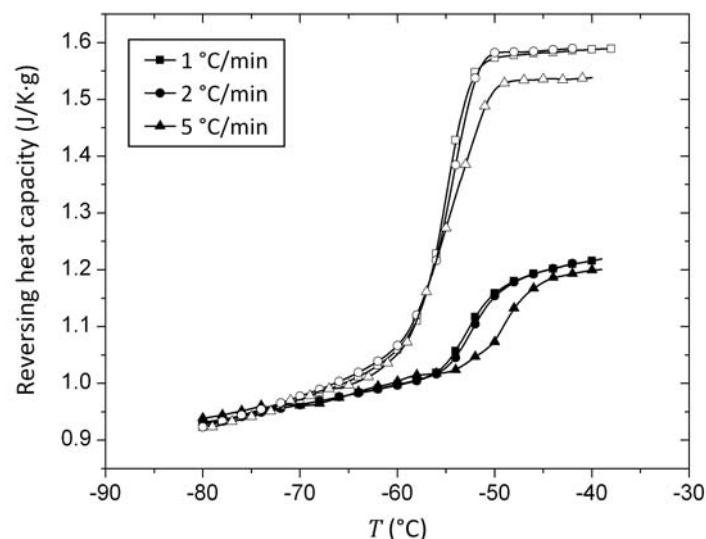


Figure B-1 Effect of heating rate on the reversing heat capacity of pure HBP suspensions (empty symbols) and on HL composites with 25% filler fraction (full symbols).

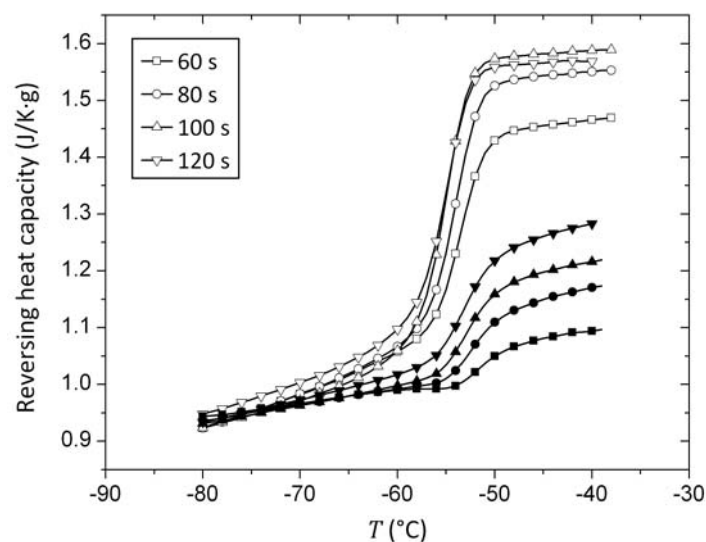


Figure B-2 Effect of modulation period on the reversing heat capacity of pure HBP suspensions (empty symbols) and on HL composites with 25% filler fraction (full symbols).

If parameters were chosen to allow coexistence of heating and cooling ramps (i.e., derivative of the modulated temperature as a function of time could be negative), no significantly different results were obtained than if only positive derivatives were chosen (“heat only” option on DSC adjusted the parameters automatically for this purpose). Based on this preliminary study, the following parameters were chosen:

- Scan rate: 1 °C/min. This ensured 7 complete oscillations to take place during the glass transition
- Oscillation period: 120 s
- Oscillation amplitude of $\pm 1^\circ\text{C}$

The suspensions were in an equilibrium state at room temperature and before the measurement they had to be cooled down to -90°C . According to McKenna *et al.* it is important that the cooling rate above the glass transition is smaller or equal to the heating rate to obtain good estimates of the enthalpic relaxation (from the integration of the non-reversing heat capacity peak)^{433,434}. Therefore, the cooling rate was set equal to the heating rate ($1^{\circ}\text{C}/\text{min}$). Annealing the material for 3 h did not significantly increase the enthalpic relaxation peak intensity, hence, the subsequent measurements were performed without annealing.

REFERENCES

1. M. Wiki, R.E. Kunz, *Wavelength-interrogated optical sensor for biochemical applications*. Opt Lett **2000**, 25, 463-465.
2. X. Cheng, D.W. Li, L.J. Guo, *A hybrid mask-mould lithography scheme and its application in nanoscale organic thin film transistors*. Nanotechnology **2006**, 17, 927-932.
3. G. Suarez, Y.H. Jin, J. Auerswald, S. Berchtold, H.F. Knapp, J.M. Diserens, Y. Leterrier, J.-A.E. Månson, G. Voirin, *Lab-on-a-chip for multiplexed biosensing of residual antibiotics in milk*. Lab Chip **2009**, 9, 1625-1630.
4. O. Kornilov, R. Wilcox, O. Gessner, *Nanograting-based compact vacuum ultraviolet spectrometer and beam profiler for in situ characterization of high-order harmonic generation light sources*. Rev Sci Instrum **2010**, 81, 063109.
5. M. Csete, A. Kohazi-Kis, V. Megyesi, K. Osvay, Z. Bor, M. Pietralla, O. Marti, *Coupled surface plasmon resonance on bimetallic films covered by sub-micrometer polymer gratings*. Org Electron **2007**, 8, 148-160.
6. A. Kocabas, A. Aydinli, *Polymeric waveguide Bragg grating filter using soft lithography*. Opt Express **2006**, 14, 10228-10232.
7. Z.N. Bao, J.A. Rogers, H.E. Katz, *Printable organic and polymeric semiconducting materials and devices*. J Mater Chem **1999**, 9, 1895-1904.
8. M.D. Austin, H.X. Ge, W. Wu, M.T. Li, Z.N. Yu, D. Wasserman, S.A. Lyon, S.Y. Chou, *Fabrication of 5 nm linewidth and 14 nm pitch features by nanoimprint lithography*. Appl Phys Lett **2004**, 84, 5299-5301.
9. S.Y. Chou, P.R. Krauss, P.J. Renstrom, *Nanoimprint lithography*. J Vac Sci Technol B **1996**, 14, 4129-4133.
10. Y. Ding, H.W. Ro, T.A. Germer, J.F. Douglas, B.C. Okerberg, A. Karim, C.L. Soles, *Relaxation behavior of polymer structures fabricated by nanoimprint lithography*. ACS Nano **2007**, 1, 84-92.
11. E. Buck, K. Petersen, M. Hund, G. Krausch, D. Johannsmann, *Decay kinetics of nanoscale corrugation gratings on polymer surface: Evidence for polymer flow below the glass temperature*. Macromolecules **2004**, 37, 8647-8652.
12. C.N. Bowman, N.A. Peppas, *Coupling of kinetics and volume relaxation during polymerizations of multiacrylates and multimethacrylates*. Macromolecules **1991**, 24, 1914-1920.
13. J. Lange, S. Toll, J.-A.E. Månson, A. Hult, *Residual-stress buildup in thermoset films cured above their ultimate glass-transition temperature*. Polymer **1995**, 36, 3135-3141.
14. Y. Hirai, S. Yoshida, N. Takagi, *47th International conference on electron ion and photon beam technology and nanofabrication (EIPBN)*, Tampa, FL, USA, **2003**, 2765-2770.
15. M. Hamdorf, D. Johannsmann, *Surface-rheological measurements on glass forming polymers based on the surface tension driven decay of imprinted corrugation gratings*. J Chem Phys **2000**, 112, 4262-4270.
16. L.E. Schmidt, Y. Leterrier, D. Schmah, J.-A.E. Månson, D. James, E. Gustavsson, L.S. Svensson, *Conversion analysis of acrylated hyperbranched polymers UV-cured below their ultimate glass transition temperature*. J Appl Polym Sci **2007**, 104, 2366-2376.
17. E. Andrzejewska, *Photopolymerization kinetics of multifunctional monomers*. Prog Poly Sci **2001**, 26, 605-665.
18. J.H. Choi, S.U. Jung, D.G. Choi, J.H. Jeong, E.S. Lee, *IEEE International symposium on advanced gate stack technology (ISAGST)*, Austin, TX, USA, **2008**, 195-201.
19. J. Lee, K. Choi, G. Kim, S. Lee, *The UV-nanoimprint lithography equipment with multi-head imprinting unit for sub-50 nm half-pitch patterns*. Microelectron Eng **2007**, 84, 963-966.
20. M. Atai, D.C. Watts, *A new kinetic model for the photopolymerization shrinkage-strain of dental composites and resin-monomers*. Dent Mater **2006**, 22, 785-791.
21. C.J.G. Plummer, L. Garamszegi, Y. Leterrier, M. Rodlert, J.-A.E. Månson, *Hyperbranched polymer layered silicate nanocomposites*. Chem Mater **2002**, 14, 486-488.
22. F. Hussain, M. Hojjati, M. Okamoto, R.E. Gorga, *Review article: Polymer-matrix nanocomposites, processing, manufacturing, and application: An overview*. J Compos Mater **2006**, 40, 1511-1575.

23. J.R. Condon, J.L. Ferracane, *In vitro wear of composite with varied cure, filler level, and filler treatment*. J Dent Res **1997**, 76, 1405-1411.
24. M.L. Sham, J.K. Kim, *Evolution of residual stresses in modified epoxy resins for electronic packaging applications*. Compos Part A-Appl Sci **2004**, 35, 537-546.
25. M. Rodlert, C.J.G. Plummer, L. Garamszegi, Y. Leterrier, H.J.M. Grunbauer, J.-A.E. Månson, *Hyperbranched polymer/montmorillonite clay nanocomposites*. Polymer **2004**, 45, 949-960.
26. J.R. Condon, J.L. Ferracane, *Assessing the effect of composite formulation on polymerization stress*. J Am Dent Assoc **2000**, 131, 497-503.
27. S. Ishizuka, M. Nakao, S. Mashiko, J. Mizuno, S. Shoji, *Fabrication of uniform gratings on composite semiconductors using UV nanoimprint lithography*. J Photopolym Sci Tech **2009**, 22, 213-217.
28. S.F. Filocamo. In *Dekker encyclopedia of nanoscience and nanotechnology, second edition*. C.I. Contescu, K. Putyera, Eds., **2009**.
29. K. Sogo, M. Nakajima, Y. Hirai, *Fabrication of anti-reflective structure by nano casting method*. J Photopolym Sci Tech **2006**, 19, 647-651.
30. M. Wang, W.Z. Wang, T.X. Liu, W.D. Zhang, *Melt rheological properties of nylon 6/multi-walled carbon nanotube composites*. Compos Sci Technol **2008**, 68, 2498-2502.
31. J.J. Cai, R. Salovey, *Model filled rubber. II. Particle composition dependence of suspension rheology*. J Polym Sci Pol Phys **1999**, 37, 815-824.
32. M. Rodlert, C.J.G. Plummer, Y. Leterrier, J.-A.E. Månson, H.J.M. Grunbauer, *Rheological behavior of hyperbranched polymer/montmorillonite clay nanocomposites*. J Rheol **2004**, 48, 1049-1065.
33. M.A. Osman, A. Atallah, *Effect of the particle size on the viscoelastic properties of filled polyethylene*. Polymer **2006**, 47, 2357-2368.
34. E. Amerio, M. Sangermano, G. Malucelli, A. Priola, G. Rizza, *Preparation and characterization of hyperbranched polymer/silica hybrid nanocoatings by dual-curing process*. Macromol Mater Eng **2006**, 291, 1287-1292.
35. M. Sangermano, E. Amerio, P. Epicoco, A. Priola, G. Rizza, G. Malucelli, *Preparation and characterization of hybrid nanocomposite coatings by cationic UV-curing and the sol-gel process of a vinyl ether based system*. Macromol Mater Eng **2007**, 292, 634-640.
36. F.S. Li, S.X. Zhou, L.M. Wu, *Effects of preparation method on microstructure and properties of UV-curable nanocomposite coatings containing silica*. J Appl Polym Sci **2005**, 98, 1119-1124.
37. P. Hajji, L. David, J.F. Gerard, J.P. Pascault, G. Vigier, *Synthesis, structure, and morphology of polymer-silica hybrid nanocomposites based on hydroxyethyl methacrylate*. J Polym Sci Pol Phys **1999**, 37, 3172-3187.
38. C.J.G. Plummer, A. Luciani, T.Q. Nguyen, L. Garamszegi, M. Rodlert, J.-A.E. Månson, *Rheological characteristics of hyperbranched polyesters*. Polym Bull **2002**, 49, 77-84.
39. J.M.J. Frechet, C.J. Hawker, I. Gitsov, J.W. Leon, *Dendrimers and hyperbranched polymers: Two families of three-dimensional macromolecules with similar but clearly distinct properties*. J Macromol Sci A **1996**, A33, 1399-1425.
40. Y.H. Kim, *Hyperbranched polymers 10 years after*. J Polym Sci Pol Chem **1998**, 36, 1685-1698.
41. B.I. Voit, *Dendritic polymers - from aesthetic macromolecules to commercially interesting materials*. Acta Polym **1995**, 46, 87-99.
42. A.W. Bosman, H.M. Janssen, E.W. Meijer, *About dendrimers: Structure, physical properties, and applications*. Chem Rev **1999**, 99, 1665-1688.
43. J.E. Klee, C. Schneider, D. Holter, A. Burgath, H. Frey, R. Mulhaupt, *Hyperbranched polyesters and their application in dental composites: Monomers for low shrinking composites*. Polym Advan Technol **2001**, 12, 346-354.
44. L.E. Schmidt, D. Schmah, Y. Leterrier, J.-A.E. Månson, *Time-intensity transformation and internal stress in UV-curable hyperbranched acrylates*. Rheol Acta **2007**, 46, 693-701.
45. R. Mezzenga, L. Boogh, J.-A.E. Månson, *A review of dendritic hyperbranched polymer as modifiers in epoxy composites*. Compos Sci Technol **2001**, 61, 787-795.
46. L.E. Schmidt, Thesis, Ecole polytechnique fédérale de Lausanne **2006**.
47. K. Cottier, M. Wiki, G. Voirin, H. Gao, R.E. Kunz, *Label-free highly sensitive detection of (small) molecules by wavelength interrogation of integrated optical chips*. Sensor Actuat A-Chem **2003**, 91, 241-251.

48. H. Lei, L.F. Francis, W.W. Gerberich, L.E. Scriven, *Stress development in drying coatings after solidification*. Aiche J **2002**, 48, 437-451.
49. J. Lange, S. Toll, J.-A.E. Månson, A. Hult, *Residual stress build-up in thermoset films cured below their ultimate glass transition temperature*. Polymer **1997**, 38, 809-815.
50. A.R. Plepys, R.J. Farris, *Cure stresses in 3-dimensionally constrained epoxy-resins*. Abstr Pap Am Chem S **1988**, 196, 77-IEC.
51. A.R. Plepys, R.J. Farris, *Evolution of residual-stresses in 3-dimensionally constrained epoxy-resins*. Polymer **1990**, 31, 1932-1936.
52. L. Lu, J.Y.H. Fuh, A.Y.C. Nee, E.T. Kang, T. Miyazawa, C.M. Cheah, *Origin of shrinkage, distortion and fracture of photopolymerized material*. Mater Res Bull **1995**, 30, 1561-1569.
53. L.F. Francis, A.V. McCormick, D.M. Vaessen, J.A. Payne, *Development and measurement of stress in polymer coatings*. J Mater Sci **2002**, 37, 4897-4911.
54. D. Alster, A.J. Feilzer, A.J. de Gee, C.L. Davidson, *Polymerization contraction stress in thin resin composite layers as a function of layer thickness*. Dent Mater **1997**, 13, 146-150.
55. M.P. Patel, M. Braden, K.W.M. Davy, *Polymerization shrinkage of methacrylate esters*. Biomaterials **1987**, 8, 53-56.
56. C. Li, K. Potter, M.R. Wisnom, G. Stringer, *In-situ measurement of chemical shrinkage of MY750 epoxy resin by a novel gravimetric method*. Compos Sci Technol **2004**, 64, 55-64.
57. R. Feng, R.J. Farris, *Influence of processing conditions on the thermal and mechanical properties of SU8 negative photoresist coatings*. J Micromech Microeng **2003**, 13, 80-88.
58. K.M. Choi, J.A. Rogers, *A photocurable poly(dimethylsiloxane) chemistry designed for soft lithographic molding and printing in the nanometer regime*. J Am Chem Soc **2003**, 125, 4060-4061.
59. M. Dewaele, D. Truffier-Boutry, J. Devaux, G. Leloup, *Volume contraction in photocured dental resins: The shrinkage-conversion relationship revisited*. Dent Mater **2006**, 22, 359-365.
60. J. Jakubiak, L.A. Linden, *Contraction (shrinkage) in polymerization*. Polimery **2001**, 46, 522-528.
61. F.C. Calheiros, R.R. Braga, Y. Kawano, R.Y. Ballester, *Relationship between contraction stress and degree of conversion in restorative composites*. Dent Mater **2004**, 20, 939-946.
62. D.C. Watts, *Reaction kinetics and mechanics in photo-polymerised networks*. Dent Mater **2005**, 21, 27-35.
63. J. Deboer, R.J. Visser, G.P. Melis, *Time-resolved determination of volume shrinkage and refractive-index change of thin polymer-films during photopolymerization*. Polymer **1992**, 33, 1123-1126.
64. M. Latorre-Garcia, C. Alvarez-Gayosso, F. Barcelo-Santana, R. Vera-Graziano, *Study of shrinkage-strain and contraction rates of commercial and experimental compomers*. Dent Mater **2006**, 22, 1063-1070.
65. S.R. Turner, B.I. Voit, T.H. Mourey, *All-aromatic hyperbranched polyesters with phenol and acetate end-groups - synthesis and characterization*. Macromolecules **1993**, 26, 4617-4623.
66. H. Ishida, D.J. Allen, *Physical and mechanical characterization of near-zero shrinkage polybenzoxazines*. J Polym Sci Pol Phys **1996**, 34, 1019-1030.
67. M. Sangermano, R.A. Ortiz, B.A.P. Urbina, L.B. Duarte, A.E.G. Valdez, R.G. Santos, *Synthesis of an epoxy functionalized spiroorthocarbonate used as low shrinkage additive in cationic UV curing of an epoxy resin*. Eur Polym J **2008**, 44, 1046-1052.
68. M.H. Chen, C.R. Chen, S.H. Hsu, S.P. Sun, W.F. Su, *Low shrinkage light curable nanocomposite for dental restorative material*. Dent Mater **2006**, 22, 138-145.
69. D. Nagai, M. Nishida, T. Nagasawa, B. Ochiai, K. Miyazaki, T. Endo, *Non-shrinking networked materials from the cross-linking copolymerization of spiroorthocarbonate with bifunctional oxetane*. Macromol Rapid Commun **2006**, 27, 921-925.
70. K.E. Atkins. In *Plastics additives: An A-Z reference*. Pritchard, Ed.; Chapman & Hall: London, **1998**.
71. T.F. Scott, A.D. Schneider, W.D. Cook, C.N. Bowman, *Photoinduced plasticity in cross-linked polymers*. Science **2005**, 308, 1615-1617.
72. J.L. Ferracane, J.C. Mitchem, *Relationship between composite contraction stress and leakage in class V cavities*. Am J Dent **2003**, 16, 239-243.

73. Y. Kinomoto, M. Torii, F. Takeshige, S. Ebisu, *Polymerization contraction stresses of resin-based composite restorations within beveled cavity preparations of Class I restorations*. Am J Dent **2003**, 16, 139.
74. A.J. Feilzer, A.J. Degee, C.L. Davidson, *Setting stress in composite resin in relation to configuration of the restoration*. J Dent Res **1987**, 66, 1636-1639.
75. J.R. Condon, J.L. Ferracane, *Reduced polymerization stress through non-bonded nanofiller particles*. Biomaterials **2002**, 23, 3807-3815.
76. Y. Eom, L. Boogh, V. Michaud, J.-A.E. Månson, *Internal stress control in epoxy resins and their composites by material and process tailoring*. Polym Compos **2002**, 23, 1044-1056.
77. B. Li, M. Liu, Q.F. Chen, *Low-stress ultra-thick SU-8 UV photolithography process for MEMS*. J Microlith Microfab **2005**, 4.
78. D.M. Vaessen, F.A. Ngantung, M.L.B. Palacio, L.F. Francis, A.V. McCormick, *Effect of lamp cycling on conversion and stress development in ultraviolet-cured acrylate coatings*. J Appl Polym Sci **2002**, 84, 2784-2793.
79. A.D. Neves, J.A.C. Discacciati, R.L. Orefice, M.I. Yoshida, *Influence of the power density on the kinetics of photopolymerization and properties of dental composites*. J Biomed Mater Res Part B Appl Biomater **2005**, 72B, 393-400.
80. N. Emami, K.J.M. Soderholm, *Influence of light-curing procedures and photo-initiator/co-initiator composition on the degree of conversion of light-curing resins*. J Mater Sci-Mater M **2005**, 16, 47-52.
81. M.F. Witzel, R.Y. Ballester, J.B.C. Meira, R.G. Lima, R.R. Braga, *Composite shrinkage stress as a function of specimen dimensions and compliance of the testing system*. Dent Mater **2007**, 23, 204-210.
82. G.A. Laughlin, J.L. Williams, J.D. Eick, *The influence of system compliance and sample geometry on composite polymerization shrinkage stress*. J Biomed Mater Res **2002**, 63, 671-678.
83. A. Plepys, M.S. Vratsanos, R.J. Farris, *Determination of residual-stresses using incremental linear elasticity*. Compos Struct **1994**, 27, 51-56.
84. H. Burrell, *High polymer theory of the wrinkling phenomenon*. Ind Eng Chem **1954**, 46, 2233-2237.
85. J.A. Payne, L.F. Francis, A.V. McCormick, *The effects of processing variables on stress development in ultraviolet-cured coatings*. J Appl Polym Sci **1997**, 66, 1267-1277.
86. A. Luciani, C.J.G. Plummer, R. Gensler, J.-A.E. Månson, *Surface pattern formation in UV-curable coatings*. J Coat Technol **2000**, 72, 161-163.
87. S.K. Basu, L.E. Scriven, L.F. Francis, A.V. McCormick, *Mechanism of wrinkle formation in curing coatings*. Prog Org Coat **2005**, 53, 1-16.
88. S.K. Basu, L.E. Scriven, L.F. Francis, A.V. McCormick, V.R. Reichert, *Wrinkling of epoxy powder coatings*. J Appl Polym Sci **2005**, 98, 116-129.
89. R. Huang, *Kinetic wrinkling of an elastic film on a viscoelastic substrate*. J Mech Phys Solids **2005**, 53, 63-89.
90. X.Y. Gong, D.R. Clarke, *On the measurement of strain in coatings formed on a wrinkled elastic substrate*. Oxid Met **1998**, 50, 355-376.
91. D. Breid, A.J. Crosby, *Surface wrinkling behavior of finite circular plates*. Soft Matter **2009**, 5, 425-431.
92. N. Bowden, S. Brittain, A.G. Evans, J.W. Hutchinson, G.M. Whitesides, *Spontaneous formation of ordered structures in thin films of metals supported on an elastomeric polymer*. Nature **1998**, 393, 146-149.
93. N. Bowden, W.T.S. Huck, K.E. Paul, G.M. Whitesides, *The controlled formation of ordered, sinusoidal structures by plasma oxidation of an elastomeric polymer*. Appl Phys Lett **1999**, 75, 2557-2559.
94. W.T.S. Huck, N. Bowden, P. Onck, T. Pardoen, J.W. Hutchinson, G.M. Whitesides, *Ordering of spontaneously formed buckles on planar surfaces*. Langmuir **2000**, 16, 3497-3501.
95. R. Schubert, F. Frost, M. Hinkefuss, R. Konieczny, B. Marquardt, R. Mehnert, M.R. Buchmeiser, *VUV-induced micro-folding of acrylate-based coatings 2. Characterization of surface properties*. Surf Coat Tech **2009**, 203, 3734-3740.
96. J.Y. Chung, T.Q. Chastek, M.J. Fasolka, H.W. Ro, C.M. Stafford, *Quantifying residual stress in nanoscale thin polymer films via surface wrinkling*. ACS Nano **2009**, 3, 844-852.

97. K. Efimenko, M. Rackaitis, E. Manias, A. Vaziri, L. Mahadevan, J. Genzer, *Nested self-similar wrinkling patterns in skins*. *Nat Mater* **2005**, *4*, 293-297.
98. K. Efimenko, J. Finlay, M.E. Callow, J.A. Callow, J. Genzer, *Development and testing of hierarchically wrinkled coatings for marine antifouling*. *ACS Appl Mater Interfac* **2009**, *1*, 1031-1040.
99. C. Jiang, S. Singamaneni, E. Merrick, V.V. Tsukruk, *Complex buckling instability patterns of nanomembranes with encapsulated gold nanoparticle arrays*. *Nano Lett* **2006**, *6*, 2254-2259.
100. K. Taguchi, S. Hirose, Y. Abe, *Photo-curing composite paint containing urushi (oriental lacquer), and wrinkled coating caused by phase separation*. *Prog Org Coat* **2007**, *58*, 290-295.
101. R.T. Pogue, L.V. Natarajan, S.A. Siwecki, V.P. Tondiglia, R.L. Sutherland, T.J. Bunning, *Monomer functionality effects in the anisotropic phase separation of liquid crystals*. *Polymer* **2000**, *41*, 733-741.
102. D.A. Tomalia, H. Baker, J. Dewald, M. Hall, G. Kallos, S. Martin, J. Roeck, J. Ryder, P. Smith, *A new class of polymers - starburst-dendritic macromolecules*. *Polym J* **1985**, *17*, 117-132.
103. E. Buhleier, W. Wehner, F. Vötle, *"Cascade"-and "nonskid-chain-like" syntheses of molecular cavity topologies*. *Synthesis* **1978**, 155-158.
104. D.A. Tomalia, H. Baker, J. Dewald, M. Hall, G. Kallos, S. Martin, J. Roeck, J. Ryder, P. Smith, *Dendritic macromolecules - synthesis of starburst dendrimers*. *Macromolecules* **1986**, *19*, 2466-2468.
105. G.R. Newkome, Z.Q. Yao, G.R. Baker, V.K. Gupta, *Cascade molecules - a new approach to micelles - a [27]-arborol*. *J Org Chem* **1985**, *50*, 2003-2004.
106. K.L. Wooley, C.J. Hawker, R. Lee, J.M.J. Frechet, *One-step synthesis of hyperbranched polyesters - molecular-weight control and chain-end functionalization*. *Polym J* **1994**, *26*, 187-197.
107. A. Sunder, J. Heinemann, H. Frey, *Controlling the growth of polymer trees: Concepts and perspectives for hyperbranched polymers*. *Chem-Eur J* **2000**, *6*, 2499-2506.
108. C.J. Hawker, R. Lee, J.M.J. Frechet, *One-step synthesis of hyperbranched dendritic polyesters*. *J Am Chem Soc* **1991**, *113*, 4583-4588.
109. D. Höltzer, A. Burgath, H. Frey, *Degree of branching in hyperbranched polymers*. *Acta Polym* **1997**, *48*, 30-35.
110. J.M.J. Frechet, *Functional polymers and dendrimers - reactivity, molecular architecture, and interfacial energy*. *Science* **1994**, *263*, 1710-1715.
111. C.J. Hawker, E.E. Malmstrom, C.W. Frank, J.P. Kampf, *Exact linear analogs of dendritic polyether macromolecules: Design, synthesis, and unique properties*. *J Am Chem Soc* **1997**, *119*, 9903-9904.
112. A. Luciani, C.J.G. Plummer, T. Nguyen, L. Garamszegi, J.-A.E. Månson, *Rheological and physical properties of aliphatic hyperbranched polyesters*. *J Polym Sci Pol Phys* **2004**, *42*, 1218-1225.
113. L. Boogh, B. Pettersson, J.-A.E. Månson, *Dendritic hyperbranched polymers as tougheners for epoxy resins*. *Polymer* **1999**, *40*, 2249-2261.
114. R. Mezzenga, L. Boogh, B. Pettersson, J.-A.E. Månson, *Chemically induced phase separated morphologies in epoxy resin-hyperbranched polymer blends*. *Macromol Sy* **2000**, *149*, 17-22.
115. L. Boogh, G. Jannerfeldt, B. Pettersson, H. Björnberg, J.-A.E. Månson, *ICCM-12 Conference, Paris, France, 1999*.
116. J.F. Hwang, J.-A.E. Månson, R.W. Hertzberg, G.A. Miller, L.H. Sperling, *Structure-property relationships in rubber-toughened epoxies*. *Polym Eng Sci* **1989**, *29*, 1466-1476.
117. J.F. Hwang, J.-A.E. Månson, R.W. Hertzberg, G.A. Miller, L.H. Sperling, *Fatigue crack-propagation of rubber-toughened epoxies*. *Polym Eng Sci* **1989**, *29*, 1477-1487.
118. D. Ratna, O. Becker, R. Krishnamurthy, G.P. Simon, R.J. Varley, *Nanocomposites based on a combination of epoxy resin, hyperbranched epoxy and a layered silicate*. *Polymer* **2003**, *44*, 7449-7457.
119. N.R. Choudhury, *Template mediated hybrid from dendrimer*. *J Sol-Gel Sci Techn* **2004**, *31*, 37-45.
120. H.H. Zou, Y.B. Zhao, W.F. Shi, *Preparation and properties of proton conducting organic-inorganic hybrid membranes based on hyperbranched aliphatic polyester and phosphoric acid*. *J Membrane Sci* **2004**, *245*, 35-40.

121. J.H. Zou, Y.B. Zhao, W.F. Shi, X.F. Shen, K.M. Nie, *Preparation and characters of hyperbranched polyester-based organic-inorganic hybrid material compared with linear polyester*. Polym Advan Technol **2005**, 16, 55-60.
122. R. Vestberg, A.M. Piekarski, E.D. Pressly, K.Y. Van Berkel, M. Malkoch, J. Gerbac, N. Ueno, C.J. Hawker, *A general strategy for highly efficient nanoparticle dispersing agents based on hybrid dendritic linear block copolymers*. J Polym Sci Pol Chem **2009**, 47, 1237-1258.
123. L. Fogelstrom, P. Antoni, E. Malmstrom, A. Hult, *UV-curable hyperbranched nanocomposite coatings*. Prog Org Coat **2006**, 55, 284-290.
124. J. Jansen, E.M.M. Debrabandervandenberg, E.W. Meijer, *Encapsulation of guest molecules into a dendritic box*. Science **1994**, 266, 1226-1229.
125. J. Jansen, R.A.J. Janssen, E.M.M. Debrabandervandenberg, E.W. Meijer, *Triplet radical pairs of 3-carboxyproxyl encapsulated in a dendritic box*. Adv Mater **1995**, 7, 561-564.
126. D.A. Tomalia, L.A. Reyna, S. Svenson, *Dendrimers as multi-purpose nanodevices for oncology drug delivery and diagnostic imaging*. Biochem Soc T **2007**, 35, 61-67.
127. C. Ternat, G. Kreutzer, C.J.G. Plummer, T.O. Nguyen, A. Herrmann, L. Ouali, H. Sommer, W. Fieber, M.I. Velazco, H.A. Klok, J.-A.E. Månson, *Amphiphilic multi-arm star-block copolymers for encapsulation of fragrance molecules*. Macromol Chem Phys **2007**, 208, 131-145.
128. D. Tomalia, P.R. Dvornic, *Catalysis - what promise for dendrimers*. Nature **1994**, 372, 617-618.
129. H.Y. Wei, H.G. Kou, W.F. Shi, K.M. Nie, Y.C. Zhan, *Photopolymerizable hyperbranched (meth)acrylated poly(amine ester)*. J Appl Polym Sci **2003**, 87, 168-173.
130. M. Sangermano, G. Malucelli, R. Bongiovanni, A. Priola, A. Harden, N. Rehnberg, *Hyperbranched polymers in cationic photopolymerization of epoxy systems*. Polym Eng Sci **2003**, 43, 1460-1465.
131. N. Moszner, T. Volkel, V. Rheinberger, *Synthesis, characterization and polymerization of dendrimers with methacrylic end groups*. Macromol Chem Phys **1996**, 197, 621-631.
132. M. Sangermano, A. Di Gianni, G. Malucelli, C. Roncuzzi, A. Priola, B. Voit, *Cationic photopolymerization of oxetane-functionalized hyperbranched polymers*. J Appl Polym Sci **2005**, 97, 293-299.
133. M. Sangermano, A. Priola, G. Malucelli, R. Bongiovanni, A. Quaglia, B. Voit, A. Ziemer, *Phenolic hyperbranched polymers as additives in cationic photopolymerization of epoxy systems*. Macromol Mater Eng **2004**, 289, 442-446.
134. J. Lange, E. Stenroos, E. Malmstrom, M. Johansson, *Barrier coatings for flexible packaging based on hyperbranched polyester resins*. Abstr Pap Am Chem S **2001**, 221, U444-U444.
135. M. Sangermano, A. Di Gianni, R. Bongiovanni, A. Priola, B. Voit, D. Pospiech, D. Appelhans, *Synthesis of fluorinated hyperbranched polymers and their use as additives in cationic photopolymerization*. Macromol Mater Eng **2005**, 290, 721-725.
136. A. Di Gianni, M. Sangermano, G. Malucelli, B. Voit, *Synthesis of alkyl-functionalized hyperbranched polymers and their use as additives in cationic photopolymerization of epoxy resins*. Macromol Mater Eng **2006**, 291, 1004-1012.
137. H.L. Wang, S.P. Xu, W.F. Shi, *Photopolymerization behaviors of hyperbranched polyphosphonate acrylate and properties of the UV cured film*. Prog Org Coat **2009**, 65, 417-424.
138. S.J. Wang, X.D. Fan, J. Kong, X. Wang, G.B. Zhang, *Synthesis and characterization of UV curable hyperbranched poly(siloxyselane)*. Acta Polym Sin **2006**, 1024-1028.
139. G.B. Zhang, X.D. Fan, Y.Y. Liu, J. Kong, S.J. Wang, *Syntheses of UV-curable hyperbranched polyseloxanes and studies on their photo-curing behavior*. Acta Polym Sin **2007**, 644-651.
140. H.G. Kou, A. Asif, W.F. Shi, *Photopolymerizable acrylated hyperbranched polyisophthalesters used for photorefractive materials I. Synthesis and characterization*. Eur Polym J **2002**, 38, 1931-1936.
141. Q.F. Si, X.D. Fan, X. Wang, S.J. Wang, *Synthesis and curing behaviors of UV curable hyperbranched polysiloxane*. Acta Polym Sin **2005**, 947-952.
142. C. Decker, *Photoinitiated crosslinking polymerisation*. Prog Poly Sci **1996**, 21, 593-650.
143. J.G. Kloosterboer. In *Advances in polymer science 84*; Springer-Verlag: Berlin Heidelberg, **1988**.
144. C. Decker, *UV-curing chemistry - past, present, and future*. J Coat Technol **1987**, 59, 97-106.

145. J.P. Fouassier, J.F. Rabek, *Radiation curing in polymer science and technology*. Elsevier Science Publishers Ltd, **1993**.
146. C. Decker, S. Biry, *Light stabilisation of polymers by radiation-cured acrylic coatings*. Prog Org Coat **1996**, 29, 81-87.
147. N. Emami, K.J.M. Soderholm, L.A. Berglund, *Effect of light power density variations on bulk curing properties of dental composites*. J Dent **2003**, 31, 189-196.
148. T. Scherzer, U. Decker, *3rd International symposium on ionizing radiation and polymers (IRaP)*, Weinbohl, Germany, **1998**, 306-312.
149. C.E. Hoyle. In *Radiation curing: Science and technology*. S.P. Pappas, Ed.; Plenum Press: New York, **1992**.
150. C.S.B. Ruiz, L.D.B. Machado, J.E. Volponi, E.S. Pino, *Oxygen inhibition and coating thickness effects on UV radiation curing of weatherfast clearcoats studied by photo-DSC*. J Therm Anal Calorim **2004**, 75, 507-512.
151. J. Nie, L.A. Linden, J.F. Rabek, J. Ekstrand, *Photocuring of mono- and di-functional (meth)acrylates with tris [2-(acryloyloxy)ethyl]isocyanurate*. Eur Polym J **1999**, 35, 1491-1500.
152. C. Decker, K. Moussa, *Kinetic-study of the cationic photopolymerization of epoxy monomers*. J Polym Sci Pol Chem **1990**, 28, 3429-3443.
153. G.B. Zhang, X.D. Fan, J. Kong, Y.Y. Liu, *Kinetic study on UV-curing of hyperbranched polysiloxane*. Polym Bull **2008**, 60, 863-874.
154. S.J. Wang, X.D. Fan, J. Kong, Y.Y. Liu, *Synthesis, characterization, and UV curing kinetics of hyperbranched polycarbosilane*. J Appl Polym Sci **2008**, 107, 3812-3822.
155. E. Andrzejewska, M.B. Bogacki, M. Andrzejewski, *The autocatalytic model of photopolymerization of dimethacrylates*. Polimery **2001**, 46, 549-551.
156. E. Andrzejewska, L.A. Linden, J.F. Rabek, *Modelling the kinetics of photoinitiated polymerization of di(meth)acrylates*. Polym Int **1997**, 42, 179-187.
157. L. Lecamp, B. Youssef, C. Bunel, P. Lebaudy, *Photoinitiated polymerization of a dimethacrylate oligomer: 2. Kinetic studies*. Polymer **1999**, 40, 1403-1409.
158. Y.F. Liu, M. Zhao, S.G. Shen, J.G. Gao, *Curing kinetics, thermal property, and stability of tetrabromo-bisphenol-A epoxy resin with 4,4'-diaminodiphenyl ether*. J Appl Polym Sci **1998**, 70, 1991-2000.
159. L. Lecamp, B. Youssef, C. Bunel, P. Lebaudy, *Photoinitiated polymerization of a dimethacrylate oligomer .1. Influence of photoinitiator concentration, temperature and light intensity*. Polymer **1997**, 38, 6089-6096.
160. O. Dudi, W.T. Grubbs, *Laser interferometric technique for measuring polymer cure kinetics*. J Appl Polym Sci **1999**, 74, 2133-2142.
161. T. Scherzer, U. Decker, *9th Tihany symposium on radiation chemistry*, Tatabanya, Hungary, **1998**, 615-619.
162. L. Lecamp, F. Houllier, B. Youssef, C. Bunel, *Photoinitiated cross-linking of a thiol-methacrylate system*. Polymer **2001**, 42, 2727-2736.
163. H.J. Timpe, B. Strehmel, F.H. Roch, K. Fritzsche, *Light-induced polymer and polymerization reactions .2. Kinetic-studies of the radical photopolymerization of butandiol 1,4-dimethacrylat in polyvinyl pyrrolidone layers by means of an isoperibolic calorimeter*. Acta Polym **1987**, 38, 238-244.
164. H. Thajudeen, V.S. Jamal Ahamed, K.T. Shabeer, *Phase transfer catalysis: polmerization kinetics and mechanism of methyl acrylate*. Int J Polym Mater **2008**, 57, 904-917.
165. W.D. Cook, *Thermal aspects of the kinetics of dimethacrylate photopolymerization*. Polymer **1992**, 33, 2152-2161.
166. N. Emami, K.J.M. Soderholm, *How light irradiance and curing time affect monomer conversion in light-cured resin composites*. Eur J Oral Sci **2003**, 111, 536-542.
167. W. Funke, *Reactive microgels - polymers intermediate in size between single molecules and particles*. Br Polym J **1989**, 21, 107-115.
168. A. Nebioglu, M.D. Soucek, *Microgel formation and thermo-mechanical properties of UV-curing unsaturated polyester acrylates*. J Appl Polym Sci **2008**, 107, 2364-2374.
169. A. Nebioglu, M.D. Soucek, *Reaction kinetics and microgel particle size characterization of ultraviolet-curing unsaturated polyester acrylates*. J Polym Sci Pol Chem **2006**, 44, 6544-6557.

170. B. Sun, T.L. Yu, *Effects of low-profile additives on the curing reaction of unsaturated polyester resins*. J Appl Polym Sci **1995**, 57, 7-23.
171. Y.S. Yang, L.J. Lee, *Microstructure formation in the cure of unsaturated polyester resins*. Polymer **1988**, 29, 1793-1800.
172. S.B. Kil, T. Augros, Y. Leterrier, J.-A.E. Manson, A. Christel, C. Borer, *Rheological properties of hyperbranched polymer/poly(ethylene terephthalate) reactive blends*. Polym Eng Sci **2003**, 43, 329-343.
173. E. Asmussen, A. Peutzfeldt, *Polymerization contraction of resin composite vs. energy and power density of light-cure*. Eur J Oral Sci **2005**, 113, 417-421.
174. R.L. Sakaguchi, H.X. Berge, *Reduced light energy density decreases post-gel contraction while maintaining degree of conversion in composites*. J Dent **1998**, 26, 695-700.
175. J.W. Stansbury, M. Trujillo-Lemon, H. Lu, X.Z. Ding, Y. Lin, J.H. Ge, *Conversion-dependent shrinkage stress and strain in dental resins and composites*. Dent Mater **2005**, 21, 56-67.
176. M. Atai, M. Ahmadi, S. Babanzadeh, D.C. Watts, *Synthesis, characterization, shrinkage and curing kinetics of a new low-shrinkage urethane dimethacrylate monomer for dental applications*. Dent Mater **2007**, 23, 1030-1041.
177. M. Wen, L.E. Scriven, A.V. McCormick, *Differential scanning calorimetry and cantilever deflection studies of polymerization kinetics and stress in ultraviolet curing of multifunctional (meth)acrylate coatings*. Macromolecules **2002**, 35, 112-120.
178. L.E. Schmidt, Y. Leterrier, J.M. Vesin, M. Wilhelm, J.-A.E. Manson, *Photo a) HL of fast UV-curing multifunctional acrylates*. Macromol Mater Eng **2005**, 290, 1115-1124.
179. S.S. Lee, A. Luciani, J.-A.E. Manson, *A rheological characterisation technique for fast UV-curable systems*. Prog Org Coat **2000**, 38, 193-197.
180. H.H. Winter, *Can the gel point of a cross-linking polymer be detected by the G' - G'' crossover*. Polym Eng Sci **1987**, 27, 1698-1702.
181. K. Hofmann, W.G. Glasser, *Cure monitoring of an epoxy-amine system by dynamic mechanical thermal-analysis (Dmta)*. Thermochim Acta **1990**, 166, 169-184.
182. J.K. Lee, J.Y. Choi, B.S. Lim, *Time-temperature-intensity-transformation cure diagram for visible light curable dimethacrylate resins*. Polym J **2003**, 35, 778-784.
183. B. Bilyeu, W. Brostow, *Separation of gelation from vitrification in curing of a fiber-reinforced epoxy composite*. Polym Compos **2002**, 23, 1111-1119.
184. A. Schiraldi, E. Pezzati, P. Baldini, *Epoxy polymers - temperature time transformation diagram by means of dsc investigations*. Thermochim Acta **1987**, 120, 315-323.
185. A. Endruweit, M.S. Johnson, A.C. Long, *Curing of composite components by ultraviolet radiation: A review*. Polym Compos **2006**, 27, 119-128.
186. P. Tomecek, V. Horakova, L. Lapcik, *The effect of various fillers on the cure behavior of an epoxy system*. J Polym Mater **2003**, 20, 399-402.
187. M.G. Lu, M. Shim, S. Kim, *Effect of filler on cure behavior of an epoxy system: Cure modeling*. Polym Eng Sci **1999**, 39, 274-285.
188. M. Ivankovic, I. Brnardic, H. Ivankovic, H.J. Mencer, *DSC study of the cure kinetics during nanocomposite formation: Epoxy/poly(oxypopylene) diamine/organically modified montmorillonite system*. J Appl Polym Sci **2006**, 99, 550-557.
189. T.M.G. Chu, J.W. Halloran, *Curing of highly loaded ceramic suspensions in acrylates*. J Am Ceram Soc **2000**, 83, 2375-2380.
190. C. Decker, L. Keller, K. Zahouily, S. Benfarhi, *Synthesis of nanocomposite polymers by UV-radiation curing*. Polymer **2005**, 46, 6640-6648.
191. E. Amerio, M. Sangermano, G. Malucelli, A. Priola, B. Voit, *Preparation and characterization of hybrid nanocomposite coatings by photopolymerization and sol-gel process*. Polymer **2005**, 46, 11241-11246.
192. F.S. Li, S.X. Zhou, B. You, L.M. Wu, *Kinetic study on the UV-induced photopolymerization of epoxy acrylate/TiO₂ nanocomposites by FTIR spectroscopy*. J Appl Polym Sci **2006**, 99, 3281-3287.
193. M. Harsch, J. Karger-Kocsis, M. Holst, *Influence of fillers and additives on the cure kinetics of an epoxy/anhydride resin*. Eur Polym J **2007**, 43, 1168-1178.
194. A. Di Gianni, R. Bongiovanni, S. Turri, F. Deflorian, G. Malucelli, G. Rizza, *UV-cured coatings based on waterborne resins and SiO₂ nanoparticles*. J Coat Technol Res **2009**, 6, 177-185.

195. C. Croutxé-Barghorn, D.-L. Versace, A. Chemtob, *RadTech Europe*, **2007**.
196. N. Altmann, P.J. Halley, *The effects of fillers on the chemorheology of highly filled epoxy resins: I. Effects on cure transitions and kinetics*. *Polym Int* **2003**, 52, 113-119.
197. J.D. Cho, H.T. Ju, J.W. Hong, *Photocuring kinetics of UV-initiated free-radical photopolymerizations with and without silica nanoparticles*. *J Polym Sci Pol Chem* **2005**, 43, 658-670.
198. F. Roman, S. Montserrat, J.M. Hutchinson, *On the effect of montmorillonite in the curing reaction of epoxy nanocomposites*. *J Therm Anal Calorim* **2007**, 87, 113-118.
199. M. Braem, V.E. Vandoren, P. Lambrechts, G. Vanherle, *Determination of Young modulus of dental composites - a phenomenological model*. *J Mater Sci* **1987**, 22, 2037-2042.
200. R. Ruggerone, C.J.G. Plummer, N.N. Herrera, E. Bourgeat-Lami, J.-A.E. Månson, *Highly filled polystyrene-laponite nanocomposites prepared by emulsion polymerization*. *Eur Polym J* **2009**, 45, 621-629.
201. R. Ruggerone, C.J.G. Plummer, N.N. Herrera, E. Bourgeat-Lami, J.-A.E. Månson. In *Nanocomposite materials*. E. Kny, Ed.; Trans Tech Publications Ltd: Zurich, **2009**.
202. R.A. Vaia, J.F. Maguire, *Polymer nanocomposites with prescribed morphology: Going beyond nanoparticle-filled polymers*. *Chem Mater* **2007**, 19, 2736-2751.
203. O. Ishai, L.J. Cohen, *Effect of fillers and voids on compressive yield of epoxy composites*. *J Compos Mater* **1968**, 2, 302-315.
204. F. Bauer, R. Mehnert, *UV curable acrylate nanocomposites: Properties and applications*. *J Polym Res* **2005**, 12, 483-491.
205. K.C.M. Nair, S. Thomas, G. Groeninckx, *Thermal and dynamic mechanical analysis of polystyrene composites reinforced with short sisal fibres*. *Compos Sci Technol* **2001**, 61, 2519-2529.
206. Y.N. Qi, F. Xu, L.X. Sun, *Thermal stability and glass transition behavior of pani/mwnt composites*. *J Therm Anal Calorim* **2008**, 94, 137-141.
207. S. Yano, K. Iwata, K. Kurita, *Physical properties and structure of organic-inorganic hybrid materials produced by sol-gel process*. *Mat Sci Eng C-Bio S* **1998**, 6, 75-90.
208. C.K. Chan, I.M. Chu, *Effect of hydrogen bonding on the glass transition behavior of poly(acrylic acid)/silica hybrid materials prepared by sol-gel process*. *Polymer* **2001**, 42, 6089-6093.
209. J.C. Huang, C.B. He, Y. Xiao, K.Y. Mya, J. Dai, Y.P. Siow, *Polyimide/POSS nanocomposites: interfacial interaction, thermal properties and mechanical properties*. *Polymer* **2003**, 44, 4491-4499.
210. H.-B. Hsueh, C.-Y. Chen, *Preparation and properties of LDHs/polyimide nanocomposites*. *Polymer* **2003**, 44, 1151-1161.
211. S.Y. Gu, J. Ren, Q.F. Wang, *Rheology of poly(propylene)/clay nanocomposites*. *J Appl Polym Sci* **2004**, 91, 2427-2434.
212. Z.-D. Wang, J.-J. Lu, S.Y. Fu, S.-Q. Jiang, X.-X. Zhao, *Studies on thermal and mechanical properties of PI/SiO₂ nanocomposite films at low temperatures*. *Compos Part A-Appl S* **2006**, 37, 74-79.
213. K.C. Krogman, T. Druffel, M.K. Sunkara, *4th Topical conference on nanoscale science and engineering of the american-institute-of-chemical-engineers*, Austin, TX, USA, **2004**, S338-S343.
214. Y. Zhang, D. Wu, Y.H. Sun, S.Y. Peng, *12th International workshop on sol-gel-science and technology*, Sydney, Australia, **2003**, 19-24.
215. T. Druffel, O. Buazza, M. Lattis, S. Farmer, M. Spencer, N. Mandzy, E.A. Grulke, *Conference on nanophotonic materials V*, San Diego, CA, USA, **2008**, F300-F300.
216. T. Druffel, O. Buazza, M. Lattis, S. Farmer, *Conference on advances in thin-film coatings for optical applications V*, San Diego, CA, USA, **2008**, A670-A670.
217. W. Caseri, *Inorganic nanoparticles as optically effective additives for polymers*. *Chem Eng Commun* **2009**, 196, 549-572.
218. J. Franc, D. Blanc, A. Zerroukhi, Y. Chalamet, A. Last, N. Destouches, *Organo-silica-titania nanocomposite elaborated by sol-gel processing with tunable optical properties*. *Mat Sci Eng B-Solid* **2006**, 129, 180-185.
219. A. Jitianu, M. Gartner, M. Zaharescu, D. Cristea, E. Manea, *Experiments for inorganic-organic hybrid sol-gel films for micro- and nano-photonics*. *Mat Sci Eng C-Bio S* **2003**, 23, 301-306.

220. R.D. Raharjo, H.Q. Lin, D.E. Sanders, B.D. Freeman, S. Kalakkunnath, D.S. Kalika, *Relation between network structure and gas transport in crosslinked poly(propylene glycol diacrylate)*. J Membrane Sci **2006**, 283, 253-265.
221. B. Singh, J. Bouchet, G. Rochat, Y. Leterrier, J.-A.E. Manson, P. Fayet, *Ultra-thin hybrid organic/inorganic gas barrier coatings on polymers*. Surf Coat Tech **2007**, 201, 7107-7114.
222. T.C. Merkel, B.D. Freeman, R.J. Spontak, Z. He, I. Pinnau, P. Meakin, A.J. Hill, *Ultraparpermeable, reverse-selective nanocomposite membranes*. Science **2002**, 296, 519-522.
223. J. Qiu, J.M. Zheng, K.V. Peinemann, *Gas transport properties in a novel poly(trimethylsilylpropyne) composite membrane with nanosized organic filler trimethylsilylglucose*. Macromolecules **2006**, 39, 4093-4100.
224. K. Yano, A. Usuki, A. Okada, *Synthesis and properties of polyimide-clay hybrid films*. J Polym Sci Pol Chem **1997**, 35, 2289-2294.
225. C.K. Lee, T.M. Don, W.C. Lai, C.C. Chen, D.J. Lin, L.P. Cheng, *Preparation and properties of nano-silica modified negative acrylate photoresist*. Thin Solid Films **2008**, 516, 8399-8407.
226. K.E. Gonsalves, L. Merhari, H.P. Wu, Y.Q. Hu, *Organic-inorganic nanocomposites: Unique resists for nanolithography*. Adv Mater **2001**, 13, 703-714.
227. T.H. Fedynyshyn, S.P. Doran, M.L. Lind, I. Sondi, E. Matijevic. In *Advances in resist technology and processing xvii, pts 1 and 2*. F.M. Houlihan, Ed., **2000**.
228. S. Lee, J. Kwak, Y. Oh, H.S. Lee, *Thermal imprint lithography onto filler incorporated composite resin*. Jpn J Appl Phys **2009**, 48, 06FH16:01-06.
229. P.T. Wang, J.B. Guo, H.H. Wang, Y. Zhang, J. Wei, *Functionalized multi-walled carbon nanotubes filled ultraviolet curable resin nanocomposites and their applications for nanoimprint lithography*. J Phys Chem C **2009**, 113, 8118-8123.
230. T. Fujigaya, S. Haraguchi, T. Fukumaru, N. Nakashima, *Development of novel carbon nanotube/photopolymer nanocomposites with high conductivity and application to nanoimprint photolithography*. Adv Mater **2008**, 20, 2151-2155.
231. S. Aura, V. Jokinen, L. Sainiemi, M. Baumann, S. Franssila, *UV-embossed inorganic-organic hybrid nanopillars for bioapplications*. J Nanosci Nanotechnol **2009**, 9, 6710-6715.
232. Y. Kuwahara, M. Morita, K. Yoshimori, K. Kumamaru, H. Endoh, T. Iwanaga, T. Nagami, T. Sawada, H. Shosenji, M. Sasaki, M. Goto, *Fabrication of nano-patterns composed of metal nanoparticles with photo-nanoimprint*. Jpn J Appl Phys **2008**, 47, 5171-5173.
233. P. Topart, R. Beaulieu, S. Leclair, M. Poirier, J. Pelletier, M. Bernier, H. Jerominek. In *Micromachining technology for micro-optics and nano-optics*. E.G. Johnson, Ed., **2003**.
234. V. Reboud, N. Kehagias, C.M.S. Torres, M. Zelsmann, M. Striccoli, M.L. Curri, A. Agostiano, M. Tamborra, M. Fink, F. Reuther, G. Gruetzner, *Spontaneous emission control of colloidal nanocrystals using nanoimprinted photonic crystals*. Appl Phys Lett **2007**, 90, 011115:011111-011113.
235. A. Bansal, H.C. Yang, C.Z. Li, R.C. Benicewicz, S.K. Kumar, L.S. Schadler, *Controlling the thermomechanical properties of polymer nanocomposites by tailoring the polymer-particle interface*. J Polym Sci Pol Phys **2006**, 44, 2944-2950.
236. S. Kang, S.I. Hong, C.R. Choe, M. Park, S. Rim, J. Kim, *Preparation and characterization of epoxy composites filled with functionalized nanosilica particles obtained via sol-gel process*. Polymer **2001**, 42, 879-887.
237. Y. Brechet, J.Y.Y. Cavaille, E. Chabert, L. Chazeau, R. Dendievel, L. Flandin, C. Gauthier, *Polymer based nanocomposites: Effect of filler-filler and filler-matrix interactions*. Adv Eng Mater **2001**, 3, 571-577.
238. K. Dahmouche, P.H. De Souza, T.J. Bonagamba, H. Paneppucci, P. Judeinstein, S.H. Pulcinelli, C.V. Santilli, *Investigation of new ion conducting ormolytes silica-polypropyleneglycol*. J Sol-Gel Sci Techn **1998**, 13, 909-913.
239. M. Misra, A. Guest, M. Tilley, *Hybrid inorganic-organic UV-curable abrasion-resistant coatings*. JOCCA-Surf Coat Int **1998**, 81, 594-595.
240. H.J. Glasel, F. Bauer, E. Hartmann, R. Mehnert, H. Mobus, V. Ptatschek, *Radiation-cured polymeric nanocomposites of enhanced surface-mechanical properties*. Nucl Instrum Meth B **2003**, 208, 303-308.

241. M.S.F. Samsudin, Z.A.M. Ishak, S.S. Jikan, Z.M. Ariff, A. Ariffin, *Effect of filler treatments on rheological behavior of calcium carbonate and talc-filled polypropylene hybrid composites*. J Appl Polym Sci **2006**, 102, 5421-5426.
242. E. Chabert, M. Bornert, E. Bourgeat-Lami, J.Y. Cavaille, R. Dendievel, C. Gauthier, U. Putaux, A. Zaoui, *Filler-filler interactions and viscoelastic behavior of polymer nanocomposites*. Mat Sci Eng A-Struct **2004**, 381, 320-330.
243. A.S. Sarvestani, E. Jabbari, *Modeling the viscoelastic response of suspension of particles in polymer solution: The effect of polymer-particle interactions*. Macromol Theor Simul **2007**, 16, 378-385.
244. R. Dangtungee, J. Yun, P. Supaphol, *Melt rheology and extrudate swell of calcium carbonate nanoparticle-filled isotactic polypropylene*. Polym Test **2005**, 24, 2-11.
245. F. Bauer, H.J. Glasel, U. Decker, H. Ernst, A. Freyer, E. Hartmann, V. Sauerland, R. Mehnert, *Trialkoxysilane grafting onto nanoparticles for the preparation of clear coat polyacrylate systems with excellent scratch performance*. Prog Org Coat **2003**, 47, 147-153.
246. F. Bauer, H. Ernst, D. Hirsch, S. Naumov, M. Pelzing, V. Sauerland, R. Mehnert, *Preparation of scratch and abrasion resistant polymeric nanocomposites by monomer grafting onto nanoparticles, 5(a) - Application of mass Spectroscopy and atomic force microscopy to the characterization of silane-modified silica surface*. Macromol Chem Phys **2004**, 205, 1587-1593.
247. Y.Y. Sun, Z.Q. Zhang, C.P. Wong, *Study on mono-dispersed nano-size silica by surface modification for underfill applications*. J Colloid Interf Sci **2005**, 292, 436-444.
248. C. Takai, M. Fuji, M. Takahashi, *A novel surface designed technique to disperse silica nano particle into polymer*. Colloid Surface A **2007**, 292, 79-82.
249. J.Q. Qin, H. Zhao, R.Q. Zhu, X.Y. Zhang, Y. Gu, *Effect of chemical interaction on morphology and mechanical properties of CPI-OH/SiO₂ hybrid films with coupling agent*. J Appl Polym Sci **2007**, 104, 3530-3538.
250. M. Pluta, A. Galeski, M. Alexandre, M.A. Paul, P. Dubois, *Poly(lactide)/montmorillonite nanocomposites and microcomposites prepared by melt blending: Structure and some physical properties*. J Appl Polym Sci **2002**, 86, 1497-1506.
251. M. Zanetti, G. Camino, P. Reichert, R. Mulhaupt, *Thermal behaviour of poly(propylene) layered silicate nanocomposites*. Macromol Rapid Commun **2001**, 22, 176-180.
252. X.P. Xia, C.S. Xie, S.Z. Cai, F. Wen, C.H. Zhu, X.L. Yang, *Effect of the loading and size of copper particles on the mechanical properties of novel Cu/LDPE composites for use in intrauterine devices*. Mat Sci Eng A-Struct **2006**, 429, 329-333.
253. A.H. Gomoll, W. Fitz, R.D. Scott, T.S. Thornhill, A. Bellare, *Nanoparticulate fillers improve the mechanical strength of bone cement*. Acta Orthop **2008**, 79, 421-427.
254. S.Y. Fu, X.Q. Feng, B. Lauke, Y.W. Mai, *Effects of particle size, particle/matrix interface adhesion and particle loading on mechanical properties of particulate-polymer composites*. Compos Part B-Eng **2008**, 39, 933-961.
255. S. Benfarhi, C. Decker, L. Keller, K. Zahouily, *Synthesis of clay nanocomposite materials by light-induced crosslinking polymerization*. Eur Polym J **2004**, 40, 493-501.
256. A. Tewari, A.M. Gokhale, *Nearest-neighbor distances between particles of finite size in three-dimensional uniform random microstructures*. Mat Sci Eng A-Struct **2004**, 385, 332-341.
257. J. Bicerano, J.F. Douglas, D.A. Brune, *Model for the viscosity of particle dispersions*. J Macromol Sci Rev Macromol Chem Phys **1999**, C39, 561-642.
258. L. Bokobza, *Multiwall carbon nanotube elastomeric composites: A review*. Polymer **2007**, 48, 4907-4920.
259. X.L. Xie, Y.W. Mai, X.P. Zhou, *Dispersion and alignment of carbon nanotubes in polymer matrix: A review*. Mat Sci Eng R **2005**, 49, 89-112.
260. M. Endo, M.S. Strano, P.M. Ajayan. In *Carbon nanotubes*, **2008**.
261. T. Kimura, H. Ago, M. Tobita, S. Ohshim, M. Kyotani, M. Yumura, *Polymer composites of carbon nanotubes aligned by a magnetic field*. Adv Mater **2002**, 14, 1380-1383.
262. K.A. Carrado, *Synthetic organo- and polymer-clays: Preparation, characterization, and materials applications*. Appl Clay Sci **2000**, 17, 1-23.
263. P.C. LeBaron, Z. Wang, T.J. Pinnavaia, *Polymer-layered silicate nanocomposites: An overview*. Appl Clay Sci **1999**, 15, 11-29.

264. E. Manias, A. Touny, L. Wu, K. Strawhecker, B. Lu, T.C. Chung, *Polypropylene/montmorillonite nanocomposites. Review of the synthetic routes and materials properties*. Chem Mater **2001**, 13, 3516-3523.
265. P. Reichert, J. Kressler, R. Thomann, R. Mulhaupt, G. Stoppelmann, *Nanocomposites based on a synthetic layer silicate and polyamide-12*. Acta Polym **1998**, 49, 116-123.
266. K. Yano, A. Usuki, A. Okada, T. Kurauchi, O. Kamigaito, *Synthesis and properties of polyimide clay hybrid*. J Polym Sci Pol Chem **1993**, 31, 2493-2498.
267. W.K. Goertzen, X. Sheng, M. Akinc, M.R. Kessler, *Rheology and curing kinetics of fumed silica/cyanate ester nanocomposites*. Polym Eng Sci **2008**, 48, 875-883.
268. R.C. Ball, P. Richmond, *Dynamics of colloidal dispersions*. Phys Chem Liq **1980**, 9, 99-116.
269. Y. Takao, M. Naito, *Particle aggregated structure in silica particle filled epoxy resin composite system*. J Chem Eng Jpn **2000**, 33, 317-322.
270. Y.J. Liu, X.L. Chen, *Evaluations of the effective material properties of carbon nanotube-based composites using a nanoscale representative volume element*. Mech Mater **2003**, 35, 69-81.
271. R.D. Maksimov, S. Gaidukovs, M. Kalnins, J. Zicans, E. Plume, *A nanocomposite based on a styrene-acrylate copolymer and native montmorillonite clay - 2. Modeling the elastic properties*. Mech Compos Mater **2006**, 42, 163-172.
272. K.K. Tseng, L.S. Wang, *Modeling and simulation of mechanical properties of nano-particle filled materials*. J Nanopart Res **2004**, 6, 489-494.
273. V. Cannillo, F. Bondioli, L. Lusvarghi, M. Montorsi, M. Avella, M.E. Errico, M. Mahnconco, *Modeling of ceramic particles filled polymer-matrix nanocomposites*. Compos Sci Technol **2006**, 66, 1030-1037.
274. K.K. Tseng, *A statistical micromechanics-based multi-scale framework for effective thermomechanical behaviours of particle reinforced composites*. Int J Solids Struct **2004**, 41, 295-304.
275. X.-G. Chen, J.-D. Guo, B. Zheng, Y.-Q. Li, S.-Y. Fu, G.-H. He, *Investigation of thermal expansion of PI/SiO₂ composite films by CCD imaging technique from -120 to 200 °C*. Compos Sci Technol **2007**, 67, 3006-3013.
276. Z. Hashin, S. Shtrikman, *A variational approach to the theory of the elastic behavior of multiphase materials*. J Mech Phys Solids **1963**, 11, 127-140.
277. J.L. Yang, Z. Zhang, A.K. Schlarb, K. Friedrich, *On the characterization of tensile creep resistance of polyamide 66 nanocomposites. Part II: Modeling and prediction of long-term performance*. Polymer **2006**, 47, 6745-6758.
278. Y. Kim, J.L. White, *Modeling of polymer/clay nanocomposite formation*. J Appl Polym Sci **2006**, 101, 1657-1663.
279. S. Paciornik, O.D.M. Gomes, A. Delarue, S. Schamm, D. Jeulin, A. Thorel, *Multi-scale analysis of the dielectric properties and structure of resin/carbon-black nanocomposites*. Eur Phys J-Appl Phys **2003**, 21, 17-26.
280. S.T. Knauert, J.F. Douglas, F.W. Starr, *The effect of nanoparticle shape on polymer-nanocomposite rheology and tensile strength*. J Polym Sci Pol Phys **2007**, 45, 1882-1897.
281. L. Berhan, A.M. Sastry, *Modeling percolation in high-aspect-ratio fiber systems. I. Soft-core versus hard-core models*. Phys Rev E **2007**, 75, 041120:041121-041128.
282. L. Berhan, A.M. Sastry, *Modeling percolation in high-aspect-ratio fiber systems. II. The effect of waviness on the percolation onset*. Phys Rev E **2007**, 75, 041121:041121-041127.
283. E.J. Garboczi, K.A. Snyder, J.F. Douglas, M.F. Thorpe, *Geometrical percolation-threshold of overlapping ellipsoids*. Phys Rev E **1995**, 52, 819-828.
284. C.Y. Li, T.W. Chou, *Continuum percolation of nanocomposites with fillers of arbitrary shapes*. Appl Phys Lett **2007**, 90, 174108:174101-174103.
285. F.H. Gojny, M.H.G. Wichmann, U. Kopke, B. Fiedler, K. Schulte, *Carbon nanotube-reinforced epoxy-compo sites: enhanced stiffness and fracture toughness at low nanotube content*. Compos Sci Technol **2004**, 64, 2363-2371.
286. E.T. Thostenson, T.-W. Chou, *Aligned multi-walled carbon nanotube-reinforced composites: Processing and mechanical characterization*. J Phys D Appl Phys **2002**, 35, L77-L80.
287. R. Kotsilkova, D. Nesheva, I. Nedkov, E. Krusteva, S. Stavrev, *Rheological, electrical, and microwave properties of polymers with nanosized carbon particles*. J Appl Polym Sci **2004**, 92, 2220-2227.

288. K. Saeed, S.-Y. Park, *Preparation of multiwalled carbon nanotube/nylon-6 nanocomposites by in situ polymerization*. J Appl Polym Sci **2007**, 106, 3729-3735.
289. A.V. Anikeenko, N.N. Medvedev, *Structure of hard sphere packings near Bernal density*. J Struct Chem **2009**, 50, 761-768.
290. K.D. Chandrasekhar, A. Venimadhav, A.K. Das, *High dielectric permittivity in semiconducting $\text{Pr}_{0.6}\text{Ca}_{0.4}\text{MnO}_3$ filled polyvinylidene fluoride nanocomposites with low percolation threshold*. Appl Phys Lett **2009**, 95, 062904:062901-062903.
291. Q. Zhang, L.A. Archer, *Poly(ethylene oxide)/silica nanocomposites: Structure and rheology*. Langmuir **2002**, 18, 10435-10442.
292. J.P. Cohenaddad, *Silica siloxane mixtures - structure of the adsorbed layer - chain-length dependence*. Polymer **1989**, 30, 1820-1823.
293. B.J. Anderson, C.F. Zukoski, *Rheology and microstructure of an unentangled polymer nanocomposite melt*. Macromolecules **2008**, 41, 9326-9334.
294. P. Rittigstein, R.D. Priestley, L.J. Broadbelt, J.M. Torkelson, *Model polymer nanocomposites provide an understanding of confinement effects in real nanocomposites*. Nat Mater **2007**, 6, 278-282.
295. J.H. vanZanten, W.E. Wallace, W.L. Wu, *Effect of strongly favorable substrate interactions on the thermal properties of ultrathin polymer films*. Phys Rev E **1996**, 53, R2053-R2056.
296. J.H. Kim, J. Jang, W.C. Zin, *Thickness dependence of the glass transition temperature in thin polymer films*. Langmuir **2001**, 17, 2703-2710.
297. A. Bansal, H.C. Yang, C.Z. Li, K.W. Cho, B.C. Benicewicz, S.K. Kumar, L.S. Schadler, *Quantitative equivalence between polymer nanocomposites and thin polymer films*. Nat Mater **2005**, 4, 693-698.
298. J. Berriot, H. Montes, F. Lequeux, D. Long, P. Sotta, *Evidence for the shift of the glass transition near the particles in silica-filled elastomers*. Macromolecules **2002**, 35, 9756-9762.
299. J. Berriot, H. Montes, F. Lequeux, D. Long, P. Sotta, *Gradient of glass transition temperature in filled elastomers*. Europhys Lett **2003**, 64, 50-56.
300. R.D. Priestley, C.J. Ellison, L.J. Broadbelt, J.M. Torkelson, *Structural relaxation of polymer glasses at surfaces, interfaces and in between*. Science **2005**, 309, 456-459.
301. A. Jitianu, A. Britchi, C. Deleanu, V. Badescu, M. Zaharescu, *Comparative study of the sol-gel processes starting with different substituted Si-alkoxides*. J Non-Cryst Solids **2003**, 319, 263-279.
302. J. Livage, C. Sanchez, *Sol-gel chemistry*. J Non-Cryst Solids **1992**, 145, 11-19.
303. R.A. Caruso, M. Antonietti, *Sol-gel nanocoating: An approach to the preparation of structured materials*. Chem Mater **2001**, 13, 3272-3282.
304. R.J.P. Corriu, D. Leclercq, *Recent developments of molecular chemistry for sol-gel processes*. Angew Chem Int Edit **1996**, 35, 1420-1436.
305. D.R. Uhlmann, G. Teowee, *Sol-gel science and technology: Current state and future prospects*. J Sol-Gel Sci Techn **1998**, 13, 153-162.
306. Z. Olejniczak, M. Leczka, K. Cholewa-Kowalska, K. Wojtach, M. Rokita, W. Mozgawa, *$\text{Si-}^{29}\text{MAS}$ NMR and FTIR study of inorganic-organic hybrid gels*. J Mol Struct **2005**, 744, 465-471.
307. K.G. Sharp, *Star alkoxysilane molecules, gels and appreciably tough glasses*. J Mater Chem **2005**, 15, 3812-3820.
308. H. Schmidt, G. Jonschker, S. Goedicke, M. Mennig, *The sol-gel process as a basic technology for nanoparticle-dispersed inorganic-organic composites*. J Sol-Gel Sci Techn **2000**, 19, 39-51.
309. C.J. Brinker, G.W. Scherer, *Sol-gel science*. Academic Press Inc, **1990**.
310. G. Schottner, *Hybrid sol-gel-derived polymers: Applications of multifunctional materials*. Chem Mater **2001**, 13, 3422-3435.
311. B.M. Novak, *Hybrid nanocomposite materials - between inorganic glasses and organic polymers*. Adv Mater **1993**, 5, 422-433.
312. M. Saric, H. Dietsch, P. Schurtenberger, *In situ polymerisation as a route towards transparent nanocomposites: Time-resolved light and neutron scattering experiments*. Colloid Surface A **2006**, 291, 110-116.

313. P. Fabbri, B. Singh, Y. Leterrier, J.-A.E. Månson, M. Messori, F. Pilati, *Cohesive and adhesive properties of polycaprolactone/silica hybrid coatings on poly(methyl methacrylate) substrates*. Surf Coat Tech **2006**, 200, 6706-6712.
314. X.H. Zhang, J.W. Yang, Z.H. Zeng, L. Huang, Y.L. Chen, H.H. Wang, *Stabilized dispersions of titania nanoparticles via a sol-gel process and applications in UV-curable hybrid systems*. Polym Int **2006**, 55, 466-472.
315. A. Di Gianni, S. Trabelsi, G. Rizza, M. Sangermano, H. Althues, S. Kaskel, B. Voit, *Hyperbranched polymer/TiO₂ hybrid nanoparticles synthesized via an in situ sol-gel process*. Macromol Chem Phys **2007**, 208, 76-86.
316. A. Bandyopadhyay, M. De Sarkar, A.K. Bhowmick, *Structure-property relationship in sol-gel derived polymer/silica hybrid nanocomposites prepared at various pH*. J Mater Sci **2006**, 41, 5981-5993.
317. Y.H. Han, A. Taylor, M.D. Mantle, K.M. Knowles, *Sol-gel-derived organic-inorganic hybrid materials*. J Non-Cryst Solids **2007**, 353, 313-320.
318. M.V. Kahraman, M. Kugu, Y. Menciloglu, N. Kayaman-Apohan, A. Gungor, *The novel use of organo alkoxy silane for the synthesis of organic-inorganic hybrid coatings*. J Non-Cryst Solids **2006**, 352, 2143-2151.
319. J. Livage, *Sol-gel processes*. Curr Opin Solid St M **1997**, 2, 132-138.
320. T. Takaki, K. Nishiura, Y. Mizuta, Y. Itou, *Advanced polymer-inorganic hybrid hard coatings utilizing in situ polymerization method*. J Nanosci Nanotechnol **2006**, 6, 3965-3968.
321. J.H. Zou, W.F. Shi, X.Y. Hong, *Characterization and properties of a novel organic-inorganic hybrid based on hyperbranched aliphatic polyester prepared via sol-gel process*. Compos Part A-Appl Sci **2005**, 36, 631-637.
322. A. Nebioglu, M.D. Soucek, *Reaction kinetics and network characterization of UV-curing polyester acrylate inorganic/organic hybrids*. Eur Polym J **2007**, 43, 3325-3336.
323. W.T.M. Jansen, J.T. van der Bruggen, J. Verhoef, A.C. Fluit, *Bacterial resistance: A sensitive issue - complexity of the challenge and containment strategy in Europe*. Drug Resist Update **2006**, 9, 123-133.
324. M.A. Moreno, L. Dominguez, T. Teshager, I.A. Herrero, M.C. Porrero, V.A.V. Network, *Antibiotic resistance monitoring: the Spanish programme*. Int J Antimicrob Ag **2000**, 14, 285-290.
325. L. Kelly, D.L. Smith, E.L. Snary, J.A. Johnson, A.D. Harris, M. Wooldridge, J.G. Morris, *Animal growth promoters: To ban or not to ban? A risk assessment approach*. Int J Antimicrob Ag **2004**, 24, 205-212.
326. W. Lukosz, D. Clerc, P.M. Nellen, C. Stamm, P. Weiss, *Output grating couplers on planar optical wave-guides as direct immunosensors*. Biosens Bioelectron **1991**, 6, 227-232.
327. P.M. Nellen, W. Lukosz, *Model experiments with integrated optical input grating couplers as direct immunosensors*. Biosens Bioelectron **1991**, 6, 517-525.
328. W. Lukosz, D. Clerc, P.M. Nellen, *Input and output grating couplers as integrated optical biosensors*. Sensor Actuat A-Phys **1991**, 25, 181-184.
329. J. Dubendorfer, R.E. Kunz, G. Jobst, I. Moser, G. Urban, *Integrated optical pH sensor using replicated chirped grating coupler sensor chips*. Sensor Actuat A-Chem **1998**, 50, 210-219.
330. F.C. Chien, C.Y. Lin, J.N. Yih, K.L. Lee, C.W. Chang, P.K. Wei, C.C. Sun, S.J. Chen, *Coupled waveguide-surface plasmon resonance biosensor with subwavelength grating*. Biosens Bioelectron **2007**, 22, 2737-2742.
331. S. Devanathan, M.C. Walker, Z. Salamon, G. Tollin, *Plasmon-waveguide resonance spectroscopy applied to three potential drug targets: Cyclooxygenase-2, hepatitis C virus RNA polymerase and integrin alpha V beta 3*. J Pharmaceut Biomed **2004**, 36, 711-719.
332. T. Kawaguchi, D.R. Shankaran, S.J. Kim, K.V. Gobi, K. Matsumoto, K. Toko, N. Miura, *Fabrication of a novel immunosensor using functionalized self-assembled monolayer for trace level detection of TNT by surface plasmon resonance*. Talanta **2007**, 72, 554-560.
333. R. Cush, J.M. Cronin, W.J. Stewart, C.H. Maule, J. Molloy, N.J. Goddard, *The resonant mirror - a novel optical biosensor for direct sensing of biomolecular interactions. 1. Principle of operation and associated instrumentation*. Biosens Bioelectron **1993**, 8, 347-353.
334. A. Brandenburg, *Differential refractometry by an integrated-optical Young interferometer*. Sensor Actuat A-Chem **1997**, 39, 266-271.

335. L.X. Yang, I. Akhatov, M. Mahinfalah, B.Z. Jang, *Nano-fabrication: A review*. J Chin Inst Eng **2007**, 30, 441-446.
336. L.G. Rosa, J. Liang, *Atomic force microscope nanolithography: dip-pen, nanoshaving, nanografting, tapping mode, electrochemical and thermal nanolithography*. J Phys-Condens Mat **2009**, 21.
337. I. Utke, P. Hoffmann, J. Melngailis, *Gas-assisted focused electron beam and ion beam processing and fabrication*. J Vac Sci Technol B **2008**, 26, 1197-1276.
338. R. Luttge, *Massively parallel fabrication of repetitive nanostructures: Nanolithography for nanoarrays*. J Phys D Appl Phys **2009**, 42, 123001.
339. K. Monkkonen, J. Lautanen, V. Kettunen, V.P. Leppanen, T.T. Pakkanen, T. Jaaskelainen, *Replication of an antireflecting element in COC plastics using a hot embossing technique*. J Mater Chem **2000**, 10, 2634-2636.
340. H. Lu, X.C. Shan, Y. Sun, S.H. Ng, A.C.W. Lu. In *International MEMS conference*; Journal of Physics: Conference Series: **2006**, 368-372.
341. J.P. Chu, H. Wijaya, C.W. Wu, T.R. Tsai, C.S. Wei, T.G. Nieh, J. Wadsworth, *Nanoimprint of gratings on a bulk metallic glass*. Appl Phys Lett **2007**, 90.
342. M.C. Paek, H.J. Ryu, D. Sur, Y. Park, K.Y. Kang, *14th International symposium on optical memory*, Jeju Isl, South Korea, **2004**, 3414-3415.
343. Y.N. Xia, J.A. Rogers, K.E. Paul, G.M. Whitesides, *Unconventional methods for fabricating and patterning nanostructures*. Chem Rev **1999**, 99, 1823-1848.
344. E. Fisslthaler, A. Blumel, K. Landfester, U. Scherf, E.J.W. List, *Printing functional nanostructures: a novel route towards nanostructuring of organic electronic devices via soft embossing, inkjet printing and colloidal self assembly of semiconducting polymer nanospheres*. Soft Matter **2008**, 4, 2448-2453.
345. H. Huang, C. Fu, *Different fabrication methods of out-of-plane polymer hollow needle arrays and their variations*. J Micromech Microeng **2007**, 17, 393-402.
346. H. Yabu, M. Shimomura, *Preparation of self-organized mesoscale polymer patterns on a solid substrate: Continuous pattern formation from a receding meniscus*. Adv Funct Mater **2005**, 15, 575-581.
347. S.Y. Chou, P.R. Krauss, P.J. Renstrom, *Imprint of sub-25 nm vias and trenches in polymers*. Appl Phys Lett **1995**, 67, 3114-3116.
348. S.Y. Chou, P.R. Krauss, P.J. Renstrom, *40th International conference on electron, ion, and photon beam technology and nanofabrication (EIBPN)*, Atlanta, GA, USA, **1996**, 4129-4133.
349. W.X. Zhou, M.B. Chan-Park, *Effect of oligomer length on the buckling of long and high aspect ratio microwalls UV embossed from oligomer/monomer mixtures*. Sensor Actuat A-Chem **2007**, 128, 12-22.
350. Y.F. Ding, H.W. Ro, J.F. Douglas, R.L. Jones, D.R. Hine, A. Karim, C.L. Soles, *Polymer viscoelasticity and residual stress effects on nanoimprint lithography*. Adv Mater **2007**, 19, 1377-+.
351. H. Magnusson, E. Malmstrom, A. Hult, *Synthesis of hyperbranched aliphatic polyethers via cationic ring-opening polymerization of 3-ethyl-3-(hydroxymethyl)oxetane*. Macromol Rapid Commun **1999**, 20, 453-457.
352. B. Kratochvil, P.K. Chattopadhyay, R.D. Krause, *Determination of olefins by direct titration with bromine in propylene carbonate*. Anal Chem **1976**, 48, 568-570.
353. M.J. Percy, J.I. Amalvy, D.P. Randall, S.P. Armes, S.J. Greaves, J.F. Watts, *Synthesis of vinyl polymer-silica colloidal nanocomposites prepared using commercial alcoholic silica sols*. Langmuir **2004**, 20, 2184-2190.
354. S.R. Raghavan, S.A. Khan, *Shear-thickening response of fumed silica suspensions under steady and oscillatory shear*. J Colloid Interf Sci **1997**, 185, 57-67.
355. K.S. Anseth, C.M. Wang, C.N. Bowman, *Reaction behavior and kinetic constants for photopolymerizations of multi(meth)acrylate monomers*. Polymer **1994**, 35, 3243-3250.
356. G.G. Stoney, *The tension of metallic films deposited by electrolysis*. Proc R Soc Lond Ser A **1909**, 82, 172-175.
357. Y. Inoue, Y. Kobatake, *Mechanics of adhesive points Part III. Evaluation of residual stress*. Appl Sci Res **1958**, A7, 314-324.

358. C.G. Dekruif, E.M.F. Vanlersel, A. Vrij, W.B. Russel, *Hard-sphere colloidal dispersions - viscosity as a function of shear rate and volume fraction*. J Chem Phys **1985**, 83, 4717-4725.
359. Z.D. Cheng, J.X. Zhu, P.M. Chaikin, S.E. Phan, W.B. Russel, *Nature of the divergence in low shear viscosity of colloidal hard-sphere dispersions*. Phys Rev E **2002**, 65.
360. G. Bossis, J.F. Brady, *The rheology of Brownian suspensions*. J Chem Phys **1989**, 91, 1866-1874.
361. J. Bender, N.J. Wagner, *Reversible shear thickening in monodisperse and bidisperse colloidal dispersions*. J Rheol **1996**, 40, 899-916.
362. D.R. Foss, J.F. Brady, *Structure, diffusion and rheology of Brownian suspensions by Stokesian dynamics simulation*. J Fluid Mech **2000**, 407, 167-200.
363. H.M. Laun, R. Bung, F. Schmidt, *Rheology of extremely shear thickening polymer dispersions (passively viscosity switching fluids)*. J Rheol **1991**, 35, 999-1034.
364. C.R. Lin, W.J. Chen, *The links-nodes-blobs model for shear-thinning-yield-stress fluids*. Colloid Polym Sci **1999**, 277, 1019-1025.
365. Q.D. Nguyen, D.V. Boger, *Measuring the flow properties of yield stress fluids*. Annu Rev Fluid Mech **1992**, 24, 47-88.
366. J.G. Curro, P. Pincus, *A theoretical basis for viscoelastic relaxation of elastomers in the long-time limit*. Macromolecules **1983**, 16, 559-562.
367. M. Kapnistos, M. Lang, D. Vlassopoulos, W. Pyckhout-Hintzen, D. Richter, D. Cho, T. Chang, M. Rubinstein, *Unexpected power-law stress relaxation of entangled ring polymers*. Nat Mater **2008**, 7, 997-1002.
368. L. Wang, Z.C. Tan, S.H. Meng, A. Druzhinina, R.A. Varushchenko, G.H. Li, *Heat capacity enhancement and thermodynamic properties of nanostructured amorphous SiO₂*. J Non-Cryst Solids **2001**, 296, 139-142.
369. D.Y. Jing, J.D. Ding, *Rheology of a polymer-based hybrid suspension composed of concentrated poly[(D,L-lactide)-co-glycolide] solution and inorganic salt particles*. Macromol Biosci **2007**, 7, 1290-1298.
370. A. Einstein, *A new determination of the molecular dimensions (vol 19, pg 289, 1906)*. Ann Phys **1911**, 34, 591-592.
371. I.M. Krieger, *Rheology of monodisperse latices*. Adv Colloid Interfac **1972**, 3, 111-136.
372. J.F. Douglas, E.J. Garboczi. In *Advances in chemical physics*, **1995**.
373. W.B. Russel, *The Huggins coefficient as a means for characterizing suspended particles*. J Chem Soc Faraday Trans 2 **1984**, 80, 31-41.
374. J.F. Brady, *The rheological behavior of concentrated colloidal dispersions*. J Chem Phys **1993**, 99, 567-581.
375. S.E. Phan, W.B. Russel, Z.D. Cheng, J.X. Zhu, P.M. Chaikin, J.H. Dunsmuir, R.H. Ottewill, *Phase transition, equation of state, and limiting shear viscosities of hard sphere dispersions*. Phys Rev E **1996**, 54, 6633-6645.
376. I.M. Krieger, T.J. Dougherty, *A mechanism for non-Newtonian flow in suspensions of rigid spheres*. T Soc Rheol **1959**, 3, 137-152.
377. E.J. Windhab, *Fluid immobilization - a structure-related key mechanism for the viscous flow behavior of concentrated suspension systems*. Appl Rheol **2000**, 10, 134-144.
378. B.J. Anderson, C.F. Zukoski, *Rheology and microstructure of entangled polymer nanocomposite melts*. Macromolecules **2009**, 42, 8370-8384.
379. D. Vickers, L.A. Archer, T. Floyd-Smith, *Synthesis and characterization of cubic cobalt oxide nanocomposite fluids*. Colloid Surface A **2009**, 348, 39-44.
380. S. Arrhenius, *Über die innere Reibung verdünnter wässriger Lösungen*. Z Phys Chem **1887**, 1, 285.
381. D.G. Thomas, *Transport characteristics of suspension. 8. A note on viscosity of Newtonian suspensions of uniform spherical particles*. J Coll Sci **1965**, 20, 267-&.
382. H. Eyring, D. Henderson, B.J. Stover, E.M. Eyring, *Statistical mechanics and dynamics*. Wiley: New York, **1964**.
383. J.L. Das Kanungo, J.L. McAtee, *Effects of polymers and clay concentrations on the viscosities of organo-smectite dispersions under high pressure*. Appl Clay Sci **1986**, 1, 285-293.
384. J.H.E. Hone, A.M. Howe, *Viscosity of colloidal suspensions in aqueous gelatin*. J Colloid Interf Sci **2002**, 251, 193-199.

385. S. Uppuluri, S.E. Keinath, D.A. Tomalia, P.R. Dvornic, *Rheology of dendrimers. I. Newtonian flow behavior of medium and highly concentrated solutions of polyamidoamine (PAMAM) dendrimers in ethylenediamine (EDA) solvent*. *Macromolecules* **1998**, *31*, 4498-4510.
386. I.B. Rietveld, D. Bedeaux, *The viscosity of solutions of poly(propylene imine) dendrimers in methanol*. *J Colloid Interf Sci* **2001**, *235*, 89-92.
387. S. Kheirandish, I. Gubaydullin, N. Willenbacher, *Shear and elongational flow behavior of acrylic thickener solutions. Part II: Effect of gel content*. *Rheol Acta* **2009**, *48*, 397-407.
388. R. Borrega, M. Cloitre, I. Betremieux, B. Ernst, L. Leibler, *Concentration dependence of the low-shear viscosity of polyelectrolyte micro-networks: From hard spheres to soft microgels*. *Europhys Lett* **1999**, *47*, 729-735.
389. H. Senff, W. Richtering, *Influence of cross-link density on rheological properties of temperature-sensitive microgel suspensions*. *Colloid Polym Sci* **2000**, *278*, 830-840.
390. I.D. Sideridou, M.M. Karabela, *Effect of the structure of silane-coupling agent on dynamic mechanical properties of dental resin-nanocomposites*. *J Appl Polym Sci* **2008**, *110*, 507-516.
391. F.D. Blum, P. Krisanangkura, *Comparison of differential scanning calorimetry, FTIR, and NMR to measurements of adsorbed polymers*. *Thermochim Acta* **2009**, *492*, 55-60.
392. B. Metin, F.D. Blum, *Segmental dynamics in poly(methyl acrylate) on silica: Effect of surface treatment*. *Langmuir* **2010**, *26*, 5226-5231.
393. S.I. Gusev, S.D. Zaitsev, Y.D. Semchikov, O.G. Zakharova, *A method for determining the molecular weight of hyperbranched polymers*. *Russ J Appl Chem* **2006**, *79*, 1338-1340.
394. H. Ishida, J.D. Miller, *Substrate effects on the chemisorbed and physisorbed layers of methacryl silane modified particulate minearals*. *Macromolecules* **1984**, *17*, 1659-1666.
395. A. Sargsyan, A. Tonoyan, S. Davtyan, C. Schick, *The amount of immobilized polymer in PMMA SiO₂ nanocomposites determined from calorimetric data*. *Eur Polym J* **2007**, *43*, 3113-3127.
396. A. Leszczynska, K. Pielichowski, *Application of thermal analysis methods for characterization of polymer/montmorillonite nanocomposites*. *J Therm Anal Calorim* **2008**, *93*, 677-687.
397. R. Sanctuary, J. Baller, J.K. Kruger, D. Schaefer, R. Bactavatchalou, B. Wetzel, W. Possart, P. Alnot, *Complex specific heat capacity of two nanocomposite systems*. *Thermochim Acta* **2006**, *445*, 111-115.
398. J. Baller, N. Becker, M. Ziehmer, M. Thomassey, B. Zielinski, U. Muller, R. Sanctuary, *Interactions between silica nanoparticles and an epoxy resin before and during network formation*. *Polymer* **2009**, *50*, 3211-3219.
399. R.B. Bogoslovov, C.M. Roland, A.R. Ellis, A.M. Randall, C.G. Robertson, *Effect of silica nanoparticles on the local segmental dynamics in poly(vinyl acetate)*. *Macromolecules* **2008**, *41*, 1289-1296.
400. H. Oh, P.F. Green, *Polymer chain dynamics and glass transition in athermal polymer/nanoparticle mixtures*. *Nat Mater* **2009**, *8*, 139-143.
401. J.L. Lewin, K.A. Maerzke, N.E. Schultz, R.B. Ross, J.I. Siepmann, *Prediction of hildebrand solubility parameters of acrylate and methacrylate monomers and their mixtures by molecular simulation*. *J Appl Polym Sci* **2010**, *116*, 1-9.
402. S.E. Harton, S.K. Kumar, H.C. Yang, T. Koga, K. Hicks, E. Lee, J. Mijovic, M. Liu, R.S. Vallery, D.W. Gidley, *Immobilized polymer layers on spherical nanoparticles*. *Macromolecules* **2010**, *43*, 3415-3421.
403. C.E. Corcione, A. Greco, A. Maffezzoli, *Time-temperature and time-irradiation intensity superposition for photopolymerization of an epoxy based resin*. *Polymer* **2005**, *46*, 8018-8027.
404. J.M. Frigerio. In *La couleur - lumière, vision et matériaux*. M. Elias, J. Lafait, Eds.; Belin: Paris, **2006**.
405. R. Chandra, R.K. Soni, S.S. Murthy, *Studies on the kinetics of radical Initiated photocopolymerisation of di(vinyl 2-hydroxy propanoate)ether of bisphenol-a and monomers*. *Polym Int* **1993**, *31*, 305-314.
406. M.R. Kamal, *Thermoset characterization for modability analysis*. *Polym Eng Sci* **1974**, *14*, 231-239.
407. H.J. Timpe, B. Strehmel, *Irradiation-induced polymer and polymerization reactions .44. On the kinetics of the free-radical photopolymerization of diacrylates in polymeric binders*. *Makromol Chem* **1991**, *192*, 779-791.

408. S. Dalle Vacche, V. Geiser, Y. Leterrier, J.-A.E. Månson, *Time-intensity superposition for photoinitiated polymerization of fluorinated and hyperbranched acrylate nanocomposites*. *Polymer* **2010**, *51*, 334-341.
409. L. Feng, B.I. Suh, *Exposure reciprocity law in photopolymerization of multi-functional acrylates and methacrylates*. *Macromol Chem Phys* **2007**, *208*, 295-306.
410. C. Decker, B. Elzaouk, D. Decker, *Kinetic study of ultrafast photopolymerization reactions*. *J Macromol Sci A* **1996**, *A33*, 173-190.
411. E.L. Rodriguez. In *Assignment of the glass transition*. R.J. Seyler, Ed.; American Society for Testing and Materials: Philadelphia **1994**.
412. H.E. Bair. In *Assignment of the glass transition*. R.J. Reyler, Ed.; American Society for Testing and Materials: Philadelphia, **1994**.
413. C.L. Hsieh, W.H. Tuan, *Thermal expansion behavior of a model ceramic-metal composite*. *Mat Sci Eng A-Struct* **2007**, *460*, 453-458.
414. L.E. Schmidt, S. Yi, Y.H. Jin, Y. Leterrier, Y.H. Cho, J.-A.E. Månson, *Acrylated hyperbranched polymer photoresist for ultra-thick and low-stress high aspect ratio micropatterns*. *J Micromech Microeng* **2008**, *18*, 045022:045021-045028.
415. P.W. de Oliveira, C. Becker-Willinger, M.H. Jilavi, *Sol-gel derived nanocomposites for optical applications*. *Adv Eng Mater* **2010**, *12*, 349-361.
416. Y.A. Shchipunov, T.Y. Karpenko, A.V. Krekoten, *Hybrid organic-inorganic nanocomposites fabricated with a novel biocompatible precursor using sol-gel processing*. *Compos Interface* **2005**, *11*, 587-607.
417. E. Amerio, Thesis, Politecnico di Torino **2008**.
418. Y.H. Jin, Y.H. Cho, L.E. Schmidt, Y. Leterrier, J.-A.E. Månson, *A fast low-temperature micromolding process for hydrophilic microfluidic devices using UV-curable acrylated hyperbranched polymers*. *J Micromech Microeng* **2007**, *17*, 1147-1153.
419. K. Cottier, R.E. Kunz, H.P. Herzig, *Efficient and practical modeling of finite waveguide grating couplers*. *Jpn J Appl Phys 1* **2004**, *43*, 5742-5746.
420. B.A. Davis, P.J. Gramman, *Compression molding*. Hanser Verlage, **2003**.
421. A.A. Akl, H. Kamal, K. Abdel-Hady, *Fabrication and characterization of sputtered titanium dioxide films*. *Appl Surf Sci* **2006**, *252*, 8651-8656.
422. S.B. Amor, L. Guedri, G. Baud, M. Jacquet, M. Ghedira, *Influence of the temperature on the properties of sputtered titanium oxide films*. *Mater Chem Phys* **2003**, *77*, 903-911.
423. S. Lee, S.G. Rhee, S.G. Oh, *Spectro-ellipsometric studies of sputtered amorphous titanium dioxide thin films: Simultaneous determination of refractive index, extinction coefficient, and void distribution*. *J Korean Phys Soc* **1999**, *34*, 319-322.
424. S. Selvarasah, S.-H. Chao, C.-L. Chen, D. Mao, J. Hopwood, S. Ryley, A. Busnaina, M.R. Dokmeci, *Society of experimental mechanics 8th international symposium on MEMS and nanotechnology*, Springfield, MA, USA, **2007**, 45-51.
425. F. Karouta, B. Doctor, A.A.M. Kok, E.J. Geluk, J.J.G.M. v.d. Tol, M.K. Smit, *ECS Meeting*, Vancouver, Canada, **2010**
426. B. Wunderlich, Y.M. Jin, A. Boller, *Mathematical-description of differential scanning calorimetry based on periodic temperature modulation*. *Thermochim Acta* **1994**, *238*, 277-293.
427. M. Reading, A. Luget, R. Wilson, *Modulated differential scanning calorimetry*. *Thermochim Acta* **1994**, *238*, 295-307.
428. J.E.K. Schawe, *Principles for the interpretation of modulated temperature DSC measurements. 1. Glass-transition*. *Thermochim Acta* **1995**, *261*, 183-194.
429. J.M. Hutchinson, *Determination of the glass transition temperature*. *J Therm Anal Calorim* **2009**, *98*, 579-589.
430. J.M. Hutchinson, S. Montserrat, *The application of modulated differential scanning calorimetry to the glass transition of polymers .1. A single-parameter theoretical model and its predictions*. *Thermochim Acta* **1996**, *286*, 263-296.
431. J.M. Hutchinson, S. Montserrat, *The application of temperature-modulated DSC to the glass transition region II. Effect of a distribution of relaxation times*. *Thermochim Acta* **2001**, *377*, 63-84.

- 432. N.R. Pradhan, G.S. Iannacchione, *Thermal properties and glass transition in PMMA plus SWCNT composites*. J Phys D Appl Phys **2010**, *43*, 305403:305401-305409.
- 433. S.L. Simon, G.B. McKenna, *Quantitative analysis of errors in TMDSC in the glass transition region*. Thermochim Acta **2000**, *348*, 77-89.
- 434. S.L. Simon, G.B. McKenna, *The effects of structural recovery and thermal lag in temperature-modulated DSC measurements*. Thermochim Acta **1997**, *307*, 1-10.

PUBLICATIONS RELATED TO THIS WORK

JOURNAL PUBLICATIONS

- V. Geiser, Y. Leterrier, J.-A.E. Månson, **“Conversion and shrinkage analysis of acrylated hyperbranched polymer nanocomposites”**, *Journal of Applied Polymer Science*, 114 (3), 1954-1963, 2009.
- S. Dalle Vacche, V. Geiser, Y. Leterrier, J.-A.E. Månson, **“Time-intensity superposition for photoinitiated polymerization of fluorinated and hyperbranched acrylate nanocomposites”**, *Polymer*, 51, 334-341, 2010.
- V. Geiser, Y.-H. Jin, Y. Leterrier, J.-A.E. Månson, **“Nanoimprint lithography with UV-curable hyperbranched polymer nanocomposites”**, accepted by *Macromolecular Symposia*.
- V. Geiser, Y. Leterrier, J.-A.E. Månson, **“Rheological behavior of concentrated hyperbranched polymer/silica nanocomposite suspensions”**, *Macromolecules*, 43, 7705-7712, 2010.
- V. Geiser, Y. Leterrier, J.-A.E. Månson, G. Voirin, M. Wiki, **“Nanoimprint lithography with UV-curable hyperbranched polymer nanocomposites for optical biosensing applications”**, accepted by *MRS Symposia Proceedings*.
- R. Ruggerone, V. Geiser, Y. Leterrier, J.-A.E. Månson, **“Immobilized polymer fraction in hyperbranched polymer/silica nanocomposite suspensions”**, accepted by *Macromolecules*.
- V. Geiser, Y. Leterrier, J.-A.E. Månson, **“HBP/silica nanostructures produced by UV-curing and sol-gel processing”**, manuscript in preparation.

CONFERENCES

- V. Geiser, Y. Leterrier, J.-A.E. Månson, **“Nano-imprint lithography with UV-curable hyperbranched polymer nanocomposites”**, in *European Polymer Conference EPF*, 2009, Graz, Austria.
- V. Geiser, Y. Leterrier, J.-A.E. Månson, G. Voirin, M. Wiki, **“Nanoimprint lithography with UV-curable hyperbranched polymer nanocomposites for optical biosensing applications”**, in *Materials Research Society Spring Meeting*, 2010, San Francisco, United States.

CURRICULUM VITAE

Valérie Geiser

Date of birth: 14th June 1980

Avenue Mon-Repos 2

Nationality: Swiss

1005 Lausanne

valerie.geiser@gmail.com

EDUCATION

11/2006 – present

Ecole Polytechnique Fédérale de Lausanne,
Laboratory of Polymer and Composite Technology,
Prof. Jan-Anders E. Månson
Ph.D. Thesis: “Low-Stress UV-Curable Hyperbranched
Polymer Nanocomposite for High Precision Devices”

10/2001 – 09/2006

Eidgenössische Technische Hochschule Zürich,
Materials Science and Engineering
Diploma Thesis: “Particle Stabilized PVDF Foams with
Piezoelectric Properties”

09/2004 – 06/2005

University of Cambridge, UK
Exchange student (ERASMUS scholarship)

WORK EXPERIENCE

09/2005 – 09/2006

PricewaterhouseCoopers, Zürich
Independence Office (Compliance)

06/2005 – 09/2005

The Welding Institute, Cambridge, UK
Internship in Materials Defect Analysis Department